Local interactions and shell-model interactions from chiral effective field theory

Lokale- und Schalenmodell-Wechselwirkungen im Rahmen der chiralen effektiven Feldtheorie
Zur Erlangung des Grades eines Doktors der Naturwissenschaften (Dr. rer. nat.)
genehmigte Dissertation von M.Sc. Frank Lukas Huth aus Friedberg (Hessen)
Tag der Einreichung: 25.06.2018, Tag der Prüfung: 11.07.2018
Darmstadt — D 17

1. Gutachten: Prof. Ph.D. Achim Schwenk
2. Gutachten: Prof. Dr. Jens Braun

TECHNISCHE
UNIVERSITÄT
DARMSTADT

Fachbereich Physik
Institut für Kernphysik
Theoriezentrum

Local interactions and shell-model interactions from chiral effective field theory
Lokale- und Schalenmodell-Wechselwirkungen im Rahmen der chiralen effektiven Feldtheorie

Genehmigte Dissertation von M.Sc. Frank Lukas Huth aus Friedberg (Hessen)

1. Gutachten: Prof. Ph.D. Achim Schwenk
2. Gutachten: Prof. Dr. Jens Braun

Tag der Einreichung: 25.06.2018
Tag der Prüfung: 11.07.2018

Darmstadt — D 17

Bitte zitieren Sie dieses Dokument als:
URN: urn:nbn:de:tuda-tuprints-76458
URL: http://tuprints.ulb.tu-darmstadt.de/7645

Abstract

The strong force is a vital contribution to both, nucleon-nucleon interactions as well as complicated nuclear many-body systems. The theory of the strong interactions is quantum chromodynamics (QCD), but it is nonperturbative in the low-energy region of interest to us. Chiral effective field theory (EFT) provides a systematic framework to derive low-energy few-body interactions and currents, based on, and consistent with all relevant symmetries of QCD. Short-distance physics is not resolved explicitly and gets absorbed in contact terms with so-called low-energy constants (LECs), which are adjusted to experimental data. A power counting scheme sorts the different contributions according to their importance and a regularization scheme removes high-momentum modes which may otherwise lead to divergences. The resulting interactions are widely used in *ab initio* many-body calculations of nuclei and nuclear matter.

Recently, efforts have been directed towards the development of local interactions from chiral EFT that can be applied directly in Quantum Monte Carlo calculations. Thus, this enables one to investigate chiral interactions in this powerful and statistically exact many body methods. In the first half of this thesis, we construct and analyze local two-body interactions from chiral EFT. In particular, we construct soft local interactions at leading order (LO), next-to-leading order (NLO), and next-to-next-to-leading order (N^2LO) by enlarging the coordinate-space cutoff. Afterwards, we present first applications of the soft local interactions in ^{16}O–^{16}O nucleus-nucleus scattering from double-folding potentials. In addition, we investigate regulator and cutoff artifacts of local chiral interactions. We study effects from the violated Fierz-rearrangement freedom on phase shifts, nuclear matter calculations, and the ^{4}He ground-state energy. For this, we vary different LO-operator combinations for interactions at LO and NLO. Furthermore, the large-cutoff behavior of local interactions at LO on phase shifts is explored for different functional forms of the regulator and for different operator combinations over a wide range of the inverse coordinate-space cutoff. We find that the broken Fierz-rearrangement freedom has sizable consequences at LO, but it is restored to a great extend at NLO, where subleading contact interactions enter. For a particular choice of those operators, nucleon-nucleon phase shifts and the deuteron ground-state energy converge to cutoff-independent plateaus. Those plateaus are at the same values, independent of the functional form of regulators we investigate. Even though, this does not imply that the power counting scheme is renormalizable, it allows the construction of harder interactions.

In the second half, we construct valence-space Hamiltonians for shell-model calculations. The residual two-body interaction is based on symmetry principles and the low-momentum expansion from chiral EFT. We adjust the LECs to ground-state and excitation energies in the valence space. In addition to the usual free-space contact interactions, we also include novel center-of-mass–dependent operators that arise due to the Galilean invariance breaking by in-medium effects. We construct interactions up to fourth order (N^3LO) for the sd and $sd + 0f_{7/2}$ valence space. In the sd shell, at N^3LO, we obtain a root-mean-square deviation to experiment of 0.16 MeV which is similar to that obtained with the phenomenological universal sd-shell interactions USDA and USDB. Even though the precision of our interactions in the $sd + 0f_{7/2}$ valence space deteriorates, they provide interesting predictions for the one-neutron dripline of isotopes from oxygen to sodium. All our interactions lead to natural LECs and show promising predictions for ground-state energies and excitation spectra, which are not considered in the data set.

Zusammenfassung

Die starke Kraft liefert einen essenziellen Beitrag, sowohl in Nukleon-Nukleon Wechselwirkungen als auch in komplizierten Vielteilchensystemen. Die Theorie der starken Wechselwirkung wird durch die Quantenchromodynamik (QCD) beschrieben, welche jedoch im für uns relevanten Niederenergiebereich nicht störungstheoretisch behandelt werden kann. Die chirale effektive Feldtheorie (EFT) bietet eine systematische Herangehensweise, um niederenergetische Wechselwirkungen und Ströme basierend auf der QCD zu konstruieren. Sie stimmt mit alle relevanten Symmetrieeigenschaften der QCD überein. Kurzreichweitige physikalische Effekte werden nicht explizit aufgelöst, sondern in sogenannten Kontakttermen mit Niedrigenergiekonstanten (engl. low-energy constant (LEC)) absorbiert. Ein Ordnungsschema sortiert verschiedene Terme nach Wichtigkeit und ein Regulierungsmechanismus schneidet hochenergetische Beiträge ab. Letztere könnten ansonsten zu Divergenzen führen. Die LECs werden mittels experimenteller Daten bestimmt. Die resultierenden Wechselwirkungen sind weit verbreitet und finden Anwendung in *ab initio* Vielteilchenberechnungen von Atomkernen und Kernmaterie.

In den letzten Jahren wurde verstärkt an der Entwicklung von lokalen Wechselwirkungen im Rahmen der chiralen EFT gearbeitet. Diese können direkt in Berechnungen mit Quantum Monte Carlo Methoden verwendet werden. So ist es jetzt möglich chirale Wechselwirkungen mit dieser statistisch exakten Vielteilchenmethoden zu untersuchen. Im ersten Teil dieser Arbeit konstruieren und analysieren wir lokale Zweiteilchenwechselwirkungen aus der chiralen EFT. Im speziellen konstruieren wir "softe" lokale Wechselwirkungen in führender Ordnung, (engl. leading order (LO)), zweiter Ordnung (NLO) und dritter Ordnung (N^{2}LO), indem wir den Koordinatenraum-Cutoff vergrößern. Wir demonstrieren unsere Wechselwirkung in ^{16}O–^{16}O Nukleus-Nukleus Streuungen mithilfe von zweifach gefalteten (double-folding) Potentialen. Im Weiteren untersuchen wir lokale Regulator und Cutoff Artefakte. Wir betrachten Effekte auf Streuphasen, Kernmaterie und die ^{4}He Bindungsenergie aufgrund der verletzten Fierz-Vertauschungsfreiheit. Dafür variieren wir verschiedene LO Operatorpaare in LO und NLO Wechselwirkungen. Zusätzlich wird das Verhalten lokaler LO Wechselwirkungen für große Cutoffs untersucht. Dazu betrachten wir verschiedene funktionale Formen der Regulatoren und verschiedene Operatorkombinationen über eine weite Spanne des inversen Koordinatenraum-Cutoffs. Wir zeigen, dass die verletzte Fierz-Vertauschungsfreiheit starken Einfluss auf LO Wechselwirkungen hat, dieser jedoch stark reduziert wird sobald man höhere Ordnungen betrachtet bei denen neue Kontakte auftreten. Für eine spezielle Wahl der Operatoren finden wir Cutoff-unabhängige Plateaus für Streuphasen und die Deuteron-Bindungsenergie. Diese Plateaus treten bei den gleichen Werten auf, unabhängig von der funktionalen Form der Regulatoren. Obwohl dies nicht bedeutet, dass das Ordnungsschema renormierbar ist, erlaubt es uns härtere Wechselwirkungen zu konstruieren.

In der zweiten Hälfte konstruieren wir Valenzraum-Hamiltonians für Berechnungen im Schalenmodell. Die resultierende Zweiteilchenwechselwirkung basiert auf den Symmetrien und der Niederimpulsentwicklung der chiralen EFT. Die LECs werden an Grundzustands- und Anregungsenergien im entsprechendem Valenzraum angepasst. Zusätzlich zu den bekannten Kontaktwechselwirkungen treten aufgrund der gebrochenen Galilei-Invarianz im Medium neue Operatorstrukturen auf, die explizit vom Schwerpunktimpuls abhängen. Wir konstruieren Wechselwirkungen bis hin zur vierten Ordnung (N^{3}LO) für den sd und $sd+0f_{7/2}$ Valenzraum. In der sd Schale erhalten wir für die N^{3}LO Wechselwirkung eine mittlere quadratische Abweichung zum Experiment von 0.16 MeV, welche vergleichbar zu der mit den Phenomenologischen universal sd-shell Wechselwirkungen USDA und USDB ist. Obwohl die Präzission unserer Wechselwirkung in der $sd + 0f_{7/2}$ Schale abnimmt, liefern sie interessante Vorhersagen für die Neutronen-Abbruchkante von Sauerstoff bis Natrium. Alle unsere Wechselwirkungen haben LECs natürlicher Größe und sie führen zu vielversprechenden Vorhersagen für Grundzustands- und Anregungsenergien.

Contents

“There is a theory which states that if ever anyone discovers exactly what the Universe is for and why it is here, it will instantly disappear and be replaced by something even more bizarre and inexplicable.

There is another theory which states that this has already happened."

— Douglas Adams, *The Restaurant at the End of the Universe*

1 Introduction

Nuclear physics predominantly studies atomic nuclei and nuclear matter, and thus, the force holding those compound objects together and governing their dynamics - the strong force. Rutherford's discovery of the atomic nucleus [1] and later the discovery of the neutron by Chadwick [2] established the rough size and building blocks of atomic nuclei. The strong interaction, which binds neutrons and protons overcoming the electromagnetic repulsion, was postulated as a fundamental force. Only a few years later, Yukawa proposed a meson-exchange model that mediates this force [3]. Various phenomenological models that incorporate this idea, such as the Paris [4] and Bonn [5, 6] potentials were constructed to describe the interaction among nucleons. Furthermore, the idea of a shell model for the nucleus was developed [7–10], which is able to explain the appearance of magic numbers in the nuclear landscape (see Fig. 1.2). In 1964, quarks were proposed as a substructure of objects like neutrons, protons, and many other particles that were previously considered to be elementary [11, 12]. Those substructures were confirmed in deep inelastic scattering experiments, where electrons are scattered of protons and nuclei, probing their structure at short distances [13, 14].

These developments paved the way for today's standard model, and the theory of strong interactions: quantum chromodynamics (QCD). The strong force is now understood as the interaction among quarks and gluons. The nuclear force, which is the interaction among neutrons and protons, is connected to the fundamental interactions through chiral effective field theory. An elaborate summary of the history of QCD is given in Ref. [15], while more information about the history of the strong force can be found in Refs. [16, 17].

1.1 Nuclear forces

Due to conceptional difficulties concerning the construction of nuclear interactions directly from QCD (see Ch. 2), so-called phenomenological interactions persisted for a long time. Those interactions typically allow all possible operator structures consistent with the symmetries expected from the nuclear Hamiltonian (see Sec. 2.3), in combination with meson-exchange interactions and/or other forms of potentials, such as a Wood-Saxon potential. The Argonne V18 (AV18) [18] interaction with an Illinois three-body potential [19] is a phenomenological interaction still used today, as it is suited for the requirements of Quantum Monte Carlo (QMC) based many-body methods [20–22].

Tremendous progress was pioneered by Weinberg in the early 1990s [23, 24]. He derived nuclear forces from an effective field theory (EFT), that are consistent with the relevant symmetries of QCD, including the spontaneously broken chiral symmetry. The so-called chiral EFT is a systematic low-energy expansion of QCD, that uses pions and nucleons as degrees of freedom, rather than quarks and gluons. Together with a power-counting scheme that determines and orders relevant contributions, two- and many-body forces for nucleons and electro-weak currents arise naturally in chiral EFT [24–29].

Considerable effort has been invested recently into the improvement of chiral interactions; see, e.g., Refs. [30–34], uncertainty estimates from chiral EFT; see e.g., Refs. [30, 35–37], and the development of local chiral interactions; see, e.g., Refs. [38–40] and minimally nonlocal interactions such as in Refs. [41, 42]. There is a wide range of applications for interactions from chiral EFT. This covers, e.g., calculations with nuclear matter [43–53] , which is an infinite system consisting of protons and neutrons. There, important variables are the densities of neutrons n_n and protons n_p, where the total baryon density $n = n_p + n_n$ is used to calculate the proton fraction $x = n_p/n$. Calculations at pure-neutron matter ($x = 0$) are particularity interesting in the derivation of the equation of state (EOS), employed to calculate and constraint properties of neutron stars [46]. The latter are unique laboratories for studying matter at its extremes with densities up to several times the saturation density [54].

Other interesting applications arise when nuclear interactions are combined with nuclear many-body methods. This approach allows to study nuclear-structure properties like, e.g., binding and excitation energies, and one- and two-nucleon driplines throughout the nuclear chart. The neutron dripline and knowledge about nuclei in its vicinity are vital input parameters to model the path of the rapid neutron-capture process (r-process) [55] of stellar nucleonsynthesis. This process takes place in regions with a high density of free neutrons. There, nuclei capture neutrons at a rate faster than they β decay, thus they become extremely neutron-rich. In the neutron-rich region, the neutron capture process slows down as it becomes energetically less favorable to accept further neutrons. The nucleus X with mass number A and proton number Z, eventually β decays into the nucleus Y with the same mass number and proton number $Z+1$, an electron e^-, and an anti-electron neutrino $\bar{\nu}_e$

$$ {}^{A}_{Z}X \longrightarrow {}^{\;\;A}_{Z+1}Y + e^- + \bar{\nu}_e \,. \tag{1.1} $$

The same mechanism repeats for the isotopes of element Y. As heavier nuclei are produced, the fission barrier is successively lowered and ultimately either spontaneous fission or neutron capture induced fission processes cause the r-process to halt. The r-process explains the existence of stable and long-lived nuclei beyond iron, aside from the slow (s-) [56] and proton (p-) [57] process. A theoretical description of the r-process requires knowledge about many properties, such as masses, matter and charge distribution, single-particle spectra and pairing contributions, as well as decay and reactivity characteristics for nuclei between the neutron dripline and the valley of β-stability [55].

Besides those input parameters for the r-process, a theoretical description of the neutron dripline is also of particular interest for experimental measurements. Experimentally the dripline is known up to oxygen isotopes, where it is located at ^{24}O [58–60]. While ^{25}O is unbound by roughly 0.73 MeV [61], the ^{26}O resonance is unbound by only about 0.02 MeV [62]. For heavier isotopes, small energy differences combined with large uncertainties in nuclei in the neutron-rich region make it difficult to determine the exact location of the dripline. In addition, for nuclei beyond oxygen, the dripline is located considerably further out, which complicates measurements (see, e.g., Ref. [63]). Hence, a theoretical prediction is useful to narrow down the search region.

Theoretical data is obtained with many-body methods. *Ab initio* methods, which employ Hamiltonians adjusted to reproduce few-body data, have tremendously improved over the past decade reaching sd-shell nuclei as well as nuclei on and close to the magic neutron numbers 20, 28, 40 and even $Z = 50$, $N = 84$. A graphical visualization of their reach (state of 2015) is presented in Fig. 1.1 (taken from Ref. [64]).

Quantum Monte Carlo methods are among those *ab initio* methods. Recent developments of local interactions from chiral effective field theory allowed for the first time QMC calculations with interactions from the latter. QMC methods include Green's function Monte Carlo (GFMC) [65, 66] and Auxiliary field diffusion Monte Carlo (AFDMC) [39, 67]. The first is predominantly, but not exclusively used to calculate nuclei, while the second is used to calculate nuclei as well as nuclear matter. Those methods are typically limited to light nuclei. However, new developments greatly expanded their range, making it even possible to perform calculations in ^{40}Ca [68, 69].

Further *ab initio* methods are the no-core shell model (NCSM) [70–74], coupled cluster (CC) theory [75–80], in-medium Similarity Renormalization Group (IM-SRG) [81–87], self-consistent Green's function methods (SCGF) [88–90], and many-body perturbation theory (MBPT) [91–96]. Medium-mass nuclei are calculated by constructing effective interactions in the shell-model framework as, e.g., in Refs. [79, 80, 82, 96, 97]. Some of these methods perform better in closed-shell, single open-shell or double open-shell nuclei, which explains the spread of the highlighted states around the $Z = 20$ magic number and the lines for $Z = 28$, 40, and 50 in Fig. 1.1. A detailed summary of the current state of nuclear structure theory is for example given in Ref. [98].

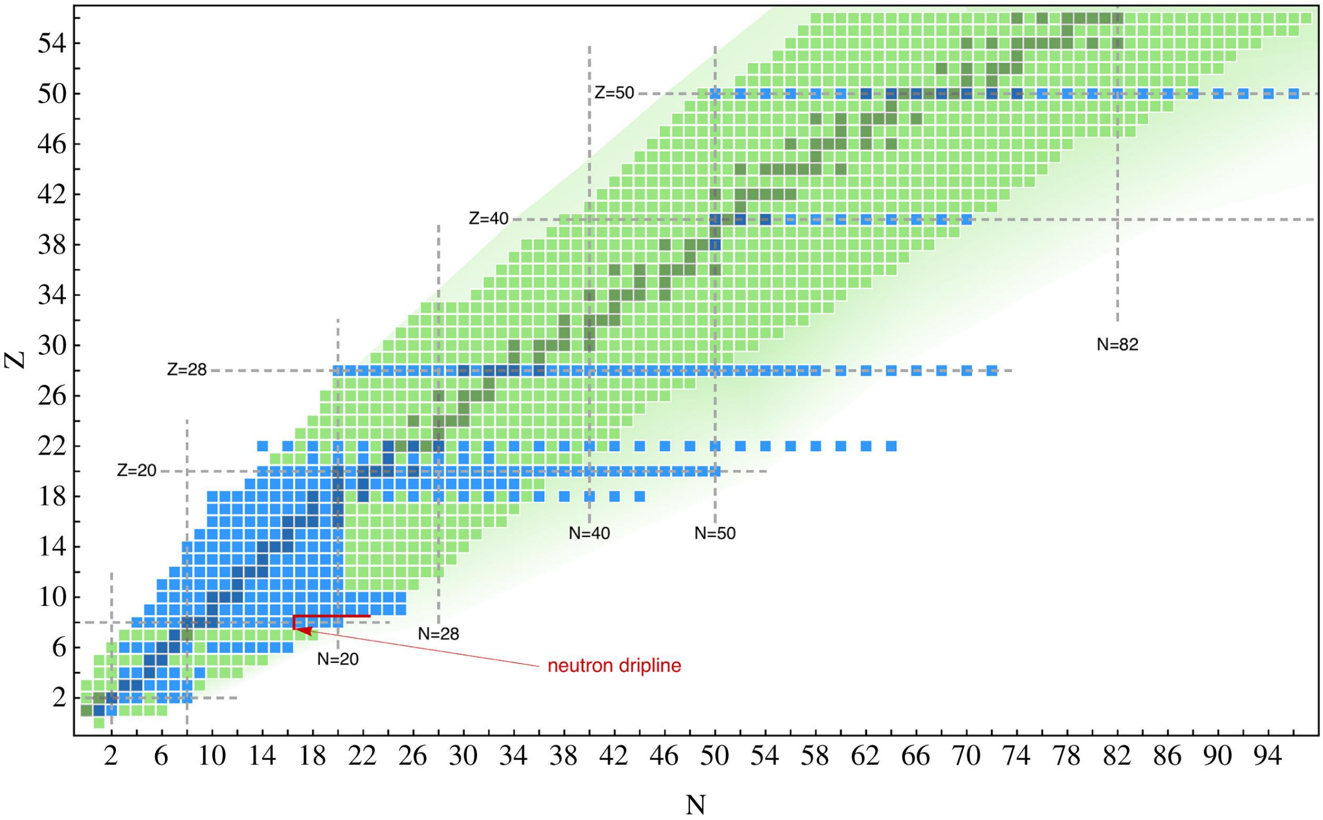

Figure 1.1.: The chart of nuclides for proton over neutron numbers with the reach of *ab initio* methods highlighted in blue (state of 2015), taken from Ref. [64]. As mentioned in the reference, the figure is for illustrative purposes only and it does not pretend to be imperatively complete. Magic neutron and proton numbers are visualized by dashed gray lines.

1.2 Nuclear Landscape

So far, we showed the range of *ab initio* methods along the lower end of the nuclear landscape. The complete nuclear chart is depicted in Fig. 1.2, as far as it is experimentally observed. Within the figure, we search for hints of nuclear shell structure. Nuclear states are colored according to their two-neutron separation energy. Separation energies, in particular the one-neutron (S_n) and one-proton (S_p) as well as the two-neutron (S_{2n}) and two-proton (S_{2p}) separation energies, indicate whether a nucleus is bound or not. The latter are given by the differences in binding energy $BE(Z,N)$:

$$\begin{aligned} S_n &= BE(Z,N) - BE(Z,N-1). \\ S_{2n} &= BE(Z,N) - BE(Z,N-2). \\ S_p &= BE(Z,N) - BE(Z-1,N). \\ S_{2p} &= BE(Z,N) - BE(Z-2,N). \end{aligned} \tag{1.2}$$

A nucleus is unbound for negative separation energies. One can determine the position of the neutron and proton driplines with the knowledge of the one- and two-nucleon (and possibly many-nucleon) separation energies. Neutrons (protons) added to a nucleus located at the neutron (proton) dripline will "drip" off instead of forming a bound nucleus, hence the name dripline.

Figure 1.2 is constructed with data from the atomic mass evaluation (AME) from 2016 and shows nuclei with proton number over neutron number. The color coding shows the size of the two-neutron separation energy S_{2n}, with purple for negative energies, blue for low energies and red for high energies. States with experimentally unknown S_{2n} are colored gray, while AME16 extrapolated states are given by unfilled

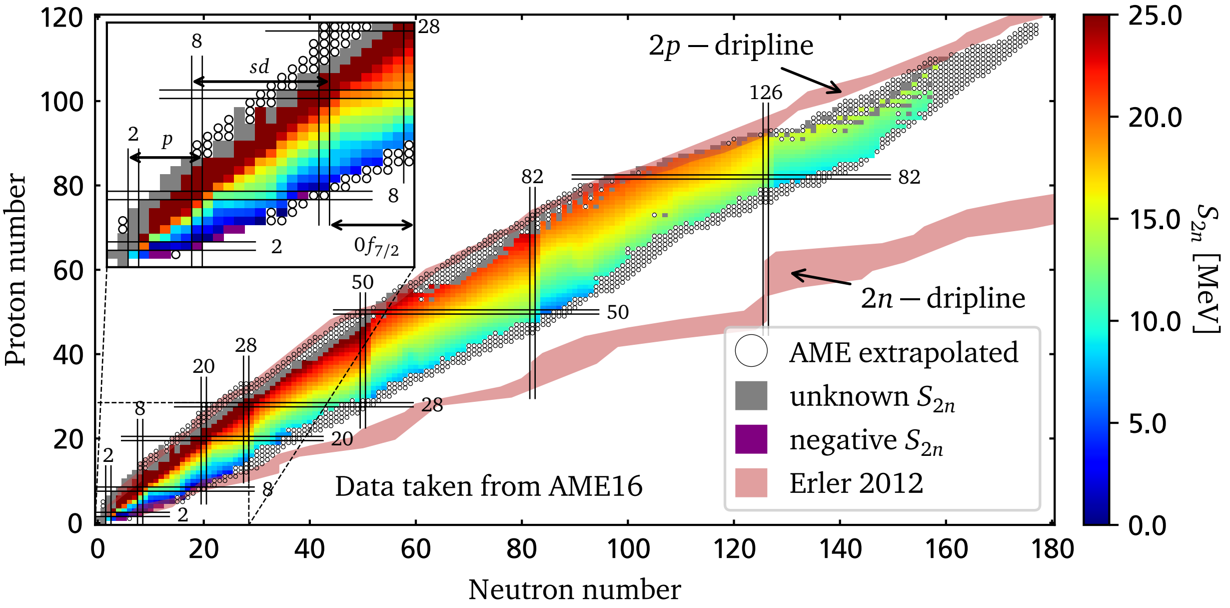

Figure 1.2.: Two-neutron separation energy S_{2n} throughout the known nuclear landscape based on data from Ref. [105]. Small values of S_{2n} are colored blue, large ones are colored red, negative values are given in purple, while unknown S_{2n} values are colored gray. The color coding is given on the right. In addition we include the extrapolated states from the AME16. They are denoted by unfilled circles. The two-neutron and two-proton driplines from Ref. [99] (Erler 2012) are colored in rose. Magic neutron and proton numbers at 2, 8, 20, 28, 50, 82, and 126 are highlighted. For visual purposes we enlarge the region from 0 to 28 neutrons and protons, which is the area of interest in this thesis. We show the shell-model valence space: p shell, sd shell, and the $0f_{7/2}$ subshell in there.

circles. The color coding is given in the bar on the right. In addition we highlight the magic numbers for neutrons and protons at 2, 8, 20, 28, 50, 82, and 126. The figure also shows theoretical estimates of the two-neutron and two-proton driplines colored in rose, obtained in Ref. [99] from density functional theory (DFT) [100] (see also Ref. [101]) with several Skyrme interactions (see, e.g., Refs. [102–104]). One can see a decrease in the two-neutron separation energy for states with two neutrons in excess of magic numbers, which indicates a nuclear shell structure. This is especially pronounced for nuclei with 52 and 84 neutrons, indicating that the magic numbers are 50 and 82. Nuclei with magic neutron (proton) numbers are stronger bound compared to nuclei in their vicinity. It costs more energy to remove a single neutron (proton) or a neutron (proton) pair out of these nuclei.

Besides the calculation of the driplines, density functional theory has a wide range of applicability. In principle, one can calculate the complete nuclear chart with those methods, but their precision is reduced compared to configuration interaction methods. As mentioned above, *ab initio* methods reach low- to medium-mass nuclei, up to medium-heavy nuclei. The calculation of open-shell nuclei has been a long-standing problem of those methods. However, recent efforts to extract valence-space interactions for shell-model calculations lead to tremendous progress for sd-shell nuclei [79, 80, 82, 96, 97] (see also Ref. [106], where NCSM and IM-SRG are merged to calculate low-mass open-shell nuclei). In the medium-mass to medium-heavy mass region, interactions still rely on calculations with shell-model codes. The interactions can either be derived from *ab initio* methods, or one can use phenomenological valence-space interactions. The latter are usually derived directly by fits to data within the shell-model framework. Although those phenomenological valence-space interactions typically lead to a precise description of experimental data, they most of the time miss a fundamental theory. Thus, they cannot be improved systematically as, e.g., the nuclear interactions from chiral EFT and it is difficult to estimate uncertainties.

1.3 Overview of main results of this thesis

To structure this thesis, we give an overview of the main results here, and then detail the organization of the thesis.

- Soft local interactions from chiral effective field theory:
  Newly developed local interactions allow for the first time to use interactions from chiral EFT in the framework of QMC calculations [39, 107]. Aside from QMC, many-body methods usually benefit from soft interactions. Typically, renormalization group (RG) methods are used to soften interactions. However, they induce both, many-body operators and nonlocal operators. We develop and investigate a new soft version of local interactions from chiral EFT by lowering the size of the momentum-space cutoff Λ, i.e., raising the coordinate-space cutoff R_0. Our findings are presented in Ch. 4 of this thesis. We also show applications of those interactions in nucleus-nucleus scattering calculations with double-folding potentials [108].

- Analyzing the Fierz-rearrangement freedom for local interaction from chiral EFT:
  Locally regularized interactions suffer from violated Fierz-rearrangement freedom. This was first found in locally regularized three-body interactions [109, 110]. We analyze this phenomenon in the two-body sector in this thesis (see also Ref. [111]). Our investigations focus on the impact on phase shifts, the ^{4}He binding energy, and the energy per particle in neutron matter calculations. We show that effects of the violated Fierz-rearrangement freedom are sizable at LO, but they are largely corrected at NLO. Further details are discussed in Ch. 5.

- Large-cutoff behavior of local chiral effective field theory interactions:
  The cutoff behavior towards large-momentum space cutoffs of nonlocally regularized interactions from chiral EFT has been investigated by Nogga, Timmermans, and van Kolck (NTvK) in Ref. [112]. They found that taking large cutoff values requires additional constants in partial waves with attractive tensor forces, to counter the contributions from the one-pion exchange potential, in order to achieve cutoff-independent results. We perform a similar investigation for local interactions, where we use the violated Fierz-rearrangement freedom to our advantage. We construct LO interactions with increasing cutoff $\Lambda \sim R_0^{-1}$, which produce cutoff-independent phase shifts without the need of counter terms. A detailed description is provided in Ch. 6 and Ref. [113].

- Shell-model interactions from chiral effective field theory in the sd valence space:
  On the one hand, recent progress in many-body methods enables *ab initio* calculations of medium-mass nuclei [64]. However, there remain unresolved issues concerning, among other things, the input Hamiltonian and as a consequence thereof large uncertainties and accuracy in general. On the other hand, traditional shell-model interactions are still widely used, as they provide a precise description of experiment, e.g., the universal sd-shell (USD) interactions USDA/USDB from Ref. [114] lead to root-mean-square deviations of $\sim$ 100 keV. There is, however, no systematic connection between those interactions and QCD. We derive effective shell-model interactions from chiral EFT by fitting the low-energy constants (LECs) directly to ground-state energies and excitation spectra in the sd valence space, and thereby combine the advantages of chiral EFT and traditional shell-model interactions. A nuclear interaction in a valence space does not fulfill all of the symmetries of a nuclear free-space interaction. Most notably, Galilean invariance is broken due to the presence of the core in the shell-model framework. This leads to new operators which explicitly depend on the center-of-mass momentum. We present those valence-space operators in Ch. 7. As a first proof of concept, we construct shell-model interactions at NLO, where leading valence-space operators enter. We compare the results to the phenomenological USDA and USDB interactions from Ref. [114] and to experimental data. Our interaction has a root-mean-square deviation from experiment of

roughly 510 keV in a dataset consisting out of 441 states in 77 sd-shell nuclei. Furthermore, it shows promising predictive power. Our findings are presented in Ch. 8 and Ref. [115].

- Subleading valence-space operators:
  Motivated by the great success of our shell-model interaction at NLO, we decided to expand our theory up to N^{3}LO, which is the subleading order for the new valence-space operators. Together with two charge-dependent operators, the N^{3}LO shell-model interaction has 63 LECs and six single-particle energies in the sd shell. With this new enhanced parameter space, we achieve a root-mean-square deviation of roughly 160 keV with respect to a slightly enlarged data set of 451 states in 77 nuclei. The new interaction has a quality comparable to that of the USDA and USDB interactions from Ref. [114]. Our results and predictions for this interaction are given in Ch. 9 of this thesis.

- First applications to cross-shell nuclei:
  We construct a shell-model interaction for neutron-rich nuclei in the $sd + 0f_{7/2}$ cross-shell to investigate the neutron dripline. The extension to such spaces proves to be complicated, as the experimental data set is more restricted, computational time increases, and one needs to be careful regarding spurious calculations that suffer from center-of-mass admixtures (see App. C of Ref. [116]). Nevertheless, we find a good agreement of neutron driplines in the lightest valence-space nuclei in our calculations. Technical details and results for those first applications are reported in Ch. 10.

- A novel approach to partial-wave decompositions:
  Along the lines of the inclusion of the new valence-space operators, we need a more generalized approach to partial-wave decompositions. In the process, we developed a computer code that generates all linearly independent NN-contact operators at a given order in the chiral power counting. This routine works for free-space contact operators as well as for center-of-mass momentum-dependent valence-space operators. A different computer code uses those contact operators as input and generates the corresponding partial-wave matrix elements automatically. Optionally, it can return the analytic structure of a given operator in a partial-wave basis. This approach can be extended to the one-pion-exchange potential. We perform a partial-wave decomposition of the latter without the need of numerical integrals. All relevant information to reconstruct this new method are detailed in App. B.

This thesis is structured as follows: In the subsequent chapter, we give a short introduction to quantum chromodynamics and nuclear forces from chiral effective field theory. We motivate the new developments for local interactions and shell-model interactions from chiral EFT in Ch. 3. General details about the fit procedure to phase shifts, as well as the new soft local interactions are presented in Ch. 4. In Ch. 5, we investigate the violation of the Fierz-rearrangement freedom in the presence of local regulators in two-body interactions from chiral EFT. We extend our investigation of local chiral regulators in Ch. 6, where we examine the large (momentum-space) cutoff behavior of interactions at leading order. In Ch. 7, we start our investigation of valence-space interactions from chiral EFT. This chapter introduces the data sets, Coulomb correction schemes, and fitting algorithms used for the shell-model fits in the subsequent chapters. Our first investigations of the sd-shell for interactions up to second order in chiral power counting are given in Ch. 8. Further investigations up to forth order in the power counting follow in Ch. 9. In Ch. 10, we consider cross-shell interactions in the sd valence space with the addition of the $0f_{7/2}$ neutron single-particle orbit. We further investigate the neutron dripline resulting from these interactions. A summary and outlook is given in Ch. 11.

In App. A, App. B, and App. C, we provide additional information for the partial-wave decomposition of the momentum-space contact operators. General mathematical tools are provided in App. A, a general ansatz for the partial-wave decomposition on the basis of mathematical tensor operators (see App. A) is given in App. B. Appendix C lists all contact operators in a mathematical tensor-operator representation. A short overview about the transformation from the partial-wave basis to the harmonic-oscillator basis, which we use for the shell-model calculations is given in App. D. Finally, we list two-body matrix elements and low-energy constants as well as single-particle energies, which we obtained in our fits in App. E.

2 The strong interaction and nuclear forces

The interaction among nucleons, i.e., protons and neutrons, is described by nuclear forces. Nucleons are not elementary particles but they have a substructure of quarks and gluons. Quarks and gluons are strongly interacting particles. In the standard model, the theory of the strong interaction is called quantum chromodynamics (QCD) [117]. Nuclear forces between two (and multiple) nucleons are a residual effect of the underlying strong interaction between quarks and gluons in different nucleons. However, various difficulties arise if one wants to extract nuclear interactions from QCD, as it cannot be treated perturbatively at low-energy scales relevant for the nuclear interaction [118, 119]. A promising approach to low-energy observables from QCD is Lattice QCD [120–126], which treats QCD on a discretized space-time grid. Lattice QCD made tremendous progress in the past years, as visualized in the light hadron mass spectrum in Fig. 2.1 taken from Ref. [127], where the pion, kaon, and Ξ (xi) mass were used as input parameters to set the light quark mass. From this the remaining hadron masses were calculated with great success. However, calculations in this framework are very involved and computationally expensive, even for small systems. Thus, we rely on different methods to describe the nuclear interaction. In this work, we use chiral effective field theory (EFT) [23, 24, 26, 27]. Chiral EFT is a systematic low-energy expansion of QCD where the relevant degrees of freedom are nucleons and pions rather than quarks and gluons. A power-counting scheme orders contributions according to their importance, and thus, provides a hierarchy of nuclear forces in the two- and many-body sector. Moreover, it enables calculations with controlled theoretical uncertainties [30, 36].

In the following, we give a brief introduction to QCD and chiral EFT. Afterwards, we provide a more detailed overview on the operators from chiral effective field theory and on symmetries of Hamiltonians for nuclear interactions.

2.1 Quantum chromodynamics

As mentioned above quantum chromodynamics describes the interaction between quarks and gluons. In the standard model, quarks are elementary spin$-1/2$ particles with positive parity. They come in six different flavors, which are labeled up (u), down (d), strange (s), charm (c), top (t), and bottom (b) (or beauty). Their antiparticles are denoted as $\overline{q}_f$, where q_f can take any quark label u, d, s, c, t, or b. We list basic properties of the quarks in Tab. 2.1. All quarks have different masses and carry a fraction of the elementary electro-magnetic (EM) charge e. The up, charm, and top quark have an EM charge of $+\frac{2}{3}e$, while the down, strange, and bottom quark carry the charge $-\frac{1}{3}e$. The respective antiparticles have the same charge, but with the opposite sign. Besides the EM charge quarks carry the charge of the strong interaction, which is called color charge (hence "chromo", Greek for color). In contrast to the EM interaction, the strong interaction has three different types of charge. The charges are labeled red (r), green (g), and blue (b). Quarks carry one kind of color charge. Anti-quarks carry an anti-color charge (anti-red ($\overline{\text{r}}$), anti-green ($\overline{\text{g}}$), anti-blue ($\overline{\text{b}}$)). The strong interaction between quarks is mediated by gluons. Gluons can change the color charge of quarks. As a consequence, they must also carry a color charge as well as an anti-color charge. This allows gluons to interact with other gluons (unlike photons, the gauge particles of quantum electrodynamics (QED)). Depending on the size of the QCD coupling constant α_S (see Fig. 2.2), gluon self interactions complicate the strong interaction at low-energies drastically, as contributions from gluon-gluon or virtual quark anti-quark vertices become large. One distinguishes between asymptotic freedom and confinement, which we introduce in the following.

At very high energy, e.g., high density and/or temperature, the strong interaction becomes weaker as the QCD coupling constant α_s becomes very small; see Fig. 2.2. This property of QCD is called asymptotic freedom [129, 130]. In this energy range, quarks and gluons appear as free particles in a quark-gluon plasma (QGP) (see Fig. 2.3) and QCD can be treated within perturbation theory. However, on earth these

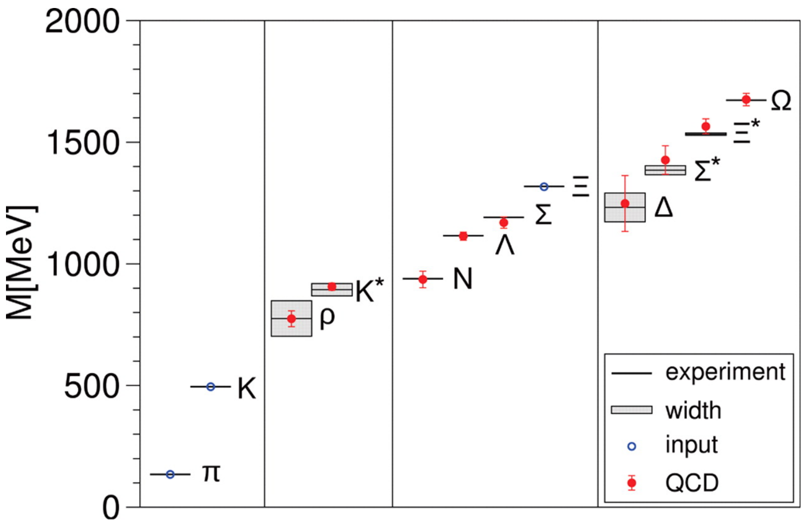

Figure 2.1.: Lattice QCD simulations of the light hadronic mass spectrum taken from Ref. [127]. Horizontal lines and bands are experimental values with uncertainties. Lattice simulations are given by red filled circles with error bars. Input parameters to set the light quark masses are depicted by blue circles.

Table 2.1.: Mass, EM charge and isospin properties for the six quark flavors up (u), down (d), strange (s), charm (c), top (t), and bottom (b), ordered with increasing mass from Ref. [128]. The b and t quark masses are given in the $\overline{\text{MS}}$ scheme (described within Ref. [128]).

quark	mass [MeV]	charge [e]	T	M_T
u	$2.2^{+0.6}_{-0.4}$	2/3	1/2	1/2
d	$4.7^{+0.5}_{-0.4}$	-1/3	1/2	-1/2
s	96^{+8}_{-4}	-1/3	0	0
c	$(1.27 \pm 0.03) \cdot 10^3$	2/3	0	0
b	$4.18^{+0.4}_{-0.3} \cdot 10^3$	-1/3	0	0
t	$(173.21 \pm 0.51 \pm 0.71) \cdot 10^3$	2/3	0	0

extreme circumstances can only be created in high-energy colliders like the Large Hardron Collider (LHC) at the Conseil Européen pour la Recherche Nucléaire (CERN) in Geneva or the Relativistic Heavy Ion Collider (RHIC) at the Brookhaven National Laboratory. Moreover, this state lasts only for very short periods of time. Further experiments are planned at the Facility for Antiproton and Ion Research (FAIR) at the Gesellschaft für Schwerionenforschung (GSI) in Darmstadt. The density and temperature regions accessible to those experiments are schematically depicted in Fig. 2.3, which shows the temperature-density relation for QCD phases.

At lower energies, with which we usually are confronted, quarks form compound particles. Quarks are "confined" in hadrons [130]. In the quark-matter phase diagram (Fig. 2.3), this is the bottom left region around one. The QCD coupling constant becomes very large in this region (see. Fig. 2.2), which causes perturbative methods to fail. Hadrons are divided into two subgroups: mesons and baryons. Mesons are made up from a quark anti-quark pair(1). Hence, they have integer values as spin quantum

---

(1) Note that this is a simplified picture. The quarks we refer to are so-called valence quarks. In QCD, virtual quark-anti-quark pairs can be produced and annihilated dynamically. They are referred to as sea quarks. There are also more exotic combinations possible, e.g., the tetraquark [131] which we will not elaborate here.

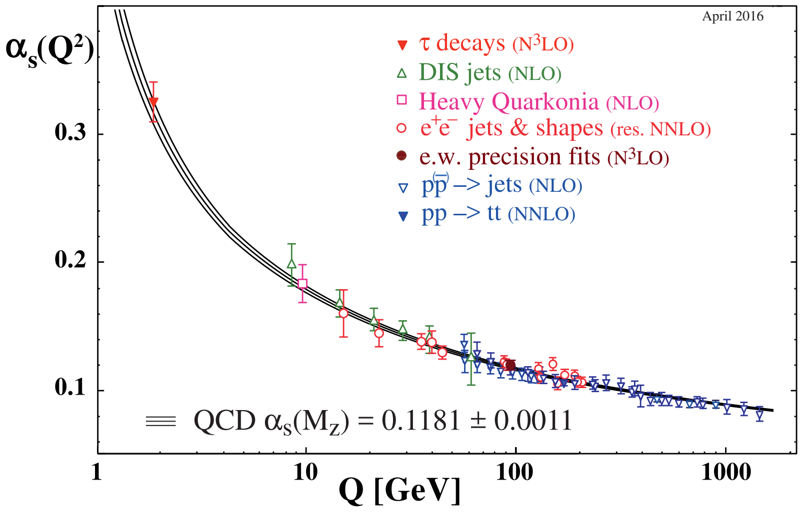

Figure 2.2.: Summary of measurements of the QCD coupling constant α_s as a function of the energy scale Q taken from Ref. [128]. The labels NLO, NNLO and N^{3}LO give the order of QCD perturbation theory which is used to extract α_s.

Table 2.2.: Mass, quark structure, EM charge and isospin properties for pions (π^+, π^-, π^0), the neutron (n), and the proton (p) from Ref. [128].

particle	quark structure	mass [MeV]	charge [e]	T	M_T
π^+	$\lvert u\bar{d}\rangle$	139.57018 ± 0.00035	+1	1	1
π^-	$\lvert \bar{u}d\rangle$	139.57018 ± 0.00035	-1	1	-1
π^0	$\frac{1}{\sqrt{2}}\left(\lvert u\bar{u}\rangle - \lvert d\bar{d}\rangle\right)$	134.97668 ± 0.0006	0	1	0
n	$\lvert udd\rangle$	939.565413 ± 0.000006	0	1/2	-1/2
p	$\lvert uud\rangle$	$938.2720813 \pm 0.0000058$	+1	1/2	1/2

number. Baryons commonly consist of three quarks$^{(2)}$ or three anti-quarks and have half-integer spin. Both, mesons and baryons have no net color charge, which is sometimes referred to as "white" or color neutral. In order to construct color neutral mesons, the quark and anti-quark need to have opposite color charge, e.g., $d_g\bar{u}_{\bar{g}}$. For baryons, each quark needs to carry a different type of color charge, e.g., $u_r u_g d_b$. Adding up the EM charges of quarks results in integer values for hadrons. We are in particular interested in pions (mesons), and neutrons and protons (baryons). Their quark structure, alongside their masses, electric charge, and isospin properties are listed in Tab. 2.2. From the data given there, one sees that the neutron mass (m_n) is slightly larger than the proton mass (m_p). This can be traced back to the quark structure. The d quark is heavier than the u quark which leads to the broken isospin symmetry, and thus, to the small mass difference between protons and neutrons. However, since the masses of the u and d quark are small, the isospin symmetry still is a good approximation ($m_p \approx m_n$).

---

(2) Also for baryons there are more exotic combinations like, e.g., the pentaquark [132].

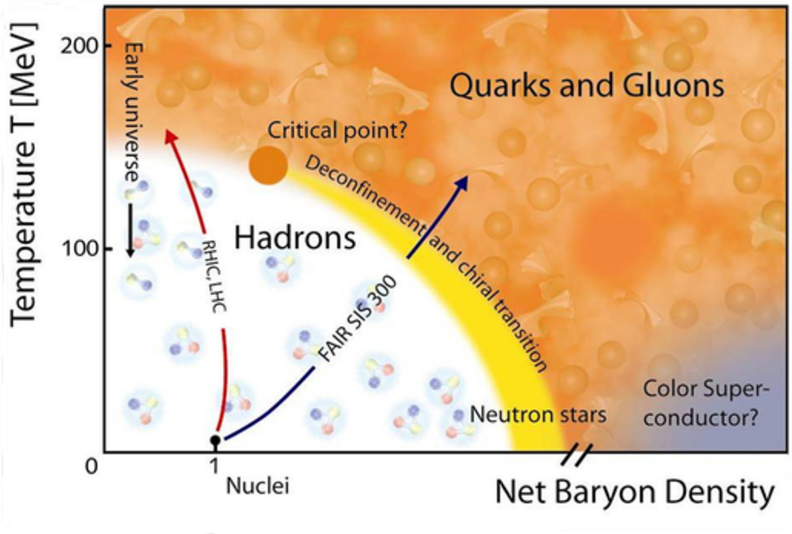

Figure 2.3.: QCD phase diagram with density-temperature regions accessible in the LHC and RHIC experiments as well as the planned range for GSI's FAIR SIS 300 experiments. Taken from Owe Philipsen "Numerical Determination of the Phase Diagram of Nuclear Matter", Gauss Centre for Supercomputing `http://www.gauss-centre.eu/gauss-centre/EN/Projects/ElementaryParticlePhysics/2015/philipsen_PDNM.html?nn=1361054`.

2.1.1 The QCD Lagrangian and chiral symmetry

QCD is invariant under local $SU(3)_c$ gauge transformations. Since a special unitary group $SU(N)$ has $N^2 - 1$ gauge fields, QCD has eight different massless gauge bosons, known as gluons. Furthermore QCD has an approximate $SU(2)$ isospin symmetry for rotations among u and d quarks which is due to the mass difference of the quarks $m_{\mathrm{c,b,t}} \gg m_{\mathrm{s}} \gg m_{\mathrm{u,d}}$. To a lesser extend, QCD is symmetric under $SU(3)$ flavor rotation among the three lightest quarks u, d, and s. Before we consider the QCD Lagrangian, we want to quickly summarize some properties of the special unitary groups.

The unitary group $U(N)$ consists of N-dimensional unitary matrices and can be written as

$$U(N) = U(1) \otimes SU(N)\,, \tag{2.1}$$

where $U(1)$ is a simple factor and $SU(N)$ is the group of N-dimensional unitary matrices U with a determinant of one $\det(U) = 1$. The group has $N^2 - 1$ generators t_i, which are N-dimensional, trace-less hermitian matrices $\mathrm{Tr}(t_i) = 0$. The generic $SU(N)$ matrix U reads

$$U = \sum_{j=1}^{N^2-1} \exp\left(i\theta_j t_j\right)\,, \tag{2.2}$$

where θ_j is a rotation angle. In $SU(2)$, the three ($2^2 - 1$) generators are proportional to the Pauli matrices

$$\sigma_1 = \begin{pmatrix} 0 & 1 \\ 1 & 0 \end{pmatrix}, \quad \sigma_2 = \begin{pmatrix} 0 & -i \\ i & 0 \end{pmatrix}, \quad \sigma_3 = \begin{pmatrix} 1 & 0 \\ 0 & -1 \end{pmatrix}. \tag{2.3}$$

The generators of the $SU(3)$ group are proportional to the eight Gell-Mann matrices [133, 134]

$$\lambda_1 = \begin{pmatrix} 0 & 1 & 0 \\ 1 & 0 & 0 \\ 0 & 0 & 0 \end{pmatrix}, \quad \lambda_2 = \begin{pmatrix} 0 & -i & 0 \\ i & 0 & 0 \\ 0 & 0 & 0 \end{pmatrix}, \quad \lambda_3 = \begin{pmatrix} 1 & 0 & 0 \\ 0 & -1 & 0 \\ 0 & 0 & 0 \end{pmatrix}, \lambda_4 = \begin{pmatrix} 0 & 0 & 1 \\ 0 & 0 & 0 \\ 1 & 0 & 0 \end{pmatrix},$$

$$\lambda_5 = \begin{pmatrix} 0 & 0 & -i \\ 0 & 0 & 0 \\ i & 0 & 0 \end{pmatrix}, \quad \lambda_6 = \begin{pmatrix} 0 & 0 & 0 \\ 0 & 0 & 1 \\ 0 & 1 & 0 \end{pmatrix}, \quad \lambda_7 = \begin{pmatrix} 0 & 0 & 0 \\ 0 & 0 & -i \\ 0 & i & 0 \end{pmatrix}, \lambda_8 = \frac{1}{\sqrt{3}} \begin{pmatrix} 1 & 0 & 0 \\ 0 & 1 & 0 \\ 0 & 0 & -2 \end{pmatrix}. \tag{2.4}$$

The relation between the Gell-Mann matrices and color-anti-color pairs is the following

$$\lambda_i \Leftrightarrow \begin{pmatrix} \mathrm{r\bar{r}} & \mathrm{r\bar{g}} & \mathrm{r\bar{b}} \\ \mathrm{g\bar{r}} & \mathrm{g\bar{g}} & \mathrm{g\bar{b}} \\ \mathrm{b\bar{r}} & \mathrm{b\bar{g}} & \mathrm{b\bar{b}} \end{pmatrix}. \tag{2.5}$$

For Pauli and Gell-Mann matrices, one can write the generators t_i as $\frac{1}{2}\sigma_i$ and $\frac{1}{2}\lambda_i$ respectively. The commutator of the generators reads

$$\left[t_i, t_j\right] = i f_{ijk} t_k, \tag{2.6}$$

with the anti-symmetric structure constant of the group f_{ijk}. For the Pauli matrices, this structure constant is the Levi-Civita-symbol ϵ_{ijk}, where $\epsilon_{ijk} = (-)1$ if i, j, and k are (anti-) cyclic permutations of the digits 123, and zero otherwise. For the Gell-Mann matrices, the structure constant takes the following values

$$f_{ijk} = \begin{cases} 1, & \text{for } ijk = 123 \\ \frac{1}{2}, & \text{for } ijk \in \{147, 165, 246, 257, 345, 376\} \\ \frac{\sqrt{3}}{2}, & \text{for } ijk \in \{458, 678\} \end{cases}, \tag{2.7}$$

where all possible cyclic index permutations have the same result, while anti-cyclic permutations change the sign. Combinations which are not listed and cannot be constructed by index permutations are zero.

We now introduce the QCD Lagrangian, which takes the following form

$$\mathcal{L}_{\mathrm{QCD}} = \bar{q}\left[i\gamma^{\mu} D_{\mu} - \mathcal{M}\right] q - \frac{1}{4} G_{\mu\nu} G^{\mu\nu}, \tag{2.8}$$

where ($\bar{q}$) q are (anti-) quark fields, which contain the different colors and quark flavor combinations. The gauge covariant derivative reads

$$D_{\mu} = \partial_{\mu} - \frac{ig}{2} \sum_{a=1}^{8} A_{\mu}^{a} \lambda_{a}, \tag{2.9}$$

with the gluon gauge fields A_{μ}^{a}, the covariant derivative ∂_{μ}, and the coupling constant g. The coupling constant g relates to the QCD coupling constant α_S from Fig. 2.2 via $g^2 = 4\pi\alpha_S$. The matrices γ^{μ} are the Dirac matrices. $G_{\mu\nu}$ is the gluon field strength tensor given by

$$G_{\mu\nu} = \partial_{\mu} A_{\nu} - \partial_{\nu} A_{\mu} - ig\left[A_{\mu}, A_{\nu}\right], \tag{2.10}$$

$$G_{\mu\nu}^{a} = \partial_{\mu} A_{\nu}^{a} - \partial_{\nu} A_{\mu}^{a} + g f_{abc} A_{\mu}^{b} A_{\nu}^{c}, \tag{2.11}$$

where f_{abc} is the anti-symmetric structure constant from Eq. (2.7) and a, b, and c run over the different colors. The matrix $\mathscr{M}$ is the mass term, which is given by

$$\mathscr{M} = \begin{pmatrix} m_\mathrm{u} & 0 \\ 0 & m_\mathrm{d} \end{pmatrix}, \tag{2.12}$$

in the two-quark Lagrangian(3). This mass term breaks the isospin $SU(2)$ symmetry (or flavor $SU(3)$ when one considers the strange quark) of QCD, due to the mass differences of the u and d quark.

Chiral symmetry

In the following, we consider only the quark part of the Lagrangian

$$\mathcal{L}_q = \sum_{i,j}^{\mathrm{u,d,s,c,b,t}} \bar{q}_i \left(i\gamma^\mu D_\mu - \mathscr{M}_{ij} \right) q_j \,. \tag{2.13}$$

In the case $m_\mathrm{u} = m_\mathrm{d} = m$ the $SU(2)$ isospin symmetry is exact and if both are equal to m_s, the $SU(3)$ flavor symmetry is exact too, and so on. However, the c, b, and t quark are much heavier in nature compared to the u, d, and s quark. Therefore, one typically only considers the u, d, and s quark, or even only the u and d quark. In the following, we focus on the u and d quark.

For an exact isospin symmetry one finds the conserved Noether currents j^a_μ

$$j^a_\mu = -\sum_{i,j}^{\mathrm{u,d}} i \frac{\partial \mathcal{L}_q}{\partial(\partial^\mu q_i)} (t^a)_{ij} q_j = \sum_{i,j}^{\mathrm{u,d}} \bar{q}_i \gamma_\mu (t^a)_{ij} q_j \,, \tag{2.14}$$

$$\partial^\mu j^a_\mu = 0 \,, \tag{2.15}$$

while for different masses the currents are not conserved, as the derivatives still depends on the mass terms

$$\partial^\mu j^a_\mu = -i \sum_{i,j}^{\mathrm{u,d}} (m_i - m_j) \bar{q}_i (t^a)_{ij} q_j \neq 0 \,. \tag{2.16}$$

In the symmetric case, the respective vector charges Q^a are obtained by volume integration over the zeroth component of the currents

$$Q^a = \int \mathrm{d}^3 x \, j^a_0(x) \,. \tag{2.17}$$

In the limit $m_\mathrm{u} = m_\mathrm{d} = 0$, the mass term vanishes completely. In addition to the flavor (isospin)-rotation invariance, the Lagrangian becomes invariant under axial flavor transformations. In this case, there are additional conserved Noether currents given by

$$j^a_{5\mu} = \sum_{i,j}^{\mathrm{u,d}} \bar{q}_i \gamma_\mu \gamma_5 (t^a)_{ij} q_j \,, \tag{2.18}$$

$$\partial^\mu j^a_{5\mu} = 0 \,, \tag{2.19}$$

---

(3) The complete matrix is given by diag(m_u, m_d,m_s,m_c,m_b,m_t).

with the conserved axial-vector charges

$$Q_5^a = \int \mathrm{d}^3x\, j_{50}^a(x)\,. \tag{2.20}$$

This can be rewritten in terms of left- (L) and right-handed (R) transformations

$$SU(2)_L \otimes SU(2)_R{}^{(4)}\,, \tag{2.21}$$

with generators $Q_L^a = \frac{1}{2}(Q^a - Q_5^a)$ and $Q_R^a = \frac{1}{2}(Q^a + Q_5^a)$. The generators fulfill the commutation relations:

$$\left[Q_{L,R}^a, Q_{L,R}^b\right] = i f_{abc} Q_{L,R}^c\,, \tag{2.22}$$

$$\left[Q_L^a, Q_R^b\right] = 0\,. \tag{2.23}$$

This symmetry, that allows us to transform left- and right-handed quark fields independently (see Eq. (2.23)), is called chiral symmetry (“chiral" in Greek is related to “hand").

Chiral symmetry breaking

As we know from experiments, quarks are not massless in nature. Thus, chiral symmetry is explicitly broken by the mass term $\mathscr{M}$ in the Lagrangian. This results in a coupling of left- and right-handed quarks. Due to the small masses of the u and d quark, the explicit symmetry breaking is rather small in the two-quark sector. In addition, chiral symmetry is also spontaneously broken. We refer to a symmetry as spontaneously broken, if a symmetry of the Lagrangian is not realized in the ground state of the system. For convenience, consider the "Mexican hat" potential in Fig. 2.4. The system is perfectly symmetric in the blue state. However, this is an unstable solution. In nature, the system will randomly pick one of the stable minimum solutions on the circle where the red state is located. This state does no longer observe the full symmetries from the blue state. It is symmetric under rotations along the z-axis (dashed circle), but moving it in any other direction costs energy.

In a world where chiral symmetry would be realized, the transformation properties of left- and right-handed quarks would lead to the appearance of parity doublets of equal mass. Take for example the ρ mesons, which are in a $J^\pi = 1^-$ state. Their parity doublet is in a $J^\pi = 1^+$ state. Experimentally, one finds the a_1 particle with these quantum numbers. But when we look at their masses, we see that they differ considerably

$$m_\rho \approx 775\ \text{MeV}\,,$$
$$m_{a_1} \approx 1260\ \text{MeV}\,.$$

However, the ρ meson splits up in an isospin triplet ρ^-, ρ^0, and ρ^+ with $m_{\rho^\pm} \approx m_{\rho^0}$, which shows an approximate isospin symmetry. One also sees the isospin symmetry in pion and nucleon masses in Tab. 2.2. This indicates that the axial symmetry $SU(2)_A$ is broken by the QCD ground state while the isospin symmetry $SU(2)_V$ is still a good approximation.

For each spontaneously broken global symmetry there appears a massless Goldstone boson, where the quantum numbers correspond to the broken symmetry [135]. Goldstone bosons correspond to excitations along the dashed circle in Fig. 2.4. For the $SU(2)_A$, the symmetries manifest in the three charges Q_5^1, Q_5^2, and Q_5^3. The the Goldstone bosons are the pseudoscalar ($J^\pi = 0^-$) pions $\pi^\pm$ and π^0. We see

---

(4) The chiral symmetry group for two flavors is actually given by $U(2)_L \otimes U(2)_R = SU(2)_L \otimes SU(2)_R \otimes U(1)_V \otimes U(1)_A$ but for our purposes it suffices to focus on the $SU(2)$ part. $U(1)_V$ is the quark number conservation and $U(1)_A$ is broken on quantum level.

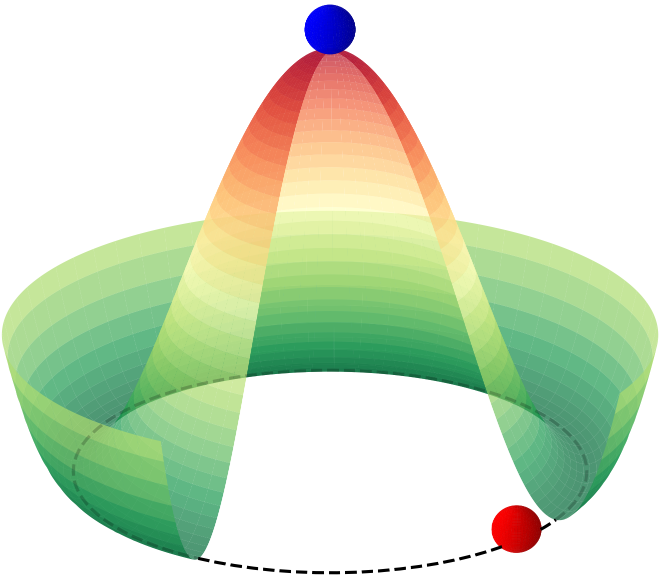

Figure 2.4.: A "Mexican hat" potential with a 90 degree cutout for visual purposes. In the blue state the system is completely symmetric. The red state has broken the symmetry.

in Tab. 2.2 that pions are not exactly massless $m_{\pi^\pm} \approx m_{\pi^0} \approx 135$ MeV $\neq 0$, which is due to the explicit symmetry breaking, as $m_\mathrm{u} \approx m_\mathrm{d} > 0$. The connection between pion-mass and quark masses are given by the Gell-Mann-Oakes-Renner relation (see, e.g., Ref. [136]),

$$m_\pi^2 F_\pi^2 \sim m_q \left\langle 0|\overline{q}q|0\right\rangle \ . \tag{2.24}$$

Pions reflect both broken symmetries: The spontaneously broken symmetry due to their mere existence and the explicitly broken symmetry due to their non-vanishing mass.

2.2 Chiral effective field theory

We want to describe the nuclear interaction, which provides an attractive force capable of forming nuclei with many nucleons inside. The physics we aim to describe plays a role at low energies, that are much smaller than the nucleon mass. As mentioned above, this interaction cannot be derived directly from QCD at the desired precision, thus, we need to take a different approach. We use an effective theory to derive the low-energy interactions. The key idea behind an effective theory is to only use relevant degrees of freedom that describe the scales of interest. One needs to define two different scales Q and Λ_b, where Q is the scale of interest and Λ_b is the so-called breakdown scale of the theory with $Q \ll \Lambda_b$. For a larger separation, Q/Λ_b becomes smaller, and higher orders in the theory are more suppressed. Physical effects beyond the breakdown scale are not resolved explicitly and get absorbed in factors known as low-energy constants (or couplings) (LECs). One then needs to construct the most general Lagrangian with those degrees of freedom that is consistent with all relevant symmetries of the underlying theory.

Chiral EFT [23, 24] is such a low-energy expansion for QCD. In the mass spectrum of hadrons with only u and d quarks as shown in Fig. 2.1, we see a large gap between the pion mass $m_\pi \approx 135$ MeV and the mass of the ρ meson $m_\rho \approx 775$ MeV (we exclude the kaon, as it contains strange quarks). Those two masses provide a good separation of scales, with the soft (low-energy) scale Q and hard (high-energy) scale Λ_b given by

$$\begin{gathered} Q \sim m_\pi \approx 135\ \text{MeV}\,, \\ m_\rho \gtrsim \Lambda_b \sim 500\ \text{MeV}\,, \\ \frac{Q}{\Lambda_b} \sim \frac{1}{4}\ \text{to}\ \frac{1}{3}\,. \end{gathered} \tag{2.25}$$

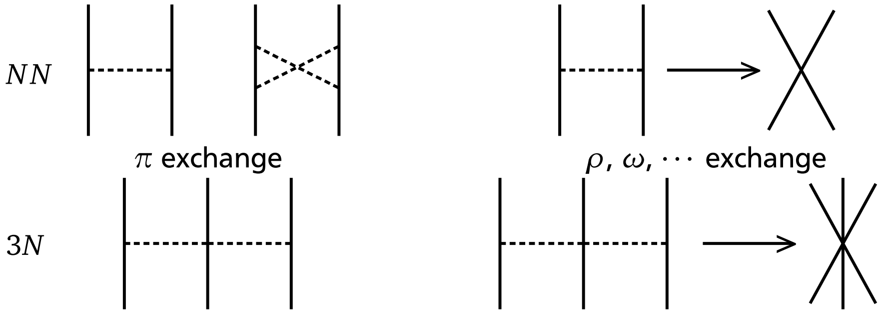

Figure 2.5.: Schematic drawings of meson exchange diagrams for nuclear forces. Solid lines represent nucleons while dashed lines represent meson exchanges. In the upper row we depict two nucleon (NN) diagrams for one- and two-pion exchanges on the left. On the right, we show that for heavier mesons, e.g., ρ-meson exchanges get absorbed into a NN-contact interaction. The lower row shows the same principle for three-nucleon ($3N$) forces.

By taking only pions and nucleons as degrees of freedom, the breakdown scale Λ_b is set such that new physical effects, e.g., ρ-meson exchanges are excluded, leading to an expansion parameter of roughly one third. As a result, the interaction explicitly contains one- and two-pion exchanges, and to a lesser extend three-pion exchanges (see, e.g., Refs. [137, 138]), as well as contact interactions between nucleons. Note that the mass difference between Δ baryons ($m_\Delta \approx 1232$ MeV) and nucleons is at roughly 300 MeV, and thus, below the breakdown scale. Chiral interactions that explicitly include intermediate Δ excitations are called Δ-full interactions [41, 42, 139–144]. We focus on Δ-less chiral EFT, where the Δ excitation is not resolved and gets absorbed into coupling constants, leading to particularly large values of the two-pion exchange couplings c_3 and c_4 [140] (see Tab. 2.4).

Contact terms are operators, accompanied by a LEC in which non-resolved structures are absorbed. We depict this schematically in Fig. 2.5. On the left-hand side, we show the Feynman diagrams for pion-exchanges in the two- and three-body sector. As pions are explicitly resolved, the diagrams enter the chiral Lagrangian. The range of the interaction is inversely proportional to the mass of the exchange particle. Thus, the one-pion exchange (OPE) is responsible for the long-range part of the interaction and the two-pion exchange (TPE) describes the intermediate-range sector. On the right-hand side, we show the exchange of heavier mesons, which would describe the short range sector. However, those high-energy degrees of freedom are not resolved in our theory, i.e., as high energies correspond to short distances, we cannot distinguish the exchange of heavy mesons from a nucleon-nucleon contact interaction in our framework. Consequently, we absorb those contributions in the LECs, which are later determined by fits to experimental data.

In modern many-body calculations, Hamiltonians from chiral EFT have replaced those from phenomenological interactions for several reasons: Chiral Hamiltonians provide a fundamental connection to QCD and can be improved systematically. Furthermore, they enable theoretical uncertainty estimates and consistent many-body forces appear naturally.

2.2.1 Weinberg power counting

In this work, we adopt the widely used Weinberg power counting (WPC) [23, 24]. With the WPC one graphically analyzes diagrams as those in Fig. 2.5 and sorts them in powers of $\left(\frac{Q}{\Lambda_b}\right)^\nu$, where ν gives the order of the interaction. Starting with leading order (LO) at $\nu = 0$, next-to-leading order (NLO) at $\nu = 2$, next-to-next-to-leading order (N^{2}LO) at $\nu = 3$, next-to-next-to-next-to-leading order (N^{3}LO) at $\nu = 4$ and so on. The order ν of an N-nucleon diagram is given via the following relation [27, 145]

$$\nu = -2 + 2N - 2C + 2L + \sum_i \left(d_i + \frac{n_i}{2} - 2 \right), \tag{2.26}$$

Table 2.3.: Diagrams to determine two-body (NN) and many-body ($3N$, $4N$, $\cdots$) forces in chiral EFT up to N^{3}LO. Contributions are ordered according to WPC. The diagrams are taken from Ref. [146]. Dashed lines symbolize pion exchanges while solid lines are nucleons. Small dots, filled circles, filled squares and empty squares refer to $\Delta_i = 0$, 1, 2 and 4 respectively (see Eq. (2.26) for details).

Order		NN	$3N$	$4N$	$\cdots$
LO	$\left(\frac{Q}{\Lambda_b}\right)^0$	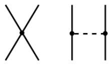	–	–	–
NLO	$\left(\frac{Q}{\Lambda_b}\right)^2$	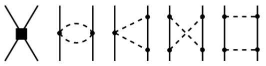	–	–	–
N^{2}LO	$\left(\frac{Q}{\Lambda_b}\right)^3$	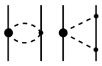	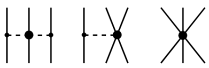	–	–
N^{3}LO	$\left(\frac{Q}{\Lambda_b}\right)^4$	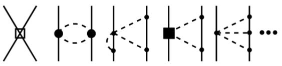	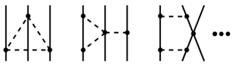		–
$\vdots$		$\vdots$	$\vdots$	$\vdots$	$\ddots$

where N is the number of participating nucleons, C the number of separately connected pieces (usually one considers only diagrams with C=1) and L the number of loops. The sum runs over all vertices in the diagram, with d_i denoting the derivatives or pion-mass insertions and n_i the number of nucleon legs in this vertex. The terms in the sum can be collected in $\Delta_i = d_i + \frac{n_i}{2} - 2$, which is always larger or equal to zero. Let us apply this to the diagrams in the upper row of Fig. 2.5, starting from left to right. In the OPE we have two vertices, where each vertex has $n_i = 2$ and in the lowest order $d_i = 1$ as one pion line enters each vertex. Thus, we find $\Delta_i = 0$ for both cases. Furthermore, $N = 2$, $C = 1$ as all lines in the diagram are connected and $L = 0$ which leads to $\nu = -2 + 4 - 2 = 0$. As a result, the OPE contributes to LO. For the two-pion exchange we find again $\Delta_i = 0$ in the lowest order (meaning not having any derivatives in the vertices). Also we find $N = 2$ and $C = 1$ but this time we have one loop $L = 1$, which leads to $\nu = 2$. Hence, the two-pion exchange first appears at NLO. The contact interaction on the right has one vertex with four nucleon legs $n = 4$. In the lowest order we have $d_i = 0$ which leads to $\Delta = 0$. Again, we have $N = 2$, $C = 1$ and since there are no loops the first contact interaction appears at $\nu = 0$, i.e., leading order. Obviously we can increase the value of d_i as higher numbers of derivatives can be taken into account, leading to contributions at higher orders. This counting scheme is applied to all possible diagrams leading to the well known ordering in Tab. 2.3 (consider also Ref. [34, 146]).

The most important contributions appear at LO, i.e., the long-range OPE, which we will discuss later, and the derivative-free short-range S-wave contacts (see Tab. 2.3). At the next order, there are two-pion exchange contributions as well as contact interactions that include derivatives. At N^{2}LO, there are corrections to the two-pion exchange in the two-body sector and leading three-body interactions appear. This list can be systematically extended, e.g., the dominant N^{5}LO contributions have been successfully implemented in the two-body sector in Ref. [147]. Three-body and higher-body forces arise naturally in chiral EFT [26, 141, 148] and the importance of three-body forces in many-body calculations is undisputed [28, 139, 149, 150]. However, our investigations on local and shell-model interactions from chiral EFT focus on two-body interactions.

One use Feynman-like rules to derive the chiral Lagrangian at a given order from diagrams in Tab. 2.3. As an example, the LO chiral Lagrangian has the following form:

$$\begin{aligned}\mathcal{L}^{\Delta=0} =& \frac{1}{2}\left(\partial_\mu \pi \cdot \partial^\mu \pi - m_\pi^2 \pi^2\right) + \overline{N}\left(i\partial_0 + \frac{g_A}{2F_\pi}\tau\sigma\cdot\nabla\pi - \frac{1}{4F_\pi^2}\tau\cdot(\pi\times\partial_0\pi)\right)N + \cdots \\ & - \frac{1}{2}C_S(\overline{N}N)(\overline{N}N) - \frac{1}{2}C_T(\overline{N}\sigma N)(\overline{N}\sigma N) + \cdots , \end{aligned} \tag{2.27}$$

where π and N are pion and nucleons fields respectively, and σ and τ are Pauli matrices for spin and isospin. The two constants g_A and F_π are the pion axial-vector coupling constant $g_A \approx 1.276$ [151] and the pion decay constant $F_\pi = 92.4$ MeV. In the second line, there are the two LO LECs C_S and C_T which need to be adjusted to experimental data. Fore a more detailed overview consider Ref. [27].

2.3 Symmetries of nuclear forces

The operator set we derive from chiral EFT as well as the operators from phenomenological interactions follow the symmetries of the nuclear Hamiltonian. We give a short summary of the relevant symmetries, which need to be fulfilled by any operator of the strong interaction.

- **Translational invariance and Galilean invariance:** In free space, the interaction must not depend on the center-of-mass (CM) position $\mathbf{R}$ and momentum $\mathbf{P}$. In the relativistic case Galilean invariance gets substituted by Lorenz invariance. As a result, we simply do not use the operators $\mathbf{R}$ and $\mathbf{P}$ to construct interactions. However, for interactions in a shell-model valence space this symmetry is broken. Thus, we will also include the CM momentum operator in the subsequent symmetry requirements.

- **Rotational invariance:** Spin, relative, and center-of-mass operators need to be coupled to an operator of rank zero, i.e., a scalar, in order to preserve the rotational invariance.

- **Hermitian operators:** As the eigenvalues are real, the Hamiltonian, i.e., the kinetic-energy term plus the potential, needs to be Hermitian. The momentum and spin operators of single particles are Hermitian ($\mathbf{p}_i^\dagger = \mathbf{p}_i$ and $\boldsymbol{\sigma}_i^\dagger = \boldsymbol{\sigma}_i$). The same holds for the relative momenta $\mathbf{p}$ and $\mathbf{p}'$ and the CM momentum $\mathbf{P}$. The momentum transfer in the exchange channel $\mathbf{k} = \frac{1}{2}(\mathbf{p}+\mathbf{p}')$ is also Hermitian, but the momentum transfer itself $\mathbf{q} = \mathbf{p} - \mathbf{p}'$ is anti Hermitian

$$\mathbf{q} = \langle \mathbf{p}|q|\mathbf{p}'\rangle = \mathbf{p} - \mathbf{p}' \tag{2.28}$$

$$\begin{aligned}\mathbf{q}^\dagger =& \langle \mathbf{p}|q^\dagger|\mathbf{p}'\rangle = (\langle \mathbf{p}'|q|\mathbf{p}\rangle)^\dagger \\ =& (\mathbf{p}'-\mathbf{p})^\dagger = \mathbf{p}' - \mathbf{p} = -\mathbf{q} .\end{aligned} \tag{2.29}$$

In total, we find that the momentum-space and spin-space operators show the following relation to their Hermitian conjugate

$$\begin{aligned}\mathbf{q}^\dagger &= -\mathbf{q} , \\ \mathbf{k}^\dagger &= \mathbf{k} , \\ \mathbf{P}^\dagger &= \mathbf{P} , \\ \boldsymbol{\sigma}_i^\dagger &= \boldsymbol{\sigma}_i , \\ i^\dagger &= -i ,\end{aligned} \tag{2.30}$$

with the complex number i. Thus our interaction can only be Hermitian if powers m_q of $\mathbf{q}^{m_q}$ and m_i of i^{m_i} add up to an even number

$$(-1)^{m_q+m_i} = 1 \tag{2.31}$$

- **Particle exchange:** The interaction must be symmetric under particle exchange. Relative momenta $\mathbf{p} = \frac{1}{2}(\mathbf{p}_1 - \mathbf{p}_2)$ are antisymmetric under particle exchange, whereas the CM momentum $\mathbf{P} = \mathbf{p}_1 + \mathbf{p}_2$ is symmetric under particle exchange. The momentum transfer as well as the momentum transfer in the exchange channel are therefore antisymmetric under particle exchange. Particle labels of spin and isospin operators interchange. In total we find:

$$\begin{aligned} \mathbf{q} &\quad\rightarrow\quad -\mathbf{q}\,. \\ \mathbf{k} &\quad\rightarrow\quad -\mathbf{k}\,. \\ \mathbf{P} &\quad\rightarrow\quad \mathbf{P}\,. \\ \boldsymbol{\sigma}_1 &\quad\leftrightarrow\quad \boldsymbol{\sigma}_2\,. \\ i &\quad\rightarrow\quad i\,. \end{aligned} \tag{2.32}$$

  The sum of the powers $m_q + m_k$ of $\mathbf{q}_q^m$ and $\mathbf{k}_k^m$, needs to be even for functions, where the spin part is positive under particle exchange (like $\boldsymbol{\sigma}_1 \cdot \boldsymbol{\sigma}_2$ or $\boldsymbol{\sigma}_1 + \boldsymbol{\sigma}_2$). In the case of functions, where the spin part is negative under particle exchange (like $\boldsymbol{\sigma}_1 \times \boldsymbol{\sigma}_2$ or $\boldsymbol{\sigma}_1 - \boldsymbol{\sigma}_2$), the sum $m_q + m_k$ has to be odd. We introduce an auxiliary operator to distinguish between spin functions that are positive or negative under particle exchange in spin space

$$O_{\sigma_1 \leftrightarrow \sigma_2} = \begin{cases} 0, & \text{positive under particle exchange in spin space} \\ 1, & \text{negative under particle exchange in spin space} \end{cases}. \tag{2.33}$$

  With this, the condition for symmetric operators under particle exchange reads

$$(-1)^{m_q + m_k} = (-1)^{O_{\sigma_1 \leftrightarrow \sigma_2}}\,. \tag{2.34}$$

- **Parity:** Parity is the mirror symmetry in configuration space

$$\begin{pmatrix} t \\ \mathbf{r} \end{pmatrix} \rightarrow \begin{pmatrix} t \\ -\mathbf{r} \end{pmatrix}.$$

  Our operators transform as follows under parity transformation:

$$\begin{aligned} \mathbf{q} &\quad\rightarrow\quad -\mathbf{q}\,. \\ \mathbf{k} &\quad\rightarrow\quad -\mathbf{k}\,. \\ \mathbf{P} &\quad\rightarrow\quad -\mathbf{P}\,. \\ \boldsymbol{\sigma}_i &\quad\rightarrow\quad \boldsymbol{\sigma}_i\,. \\ i &\quad\rightarrow\quad i\,. \end{aligned} \tag{2.35}$$

  Consequently, operators require to be even in powers of momenta in order to respect parity. The powers m_P, m_q, and m_k of the momenta $\mathbf{P}$, $\mathbf{q}$, and $\mathbf{k}$ need to fulfill

$$(-1)^{m_P + m_q + m_k} = 1\,. \tag{2.36}$$

- **Time reversal:** Interactions need to be symmetric under the transformation

$$\begin{pmatrix} t \\ \mathbf{r} \end{pmatrix} \rightarrow \begin{pmatrix} -t \\ \mathbf{r} \end{pmatrix}.$$

Momenta, and angular momenta (as well as spins) are antisymmetric under time reversal. However, position coordinates are not affected by the time-reversal operator. We find for the momentum-space operators under time reversal

$$\begin{aligned} \mathbf{q} &\rightarrow -\mathbf{q}\,. \\ \mathbf{k} &\rightarrow -\mathbf{k}\,. \\ \mathbf{P} &\rightarrow -\mathbf{P}\,. \\ \boldsymbol{\sigma}_i &\rightarrow -\boldsymbol{\sigma}_i\,. \\ i &\rightarrow -i\,. \end{aligned} \tag{2.37}$$

We need to count powers of of Pauli matrices m_σ, where we do not differentiate between $\boldsymbol{\sigma}_1$ and $\boldsymbol{\sigma}_2$, e.g., operators like $\boldsymbol{\sigma}_1 + \boldsymbol{\sigma}_2$ have $m_\sigma = 1$ and operators like $\boldsymbol{\sigma}_1 \cdot \boldsymbol{\sigma}_2$ and $\boldsymbol{\sigma}_1 \times \boldsymbol{\sigma}_2$ have $m_\sigma = 2$. With this we find

$$(-1)^{m_P + m_q + m_k + m_i + m_\sigma} = 1 \tag{2.38}$$

In summary, the set of equations our interactions need to fulfill to respect all symmetries, is given by

$$(-1)^{m_q + m_i} = 1\,. \tag{2.39}$$

$$(-1)^{m_q + m_k} = (-1)^{O_{\sigma_1 \leftrightarrow \sigma_2}}\,. \tag{2.40}$$

$$(-1)^{m_P + m_q + m_k} = 1\,. \tag{2.41}$$

$$(-1)^{m_P + m_q + m_k + m_i + m_\sigma} = 1\,. \tag{2.42}$$

We can identify short-range operators of the strong interaction at any given order, by following those symmetries.

2.4 Nuclear forces from chiral effective field theory

From the most general Lagrangian, one can determine the operators for the nuclear potential. A typical two-body interaction from chiral EFT has a long- and intermediate-ranged part which is governed mainly by one- and two-pion exchanges, and a short-ranged part, governed by NN contact interactions. The NN potential takes the form

$$V = V_\pi + V_{\text{cont}}\,, \tag{2.43}$$

with the pion-exchange part V_π and the nucleon contact part V_{cont}.

2.4.1 Pion-exchange interactions

The pionic part is a sum over all pion-exchange contributions $V_\pi = V_{1\pi} + V_{2\pi} + V_{3\pi} + \mathcal{O}\left(V_{4\pi}\right)$, where $V_{i\pi}$ denotes the exchange of i pions. Each i-pion exchange contains contributions from different orders of the WPC $V_{i\pi}^{(\nu)}$:

$$\begin{aligned} V_{1\pi} &= V_{1\pi}^{(0)} + V_{1\pi}^{(2)} + V_{1\pi}^{(3)} + V_{1\pi}^{(4)} + V_{1\pi}^{(5)} + \cdots\,, \\ V_{2\pi} &= V_{2\pi}^{(2)} + V_{2\pi}^{(3)} + V_{2\pi}^{(4)} + V_{2\pi}^{(5)} + \cdots\,, \\ V_{3\pi} &= V_{3\pi}^{(4)} + V_{3\pi}^{(5)} + \cdots\,. \end{aligned} \tag{2.44}$$

In momentum space, one usually writes pion-exchange interactions at a given order like

$$\begin{aligned}\langle\mathbf{p}|V_\pi|\mathbf{p}'\rangle \equiv& V_\pi(\mathbf{p},\mathbf{p}')\\ =& V_C+\boldsymbol{\tau}_1\cdot\boldsymbol{\tau}_2W_C+(V_S+\boldsymbol{\tau}_1\cdot\boldsymbol{\tau}_2W_S)\boldsymbol{\sigma}_1\cdot\boldsymbol{\sigma}_2+(V_{LS}+\boldsymbol{\tau}_1\cdot\boldsymbol{\tau}_2W_{LS})\left(i\frac{\boldsymbol{\sigma}_1+\boldsymbol{\sigma}_2}{2}\right)\cdot(\mathbf{q}\times\mathbf{k})\\ &+(V_T+\boldsymbol{\tau}_1\cdot\boldsymbol{\tau}_2W_T)(\boldsymbol{\sigma}_1\cdot\mathbf{q})(\boldsymbol{\sigma}_2\cdot\mathbf{q})+(V_{\sigma L}+\boldsymbol{\tau}_1\cdot\boldsymbol{\tau}_2W_{\sigma L})(\boldsymbol{\sigma}_1\cdot(\mathbf{q}\times\mathbf{k}))(\boldsymbol{\sigma}_2\cdot(\mathbf{q}\times\mathbf{k}))\,,\end{aligned}\tag{2.45}$$

with the finial and initial relative momenta

$$\mathbf{p}=\frac{1}{2}(\mathbf{p}_1-\mathbf{p}_2)\quad\text{and}\quad\mathbf{p}'=\frac{1}{2}(\mathbf{p}'_1-\mathbf{p}'_2)\,.^{(5)}\tag{2.46}$$

In general the functions $V_{C,S,LS,T,\sigma L}$ and $W_{C,S,LS,T,\sigma L}$ depend on the relative momenta $\mathbf{p}$ and $\mathbf{p}'$. The operators, $\mathbf{q}$ and $\mathbf{k}$ represent the momentum transfer and the average momentum respectively, given by

$$\begin{aligned}\mathbf{q}&=(\mathbf{p}-\mathbf{p}')\,,\\ \mathbf{k}&=\frac{1}{2}(\mathbf{p}+\mathbf{p}')\,.\end{aligned}\tag{2.47}$$

The indices refer to the momenta of particle one and two. Spin and isospin Pauli matrices for particle i are denoted by $\boldsymbol{\sigma}_i$ and $\boldsymbol{\tau}_i$ respectively. The potentials W_x are all accompanied by the isospin operator $\boldsymbol{\tau}_1\cdot\boldsymbol{\tau}_2$. The subscript x in W_x and V_x refers to C for central, S for central with spin dependence $(\boldsymbol{\sigma}_1\cdot\boldsymbol{\sigma}_2)$, LS for spin orbit (vector), T for tensor, and σL for a tensor in $\mathbf{q}\times\mathbf{k}$. Central, vector and tensor refer to the operator structure in spin space (more on this in App. B).

One-pion exchange

The OPE already contributes at LO. The momentum space representation reads

$$\langle\mathbf{p}|V_{1\pi}^{(0)}|\mathbf{p}'\rangle=V_{1\pi}^{(0)}(\mathbf{p},\mathbf{p}')=-\left(\frac{g_A}{2F_\pi}\right)^2\frac{(\boldsymbol{\sigma}_1\cdot\mathbf{q})(\boldsymbol{\sigma}_2\cdot\mathbf{q})}{\mathbf{q}^2+m_\pi^2}\boldsymbol{\tau}_1\cdot\boldsymbol{\tau}_2\,,\tag{2.48}$$

with the pion axial-vector coupling constant $g_A = 1.276$ [151], the pion decay constant $F_\pi = 92.4$ MeV, and pion mass m_π, where the charge independent version uses the average pion mass $m_\pi^{\text{av}} = 138.039$ MeV. At LO, the OPE is charge independent (CI). A charge-dependent (CD) version, is used starting at NLO. It takes the form

$$V_{1\pi}^{\text{CD}}(\mathbf{p},\mathbf{p}')=-V_{1\pi}(\mathbf{p},\mathbf{p}',m_{\pi^0})+2(-1)^{T+1}V_{1\pi}(\mathbf{p},\mathbf{p}',m_{\pi^\pm}),\tag{2.49}$$

with the isospin T and

$$V_{1\pi}(\mathbf{p},\mathbf{p}',m_\pi)=-\left(\frac{g_A}{2F_\pi}\right)^2\frac{(\boldsymbol{\sigma}_1\cdot\mathbf{q})(\boldsymbol{\sigma}_2\cdot\mathbf{q})}{\mathbf{q}^2+m_\pi^2}\,.\tag{2.50}$$

In some cases the CD version is already used at LO see, e.g., Refs. [39, 152]), because it simplifies comparison with higher orders. For the same reason we use a charge dependent version at LO.

One-loop diagrams and coupling constant corrections that appear at higher orders (Goldberger-Treiman discrepancy), are typically dealt with by changing the axial coupling g_A from 1.276 to 1.29 (see for example Refs. [27, 152, 153]). Further relativistic corrections appear at N^{3}LO, which lead to

$$V_{1\pi}^{(4)}(\mathbf{p},\mathbf{p}')=\frac{p^2+p'^2}{2m^2}\left(\frac{g_A}{2F_\pi}\right)^2\frac{(\boldsymbol{\sigma}_1\cdot\mathbf{q})(\boldsymbol{\sigma}_2\cdot\mathbf{q})}{\mathbf{q}^2+m_\pi^2}\boldsymbol{\tau}_1\cdot\boldsymbol{\tau}_2\,,\tag{2.51}$$

where m is the nucleon mass.

---

(5) The general expression for the relative momentum is $\mathbf{p}=(\mathbf{p}_1m_2-\mathbf{p}_2m_1)/(m_1+m_2)$. In the two-nucleon system one usually takes $m_n\approx m_p\approx m$, with the nucleon mass m which leads to the expressions above.

Two-pion exchange

Contributions of the TPE enter at NLO. The diagrams lead to the following contributions [154]

$$\begin{aligned} W_C^{(2)}(\mathbf{p},\mathbf{p}') &= \frac{L(\tilde{\Lambda},\mathbf{q})}{384\pi^2 F_\pi^4}\left(4m_\pi^2(1+4g_A^2-5g_A^5)+\mathbf{q}^2(1+10g_A^2-23g_A^4)-\frac{48g_A^4 m_\pi^4}{\omega^2}\right), \\ V_T^{(2)}(\mathbf{p},\mathbf{p}') &= -\frac{3g_A^4}{64\pi^2 F_\pi^4}L(\tilde{\Lambda},\mathbf{q}), \\ V_S^{(2)}(\mathbf{p},\mathbf{p}') &= -\mathbf{q}^2 V_T^{(2)}(\mathbf{p},\mathbf{p}'), \end{aligned} \tag{2.52}$$

where $\omega = \sqrt{4m_\pi^2+\mathbf{q}^2}$ and the logarithmic function L is given by

$$L(\tilde{\Lambda},\mathbf{q}) = \frac{\omega}{2|\mathbf{q}|}\log\left[\frac{\tilde{\Lambda}\tilde{\omega}^2-2m_\pi^2\mathbf{q}^2+\tilde{\Lambda}\sqrt{\tilde{\Lambda}^2-4m_\pi^2}|\mathbf{q}|\omega}{2m_\pi^2(\tilde{\Lambda}^2+\mathbf{q}^2)}\right], \tag{2.53}$$

with $\tilde{\omega} = \sqrt{2m_\pi^2+\mathbf{q}^2}$. Here $\tilde{\Lambda}$ denotes the cutoff of the spectral-function renormalization (SFR) which is presented in Ref. [155] to renormalize divergent integrals over the pion loops. In the limit $\tilde{\Lambda} \to \infty$, we find

$$\lim_{\tilde{\Lambda}\to\infty} L(\tilde{\Lambda},\mathbf{q}) = \frac{\omega}{q}\log\left[\frac{\omega+q}{2m_\pi}\right].^{(6)} \tag{2.54}$$

The result for infinite cutoff in the SFR agrees with that of the dimensional regularization (DR) (see, e.g., Ref. [27] for details on DR). First corrections appear at N^{2}LO, which read:

$$\begin{aligned} V_C^{(3)}(\mathbf{p},\mathbf{p}') &= \frac{3g_A^2}{16\pi F_\pi^4}\tilde{\omega}^2\left(2m_\pi^2(c_3-2c_1)+c_3\mathbf{q}^2\right)A(\tilde{\Lambda},q), \\ W_T^{(3)}(\mathbf{p},\mathbf{p}') &= -\frac{g_A^2}{32\pi F_\pi^4}c_4\omega^2 A(\tilde{\Lambda},q), \\ W_S^{(3)}(\mathbf{p},\mathbf{p}') &= -\mathbf{q}^2 W_T^{(3)}(\mathbf{p},\mathbf{p}'), \end{aligned} \tag{2.55}$$

where A is given by

$$A(\tilde{\Lambda},q) = \frac{1}{2q}\arctan\left(\frac{q(\tilde{\lambda}-2m_\pi)}{\mathbf{q}^2+2\tilde{\Lambda}m_\pi}\right). \tag{2.56}$$

Similar to the L function, the SFR scheme is connected to DR for infinite cutoff

$$\lim_{\tilde{\Lambda}\to\infty} A(\tilde{\Lambda},\mathbf{q}) = \frac{1}{2q}\arctan\left(\frac{q}{2m_\pi}\right). \tag{2.57}$$

In Eq. (2.55), there are three low-energy constants c_1, c_3, and c_4 (c_2 contributions vanish at this order). At N^{3}LO, new pion-nucleon LECs appear, which are labeled $\bar{d}_1+\bar{d}_2$, $\bar{d}_3$, $\bar{d}_5$, and $\bar{d}_{14}-\bar{d}_{15}$. At N^{4}LO, additional constants enter in the pion exchange, denoted by $\bar{e}_{14,15,16,17,18}$ [30, 140, 152]. For local interactions in Chs. 4 - 5, we use the same LECs as in Ref. [39], which are taken from Ref. [153]. In Ch. 7 and subsequent chapters, we use the pion LECs from Ref. [30], which are fitted to experimental πN scattering data, and are consistent with measurements from Refs. [156–158] (see also Refs. [153, 159]). We list all pion LECs that are used in this work in Tab. 2.4. The remaining expressions of the pion exchange at N^{3}LO and beyond can be found in Refs. [30, 31, 34, 138, 152, 161].

---

(6) We use $q = |\mathbf{q}|$ from now on, but one needs to be aware that q depends on the angle between $\mathbf{p}$ and $\mathbf{p}'$ as we will see in App. B.

Table 2.4.: Low-energy constants as they appear in pion exchanges at N^{2}LO and N^{3}LO. The c_i are in units of GeV^{-1}, and $\bar{d}_i$ in units of GeV^{-2}. For our calculations, we take the values from Ref. [153], where π-LECs at N^{3}LO are taken from Ref. [160].

Order	c_1	c_2	c_3	c_4	$\bar{d}_1+\bar{d}_2$	$\bar{d}_3$	$\bar{d}_5$	$\bar{d}_{14}-\bar{d}_{15}$
N^{2}LO	−0.81	–	−3.40	3.40	–	–	–	–
N^{3}LO	−0.81	3.28	−3.40	3.40	3.06	−3.27	0.45	−5.65

2.4.2 Contact interactions

In the two-nucleon sector, one encounters new contact interactions at each even power of ν (odd powers of momenta are incompatible with the symmetries mentioned in Sec. 2.3). At leading order, contact interactions are free of any derivatives, i.e., interactions do not depend on relative momenta $\mathbf{p}$ and $\mathbf{p}'$. At NLO, we encounter contact interactions that are proportional to momentum squared. There are new contact interactions with momentum to the power of $\nu = 4$ at N^{3}LO, and so forth. The number of contact operators increases with order, and each operator is accompanied by a LEC. We adjust those LECs either to NN phase shifts as described in Ch. 4 or to nuclear ground-state and excitation energies as described in Ch. 7. Symmetries allow us to reduce the number of LECs at each order, if certain conditions are met. This reduction is due to the Fierz ambiguity or Fierz-rearrangement freedom, which is violated for locally regularized interactions cf. Ch. 5 and Ref. [111].

In a Fierz-reduced operator set, we find two linear independent contact interactions at LO, seven new contact interactions at NLO, 15 new ones at N^{3}LO, and 26 new LECs at N^{5}LO. In the following we present those operator structures at LO, NLO, and N^{3}LO.

Leading order

At LO, we have in principle four different possible operators

$$V_{\text{cont}}^{(0)}(\mathbf{p},\mathbf{p}') = C_{\mathbb{1}} + C_\sigma\, \boldsymbol{\sigma}_1\cdot\boldsymbol{\sigma}_2 + C_\tau\, \boldsymbol{\tau}_1\cdot\boldsymbol{\tau}_2 + C_{\sigma\tau}\, \boldsymbol{\sigma}_1\cdot\boldsymbol{\sigma}_2\boldsymbol{\tau}_1\cdot\boldsymbol{\tau}_2\,, \tag{2.58}$$

with LECs $C_{\mathbb{1}}$, C_σ, C_τ, and $C_{\sigma\tau}$. Those operators build an over-complete set. It is sufficient to pick any two operators that are linearly independent in S waves, i.e., all but the combination $\mathbb{1}$ and $(\boldsymbol{\sigma}_1\cdot\boldsymbol{\sigma}_2)(\boldsymbol{\tau}_1\cdot\boldsymbol{\tau}_2)$. The common choice is to pick the operator pair $\mathbb{1}$ and $\boldsymbol{\sigma}_1\cdot\boldsymbol{\sigma}_2$,

$$V_{\text{cont}}^{(0)}(\mathbf{p},\mathbf{p}') = C_S + C_T\, \boldsymbol{\sigma}_1\cdot\boldsymbol{\sigma}_2\,, \tag{2.59}$$

where the LECs for this choice are typically renamed to C_S and C_T. The complete LO potential is then given by

$$V_{\text{LO}}(\mathbf{p},\mathbf{p}') = V_{1\pi}^{(0),\text{CD}}(\mathbf{p},\mathbf{p}') + C_S + C_T\boldsymbol{\sigma}_1\cdot\boldsymbol{\sigma}_2\,. \tag{2.60}$$

The LECs at leading order are given in units of GeV^{-2} or fm^2.

In addition to the charge-dependent OPE, one can introduce an isospin-breaking (ISB) and charge independence-breaking (CIB) contact at LO. Those contacts are typically adjusted to reproduce the proton-proton (pp) and neutron-neutron (nn) scattering lengths. In this work, we adopt the definition from Ref. [39].

NLO and N^{2}LO

The seven LECs and operators at NLO are typically chosen as

$$\begin{aligned}V^{(2)}_{\mathrm{cont}}(\mathbf{p},\mathbf{p}') =& C_1\mathbf{q}^2 + C_2\mathbf{k}^2 + \left(C_3\mathbf{q}^2 + C_4\mathbf{k}^2\right)\boldsymbol{\sigma}_1\cdot\boldsymbol{\sigma}_2 + \frac{i}{2}C_5\,(\boldsymbol{\sigma}_1+\boldsymbol{\sigma}_2)\cdot(\mathbf{q}\times\mathbf{k})\\ &+ C_6(\boldsymbol{\sigma}_1\cdot\mathbf{q})(\boldsymbol{\sigma}_2\cdot\mathbf{q}) + C_7(\boldsymbol{\sigma}_1\cdot\mathbf{k})(\boldsymbol{\sigma}_2\cdot\mathbf{k})\,.\end{aligned} \tag{2.61}$$

The non-reduced set also includes all operators from above with an additional $\boldsymbol{\tau}_1\cdot\boldsymbol{\tau}_2$ operator. The LECs C_i at NLO are given in units of GeV^{-4} or fm^4. The complete two-body potentials at NLO and N^{2}LO are given by

$$V_{\mathrm{NLO}}(\mathbf{p},\mathbf{p}') = V_{\mathrm{LO}}(\mathbf{p},\mathbf{p}')\big|_{g_A\to 1.29} + V^{(2)}_{2\pi}(\mathbf{p},\mathbf{p}') + V^{(2)}_{\mathrm{cont}}(\mathbf{p},\mathbf{p}')\,, \tag{2.62}$$

$$V_{\mathrm{N^2LO}}(\mathbf{p},\mathbf{p}') = V_{\mathrm{NLO}}(\mathbf{p},\mathbf{p}') + V^{(3)}_{2\pi}(\mathbf{p},\mathbf{p}')\,, \tag{2.63}$$

respectively.

N^{3}LO and N^{4}LO

At N^{3}LO, the 15 linearly independent contributions read

$$\begin{aligned}V^{(4)}_{\mathrm{cont}}(\mathbf{p},\mathbf{p}') =& D_1\mathbf{q}^4 + D_2\mathbf{k}^4 + D_3\mathbf{q}^2\mathbf{k}^2 + D_4(\mathbf{q}\times\mathbf{k})^2 + \left(D_5\mathbf{q}^4 + D_6\mathbf{k}^4 + D_7\mathbf{q}^2\mathbf{k}^2 + D_8(\mathbf{q}\times\mathbf{k})^2\right)(\boldsymbol{\sigma}_1\cdot\boldsymbol{\sigma}_2)\\ &+ D_9\frac{i}{2}\mathbf{q}^2\,(\mathbf{q}\times\mathbf{k})\cdot(\boldsymbol{\sigma}_1+\boldsymbol{\sigma}_2) + D_{10}\frac{i}{2}\mathbf{k}^2\,(\mathbf{q}\times\mathbf{k})\cdot(\boldsymbol{\sigma}_1+\boldsymbol{\sigma}_2) + D_{11}\mathbf{q}^2(\mathbf{q}\cdot\boldsymbol{\sigma}_1)(\mathbf{q}\cdot\boldsymbol{\sigma}_2)\\ &+ D_{12}\mathbf{k}^2(\mathbf{q}\cdot\boldsymbol{\sigma}_1)(\mathbf{q}\cdot\boldsymbol{\sigma}_2) + D_{13}\mathbf{q}^2(\mathbf{k}\cdot\boldsymbol{\sigma}_1)(\mathbf{k}\cdot\boldsymbol{\sigma}_2)\\ &+ D_{14}\mathbf{k}^2(\mathbf{k}\cdot\boldsymbol{\sigma}_1)(\mathbf{k}\cdot\boldsymbol{\sigma}_2) + D_{15}((\mathbf{q}\times\mathbf{k})\cdot\boldsymbol{\sigma}_1)((\mathbf{q}\times\mathbf{k})\cdot\boldsymbol{\sigma}_2)\,.\end{aligned} \tag{2.64}$$

Similar to NLO, the non-reduced set contains all operators from above with an additional $\boldsymbol{\tau}_1\cdot\boldsymbol{\tau}_2$ operator. At this order, the LECs are labeled D_i and they are given in units of GeV^{-6} or fm^6. The complete two-body interaction at N^{3}LO takes the form:

$$V_{\mathrm{N^3LO}}(\mathbf{p},\mathbf{p}') = V_{\mathrm{N^2LO}}(\mathbf{p},\mathbf{p}') + V^{(4),\mathrm{CD}}_{1\pi}(\mathbf{p},\mathbf{p}') + V^{(4)}_{2\pi}(\mathbf{p},\mathbf{p}') + V^{(4)}_{3\pi}(\mathbf{p},\mathbf{p}') + V^{(4)}_{\mathrm{cont}}(\mathbf{p},\mathbf{p}')\,. \tag{2.65}$$

At N^{4}LO, there are only corrections to the pion-exchange potential and no new nucleon-nucleon LECs

$$V_{\mathrm{N^4LO}}(\mathbf{p},\mathbf{p}') = V_{\mathrm{N^3LO}}(\mathbf{p},\mathbf{p}') + V^{(5)}_{1\pi}(\mathbf{p},\mathbf{p}') + V^{(5)}_{2\pi}(\mathbf{p},\mathbf{p}') + V^{(5)}_{3\pi}(\mathbf{p},\mathbf{p}')\,. \tag{2.66}$$

2.5 Determination of low-energy constants

The low-energy constants from the nucleon contact interactions are determined by adjusting the interactions to experimental data. In the two-body sector, this can be the deuteron binding energy and nucleon-nucleon scattering data. The latter can be decomposed into partial waves, where the resulting semi-empirical values are so-called phase shifts. Nucleon-Nucleon phase shifts reflect the influence of the two-body potential on the infinite range behavior of the scattering wave function. In comparison to a plane wave. This difference is given by a phase, hence phase shifts.

In this work, we use phase-shift values from the widely known partial-wave analysis (PWA) from Ref. [162]. Phase shifts depend on angular-momentum quantum numbers l and j, spin s, and isospin T, where the orbital angular momentum l and the spin s are coupled to the total angular momentum j denoted by $(ls)j$. The isospin T itself is redundant as it depends on l and s via the Pauli principle:

Table 2.5.: Spectroscopic notation of orbital angular momenta l. We show the notation from $l=0$ to $l=4$. Starting with $l=3$ the spectroscopic notation goes on alphabetically. In the last line, we show the form of the corresponding spherical-harmonic function with the projection of l set to zero; $m_l=0$.

l	0	1	2	3	4	$\cdots$
letter	S	P	D	F	G	$\cdots$
Y_{l0}						$\cdots$

$l+s+T=\text{odd}$ for fermions. Phase shifts depend on the energy, where one typically considers the energy in the laboratory system E_{lab}. The laboratory energy is given by a sum over the energy in the relative system (rel) and the energy in the center-of-mass system (CM):

$$\begin{aligned} E_{\text{lab}} &= E_{\text{rel}} + E_{\text{CM}} \\ &= \frac{\mathbf{p}^2}{2\mu} + \frac{\mathbf{P}^2}{2M}\,, \end{aligned} \tag{2.67}$$

with the center-of-mass momentum in the two-body system $\mathbf{P}=\mathbf{p}_1+\mathbf{p}_2$, the total mass $M=\sum_i m_i = m_1+m_2 \approx 2m$, and the reduced mass $\mu=\frac{m_1 m_2}{m_1+m_2}\approx\frac{m}{2}$. In the laboratory system, one considers a projectile or beam that hits a fixed, motionless target ($\mathbf{p}_2=0$). For the two-nucleon system this leads to the relation $E_{\text{rel}}=E_{\text{CM}}$, and thus, $E_{\text{lab}}=2E_{\text{rel}}$.

Phase shifts at a given laboratory energy E_{lab} and in a given partial wave are denoted by $\delta_l^{jst}(E_{\text{lab}})$ or in the spectroscopic notation $\delta_{(2s+1)l_j}(E_{\text{lab}})$. In the spectroscopic notation the orbital angular momentum is denoted by a letter instead of a number. The transformation is given in Tab. 2.5.

2.5.1 Lippmann-Schwinger equation

The Lippmann-Schwinger equation (LSE) [163] is an indirect approach of solving the Schrödinger equation (SE) for a scattering problem. In the LSE, one needs to solve the so-called T-matrix, which is given by

$$\boldsymbol{T}(E_{\mathbf{p}'})\,|\phi_{\mathbf{p}'}\rangle = \boldsymbol{V}\,|\phi_{\mathbf{p}'}\rangle + \boldsymbol{V}\lim_{\epsilon\to 0}\frac{2\mu}{p'^2-\boldsymbol{p}^2+i\epsilon}\boldsymbol{T}(E_{\mathbf{p}'})\,|\phi_{\mathbf{p}'}\rangle\,, \tag{2.68}$$

with the relative-momentum operator $\boldsymbol{p}$ in the denominator. Furthermore, the $+i\epsilon$ term is introduced in the derivation of the LSE to avoid singularities in the denominator. The plane-wave states contain momentum, spin and isospin quantum numbers

$$|\phi_{\mathbf{p}'}\rangle \equiv |\mathbf{p}', s m_s, T m_T\rangle\,, \tag{2.69}$$

with spin and spin projection s, m_s and isospin and isospin projection T, m_T. The solution of Eq. (2.68) in a partial-wave basis reduces to a simple matrix inversion, instead of the solution of differential equations in the SE. The T-matrix can be expanded in a partial-wave basis, where a connection between the scattering matrix (S-matrix) and the on-shell T-matrix takes the form

$$S_{ll'}^{sjt}(p) = \delta_{ll'} - 2\pi i\mu p\, T_{ll'}^{sjt}(E_p, p, p)\,, \tag{2.70}$$

with $T^{sjt}_{ll'}(E_{p''},p,p') \equiv \langle p(ls)jt|T(E_{p''})|p'(l's)jt\rangle$. On-shell refers to elements with $p=p'=p''$. The S-matrix itself is connected to phase shifts. Partial waves with $l=j$ are uncoupled waves. In those channels there is only one individual phase shift and no admixture of states with different orbital angular momenta l'. In this case, the S-matrix is given by

$$S^{sjt}_{l=j,l'=j}(p) = \exp\left[2i\delta^{sjt}_{l}(E_p)\right]. \tag{2.71}$$

For $l \neq j$, one is in general confronted with coupled systems. These systems consist of one partial wave with $l=j-1$ and one with $l=j+1$, which we define as $l_<$ and $l_>$, respectively. The ${}^3P_0$ wave is the only exception to this rule. It cannot be coupled as $l_< = -1$ does not exist. All other partial waves with $l \neq j$ are coupled to a wave with different l but equal j. Those coupled systems are for example the ${}^3S_1 -{}^3D_1$, ${}^3P_2 -{}^3F_2$, and ${}^3D_3 -{}^3G_3$ channels. The S-matrix for coupled channels reads:

$$S^{sjt}_{l,l'}(p) = \begin{pmatrix} \cos\left(2\epsilon_j(E_p)\right)\exp\left[2i\delta^{sjt}_{l_<}(E_p)\right] & i\sin\left(2\epsilon_j(E_p)\right)\exp\left[i\left(\delta^{sjt}_{l_<}(E_p)+\delta^{sjt}_{l_>}(E_p)\right)\right] \\ i\sin\left(2\epsilon_j(E_p)\right)\exp\left[i\left(\delta^{sjt}_{l_<}(E_p)+\delta^{sjt}_{l_>}(E_p)\right)\right] & \cos\left(2\epsilon_j(E_p)\right)\exp\left[2i\delta^{sjt}_{l_>}(E_p)\right] \end{pmatrix},^{(7)} \tag{2.72}$$

with the phase shifts $\delta_<$ and $\delta_>$ and the mixing angle ϵ_j, which connects the coupled channels with each other. Like for phase shifts, semi-empirical data for mixing angles is also available in Ref. [162].

2.6 Regulators

The calculation of Eq. (2.68) is a numerical task that requires a finite matrix representation of V, so that V can be cut off for large momenta. In addition, diverging contributions at zero distance (i.e., large momenta) from the pion exchange need to be removed. This procedure is reasonable, as the effective theory is valid only for momenta $Q \ll \Lambda_b \sim 500$ MeV. However, cutting off parts of the interaction introduces artifacts which need to be studied. Nonlocal interactions are typically regularized with nonlocal regulators of the form:

$$f^{\,\mathrm{nonloc}}(\mathbf{p},\mathbf{p}') = \exp\left[-\frac{p^n + p'^n}{\Lambda^n}\right], \tag{2.73}$$

where the cutoff is chosen similar to the breakdown scale $\Lambda \simeq \Lambda_b$, and n takes even integer values. This regulator function is then multiplied to the interaction:

$$V(\mathbf{p},\mathbf{p}') \mapsto V(\mathbf{p},\mathbf{p}')f^{\,\mathrm{nonloc}}(\mathbf{p},\mathbf{p}'). \tag{2.74}$$

The interaction is driven towards zero for large values p and p', as $f^{\,\mathrm{nonloc}}$ decreases. It is hardly affected by the regulator for small values of p and p'. This kind of regulators were used for example in Refs. [34, 153]. Regulator artifacts are estimated by probing several cutoffs. This leads to a whole family of interactions that vary in a certain range of cutoffs.

Local potentials are regularized by local regulators, to preserve their locality. This means that the regulator function in coordinate space may only depend on $\mathbf{r}$. In this work, we will closely follow the approach from Ref. [39], where the long- and short-range regulators are used to regularize pion-exchange contributions and contact interactions, respectively. We elaborate on local regulators that are considered within this thesis in Ch. 4, and further investigate effects (see Ch. 5) and different forms (see Ch. 6) of such regulators.

---

(7) The phase shifts we list here are so called "bar" phase shifts, which is the notation used in Ref. [162].

2.7 Uncertainty estimates from chiral effective field theory

The operator structure from above, and regulator functions are nothing new and phenomenological nuclear interactions have always been using similar constructs. One example is the Argonne V18 (AV18) [18] interaction from 1995, where the first 14 operators are given by

$$\mathcal{O}_{\mathrm{AV18}}^{p=1,14} = \left\{\mathbb{1}, \boldsymbol{\sigma}_1 \cdot \boldsymbol{\sigma}_2, S_{ij}, \mathbf{l}\cdot\mathbf{s}, \boldsymbol{l}^2, \boldsymbol{l}^2(\boldsymbol{\sigma}_1 \cdot \boldsymbol{\sigma}_2), (\mathbf{l}\cdot\mathbf{s})^2\right\} \otimes \{\mathbb{1}, \boldsymbol{\tau}_1 \cdot \boldsymbol{\tau}_2\} , \tag{2.75}$$

with a tensor operator S_{ij} that is similar to $(\mathbf{q}\cdot\boldsymbol{\sigma}_1)(\mathbf{q}\cdot\boldsymbol{\sigma}_2)$, a spin orbit operator $\mathbf{l}\cdot\mathbf{s}$ similar to $\frac{i}{2}(\boldsymbol{\sigma}_1 + \boldsymbol{\sigma}_2)\cdot(\mathbf{q}\times\mathbf{k})$ and so on. This similar structure of the operators is due to the symmetries that the nuclear interaction needs to fulfill (see Sec. 2.3).

The benefit of chiral EFT, or an EFT in general, is that we have a systematic low-energy expansion of operators. The power counting scheme states which contributions are most important and which enter at higher orders. We can further estimate the impact of those terms which we are neglecting, i.e., which contribute at the next higher order. Thus, chiral EFT provides not only systematically improvable results, but also enables a theoretically motivated uncertainty estimate and many-body contributions enter naturally. Historically, uncertainty estimates in chiral EFT have been obtained by the variation of the cutoff Λ in a certain range [153, 159]. This approach tends to overestimate uncertainties of orders where no new NN LECs enter (e.g., at N^{2}LO ($\nu = 3$)). The EFT uncertainty discussed in Ref. [30], considers data from calculations at lower orders in the power counting. This approach can be traced back to a simplified version of uncertainty estimates from Bayesian statistics as shown in Refs. [35, 36] (see also Ref. [37] on this topic). A similar approach is taken in Ref. [164]. Uncertainty estimates make use of the knowledge we have from the power counting and they do only depend on the cutoff under consideration (and not a whole range of cutoffs).

Following Ref. [30], the uncertainty depends on the expansion parameter Q/Λ, with the cutoff Λ. As mentioned above, Q represents typical momenta, which are of the order of the pion mass, and/or the actual pion mass. In the uncertainty estimate we take Q as

$$Q = \max(p, m_\pi) , \tag{2.76}$$

where p is a typical momentum of the system (e.g., the relative momentum in the two-body system). In the two-body system, it can be related to the lab energy from Eq. (2.67) by $p = \sqrt{m\,E_{\mathrm{lab}}/2}$. Starting with $E_{\mathrm{lab}} \approx 40$ MeV the relative momentum becomes larger than the pion mass. For a quantity X we estimate the correction due to neglected higher orders ΔX. At LO ($\nu = 0$) we estimate the influence at the order $\nu = 2$ (NLO) as there are no contributions at $\nu = 1$. The uncertainty estimate at LO is given by

$$\Delta X^{(0)}(p) = \left(\frac{Q}{\Lambda}\right)^2 |X^{(0)}(p) - X^{\mathrm{free}}(p)| , \tag{2.77}$$

where $X^{\mathrm{free}}(p)$ is the expectation value of the system without the presence of the interaction. For phase shifts $X^{\mathrm{free}}(p) = 0$. At any higher oder, the uncertainty estimate reads:

$$\begin{aligned}\Delta X^{(\nu>1)} = \max\Bigg\{&\left(\frac{Q}{\Lambda}\right)^{\nu+1} |X^{(0)}(p) - X^{\mathrm{free}}(p)|, \left(\frac{Q}{\Lambda}\right)^{\nu-1} |X^{(0)}(p) - X^{(2)}(p)|, \\ &\left(\frac{Q}{\Lambda}\right)^{\nu-2} |X^{(2)}(p) - X^{(3)}(p)|, \cdots, \left(\frac{Q}{\Lambda}\right)^{1} |X^{(\nu-1)}(p) - X^{(\nu)}(p)|\Bigg\} .\end{aligned} \tag{2.78}$$

Thereby one estimates the uncertainty by the deviation between two subsequent orders or the LO value, weighted with the expansion parameter to a certain power.

3 New developments in chiral effective field theory

In this thesis, we investigate new developments in the application of chiral EFT. The first half of this thesis focuses on local interactions from chiral EFT. The general idea to have local nuclear interactions is nothing new, and local phenomenological interactions have been around since decades (e.g., the AV18 interaction [18](1)). However, local interactions from chiral EFT is a topic of recent research [38–41, 107, 165]. It allowed for the first time to combine interactions from chiral EFT with the precision Quantum Monte Carlo (QMC) methods [39, 66, 67, 109, 165–169], which is leading to systematically improvable many-body calculations based on *ab initio* few-nucleon forces with controlled theoretical uncertainties.

The second half of this thesis focuses on the implementation of chiral EFT in a shell-model valence space. The nuclear shell model [7–9] is a very successful many-body method, which is widely used for the calculation of nuclear-structure properties in the medium to medium-heavy mass region of the nuclear chart. Typically, the model space for shell-model calculations include one major harmonic-oscillator (HO) shell, or extensions by including another full shell or some of the lowest-lying subshells. In order to perform calculations with the nuclear shell model, one requires matrix elements that describe the interaction among nucleons in the valence space under consideration. [116]. There are two common approaches to arrive at these valence-space interactions, which can be divided into so called two-body matrix elements (TBMEs) and single-particle energies (SPEs). First, there are the traditional approaches, where an effective interaction is constructed in a specific valence space by fitting free parameters to experimental properties in the model space. These parameters can either be theoretically motivated, or one can use the TBMEs and SPEs directly as parameters. A very promising example are the USDA and USDB interaction from Ref. [114], which reproduce the experimental data with a root mean square (RMS) deviation of only a few hundred keV. Second, valence-space interactions can be derived using modern *ab initio* methods, which can then be used in shell-model calculations. Among those methods are many-body perturbation theory (MBPT) [91, 92, 95, 96], the no-core shell model (NCSM) [73, 74], coupled-cluster theory (CC) [78–80] and the in-medium similarity renormalization group (IM-SRG) [64, 81–83]. All of those methods start from a few-body Hamiltonian, which typically consists of two- and three-body interactions from chiral effective field theory (EFT). These methods do not achieve the same accuracy as the traditional methods, but they can provide uncertainty estimates. Our goal is to combine the systematics of forces from chiral EFT with the high-precision of effective interactions from phenomenology. For this we construct an effective valence-space Hamiltonian, based on operators from chiral EFT by adjusting the LECs to nuclear ground-state energies and excitation spectra in shell-model valence spaces. Valence-space Hamiltonians contain novel operators, which appear due to broken free-space symmetries by the presence of a core. In the second section of this chapter we present those new operators and sort them into the Weinberg power counting scheme.

3.1 Local chiral interactions

Locality of interactions is a crucial requirement of some many-body methods like QMC. Also other frameworks can profit from local interactions in terms of simplified calculations and reduced computational time like, e.g., the double-folding formalism, which we investigated in Ref. [108]. This technique requires self-consistent calculations involving multiple three-dimensional integrals in each iteration. Local interactions facilitate those calculations dramatically, as locality effectively reduces the number of integrals one needs to evaluate. However, we found there, that out of the existing local interactions from Ref. [39],

---

(1) Some operator terms in this interaction are technically not local, e.g., the spin-orbit force $\mathbf{l} \cdot \mathbf{s}$. They can, however, be treated in a controlled way within QMC methods.

only the softest interaction with R_0 = 1.2 fm converges at all orders up to N^{2}LO. We construct new soft local interactions at R_0 = 1.4, and 1.6 fm for the application in nucleus-nucleus scattering and fusion in Ref. [108]. For consistency, we also construct an interaction at R_0 = 1.2 fm. We further elaborate on the construction of these new soft interactions and show one application for the elastic ^{16}O–^{16}O cross section in Ch. 4 of this thesis.

Violated Fierz-rearrangement freedom is a known problem in locally regularized three-body interactions [107, 109, 170]. In the three-body sector at N^{2}LO one is confronted with a variety of possible operators. As one example, Ref. [109] investigates the three-nucleon ($3N$) contact term (V_E), which is the last diagram in the N^{2}LO three-body sector in Tab. 2.3. The potential reads

$$V_E = \frac{c_E}{\Lambda_\chi F_\pi^4} \sum_{i<j<k} \sum_{\text{cyc.}} \boldsymbol{O}_{ijk} f_{\text{short}}(r_{kj}, R_{3N}) f_{\text{short}}(r_{ij}, R_{3N}), \tag{3.1}$$

with the chiral symmetry-breaking scale Λ_χ, the $3N$ LEC c_E, the coordinate-space cutoff R_{3N} and short-range regulator

$$f_{\text{short}}(r_{ij}, R_{3N}) = \frac{1}{\pi\Gamma(3/4)R_{3N}^3} \exp\left(-\left(\frac{r_{ij}}{R_{3N}}\right)^4\right). \tag{3.2}$$

The latter is labeled $\delta_{R_{3N}}(r)$ in Ref. [109]. The distance r_{ij} is the relative distance between particle i and j. The first sum runs over the three single-particle labels i,j, and k and the second sum over all cyclic permutations of those indices (for more details see Ref. [171]). There are several options allowed by symmetries for the operator $\boldsymbol{O}_{ijk}$. Possible choices are

$$\left\{\mathbb{1}, \boldsymbol{\sigma}_i \cdot \boldsymbol{\sigma}_j, \boldsymbol{\tau}_i \cdot \boldsymbol{\tau}_j, (\boldsymbol{\sigma}_i \cdot \boldsymbol{\sigma}_j)(\boldsymbol{\tau}_i \cdot \boldsymbol{\tau}_j), (\boldsymbol{\sigma}_i \cdot \boldsymbol{\sigma}_j)(\boldsymbol{\tau}_i \cdot \boldsymbol{\tau}_k), \left[(\boldsymbol{\sigma}_i \times \boldsymbol{\sigma}_j) \cdot \boldsymbol{\sigma}_k\right]\left[(\boldsymbol{\tau}_i \times \boldsymbol{\tau}_j) \cdot \boldsymbol{\tau}_k\right]\right\}. \tag{3.3}$$

For nonlocal regulators, this set can be reduced due to a single operator due to symmetries. This is referred to as Fierz-rearrangement freedom. However, in Ref. [109] was found that this rearrangement freedom is violated when local regulators are used. As a consequence, the choice of $\boldsymbol{O}_{ijk}$ does effect the result of the interaction.

Similar to the three-body sector, the Fierz-rearrangement freedom is violated for local regulators in two-nucleon interactions. In Ref. [111] we investigated the extend of this violation. We see similar problems due to the broken Fierz-rearrangement freedom in LO interactions. Local regulators do interfere with the partial-wave decomposition of nuclear interactions. This leads to a sensitivity on the choice of the LO operators in partial waves with odd orbital angular momenta. However, we find that differences at LO are greatly reduced at NLO. Our findings from Ref. [111] are detailed in Ch. 5 of this thesis.

We further investigate the large (momentum-space) cutoff behavior of local regulators at LO. This relates to the coordinate-space cutoff via $\Lambda \sim R_0^{-1}$. Such a renormalization behavior has already been studied for nonlocal regulators with cutoffs from $\Lambda = 2 - 20$ fm^{-1} in 2005 in Ref. [112], where it was found that the Weinberg power counting leads to cutoff independent results in channels, where the tensor-force of the OPE is repulsive, in channels with spin $S = 0$, as well as in the $^3S_1$ channel. The latter has a contact term already at LO. In partial-wave channels in which the tensor-force of the one-pion exchange is attractive and no contacts are present at LO like, e.g., the $^3P_0$ channel. A strong cutoff dependence was observed as well as the appearance of spurious bound states. To obtain cutoff-independent interactions, it is suggested to introduce additional contact interactions to balance this attraction in the affected channels, so-called counterterms.

In our investigation in Ref. [113], we consider coordinate space-cutoffs from $R_0^{-1} = 0.8 - 10$ fm^{-1} for different sets of operators(2) and different regulator functions. For most operator combinations we find

---

(2) The Fierz-rearrangement freedom is violated for local interactions, which makes the choice of LO operators relevant. For more information see Ref. [111] and Ch. 5

similar results as in Ref. [112]. However, for one particular choice of operators ($\mathbb{1}$ and $\boldsymbol{\sigma}_1 \cdot \boldsymbol{\sigma}_2$), we find that the cutoff artifacts work to our advantage. The admixture of the S-wave contact operators to higher partial waves by the local regulator leads to cutoff-independent results in all partial waves. All of our findings from Ref. [113] are presented in Ch. 6.

3.2 Novel operators for valence-space interactions from chiral EFT

We discussed all free-space operators from chiral EFT up to N^{3}LO in Ch. 2. As mentioned in Sec. 2.3, the presence of a core in the shell-model framework breaks the Galilean invariance, as it provides a reference frame to the system. Hence, valence-space operators may explicitly depend on the center-of-mass (CM) momentum $\mathbf{P}$. Note that the CM operators at NLO have already been investigated in the context of Fermi liquid theory in Ref. [172], and they take a similar form as the antisymmetric spin-orbit operators presented in Ref. [173]. We determine the CM momentum-dependent operators by following the remaining symmetries of the strong interaction from Sec. 2.3. First contributions of those novel operators appear at NLO, subleading contributions appear at N^{3}LO. As those contributions appear exclusively in our valence-space (vs) interactions, we will label interactions that feature those operators as NLO$_{\mathrm{vs}}$, N^{2}LO$_{\mathrm{vs}}$, and N^{3}LO$_{\mathrm{vs}}$. The new contact operators are accompanied by LECs, just like the free-space contact operators. We label vs LECs at NLO with P_i and those at N^{3}LO with Q_i. In the following, we list the operators according to their order and spin structure as central, vector, and tensor operators.

3.2.1 New operators at next-to-leading order

Contact operators at NLO are proportional to the momentum square. The valence-space operator structures that appear are consequently $\sim P^2$, $\sim qP$, and $\sim kP$. We list the possible, linearly independent contributions below:

- **Central Operators**
  Following the symmetries from Sec. 2.3, we find two linearly independent central operators:
  $$\mathbf{P}^2,\ \mathbf{P}^2(\boldsymbol{\sigma}_1 \cdot \boldsymbol{\sigma}_2)\,. \tag{3.4}$$
  These operators contribute to relative S waves.

- **Vector operators**
  At NLO, we find vector operators which are antisymmetric in spin space. These operators were first detailed in Ref. [172] in the context of Fermi liquid theory. They are called difference- (diff) and cross-vector operators, denoted by D_{12} and A_{12} respectively. The operators read
  $$D_{12}(\mathbf{q},\mathbf{P}) = i(\mathbf{q} \times \mathbf{P}) \cdot (\boldsymbol{\sigma}_1 - \boldsymbol{\sigma}_2)\,, \tag{3.5}$$
  $$A_{12}(\mathbf{k},\mathbf{P}) = (\mathbf{k} \times \mathbf{P}) \cdot (\boldsymbol{\sigma}_1 \times \boldsymbol{\sigma}_2)\,. \tag{3.6}$$
  The operators have a similar structure as the antisymmetric spin-orbit interactions in the context of shell-model interactions as in Ref. [173]. A partial-wave decomposition of those operators shows, that they only contribute if the initial and final spin differ. In particular, those operators contribute to the relative, mixed partial waves
  $$^3S_1 - {}^1P_1 \qquad \text{and} \qquad {}^1S_0 - {}^3P_j\,.$$

- **Tensor operators**
  There is one linear independent tensor operator, which has also been investigated in Ref. [172]. The CM tensor operator at NLO reads
  $$(\mathbf{P} \cdot \boldsymbol{\sigma}_1)(\mathbf{P} \cdot \boldsymbol{\sigma}_2)\,. \tag{3.7}$$
  This operator contributes to relative S waves.

Together with the LECs, the valence-space interaction at NLO reads

$$V_{\mathrm{vs}}^{(\nu=2)}(\mathbf{p},\mathbf{p}',\mathbf{P}) = (P_1 + P_2\boldsymbol{\sigma}_1\cdot\boldsymbol{\sigma}_2)\mathbf{P}^2 + P_3 i(\boldsymbol{\sigma}_1-\boldsymbol{\sigma}_2)\cdot(\mathbf{q}\times\mathbf{P}) + P_4(\boldsymbol{\sigma}_1\times\boldsymbol{\sigma}_2)\cdot(\mathbf{k}\times\mathbf{P}) \\ + P_5(\boldsymbol{\sigma}_1\cdot\mathbf{P})(\boldsymbol{\sigma}_2\cdot\mathbf{P})\,. \tag{3.8}$$

Free-space LECs and valence-space LECs are determined by fitting the interaction to nuclear ground-state and excitation energies in the valence-space under consideration. More information about the operators at NLO are given in App. C.2.

3.2.2 New operators at next-to-next-to-next-to-leading order

Contact operators at N^{3}LO are proportional to momentum to the power of four. For the valence-space operators, the possible combinations are $\sim P^4$, $\sim P^3 \otimes \{q, k\}$, $\sim P^2 \otimes \left\{q^2, qk, k^2\right\}$, and $\sim P \otimes \left\{q^3, q^2k, qk^2, k^3\right\}$. Here, we use $\otimes$ to distinguish between CM and relative coordinates. The allowed operator structures need to fulfill Eqs. (2.39) - (2.42) from Sec 2.3. We list the possible, linear independent contributions below:

- **Central operators**
  For central operators, the conditions are fulfilled when m_q, m_k, m_i, m_P, and m_σ all take even values (see Eqs. (2.39) - (2.42)). We find the following central valence-space operators at N^{3}LO:
  $$\left\{\mathbf{q}^2\mathbf{P}^2,\, (\mathbf{q}\times\mathbf{P})^2,\, \mathbf{k}^2\mathbf{P}^2,\, (\mathbf{k}\times\mathbf{P})^2,\, \mathbf{P}^4\right\} \otimes \{\mathbb{1},\, (\boldsymbol{\sigma}_1\cdot\boldsymbol{\sigma}_2)\}\,. \tag{3.9}$$
  Each operator in the left parenthesis either appears with the identity operator in spin space, or with the scalar product $\boldsymbol{\sigma}_1\cdot\boldsymbol{\sigma}_2$. In total we find ten new linearly independent central operators.

- **Vector operators**
  We find 16 new linearly independent vector operators. One of those operators does only contribute for different final and initial isospin, and thus, it cannot be used for the strong interaction. This leaves us with 15 new operators. In order to keep a structured oversight, we split up the vector contributions according to the spin structure, leading to three groups, which are proportional to $(\boldsymbol{\sigma}_1-\boldsymbol{\sigma}_2)$, $(\boldsymbol{\sigma}_1\times\boldsymbol{\sigma}_2)$, or $(\boldsymbol{\sigma}_1+\boldsymbol{\sigma}_2)$.
  - $(\boldsymbol{\sigma}_1-\boldsymbol{\sigma}_2)$:
    Following Eqs. (2.39) - (2.42) from Sec 2.3, we find m_i, m_q, and m_P need to be odd, while m_k needs to be even to fulfill symmetry constraints. This leads to the following operator structure:
    $$i(\boldsymbol{\sigma}_1-\boldsymbol{\sigma}_2)\cdot\left\{\begin{array}{l} (\mathbf{q}\times\mathbf{P})\left\{\begin{array}{l}\mathbf{q}^2\\ \mathbf{k}^2\\ \mathbf{P}^2\end{array}\right. \\ (\mathbf{k}\times\mathbf{P})(\mathbf{q}\cdot\mathbf{k}) \\ (\mathbf{q}\times\mathbf{k})(\mathbf{k}\cdot\mathbf{P}) \\ ((\mathbf{q}\times\mathbf{k})\times(\mathbf{k}\times\mathbf{P})) \end{array}\right. . \tag{3.10}$$
  - $(\boldsymbol{\sigma}_1\times\boldsymbol{\sigma}_2)$:
    To fulfill the symmetry requirements, we need odd m_k and m_P and even values for m_i and m_q. This leads to
    $$(\boldsymbol{\sigma}_1\times\boldsymbol{\sigma}_2)\cdot\left\{\begin{array}{l} (\mathbf{k}\times\mathbf{P})\left\{\begin{array}{l}\mathbf{q}^2\\ \mathbf{k}^2\\ \mathbf{P}^2\end{array}\right. \\ (\mathbf{q}\times\mathbf{P})(\mathbf{q}\cdot\mathbf{k}) \\ (\mathbf{q}\times\mathbf{k})(\mathbf{q}\cdot\mathbf{P}) \end{array}\right. . \tag{3.11}$$

As mentioned above, the operator $(\boldsymbol{\sigma}_1 \times \boldsymbol{\sigma}_2) \cdot ((\mathbf{q} \times \mathbf{P}) \times (\mathbf{q} \times \mathbf{k}))$ would in principle also belong to this group, but it breaks isospin. This can be seen when one performs the partial-wave decomposition. The relative partial waves, to which this operator contributes connect odd values for $l+s$ with even values $l'+s'$. Following the Pauli principle, t is even for odd $l+s$ and t' must be odd for even $l'+s'$. Thus, we omit this structure in the following.

- $(\boldsymbol{\sigma}_1 + \boldsymbol{\sigma}_2)$:
  For this operator, we see that m_i, m_q, and m_k need to be odd, while m_P needs to be even. This allows the following CM-momentum dependent operator structures:

$$\frac{i}{2}(\boldsymbol{\sigma}_1 + \boldsymbol{\sigma}_2) \cdot \begin{cases} (\mathbf{q} \times \mathbf{k})\mathbf{P}^2 \\ (\mathbf{k} \times \mathbf{P})(\mathbf{P} \cdot \mathbf{q}) \\ (\mathbf{q} \times \mathbf{P})(\mathbf{P} \cdot \mathbf{k}) \\ ((\mathbf{k} \times \mathbf{P}) \times (\mathbf{q} \times \mathbf{P})) \end{cases} . \tag{3.12}$$

- **Tensor operators**
  We find seven new tensor operators that are consistent with the symmetries at this order. The tensor operators are given by

$$\begin{aligned} &(\mathbf{P} \cdot \boldsymbol{\sigma}_1)(\mathbf{P} \cdot \boldsymbol{\sigma}_2) \begin{cases} \mathbf{q}^2 \\ \mathbf{k}^2 \\ \mathbf{P}^2 \end{cases} . \\ &(\mathbf{q} \cdot \boldsymbol{\sigma}_1)(\mathbf{q} \cdot \boldsymbol{\sigma}_2)\mathbf{P}^2 . \\ &(\mathbf{k} \cdot \boldsymbol{\sigma}_1)(\mathbf{k} \cdot \boldsymbol{\sigma}_2)\mathbf{P}^2 . \\ &((\mathbf{q} \times \mathbf{P}) \cdot \boldsymbol{\sigma}_1)((\mathbf{q} \times \mathbf{P}) \cdot \boldsymbol{\sigma}_2) . \\ &((\mathbf{k} \times \mathbf{P}) \cdot \boldsymbol{\sigma}_1)((\mathbf{k} \times \mathbf{P}) \cdot \boldsymbol{\sigma}_2) . \end{aligned} \tag{3.13}$$

In total, there are 32 new linearly independent valence-space operators at N^{3}LO. Together with the LECs, which we label Q_i, the valence-space interaction at this order reads

$$\begin{aligned} V_{\text{vs}}^{(\nu=4)}(\mathbf{p}, \mathbf{p}', \mathbf{P}) =& Q_1 \mathbf{q}^2 \mathbf{P}^2 + Q_2 (\mathbf{q} \times \mathbf{P})^2 + Q_3 \mathbf{k}^2 \mathbf{P}^2 + Q_4 (\mathbf{k} \times \mathbf{P})^2 + Q_5 \mathbf{P}^4 \\ &+ \left(Q_6 \mathbf{q}^2 \mathbf{P}^2 + Q_7 (\mathbf{q} \times \mathbf{P})^2 + Q_8 \mathbf{k}^2 \mathbf{P}^2 + Q_9 (\mathbf{k} \times \mathbf{P})^2 + Q_{10} \mathbf{P}^4 \right) (\boldsymbol{\sigma}_1 \cdot \boldsymbol{\sigma}_2) \\ &+ i\, (\boldsymbol{\sigma}_1 - \boldsymbol{\sigma}_2) \cdot \left[(\mathbf{q} \times \mathbf{P}) \left(Q_{11} \mathbf{q}^2 + Q_{12} \mathbf{k}^2 + Q_{13} \mathbf{P}^2 \right) + Q_{14} (\mathbf{k} \times \mathbf{P}) (\mathbf{q} \cdot \mathbf{k}) \right. \\ &\left. + Q_{15} (\mathbf{q} \times \mathbf{k}) (\mathbf{k} \cdot \mathbf{P}) + Q_{16} ((\mathbf{q} \times \mathbf{k}) \times (\mathbf{q} \times \mathbf{P})) \right] \\ &+ (\boldsymbol{\sigma}_1 \times \boldsymbol{\sigma}_2) \cdot \left[(\mathbf{k} \times \mathbf{P}) \left(Q_{17} \mathbf{q}^2 + Q_{18} \mathbf{k}^2 + Q_{19} \mathbf{P}^2 \right) + Q_{20} (\mathbf{q} \times \mathbf{P}) (\mathbf{q} \cdot \mathbf{k}) \right. \\ &\left. + Q_{21} (\mathbf{q} \times \mathbf{k}) (\mathbf{q} \cdot \mathbf{P}) \right] \\ &+ \frac{i}{2} (\boldsymbol{\sigma}_1 + \boldsymbol{\sigma}_2) \cdot \left[Q_{22} (\mathbf{q} \times \mathbf{k}) \mathbf{P}^2 + Q_{23} (\mathbf{k} \times \mathbf{P}) (\mathbf{q} \cdot \mathbf{P}) + Q_{24} (\mathbf{q} \times \mathbf{P}) (\mathbf{k} \cdot \mathbf{P}) \right. \\ &\left. + Q_{25} ((\mathbf{q} \times \mathbf{P}) \times (\mathbf{k} \times \mathbf{P})) \right] + \left(Q_{26} \mathbf{q}^2 + Q_{27} \mathbf{k}^2 + Q_{28} \mathbf{P}^2 \right) (\mathbf{P} \cdot \boldsymbol{\sigma}_1)(\mathbf{P} \cdot \boldsymbol{\sigma}_2) \\ &+ \left(Q_{29} (\mathbf{q} \cdot \boldsymbol{\sigma}_1)(\mathbf{q} \cdot \boldsymbol{\sigma}_2) + Q_{30} (\mathbf{k} \cdot \boldsymbol{\sigma}_1)(\mathbf{k} \cdot \boldsymbol{\sigma}_2) \right) \mathbf{P}^2 \\ &+ Q_{31} \left[(\mathbf{q} \times \mathbf{P}) \cdot \boldsymbol{\sigma}_1 \right] \left[(\mathbf{q} \times \mathbf{P}) \cdot \boldsymbol{\sigma}_2 \right] + Q_{32} \left[(\mathbf{k} \times \mathbf{P}) \cdot \boldsymbol{\sigma}_1 \right] \left[(\mathbf{k} \times \mathbf{P}) \cdot \boldsymbol{\sigma}_2 \right] . \end{aligned} \tag{3.14}$$

Remarks on the implementation of center-of-mass momentum operators

We investigate the NLO$_{\text{vs}}$ interaction with 14 LECs, the N^{2}LO$_{\text{vs}}$ interaction also with 14 LECs, and the N^{3}LO$_{\text{vs}}$ interaction with 61 LECs. In addition we consider a N^{3}LO$_{\text{NLO,vs}}$ interaction with 29 LECs. The latter contains all free-space contributions up to N^{3}LO plus valence-space contributions from NLO. To use these interactions in the shell-model framework, we need to decompose them into partial waves. The partial-wave decomposed matrix elements are then transformed with a generalized Talmi-Moshinsky transformation from Ref. [115] to the harmonic-oscillator (HO) basis. We provide a new approach to the partial-wave decomposition (PWD) of interaction from chiral EFT in App. B. This approach uses a (mathematical) tensor-operator representation, which is given in App. C. Following the steps in App. B, we construct a computer code, capable of transforming any contact operator from chiral EFT directly into partial waves. More details about the transformation to the HO basis are given in chapter 7.

3.2.3 Applications

We implement the CM operators in shell-model interactions, where they lead to significant improvement of the root-mean-square deviation to experiment. We investigate first applications in Ch. 8 and Ref. [115], where we construct shell-model interactions from chiral EFT up to NLO in the sd shell. A general introduction to those interactions is provided in Ch. 7. In Ch. 9 we continue our research by including valence-space operators at N^{3}LO. As we will show, this leads to a precise description of experiment, and the interaction is comparable to the USDA and USDB interactions from Ref. [114]. Motivated by the encouraging results in the sd shell, we extend our model space by including the $0f_{7/2}$ neutron subshell. This allows us to study the very neutron-rich region of medium-mass nuclei. Results for this cross-shell interaction are presented in Ch. 10.

4 Construction of soft, local interactions and applications

Most many-body methods profit from soft interactions in terms of improved convergence. For this purpose, there exist multiple renormalization-group (RG) methods to soften few-body interactions. Among those are for example the $V_{\text{low}k}$ method [174, 175] and the similarity renormalization group (SRG) [175–185]. Another approach to obtain soft interactions is the unitary correlation operator method (UCOM) [180, 186]. The impact of RG methods on the momentum-space matrix elements is demonstrated in Fig. 4.1, where the upper panel shows the $V_{\text{low}k}$ method and the lower panel shows the SRG method. Both methods have a parameter to control the “softness". In the case of $V_{\text{low}k}$, matrix elements for large values of k and/or k' are pushed towards zero as the parameter Λ decreases. Simultaneously, matrix elements at small momenta are enhanced, resulting in box-like momentum-space matrix representation in the right panel. As Λ decreases the size of this box decreases. Note that we denote relative momenta as p and p' in this thesis and not as k and k' as in the figure. The lower row demonstrates the impact of the SRG method. The SRG flow-parameter λ decreases from the left to the right. In the process the interaction is pushed more and more towards a diagonal form. In both methods, $V_{\text{low}k}$ and SRG, matrix elements between low and high momenta are decoupled. While RG methods lead to softer interactions, they induce many-body operators, even if the initial interaction is a pure two-body interaction, and they introduce nonlocal contributions. Depending on the many-body method at hand, locality might be a vital component for the method to work. This is what motivates us to develop soft local interactions, by adjusting the coordinate-space cutoff accordingly, such that they can directly be used in many-body calculations. We present interactions with coordinate-space cutoffs $R_0 =$ 1.2, 1.4, and 1.6 fm at LO, NLO, and N^{2}LO.

In the following, we show the functional form of local chiral interactions as introduced in Refs. [38–40]. Afterwards, we discuss details about the fitting procedure. We then present the new local interactions and show the application to ^{16}O–^{16}O scattering.

4.1 Local chiral nucleon-nucleon potentials

We construct our interactions as suggested in Refs. [38, 39, 41, 165]. The NN potential is a sum of long-range pion-exchange interactions and short-range contact interactions

$$V_{NN}(\mathbf{r}) = V_\pi(\mathbf{r}) + V_{\text{cont}}(\mathbf{r}) \mapsto V_\pi(\mathbf{r}) f_{\text{long}}(\mathbf{r}, R_L) + V_{\text{cont}}(\mathbf{r}) f_{\text{short}}(\mathbf{r}, R_S)\,, \tag{4.1}$$

where in coordinate space we regularize the different contributions using

$$f_{\text{long}}(\mathbf{r}, R_L) = \left(1 - \exp\left[-\left(\frac{r}{R_L}\right)^{n_1}\right]\right)^{n_2}\,, \tag{4.2}$$

$$f_{\text{short}}(\mathbf{r}, R_S) = \frac{n}{4\pi\Gamma(3/n)R_S^3}\exp\left[-\left(\frac{r}{R_S}\right)^{n}\right]\,, \tag{4.3}$$

with the long-range regulator, $f_{\text{long}}(\mathbf{r}, R_L)$ and long-range coordinate-space cutoff R_L, short-range regulator $f_{\text{short}}(\mathbf{r}, R_S)$ and short-range cutoff R_S, and exponents n_1, n_2, and n which take integer values (n_1 and n take even values). We use $R_S = R_L = R_0$ as in Refs. [38, 39]. In this chapter, we use $n_1 = n = 4$ and $n_2 = 1$, which leads to the following expressions:

$$f_{\text{l}}(r, R_0) = 1 - e^{-(r/R_0)^4}\,, \tag{4.4}$$

$$f_{\text{s}}(r, R_0) = \frac{e^{-(r/R_0)^4}}{\pi\Gamma(3/4)R_0^3}\,. \tag{4.5}$$

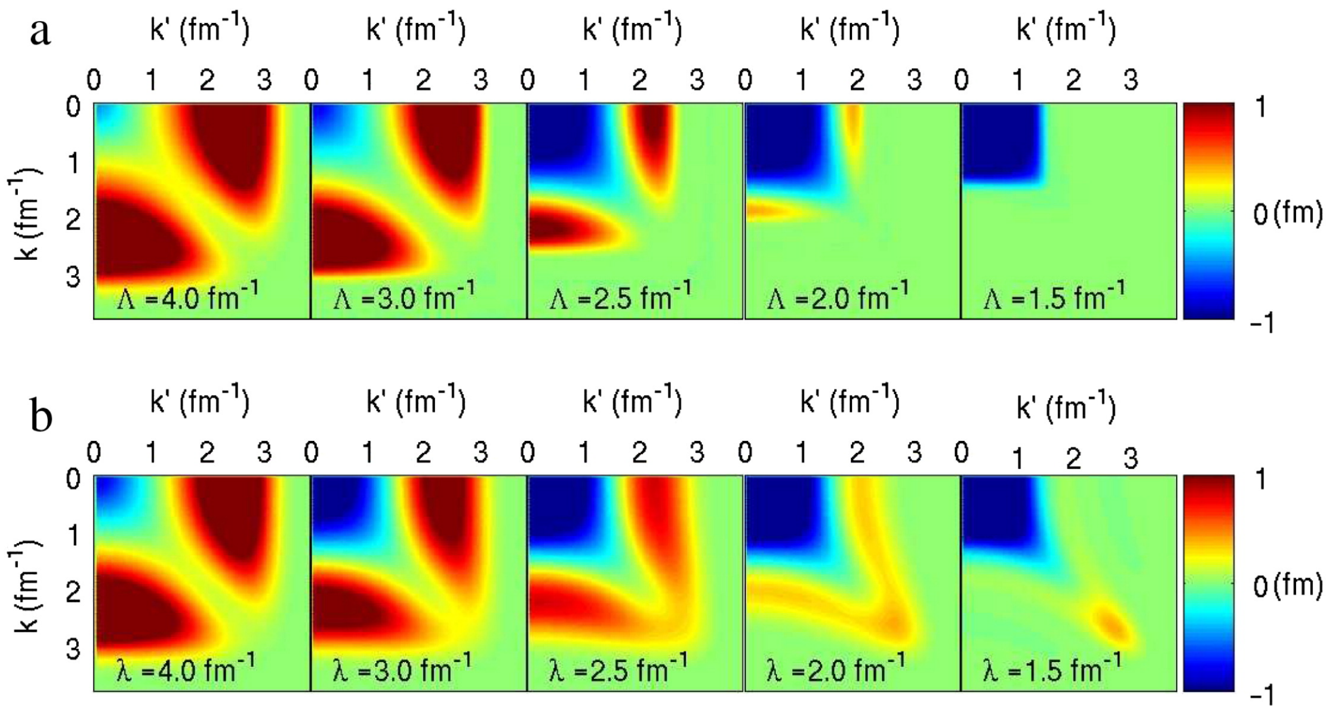

Figure 4.1.: Impact of RG methods on momentum-space matrix elements of a two-body interaction taken from Ref. [175]. The upper row (a) shows the $V_{\text{low}k}$ method for different Λ values, the lower row (b) shows the SRG method for different flow parameters λ. The color coding refers to the size of the momentum-space matrix elements. Large positive (negative) matrix elements are colored red (blue). Vanishing contributions are colored green. The color coding is given in the bar on the right of each row.

4.1.1 Leading order

In coordinate space, the LO potential is defined by

$$V_{NN}^{\text{LO}}(r,R_0) = V_{\text{OPE}}^{\text{LO}}(r,R_0) + V_{\text{cont}}^{\text{LO}}(r,R_0)\,, \tag{4.6}$$

The OPE interaction has the form

$$V_{\text{OPE}}^{\text{LO}}(r,R_0) = \frac{m_\pi^3}{12\pi}\left(\frac{g_A}{2F_\pi}\right)^2 \boldsymbol{\tau}_1\cdot\boldsymbol{\tau}_2\,\frac{e^{-m_\pi r}}{m_\pi r}\left[\boldsymbol{\sigma}_1\cdot\boldsymbol{\sigma}_2 + \left(1+\frac{3}{m_\pi r}+\frac{3}{(m_\pi r)^2}\right)S_{12}\right] f_{\text{long}}(r,R_0)\,, \tag{4.7}$$

with the pion mass m_π, the axial coupling constant g_A, and the pion-decay constant F_π as in Ch. 2. The tensor operator is given by $S_{12} = 3(\boldsymbol{\sigma}_1\cdot\mathbf{e}_r)(\boldsymbol{\sigma}_2\cdot\mathbf{e}_r) - \boldsymbol{\sigma}_1\cdot\boldsymbol{\sigma}_2$, with the unit vector $\mathbf{e}_r$ in direction of $\mathbf{r}$. The short-range contact interaction at LO reads

$$V_{\text{cont}}^{\text{LO}}(r,R_0) = (C_S + \boldsymbol{\sigma}_1\cdot\boldsymbol{\sigma}_2 C_T)\, f_{\text{short}}(r,R_0)\,, \tag{4.8}$$

with the LECs C_S and C_T.

4.1.2 Next-to-leading order

Leading two-pion exchange contributions enter at NLO. We use spectral-function regularization (SFR) as in Ref. [39]. The two-pion exchange contributions at this order read

$$W_C^{(\nu=2)}(r) = \frac{1}{2\pi^2 r} \int_{2m_\pi}^{\tilde{\Lambda}} \mathrm{d}\mu \mu e^{-\mu r} \eta_C^{(\nu=2)}(\mu) , \tag{4.9}$$

$$V_S^{(\nu=2)}(r) = \frac{1}{3\pi^2 r} \int_{2m_\pi}^{\tilde{\Lambda}} \mathrm{d}\mu \mu e^{-\mu r} \rho_S^{(\nu=2)}(\mu) , \tag{4.10}$$

$$V_T^{(\nu=2)}(r) = -\frac{1}{6\pi^2 r^3} \int_{2m_\pi}^{\tilde{\Lambda}} \mathrm{d}\mu \mu e^{-\mu r} \rho_T^{(\nu=2)}(\mu) \left(3 + 3\mu r + \mu^2 r^2\right) , \tag{4.11}$$

with the spectral functions

$$\eta_c^{(\nu=2)}(\mu) = \frac{1}{768\pi F_\pi^4} \frac{\sqrt{\mu^2 - 4m_\pi^2}}{\mu} \left[4m_\pi^2 (5g_A^4 - 4g_A^2 - 1) - \mu^2 (23 g_A^4 - 10 g_A^2 - 1) + \frac{48 g_A^4 m_\pi^4}{4m_\pi^2 - \mu^2} \right] , \tag{4.12}$$

$$\rho_T^{(\nu=2)}(\mu) = \frac{3 g_A^4}{128\pi F_\pi^4} \frac{\sqrt{\mu^2 - m_\pi^2}}{\mu} , \tag{4.13}$$

$$\rho_S^{(\nu=2)}(\mu) = \mu^2 \rho_T^{(\nu=2)}(\mu) . \tag{4.14}$$

The two-pion–exchange interaction is constructed according to the contributions from Eq. (2.45).

New NN contact interactions appear at NLO, which depend on the momentum transfers $\mathbf{q}$ and $\mathbf{k}$. As described in Ref. [39], $\mathbf{q}$ is preferred over $\mathbf{k}$, as $\mathbf{q}$ transforms to $\mathbf{r}$, and thus, preserves the locality of the interaction. In momentum space, one takes the following operators

$$\begin{aligned} V_{\text{cont}}^{(\nu=2)}(\mathbf{p}, \mathbf{p}') = & \left(C_1 + C_2 \boldsymbol{\tau}_1 \cdot \boldsymbol{\tau}_2 + C_3 \boldsymbol{\sigma}_1 \cdot \boldsymbol{\sigma}_2 + C_4 \boldsymbol{\sigma}_1 \cdot \boldsymbol{\sigma}_2 \boldsymbol{\tau}_1 \cdot \boldsymbol{\tau}_2 \right) \mathbf{q}^2 \\ & + C_5 i \frac{1}{2} (\boldsymbol{\sigma}_1 + \boldsymbol{\sigma}_2) \cdot (\mathbf{q} \times \mathbf{k}) + \left(C_6 + C_7 \boldsymbol{\tau}_1 \cdot \boldsymbol{\tau}_2\right) (\boldsymbol{\sigma}_1 \cdot \mathbf{q})(\boldsymbol{\sigma}_2 \cdot \mathbf{q}) . \end{aligned} \tag{4.15}$$

The only $\mathbf{k}$ dependence that cannot be removed by choosing alternative operators is the vector operator $C_5 i \frac{1}{2} (\boldsymbol{\sigma}_1 + \boldsymbol{\sigma}_2) \cdot (\mathbf{q} \times \mathbf{k})$. The treatment of this operator is described in Eq. (B3) of Ref. [39]. The coordinate-space representation is given as

$$\begin{aligned} V_{\text{cont}}^{(\nu=2)}(\mathbf{r}) = \Bigg[& -\left(C_1 + C_2 \boldsymbol{\tau}_1 \cdot \boldsymbol{\tau}_2 + C_3 \boldsymbol{\sigma}_1 \cdot \boldsymbol{\sigma}_2 + C_4 \boldsymbol{\sigma}_1 \cdot \boldsymbol{\sigma}_2 \boldsymbol{\tau}_1 \cdot \boldsymbol{\tau}_2\right) \Delta + \frac{C_5}{2} \mathbf{L} \cdot \mathbf{S} \frac{1}{r} \frac{\partial}{\partial r} \\ & + \left(C_6 + C_7 \boldsymbol{\tau}_1 \cdot \boldsymbol{\tau}_2\right) \left((S_{12} + \boldsymbol{\sigma}_1 \cdot \boldsymbol{\sigma}_2) (\frac{1}{r} \frac{\partial}{\partial r} - \frac{\partial^2}{\partial r^2}) - \boldsymbol{\sigma}_1 \cdot \boldsymbol{\sigma}_2 \frac{1}{r} \frac{\partial}{\partial r} \right) \Bigg] f_{\text{short}}(r, R_0) , \end{aligned} \tag{4.16}$$

with the spin orbit operator $\mathbf{l} \cdot \mathbf{s} = \frac{1}{2} \left(\mathbf{j}^2 - \mathbf{l}^2 - \mathbf{s}^2\right)$. The derivative of the short-range regulator using Eq. (4.3) reads

$$\Delta f_{\text{short}}(\mathbf{r}, R_0) = \left(\frac{\partial^2}{\partial r^2} + \frac{2}{r} \frac{\partial}{\partial r} \right) f_{\text{short}}(\mathbf{r}, R_0) , \tag{4.17}$$

$$\frac{\partial}{\partial r} f_{\text{short}}(\mathbf{r}, R_0) = -\frac{n}{R_0^n} r^{n-1} f_{\text{short}}(\mathbf{r}, R_0) , \tag{4.18}$$

$$\frac{\partial^2}{\partial r^2} f_{\text{short}}(\mathbf{r}, R_0) = \left(\frac{n^2}{R_0^{2n}} r^{2n-2} - \frac{n(n-1)}{R_0^n} r^{n-2} \right) f_{\text{short}}(\mathbf{r}, R_0) . \tag{4.19}$$

4.1.3 Next-to-next-to-leading order

At N^{2}LO, corrections to the TPE enter, but no new NN contact interactions appear. As described in Ref. [39], the SFR integrals at N^{2}LO can be carried out analytically, leading to the contributions

$$\begin{aligned}
V_C^{(\nu=3)}(r) = &\frac{3g_A^2}{32\pi^2 F_\pi^4}\frac{e^{-2x}}{r^6}\left[2c_1x^2(1+x)^2+c_3(6+12x+10x^2+4x^3+x^4)\right] \\
&-\frac{3g_A^2}{128\pi^2F_\pi^4}\frac{e^{-y}}{r^6}\Big[4c_1x^2\left(2+y(2+y)-2x^2\right) \\
&+c_3\left(24+24y+12y^2+4y^3+y^4)-4x^2(2+2y+y^2)+4x^4\right)\Big],
\end{aligned} \tag{4.20}$$

$$\begin{aligned}
W_S^{(\nu=3)}(r) = &\frac{g_A^2}{48\pi^2 F_\pi^4}\frac{e^{-2x}}{r^6}c_4(1+x)(3+3x+2x^2) \\
&-\frac{g_A^2}{384\pi^2F_\pi^4}\frac{e^{-y}}{r^6}c_4\left[24+24y+12y^2+4y^3+y^4-4x^2(2+2y+y^2)\right],
\end{aligned} \tag{4.21}$$

$$\begin{aligned}
W_T^{(\nu=3)}(r) = &-\frac{g_A^2}{48\pi^2 F_\pi^4}\frac{e^{-2x}}{r^6}c_4(1+x)(3+3x+x^2) \\
&+\frac{g_A^2}{768\pi^2F_\pi^4}\frac{e^{-y}}{r^6}c_4\left[48+48y+24y^2+7y^3+y^4-4x^2(8+5y+y^2)\right],
\end{aligned} \tag{4.22}$$

with $x \equiv m_\pi r$, $y \equiv \tilde{\Lambda} r$, and the pion LECs $c_1 = -0.81\ \text{GeV}^{-1}$, $c_3 = -3.4\ \text{GeV}^{-1}$, and $c_4 = 3.4\ \text{GeV}^{-1}$. All local interactions constructed in this thesis use the spectral function cutoff $\tilde{\Lambda} = 1000$ MeV. Leading three-body interactions appear at N^{2}LO, but we do not further investigate them.

4.2 Fit to phase shifts

With the interactions in place, we adjust our low-energy constants by fitting semi-empirical NN phase shifts from the partial-wave analysis (PWA) [162]. This is realized by means of least-square minimization of a χ^2 value with respect to the LECs. The χ^2 value is obtained by

$$\chi^2 = \sum_i^{\text{data set}} \left(\frac{\delta_i^{\text{PWA}}-\delta_i^{\text{th}}}{\Delta\delta_i}\right)^2 , \tag{4.23}$$

where δ_i^{PWA} is data taken from Ref. [162]$^{(1)}$, and δ_i^{th} are theoretical phase shifts obtained by solving the LSE from Eq. (2.68) with our interaction. The index i runs over a certain set of partial-waves and a certain set of energies. The uncertainty $\Delta\delta_i$ is expressed via

$$\Delta\delta_i^2 = (\Delta\delta_i^{\text{PWA}})^2 + (\Delta\delta_i^{\text{th}})^2 + (\Delta\delta_i^{\text{num}})^2 , \tag{4.24}$$

where $\Delta\delta_i^{\text{PWA}}$ is the uncertainty from the PWA, $\Delta\delta_i^{\text{th}}$ is the theoretical model uncertainty for the chiral interactions, and $\Delta\delta_i^{\text{num}}$ is due to numerical errors. For the theoretical model uncertainty we use a similar approach to the one proposed in Ref. [33]. We use $Q = \max(m_\pi, P)$ over Λ, where P is a typical momentum scale of the system. With this we obtain the following uncertainties

$$\begin{aligned}
\Delta\delta_i^{\text{th,LO}} &= \left(\frac{Q}{\Lambda}\right)^2 C , \\
\Delta\delta_i^{\text{th,NLO}} &= \left(\frac{Q}{\Lambda}\right)^3 C , \\
\Delta\delta_i^{\text{th,N}^2\text{LO}} &= \left(\frac{Q}{\Lambda}\right)^4 C ,
\end{aligned} \tag{4.25}$$

---

(1) The data is available on the website `http://nn-online.org/`.

with $\Lambda = 400$ MeV (see Ref. [66]) and $C = 1^\circ$ to have a dimensionless χ^2 value. The PWA and numerical uncertainties in $\Delta\delta_i$ are negligible compared to this theoretical model uncertainty.

Considered partial waves and energies in the fit depend on the order in the chiral power-counting. At LO and NLO, we fit to the energy points

$$\begin{aligned} \text{LO}&: 1,\, 5,\, 10,\, 25,\, 50 \text{ MeV}\,, \\ \text{NLO}&: 1,\, 5,\, 10,\, 25,\, 50,\, 100,\, 150 \text{ MeV}\,, \end{aligned} \tag{4.26}$$

respectively. At LO, we fit to phase shifts in the two S-wave channels, while at NLO we consider the S-wave and P-wave channels, as well as the ${}^3S_1 - {}^3D_1$ mixing angle ϵ_1. The partial waves we consider at a certain order are listed below:

$$\begin{aligned} \text{LO}&: {}^1S_0,\, {}^3S_1\,, \\ \text{NLO}&: {}^1S_0,\, {}^3S_1,\, {}^1P_1,\, {}^3P_0,\, {}^3P_1,\, {}^3P_2,\, \epsilon_1\,. \end{aligned} \tag{4.27}$$

Energies and partial waves to which we fit at N^{2}LO are the same as at NLO.

We use an existing automatic differentiation package [187] for the optimization. With this, we obtain numerical gradients for the fits, which we feed into Python's BFGS (and L-BFGS-B) minimization routine. This algorithm is a quasi-Newton method, named after its founders Broyden, Fletcher, Goldfarb, and Shanno [188]. The resulting LECs for R_0 = 1.2, 1.4, and 1.6 fm at LO, NLO, and N^{2}LO are given in Tab. 4.1. We show the phase shifts for R_0 = 1.4 fm in the ${}^1S_0$, ${}^3S_1$, ${}^1P_1$, ${}^3P_0$, ${}^3P_1$, and ${}^3P_2$ channels at LO, NLO, and N^{2}LO in Fig. 4.2, alongside the values of the PWA from Ref. [162]. Similar to Ref. [30], uncertainties from lower orders in the power counting include all results of subsequent higher orders, i.e., the LO uncertainty is enlarged to include the results at NLO and N^{2}LO and the NLO uncertainty is enlarged to include results at N^{2}LO.

We see a very good reproduction of the PWA phase shifts and systematic improvement between the different orders in Fig. 4.2. The uncertainty bands tend to be larger for channels that have not been included in the LO fit, in particular for the P-wave channels. Although the later applications use the interaction for R_0 = 1.2 fm from Ref. [39], we constructed our version for R_0 = 1.2 fm as a comparison. Our LECs for R_0 = 1.2 fm at LO, NLO, and N^{2}LO are very similar to those from Ref. [39](2). The small differences can be explained by the different models used for theoretical uncertainties. In the last row of Tab. 4.1, we show the deuteron binding energy. Similar to what we saw for the phase shifts of the interactions at $R_0 = 1.4$ fm, there is a systematic improvement in the deuteron binding energy, moving towards the experimental value $E_d = 2.224$ MeV for all cutoffs. The binding energy was not used to constrain the fit. Binding energies at NLO (N^{2}LO) hardly differ between the different cutoffs, leading to a spread of only 10 (17) keV. However, at LO, the deuteron binding energy increases with increasing cutoff, leading to a spread of 244 keV.

4.3 Soft interactions

Originally, phenomenological interactions are constructed with a so-called hard core. We show an example for such interactions, taken from Ref. [189] in Fig. 4.3. The depicted interactions all show a strong short-range repulsion in the two-nucleon interaction, centered at zero distance. Naively spoken, short-range effects in coordinate-space reflect on the high-energy region in momentum-space, and the long-range behavior reflects on the low-momentum region. The exact connection is given via Fourier transformation

$$\langle \mathbf{p} | V | \mathbf{p}' \rangle = \int \mathrm{d}\mathbf{r} \int \mathrm{d}\mathbf{r}' e^{-i\mathbf{p}\cdot\mathbf{r}} \langle \mathbf{r} | V | \mathbf{r}' \rangle \, e^{i\mathbf{p}'\cdot\mathbf{r}'}\,. \tag{4.28}$$

---

(2) Note that for the fits in Ref. [39], a different sign convention is used for C_5.

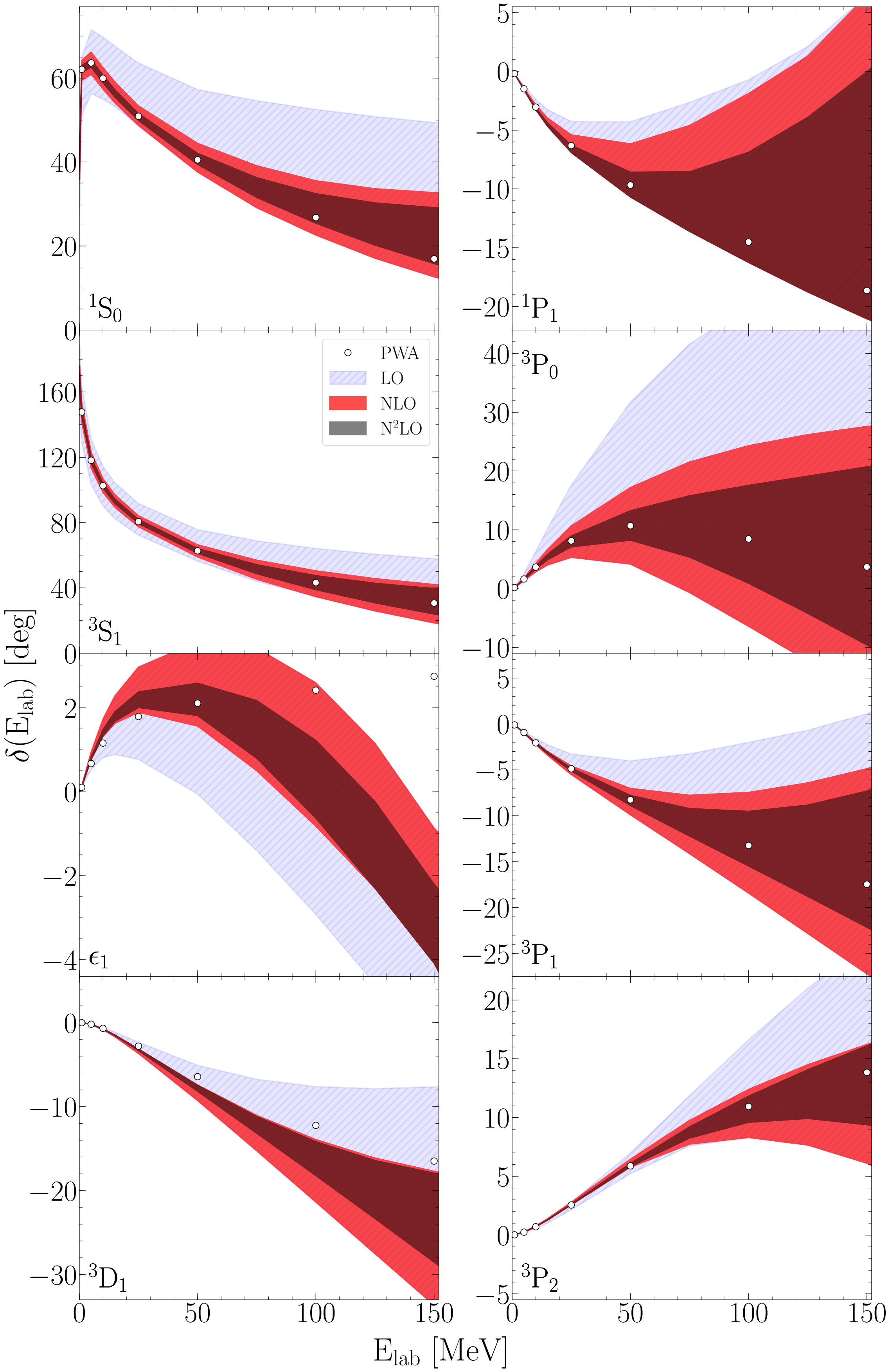

Figure 4.2.: Phase shift over the laboratory energy for the local interaction with cutoff $R_0 = 1.4$ fm at LO, NLO, and N^{2}LO in comparison to the PWA [162]. The uncertainties we show are obtained as in Ref. [30]. The partial-wave labels are given either in the lower left or upper left corner of each panel.

Table 4.1.: Low-energy constants for $R_0 = 1.2$, 1.4, and 1.6 fm at LO, NLO, and N^{2}LO. The LECs C_S and C_T are in fm^2 and C_1 – C_7 are given in fm^4. We use the spectral-function cutoff $\tilde{\Lambda} = 1000$ MeV to regularize the spectral-function integrals in the two-pion exchange. In the last row, we show the resulting deuteron binding energy in MeV. The experimental value is $E_d = 2.224$ MeV. The deuteron binding energy is not used as a constraint in the fit.

LEC	$R_0 = 1.2$ fm			$R_0 = 1.4$ fm			$R_0 = 1.6$ fm		
	LO	NLO	N^{2}LO	LO	NLO	N^{2}LO	LO	NLO	N^{2}LO
C_S	-1.73822	0.08014	2.52206	-2.67548	-0.48049	1.33129	-3.59350	-0.98802	0.53799
C_T	0.15933	0.72920	0.17860	-0.02052	0.72271	0.36332	-0.19004	0.65965	0.49471
C_1		0.21164	-0.10820		0.12372	-0.10437		-0.09759	-0.20581
C_2		0.20931	0.05418		0.30164	0.18769		0.39281	0.36809
C_3		-0.15593	-0.16716		-0.22387	-0.21704		-0.31065	-0.27847
C_4		0.09170	0.10342		0.19222	0.16597		0.31177	0.26704
C_5		-2.11167	-1.91128		-2.26751	-2.08337		-2.41639	-2.28180
C_6		0.34301	0.20470		0.47105	0.35468		0.60306	0.53604
C_7		-0.37569	-0.32822		-0.57841	-0.52886		-0.79838	-0.78955
E_d	1.799	2.141	2.195	1.886	2.151	2.193	2.043	2.147	2.178

We speak of a soft interaction, when this repulsive core at zero distance in coordinate space is suppressed. In momentum space, the interaction does not couple large and small momenta with each other, similar to the right-hand side of Fig. 4.1. In this case, integrals over momenta are much simpler to solve numerically, as one does not need to go to large momenta in order to describe low-energy physics. We want to clarify that the potential itself is not observable, so whether the potential has a hard core or is soft is a technical, not physical aspect.

Our goal is to construct soft local interactions by choosing the cutoff accordingly. The momentum-space cutoff Λ is related to the inverse of the coordinate-space cutoff R_0. Larger coordinate-space cutoffs, like R_0 = 1.4 or 1.6 fm, reduce the strength of the repulsive core. In momentum space, a lower Λ suppresses off-diagonal momentum-space matrix elements. Even though, this effect is smaller compared to RG methods, our interactions remain local. In Figure 4.4, we show our coordinate-space potentials in the $^1S_0$ wave (left) and the $^3S_1$ wave (right) at N^{2}LO, for R_0 = 1.2, 1.4 and 1.6 fm. We obtain the hardest interaction for R_0 = 1.2 fm (red line). This is evident, as that interaction shows the strongest repulsion at zero distance. As we increase R_0, this repulsion is successively lowered, and the interaction becomes softer. Note that all interactions which we construct, are much softer than the phenomenological interactions (see Fig. 4.3). We depict the corresponding momentum-space matrix elements for our chiral interactions, which we obtained with Fourier transformation in Fig. 4.5. In the left column, we present those for the $^1S_0$ wave for R_0 = 1.2, 1.4 and 1.6 fm from top to bottom. Results for the $^3S_1$ wave are shown in the right column. We show the momentum-space potential in three dimensions, a contour plot on the bottom and a projection on the $p-V$ plane. For the $^1S_0$ potential, it is easily visible that the off-diagonal matrix elements decrease as the coordinate-space cutoff is increased. Also in the $p-V$ plane it is evident that the matrix elements approach zero much faster for larger coordinate-space cutoffs. Simultaneously, the interaction at zero momentum increases in absolute value from R_0 = 1.2 fm to R_0 = 1.6 fm. The minimum for R_0 = 1.2, 1.4, and 1.6 fm decreases from -49.83 MeV fm^3 to -50.69 MeV fm^3 to -51.02 MeV fm^3, respectively. We find the same behavior for the $^3S_1$ wave. It can best be seen by comparing the projection on the $p-V$ plane. There is a narrow non-zero contribution around $p \approx 5$ fm^{-1} in the upper panel for $R_0 = 1.2$ fm.

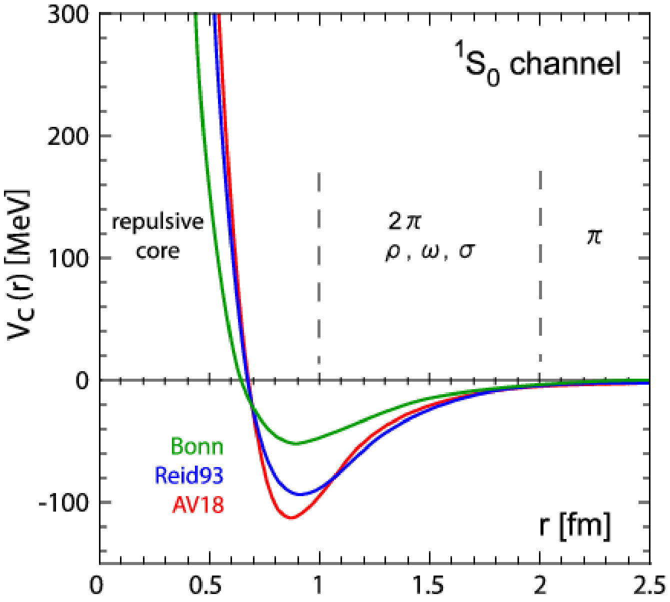

Figure 4.3.: Coordinate-space matrix elements in the ${}^1S_0$ wave of the phenomenological Bonn, Reid93, and AV18 interactions taken from Ref. [189]. All interactions show a repulsive hard core and a similar long-range behavior that is governed by the OPE.

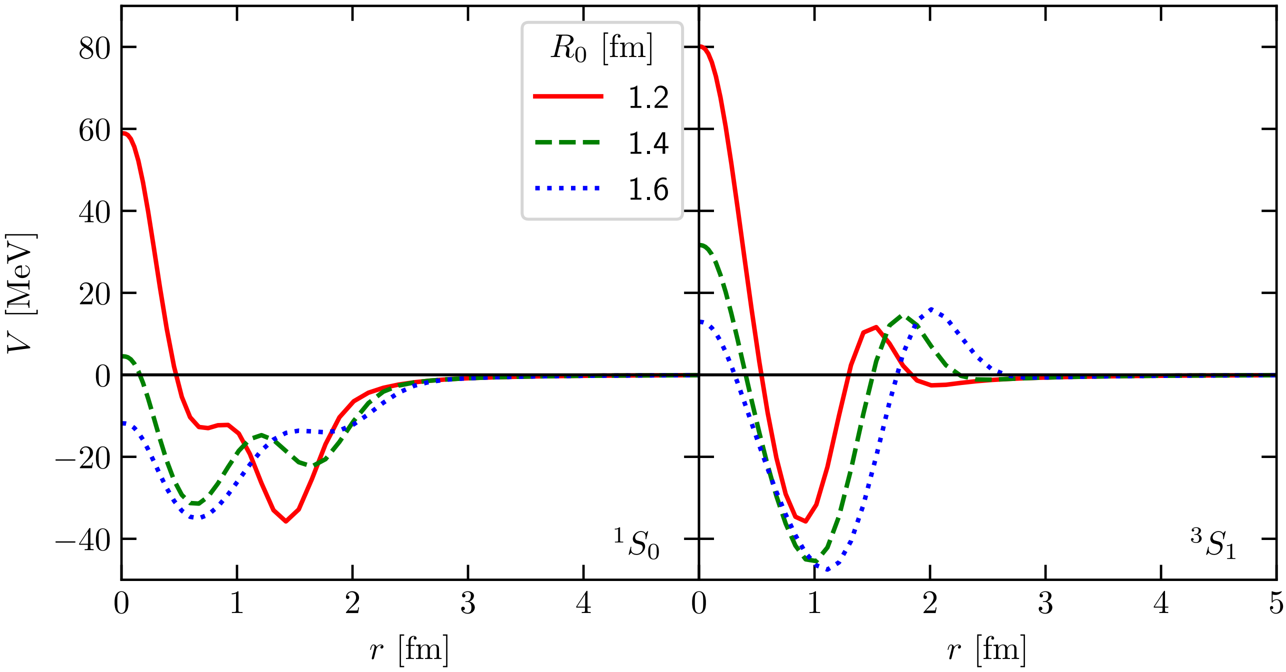

Figure 4.4.: Coordinate-space matrix elements of local interactions at N^{2}LO in the ${}^1S_0$ channel (left) and the ${}^3S_1$ channel (right). We show the matrix elements for R_0=1.2, 1.4, and 1.6 fm.

This contribution increases in value but is on the same time shifted towards lower momenta, as we increase the coordinate-space cutoff. At R_0 = 1.4 fm the contribution is at $p \approx$ 4 fm^{-1} and at R_0 = 1.6 fm, the contribution is centered around $p \approx$ 3.8 fm^{-1}. Similar as in the $^1S_0$ wave, we find that the absolute value of the interaction at zero momentum increases. For R_0 = 1.2, 1.4 and 1.6 fm we find $V(0,0) = -15.88$, -16.61, and -16.77 MeV fm^3 respectively. Comparing the contour plots on the bottom, we find more zero-crossings as the coordinate-space cutoff increases. Those are contributions which lie outside of the observation range for R_0 = 1.2 fm, and are shifted towards the diagonal for larger R_0.

When we increase the coordinate-space cutoff, we detect a similar behavior for the matrix elements, as we observed for potentials from RG methods. However, our interactions are not as soft as those from RG methods, but they keep their local structure and we do not induce any many-body forces in the process. Depending on the many-body method at hand, one can directly use our interactions without any further treatment. We present one application in the following section.

4.4 Application to ^{16}O–^{16}O scattering

As an application we implemented our interactions at R_0 = 1.2, 1.4 and 1.6 fm in nucleus-nucleus scattering calculations by means of double-folding techniques [108, 190]. We find that double-folding potentials obtained from local interactions with cutoffs below $R_0 \sim$ 1.2 fm do not converge for this method (not shown in the figure). Results for interactions at R_0 = 1.2, 1.4 and 1.6 fm are presented in Fig. 4.6 (note that for R_0 = 1.2 fm, the interaction from Ref. [39] is used in the calculation). We show the elastic cross section of ^{16}O–^{16}O scattering divided by the Mott cross section over the angle θ at a laboratory energy of 350 MeV, calculated with our interactions in comparison to experimental results from Ref. [191]. We display the interaction with R_0 = 1.4 fm at LO, NLO, N^{2}LO. For the other two cutoffs we show the interaction at N^{2}LO. At N^{2}LO, we provide the band obtained from cutoff variation. The theory provides a good description of the experimental data, especially at small angles. At larger angles, this description deteriorates but the shape is still reproduced. The spread between the different cutoffs at N^{2}LO is used as a rough estimate of the theoretical uncertainty. At small angles, all orders as well as the interactions at different cutoffs are in very good agreement. At larger angles, the different orders deviate, but the results for interactions with different cutoffs at N^{2}LO still remain close to each other, and close to experiment. Those results are promising, especially considering that no additional parameters have been adjusted to reproduce the cross section. A more detailed description of the double-folding method and further results are presented in Ref. [108].

4.5 Summary of main results

To summarize the key aspects of this chapter:

- We use the description from Ref. [39] to construct local interactions from chiral EFT. Many-body methods often profit from soft interactions in terms convergence. However, common RG approaches to construct soft interactions destroy the locality. For this reason we constructed softer interaction by raising the coordinate-space cutoff R_0, which is synonymous to lowering the momentum-space cutoff Λ. Resulting interactions are not as soft as those obtained from RG methods, but, they are softer than typical interactions from chiral EFT and they remain local.

- We constructed interactions with R_0 = 1.2, 1.4, and 1.6 fm at LO, NLO, and N^{2}LO by fits to phase shifts from the PWA [162]. Furthermore, we presented applications of those interactions in elastic ^{16}O–^{16}O scattering. Our interactions show a good agreement with experiment at small angles and a systematic order-by-order improvement. It will be interesting to see how the inclusion of three-nucleon forces and the expansion to triple-folding potentials affect this result.

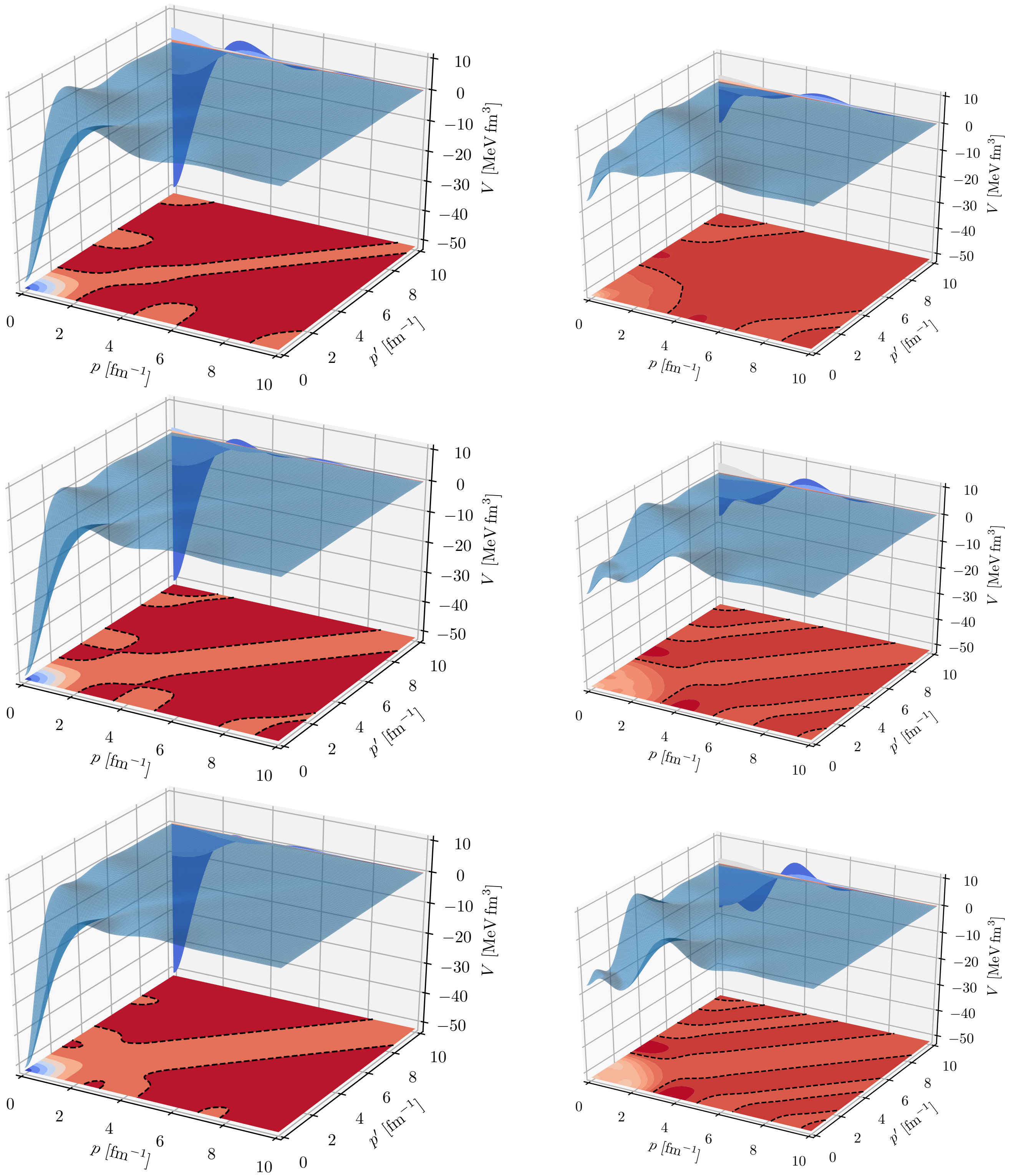

Figure 4.5.: Momentum-space matrix elements for local interactions at N^{2}LO in the $^1S_0$ channel (left) and $^3S_1$ channel (right). From top to bottom, we show the matrix elements for R_0=1.2, 1.4, and 1.6 fm at N^{2}LO. We depict a two-dimensional projection of V on the $p - V$ plane and a contour map on the pp' plane. The color coding ranges from -50 MeV (blue) to 5 MeV (red). Crossings at $V = 0$ MeV are contoured by a black, dashed line.

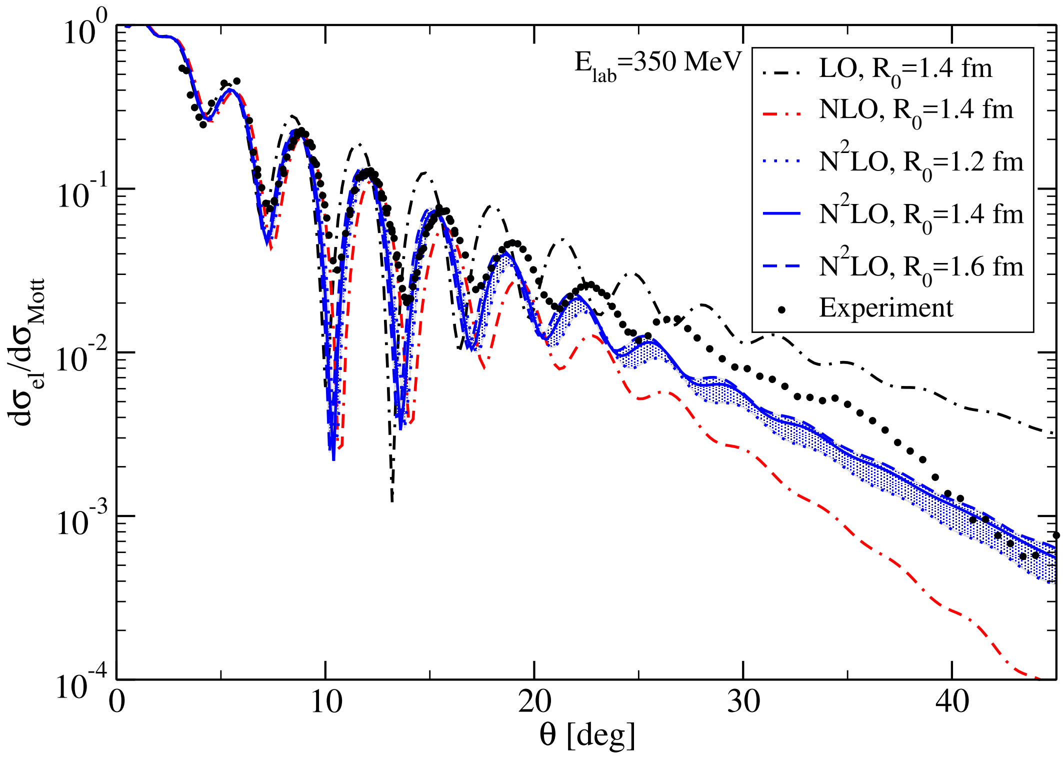

Figure 4.6.: Elastic ^{16}O–^{16}O scattering cross section divided by the Mott cross section at $E_{\mathrm{lab}} = 350$ MeV versus the angle θ, taken from Ref. [108]. The figure shows interactions for R_0 = 1.2, 1.4, and 1.6 fm at N^{2}LO, as well as results at LO and NLO for R_0 = 1.4 fm in comparison to experimental measurements from Ref. [191]. Results for R_0 are obtained with the interaction from Ref. [39].

5 Investigating the Fierz-rearrangement freedom for local interactions

It has been found that local regulator functions introduce sizable regulator artifacts [107, 109, 170]. First, one finds less repulsion from the $3N$ two-pion-exchange interaction than for typical nonlocal regulators, and second, there is a violation of the Fierz-rearrangement freedom for the short-range $3N$ contact interactions, i.e., calculations depend on the choice of the short-range operators; see also Ref. [110].

While all regulator functions introduce regulator artifacts at finite cutoffs, effects originating from the violated Fierz ambiguity have been found to be larger than or comparable to other sources of uncertainty, as demonstrated in Refs. [166, 170]. This additional regulator artifact is present for local short-range regulators [107, 192], but not for typical nonlocal short-range regulators used in previously derived nonlocal $3N$ interactions [148, 171].

A similar violation of the Fierz ambiguity also appears in locally regularized two-nucleon interactions from chiral EFT. Based on power counting arguments, one would expect these effects to be even larger in the NN than in the $3N$ sector. In this chapter, we explore the violation of the Fierz ambiguity at leading order (LO) in the NN sector and investigate the effects of this violation on the local coordinate-space interactions of Refs. [38, 39].

We study phase shifts, the ground-state energy of ^{4}He using the Green's function Monte Carlo (GFMC) method, and the energy per particle of neutron matter using the auxiliary-field diffusion Monte Carlo (AFDMC) method [65] for different short-range operator combinations. After investigating this regulator artifact at LO, we show that at next-to-leading order (NLO) the Fierz-rearrangement freedom is partially restored and the remaining violation is smaller than typical chiral uncertainty estimates. We emphasize that this effect is not present in nonlocal NN interactions [32–34, 153, 159] or semilocal interactions [30, 31]. The results and ideas which we discuss here have been published by us in Ref. [111].

5.1 Fierz-rearrangement freedom

As discussed before, the NN interaction at LO (Q^0) in Weinberg power counting has two contributions: The local one-pion–exchange interaction (see Eq. (4.7)) and momentum-independent contact interactions. The most general set of LO contact interactions consistent with the symmetries is given by the spin-isospin operators $\mathbb{1}, \sigma_{12} = \boldsymbol{\sigma}_1 \cdot \boldsymbol{\sigma}_2, \tau_{12} = \boldsymbol{\tau}_1 \cdot \boldsymbol{\tau}_2$, and $\sigma_{12}\tau_{12}$.

$$V_{\text{cont}}^{(0)} = C_{\mathbb{1}} + C_\sigma \sigma_{12} + C_\tau \tau_{12} + C_{\sigma\tau} \sigma_{12}\tau_{12} \,. \tag{5.1}$$

Even though antisymmetry is a basic symmetry only of the many-body states, in the following we study the antisymmetrized potential to explain the origin of the Fierz-rearrangement freedom. The interaction after antisymmetrization, V_{as}, is given by

$$V_{\text{as}}(\mathbf{q},\mathbf{k}) = \frac{1}{2}\left(V(\mathbf{q},\mathbf{k}) - \mathscr{A}[V(\mathbf{q},\mathbf{k})]\right) , \tag{5.2}$$

with the antisymmetrizer $\mathscr{A}$ defined via

$$\mathscr{A}[V(\mathbf{q},\mathbf{k})] = \frac{1}{4}(1+\sigma_{12})(1+\tau_{12})V\left(\mathbf{q} \to -2\mathbf{k}, \mathbf{k} \to -\frac{1}{2}\mathbf{q}\right) . \tag{5.3}$$

Performing the antisymmetrization for the LO contact interaction explicitly, we find [39]

$$\begin{aligned}
V^{(0)}_{\text{cont,as}} &= \frac{1}{2}\left(1-\frac{1}{4}(1+\sigma_{12})(1+\tau_{12})\right)V^{(0)}_{\text{cont}} \\
&= \left(\frac{3}{8}C_{\mathbb{1}}-\frac{3}{8}C_{\sigma}-\frac{3}{8}C_{\tau}-\frac{9}{8}C_{\sigma\tau}\right)\mathbb{1}+\left(-\frac{1}{8}C_{\mathbb{1}}+\frac{5}{8}C_{\sigma}-\frac{3}{8}C_{\tau}+\frac{3}{8}C_{\sigma\tau}\right)\sigma_{12} \\
&\quad+\left(-\frac{1}{8}C_{\mathbb{1}}-\frac{3}{8}C_{\sigma}+\frac{5}{8}C_{\tau}+\frac{3}{8}C_{\sigma\tau}\right)\tau_{12}+\left(-\frac{1}{8}C_{\mathbb{1}}+\frac{1}{8}C_{\sigma}+\frac{1}{8}C_{\tau}+\frac{3}{8}C_{\sigma\tau}\right)\sigma_{12}\tau_{12} \\
&= \tilde{C}_S+\tilde{C}_T\sigma_{12}+\left(-\frac{2}{3}\tilde{C}_S-\tilde{C}_T\right)\tau_{12}+\left(-\frac{1}{3}\tilde{C}_S\right)\sigma_{12}\tau_{12}\,. \qquad (5.4)
\end{aligned}$$

As can be seen, there are only two independent couplings $\tilde{C}_S$ and $\tilde{C}_T$ at LO after antisymmetrization, and these two couplings contribute to the two possible S-wave scattering channels. Thus, only two out of the four operator structures are necessary to describe the contact physics at LO while the remaining operator structures are recovered after antisymmetrization. In principle, any linearly independent(1) combination of two out of the four contact interactions can be chosen, which is used to reduce the number of LECs when constructing chiral NN interactions. This reduction is called Fierz ambiguity or Fierz-rearrangement freedom.

As mentioned in Ch. 2, chiral EFT is a low-momentum theory and, thus, when using chiral interactions in few- and many-body calculations, it is necessary to apply momentum-dependent regulator functions to cut off high-momentum modes that would otherwise lead to divergences. In general, the regulator function can depend on both momentum scales, $f_R(\mathbf{q},\mathbf{k})$. Let us now consider the preceding argument with a regulator for the short-range potential included. The Fierz ambiguity is preserved if the regulator commutes with the antisymmetrizer, i.e., when

$$f_R(\mathbf{q},\mathbf{k}) = f_R\left(-2\mathbf{k},-\frac{1}{2}\mathbf{q}\right). \qquad (5.5)$$

In this case the regulator is just a prefactor in Eqs. (5.2) and (5.4) and does not affect the antisymmetrization procedure: There are still only two independent contact operators at LO. The condition in Eq. (5.5) is fulfilled only when the regulator is a symmetric and even function of $\mathbf{q}$ and $2\mathbf{k}$. This is equivalent to regulating the short-range contact interactions with symmetric and even functions of $\mathbf{p}$ and $\mathbf{p}'$, as has been done for previously derived nonlocal [32–34, 153, 159] and semilocal interactions [30, 31], which use the functional form

$$f_R(\mathbf{p},\mathbf{p}') = \exp\left[-\left(\frac{\mathbf{p}}{\Lambda}\right)^{2n}\right]\exp\left[-\left(\frac{\mathbf{p}'}{\Lambda}\right)^{2n}\right], \qquad (5.6)$$

where n takes integer values.

In contrast, local regulators $f_R(\mathbf{q})$ violate the Fierz-rearrangement freedom, because they do not commute with the antisymmetrizer. Introducing the momentum-exchange operator $\mathscr{P}^{\text{m}}$, where $\mathscr{P}^{\text{m}}f(\mathbf{q},\mathbf{k}) = f(-2\mathbf{k},-\frac{1}{2}\mathbf{q})$, the antisymmetrized interaction with local regulators is given by

---

(1) The combination $\mathbb{1}$ and $\sigma_{12}\tau_{12}$ yields the same value in the $^3S_1$ and $^1S_0$ channel and is, thus, linearly dependent in S-wave channels.

$$
\begin{aligned}
V^{(0,\mathrm{loc})}_{\mathrm{cont,as}} =& \frac{1}{2}\left(1-\frac{\mathscr{P}^{\mathrm{m}}}{4}(1+\sigma_{12})(1+\tau_{12})\right)V^{(0)}_{\mathrm{cont}} f_R(\mathbf{q}) \\
=& \mathbb{1}\left(\frac{C_{\mathbb{1}}}{2} f_R(\mathbf{q}) - \frac{1}{8}\left(C_{\mathbb{1}}+3C_\sigma+3C_\tau+9C_{\sigma\tau}\right) f_R(2\mathbf{k})\right) \\
&+\sigma_{12}\left(\frac{C_\sigma}{2} f_R(\mathbf{q}) - \frac{1}{8}\left(C_{\mathbb{1}}-C_\sigma+3C_\tau-3C_{\sigma\tau}\right) f_R(2\mathbf{k})\right) \\
&+\tau_{12}\left(\frac{C_\tau}{2} f_R(\mathbf{q}) - \frac{1}{8}\left(C_{\mathbb{1}}+3C_\sigma-C_\tau-3C_{\sigma\tau}\right) f_R(2\mathbf{k})\right) \\
&+\sigma_{12}\tau_{12}\left(\frac{C_{\sigma\tau}}{2} f_R(\mathbf{q}) - \frac{1}{8}\left(C_{\mathbb{1}}-C_\sigma-C_\tau+C_{\sigma\tau}\right) f_R(2\mathbf{k})\right),
\end{aligned}
\tag{5.7}
$$

where $f_R(\mathbf{q}) \neq f_R(2\mathbf{k})$. All of the above combinations of LECs are linearly independent and, thus, the Fierz-rearrangement freedom is violated. This violation of the Fierz ambiguity is a manifestation of the fact that introducing a regulator function affects terms beyond the order at which one is working, and should be corrected when subleading contact operators are included. Here we illustrate this explicitly by using a Gaussian local regulator, $f_R(\mathbf{q}) = \exp(-(q/\Lambda)^2)$, such that $\mathscr{P}^{\mathrm{m}} f_R(\mathbf{q}) = f_R(2\mathbf{k}) = \exp(-4(k/\Lambda)^2)$. Expressing $\mathbf{k}$ in terms of $\mathbf{q}$, $\mathbf{p}$, and $\mathbf{p}'$, we can write

$$
\begin{aligned}
\mathscr{P}^{\mathrm{m}} f_R(\mathbf{q}) &= \exp\left(-\frac{q^2}{\Lambda^2}\right)\exp\left(-\frac{4\mathbf{p}\cdot\mathbf{p}'}{\Lambda^2}\right) \\
&= f_R(\mathbf{q})\left(1-\frac{4\mathbf{p}\cdot\mathbf{p}'}{\Lambda^2}+\mathscr{O}\left((Q/\Lambda)^4\right)\right).
\end{aligned}
\tag{5.8}
$$

Inserting Eq. (5.8) into Eq. (5.7), we find

$$
V^{(0,\mathrm{loc})}_{\mathrm{cont,as}} = \left(\tilde{C}_S + \tilde{C}_T\sigma_{12} + \left(-\frac{2}{3}\tilde{C}_S - \tilde{C}_T\right)\tau_{12} + \left(-\frac{1}{3}\tilde{C}_S\right)\sigma_{12}\tau_{12}\right) f_R(\mathbf{q}) + V^f_{\mathrm{corr}}(\mathbf{p}\cdot\mathbf{p}'),
\tag{5.9}
$$

where $V^f_{\mathrm{corr}}(\mathbf{p}\cdot\mathbf{p}')$ captures the higher-order effects $\sim\ 4\mathbf{p}\cdot\mathbf{p}'/\Lambda^2 + \mathscr{O}((Q/\Lambda)^4)$ in Eq. (5.8). Reexpressing $\mathbf{p}$ and $\mathbf{p}'$ in terms of $\mathbf{q}$ and $\mathbf{k}$, the first correction term in Eq. (5.8) can be rewritten as

$$
-\frac{4\mathbf{p}\cdot\mathbf{p}'}{\Lambda^2} = -\frac{4}{\Lambda^2}k^2 + \frac{1}{\Lambda^2}q^2 .
\tag{5.10}
$$

These operators will be introduced at NLO in chiral EFT, and, analogously, the higher-order corrections $\mathscr{O}((Q/\Lambda)^4)$ will be included at next-to-next-to-next-to-leading order (N^{3}LO) and beyond.

The higher-order terms $V^f_{\mathrm{corr}}(\mathbf{p}\cdot\mathbf{p}')$ depend on both the explicit form of the chosen regulator and on the order at which one is working. Because the correction terms depend on the angles between the nucleons, they contribute to higher partial waves (nonlocal regulators only depend on the magnitudes p and p'). As a consequence, while, e.g., the LO contact interactions only describe the two S-wave channels, the use of local regulators leads to a mixing of these contributions into higher partial waves.

More generally, every regulator that respects the Fierz-rearrangement freedom is an even function of $\mathbf{p}$ and $\mathbf{p}'$. Then, every regulator that mixes LO physics into partial waves with odd l, e.g., P waves, and as a consequence contains terms of the form $(\mathbf{p}\cdot\mathbf{p}')^{2n+1}$, violates the Fierz-rearrangement freedom. Thus, it follows that a violation of the Fierz-rearrangement freedom is equivalent to a mixing of the S-wave contact interactions into odd-l partial waves. In contrast, mixing of LO contact physics into partial waves with the same S and T ($\Delta l = 2n$) is compatible with the Fierz-rearrangement freedom.

Let us consider the violation of the Fierz ambiguity at LO from the point of view of a partial-wave decomposition. We again consider a Gaussian regulator in $\mathbf{q}$. This regulator can be rewritten as

$$
\exp\left(-\frac{\mathbf{p}^2+\mathbf{p}'^2}{\Lambda^2}\right)\exp\left(i\frac{(-2i\mathbf{p}\cdot\mathbf{p}')}{\Lambda^2}\right),
\tag{5.11}
$$

where the first factor is a typical nonlocal Gaussian regulator. The second factor, however, depends on the angle between $\mathbf{p}$ and $\mathbf{p}'$. Expanding this second exponential function in partial waves, we find

$$\exp\left(i\frac{(-2i\mathbf{p}\cdot\mathbf{p}')}{\Lambda^2}\right) = 4\pi\sum_{lm} i^l j_l\left(\frac{-2ipp'}{\Lambda^2}\right) Y^*_{lm}(\Omega_{p'})Y_{lm}(\Omega_p)\,, \tag{5.12}$$

with j_l a spherical Bessel function, and Y_{lm} a spherical harmonic. We can now compare the radial part for this local regulator to a nonlocal LO contact interaction with a Gaussian regulator $f_R(p,p') = \exp\left(\frac{-(p^2+p'^2)}{\Lambda^2}\right)$, in a partial-wave basis. The nonlocal potential leads to

$$\langle plm|\mathrm{V}^{\mathrm{nonloc}}_{\mathrm{LO}}(\mathbf{p},\mathbf{p}')|p'l'm'\rangle = 4\pi C\delta_{l0}\delta_{l'0}\delta_{m0}\delta_{m'0}f_R(p,p')\,, \tag{5.13}$$

while the local version takes the form

$$\langle plm|\mathrm{V}^{\mathrm{loc}}_{\mathrm{LO}}(\mathbf{p},\mathbf{p}')|p'l'm'\rangle = 4\pi C\delta_{ll'}\delta_{mm'}i^l j_l\left(\frac{-2ipp'}{\Lambda^2}\right) f_R(p,p')\,, \tag{5.14}$$

where C is a constant. One can easily see that the nonlocal LO interaction in Eq. (5.13) only contributes for $l = l' = 0$ (S waves). The local interaction of Eq. (5.14), on the other hand, contributes to each partial wave with $l = l'$.

In a similar way, the propagator of the OPE, $1/(q^2+m_\pi^2)$ (see Eq. (B.45)) depends on the angle between $\mathbf{p}$ and $\mathbf{p}'$ which mixes contributions into all partial-waves, even in the absence of regulators.

This regulator-induced contribution to all partial waves complicates fitting procedures and leads to increased theoretical uncertainties. The interaction is, however, accompanied by a Bessel function in p and p' that, for increasing orbital angular momentum l, shifts the mixed contributions to larger momenta, where they are suppressed by the regulator $f_R(p,p')$ itself. Though the preceding argument was for a specific regulator function, we expect that the violation of the Fierz-rearrangement freedom has the largest effect for partial waves with small orbital angular momenta, while large-l partial waves are protected by the angular-momentum barrier.

5.2 Local chiral potentials

We now investigate the impact of the violation of Fierz ambiguity on the LO interaction with local short- and long-range regulators as in Eq. (4.3) and Eq. (4.2). As in the chapter before, we choose the local cutoff $R_S = R_L = R_0$, $n = n_1 = 4$, and $n_2 = 1$. For the OPE we use the same expression as in Eq. (4.7), for the contact interaction we investigate different operator combinations from Eq. (5.1). If the Fierz-rearrangement freedom is respected, physical observables are independent of the choice of any linearly independent set of two out of the four operators in Eq. (5.1). For local regulators, this is not the case and we investigate this effect by constructing LO potentials for all possible pairs of contact operators. In each case, we fit the two LECs to phase shifts in the two S-wave channels. More precisely, we fit the spin-isospin LECs to these phase shifts, which we label according to the spin and isospin quantum numbers, C_{ST}, instead of using the standard partial-wave notation, $C_{^{2S+1}L_J}$. We reconstruct the operator LECs of Eq. (5.1) according to

$$\begin{pmatrix} C_{00} \\ C_{01} \\ C_{10} \\ C_{11} \end{pmatrix} = \begin{pmatrix} 1 & -3 & -3 & 9 \\ 1 & -3 & 1 & -3 \\ 1 & 1 & -3 & -3 \\ 1 & 1 & 1 & 1 \end{pmatrix} \begin{pmatrix} C_{\mathbb{1}} \\ C_\sigma \\ C_\tau \\ C_{\sigma\tau} \end{pmatrix}. \tag{5.15}$$

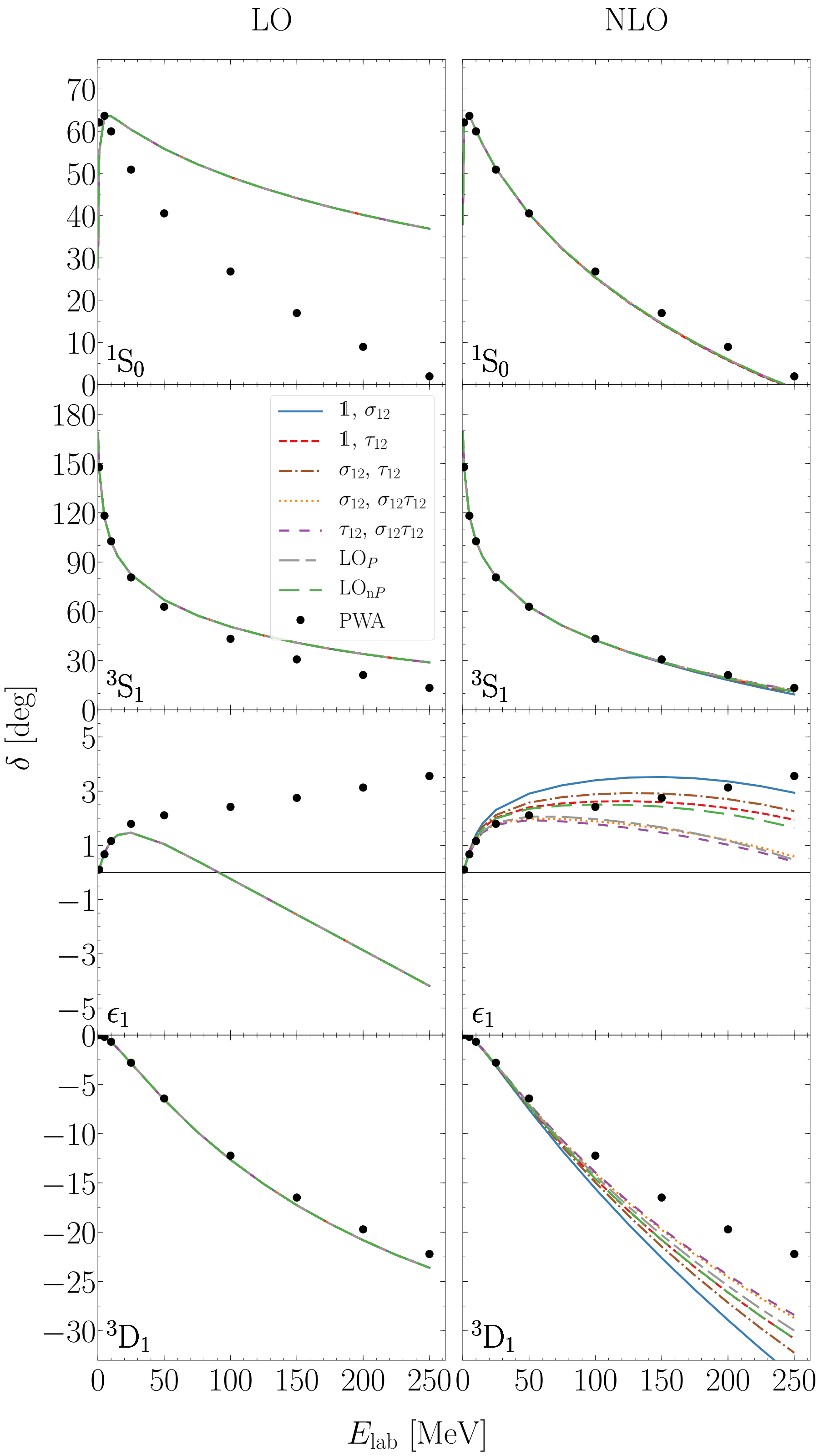

Figure 5.1.: Phase shifts for the $^1S_0$, $^3S_1$, and $^3D_1$ channels and the $J = 1$ mixing angle ϵ_1 for $R_0 = 1.0$ fm at LO and NLO. The S-wave phase shifts are fit and independent of the choice of the LO short-range operators. The lines for different operator choices overlap except in the case of the mixing angle ϵ_1 and the $^3D_1$ partial wave at NLO.

Note that we exclude the pair $\mathbb{1}, \sigma_{12}\tau_{12}$ from consideration, because the operators of this pair are linearly dependent in the two S-wave channels.

We fit the LECs C_{01} and C_{10} to the ${}^1S_0$ and ${}^3S_1$ neutron-proton phase shifts from the partial-wave analysis of Ref. [162] (PWA) for cutoffs in the range $R_0 = 1.0 - 1.2$ fm. While fitting to phase shifts contains inherent drawbacks, our goal in this work is not to produce high-precision potentials. Nevertheless, we plan to fit to scattering data in future work.

We perform least-square optimizations by following the same strategy as in Sec. 4.2 with theoretical uncertainties given by

$$\Delta\delta_i^{\text{th,LO}} = \left(\frac{Q}{\Lambda}\right)^2 C\,, \tag{5.16}$$

$$\Delta\delta_i^{\text{th,NLO}} = \left(\frac{Q}{\Lambda}\right)^3 C\,, \tag{5.17}$$

where we take $\Lambda = 500$ MeV (400 MeV) for $R_0 = 1.0$ fm (1.2 fm) (see Ref. [66]) and $C = 1°$. When studying ${}^4\text{He}$, we choose the momentum scale associated with the average density in ${}^4\text{He}$, $P \approx 290$ MeV, and when studying neutron matter, we choose P to be the average momentum in a Fermi gas, $P = \sqrt{3/5}k_F$, with the Fermi momentum k_F. The PWA and numerical uncertainties in $\Delta\delta_i$ are negligible compared to this theoretical model uncertainty.

Table 5.1.: Operator LECs and spin-isospin LECs C_{00} and C_{11} for all investigated LO operator combinations. The cutoff R_0 is given in fm and the LEC values are given in fm^2. The spin-isospin LECs C_{01} (C_{10}) are -1.831 fm^2 (-0.317 fm^2) for $R_0 = 1.0$ fm and -2.216 fm^2 (-1.579 fm^2) for $R_0 = 1.2$ fm.

Operators	R_0	$C_{\mathbb{1}}$	C_σ	C_τ	$C_{\sigma\tau}$	C_{00}	C_{11}
$\mathbb{1}$, σ_{12}	1.0	−0.696	0.378	0.000	0.000	−1.831	−0.317
	1.2	−1.738	0.159	0.000	0.000	−2.216	−1.579
$\mathbb{1}$, τ_{12}	1.0	−1.452	0.000	−0.378	0.000	−0.317	−1.831
	1.2	−2.057	0.000	−0.159	0.000	−1.579	−2.216
σ_{12}, τ_{12}	1.0	0.000	0.726	0.348	0.000	−3.222	1.074
	1.2	0.000	1.028	0.869	0.000	−5.693	1.898
σ_{12}, $\sigma_{12}\tau_{12}$	1.0	0.000	0.378	0.000	0.232	0.951	0.610
	1.2	0.000	0.159	0.000	0.579	4.737	0.739
τ_{12}, $\sigma_{12}\tau_{12}$	1.0	0.000	0.000	−0.378	0.484	5.492	0.106
	1.2	0.000	0.000	−0.159	0.686	6.649	0.526
LO$_P$	1.0	−1.980	−0.415	−0.793	0.101	2.548	−3.087
	1.2	−2.208	−0.346	−0.505	0.180	1.962	−2.879
LO$_{nP}$	1.0	−0.403	0.323	−0.055	0.134	0.000	0.000
	1.2	−0.712	0.317	0.158	0.237	0.000	0.000

For all operator pairs, we present the fitted operator LECs, as well as the spin-isospin LECs C_{00} and C_{11} in Table 5.1 and show the phase shifts at LO in the left panels of Figs. 5.1–5.3. The NLO results shown in the right panels will be discussed in Sec. 5.4.

We begin by examining the ${}^1S_0$, ${}^3S_1$, and ${}^3D_1$ phase shifts as well as the $J = 1$ mixing angle in Fig. 5.1 for $R_0 = 1.0$ fm, in comparison to the PWA. The results for $R_0 = 1.2$ fm are qualitatively similar; see Fig. 5.4 for an example for the ${}^1P_1$ wave. The spin-isospin LECs C_{01} and C_{10} are fit and, thus, independent

Table 5.2.: Operator LECs for all investigated NLO operator combinations. The cutoff R_0 is given in fm and the LEC values are given in fm^2 for $C_{\mathbb{1}}$, C_σ, C_τ, and, $C_{\sigma\tau}$ and in fm^4 for C_1 – C_7.

Operators	R_0	$C_{\mathbb{1}}$	C_σ	C_τ	$C_{\sigma\tau}$	C_1	C_2	C_3	C_4	C_5	C_6	C_7
$\mathbb{1}$, σ_{12}	1.0	2.080	1.036	0.000	0.000	0.285	0.184	−0.120	0.063	−2.241	0.304	−0.286
	1.2	0.080	0.729	0.000	0.000	0.212	0.209	−0.156	0.092	−2.112	0.343	−0.376
$\mathbb{1}$, τ_{12}	1.0	−0.830	0.000	−0.192	0.000	0.102	−0.000	−0.149	−0.049	−1.373	0.171	−0.102
	1.2	−1.489	0.000	−0.613	0.000	−0.104	0.051	−0.298	0.035	−1.285	0.391	−0.293
σ_{12}, τ_{12}	1.0	0.000	0.296	−0.144	0.000	0.174	0.061	−0.131	−0.012	−1.698	0.205	−0.161
	1.2	0.000	0.518	−0.562	0.000	0.076	0.216	−0.255	0.139	−1.923	0.443	−0.461
σ_{12}, $\sigma_{12}\tau_{12}$	1.0	0.000	−0.133	0.000	0.477	0.280	−0.027	−0.109	−0.026	−1.743	0.093	−0.052
	1.2	0.000	0.054	0.000	0.651	0.381	0.028	−0.131	0.058	−2.079	0.149	−0.179
τ_{12}, $\sigma_{12}\tau_{12}$	1.0	0.000	0.000	0.173	0.402	0.292	−0.016	−0.091	−0.036	−1.792	0.083	−0.045
	1.2	0.000	0.000	−0.071	0.681	0.373	0.023	−0.142	0.064	−2.059	0.155	−0.183
LO$_P$	1.0	3.517	0.409	0.414	1.246	0.562	0.053	−0.059	0.054	−2.524	0.113	−0.101
	1.2	0.843	−0.236	−0.364	1.101	0.473	0.024	−0.159	0.118	−2.201	0.168	−0.206
LO$_{\mathrm{n}P}$	1.0	−0.254	0.173	−0.004	0.085	0.191	0.027	−0.116	−0.032	−1.667	0.156	−0.111
	1.2	−0.717	0.290	0.189	0.239	0.234	0.067	−0.109	−0.004	−1.927	0.170	−0.187

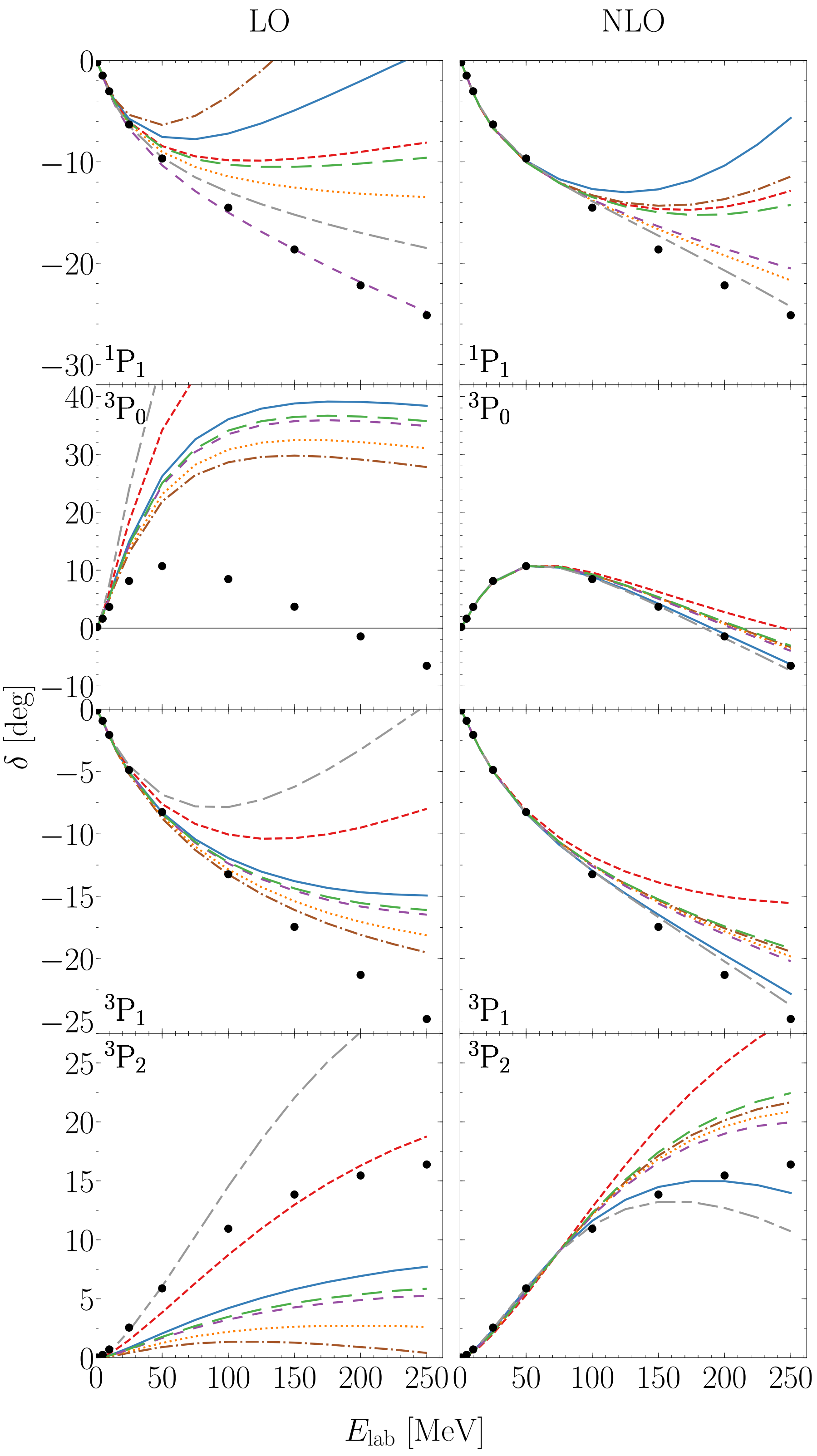

Figure 5.2.: Phase shifts for the $^1P_1$ and triplet ^3P_J waves for $R_0 = 1.0$ fm. The legend is as in Fig. 5.1.

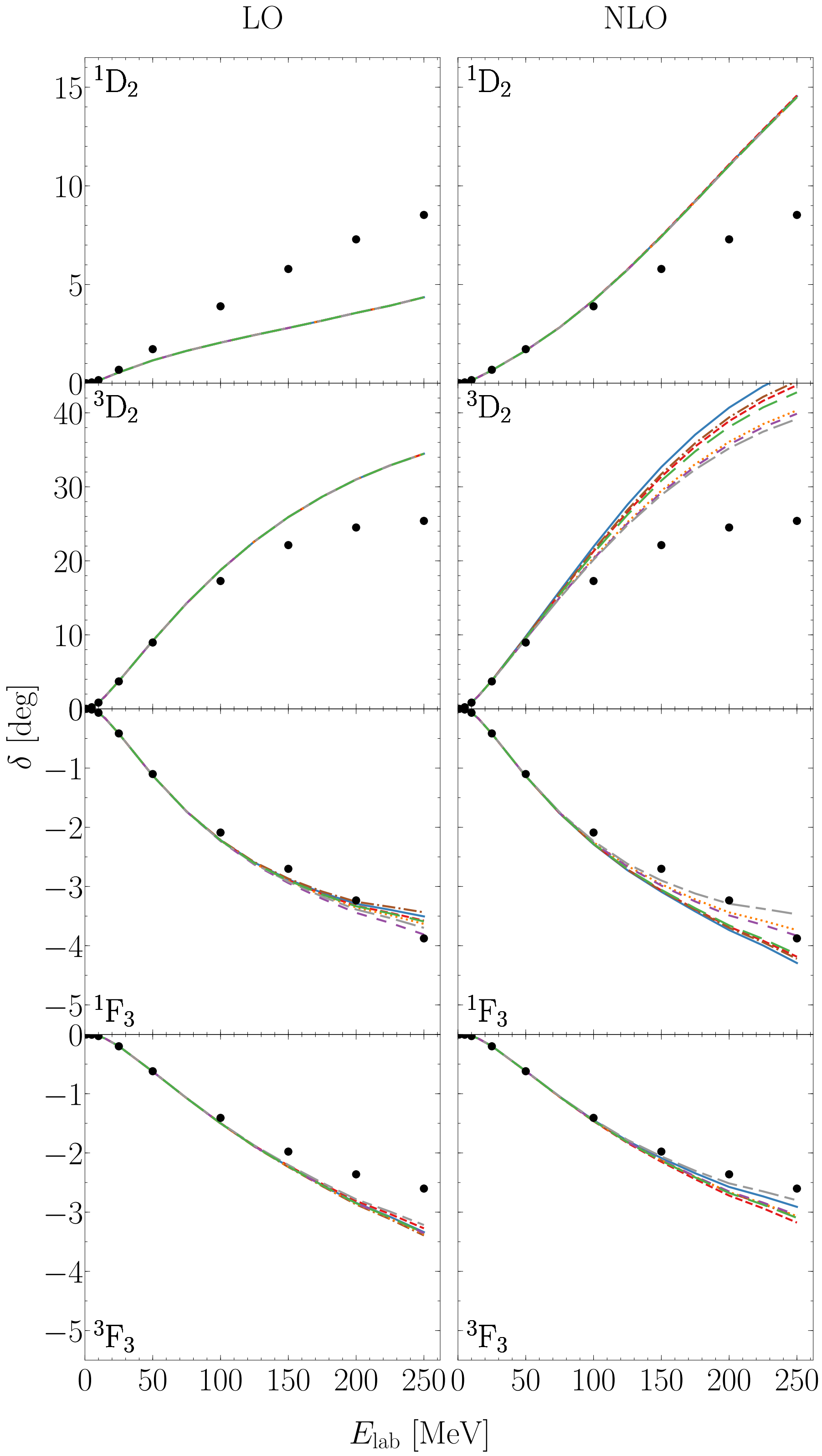

Figure 5.3.: Phase shifts for the $^1D_2$, $^3D_2$, $^1F_3$, and $^3F_3$ partial waves for $R_0 = 1.0$ fm. The legend is as in Fig. 5.1.

of the operator choice. Because these LECs enter the two S-wave and the ${}^3D_1$ phase shifts, we do not observe any dependence on the operator choice in those channels. The lines for all operator pairs overlap for the ${}^1S_0$, ${}^3S_1$, and ${}^3D_1$ channels and the mixing angle. The obtained phase shifts are very close to the corresponding phase shifts of Ref. [39]. Furthermore, for all potentials we find the same deuteron binding energy of $E_d = 1.790$ MeV $(1.799$ MeV$)$ for $R_0 = 1.0\ \mathrm{fm}$ $(1.2\ \mathrm{fm})$.

While C_{01} and C_{10} do not depend on the chosen operator structure, it is immediately clear from Eq. (5.15) that the operator LECs as well as the spin-isospin LECs C_{00} and C_{11} do. When comparing the C_{00} and C_{11} values for two different operator combinations in Table 5.1, one can see that the Fierz-rearrangement freedom is violated for local regulators. Considering, e.g., the operator combination $\mathbb{1}, \sigma_{12}$ one obtains $C_{00} = C_{01}$ and $C_{11} = C_{10}$. For the combination $\mathbb{1}, \tau_{12}$, instead, one finds $C_{00} = C_{10}$ and $C_{11} = C_{01}$. As a consequence, the phase shifts in the corresponding spin-isospin channels are not independent of the operator choice when local regulators are used.

We show the phase shifts in the ${}^1P_1$ (determined by C_{00}) and in the ${}^3P_J$ (determined by C_{11}) partial waves at LO in the upper panels of Fig. 5.2 for $R_0 = 1.0\ \mathrm{fm}$. At low energies, the results agree very well with the PWA, and different choices for the operator pair lead to the same phase shifts, as expected. At higher energies, however, the subleading corrections become more important and the phase shifts begin to disagree considerably with the PWA as well as with each other. For all P waves, at energies above ≈ 20 MeV, the choice of the operator pair clearly affects the phase-shift prediction and we observe a large variation for the resulting phase shifts. This variation follows the ordering expected from Table 5.1. In the ${}^1P_1$ partial wave, e.g., the variation ranges from results for the $\tau_{12}, \sigma_{12}\tau_{12}$ interaction, which describe the PWA results very well, to results for the σ_{12}, τ_{12} interaction that even change sign at 130 MeV.

Because the ${}^1P_1$ phase shift experiences a sizable effect, we show it again in Fig. 5.4 for the two operator pairs that give the extreme results and for both cutoffs. For $R_0 = 1.0\ \mathrm{fm}$, we additionally show the uncertainties according to the prescription of Ref. [30] (EKM uncertainties) at LO. We observe that the violation of the Fierz ambiguity is slightly worse for $R_0 = 1.2\ \mathrm{fm}$, which is expected based on the corresponding smaller momentum-space cutoff and, thus, larger correction terms. We also find, that the uncertainty due to the violation of the Fierz ambiguity is probed neither by varying the cutoff, which has been regarded as a tool for assessing the uncertainty due to neglecting higher-order contact operators, nor by the EKM uncertainties.

In Fig. 5.3 we show phase shifts for the ${}^1D_2$, ${}^3D_2$, ${}^1F_3$, and ${}^3F_3$ partial waves for $R_0 = 1.0\ \mathrm{fm}$. For the D waves, only the S-wave spin-isospin LECs enter, and, thus, the LO phase shifts are independent of the short-range operators. For the F-wave phase shifts, the dependence on the short-range operator structure is nonnegligible only at energies larger than 200 MeV, because the higher-l phase shifts are protected by the angular-momentum barrier. These findings are consistent with our expectations based on the discussion around Eqs. (5.13) and (5.14).

In addition to NN scattering phase shifts, we investigate the impact of different operator choices on other physical observables. In particular, we study the ${}^4\mathrm{He}$ ground-state energy E using the GFMC method, and the neutron-matter energy per particle E/N at different densities using the AFDMC method. The results are shown in Fig. 5.5 for all operator combinations, together with the corresponding EKM uncertainties as error bars. We also show the spread of all operator pairs as shaded regions. If the Fierz-rearrangement freedom were respected, the spread would vanish.

For the ${}^4\mathrm{He}$ ground-state energy, we observe a sizable dependence on the LO operator choice. The ${}^4\mathrm{He}$ ground-state energy varies between -35.4 MeV and -44.1 MeV, the $\mathbb{1}, \tau_{12}$ interaction being an outlier due to strong P-wave attraction (excluding this operator choice, the ground-state energy only varies between -35.4 MeV and -38.8 MeV.) The spread for the different operator combinations is ~ 9 MeV and comparable to the EKM uncertainties at this order.

In the case of neutron matter, the energy per neutron at half saturation density $n_0/2$ (at n_0), with $n_0 = 0.16\ \mathrm{fm}^{-3}$, ranges between 11.2 (16.3) MeV for the pair $\mathbb{1}, \sigma_{12}$ and 13.3 (22.1) MeV for the pair σ_{12}, τ_{12}. The spread due to the violation of Fierz-rearrangement freedom is again comparable to the size of the EKM uncertainties for these interactions, which has also been observed for the leading $3N$

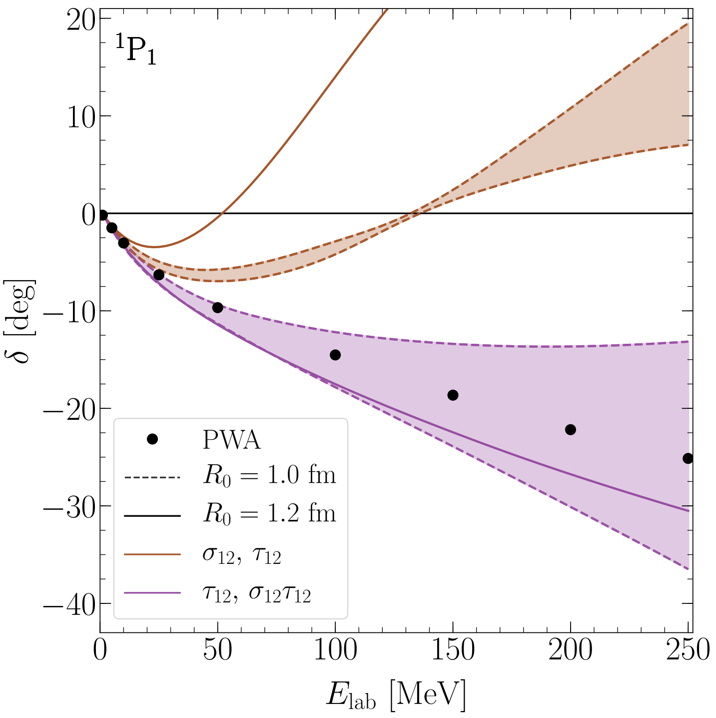

Figure 5.4.: Phase shift as a function of laboratory energy in the $^1P_1$ channel for the two interactions that give the most extreme results: the σ_{12}, τ_{12} and $\tau_{12}, \sigma_{12}\tau_{12}$ interactions. We show the results for $R_0 = 1.0$ fm with EKM uncertainty estimates (bands, see text) and the results for $R_0 = 1.2$ fm as solid lines. The color scheme is as in Fig. 5.1.

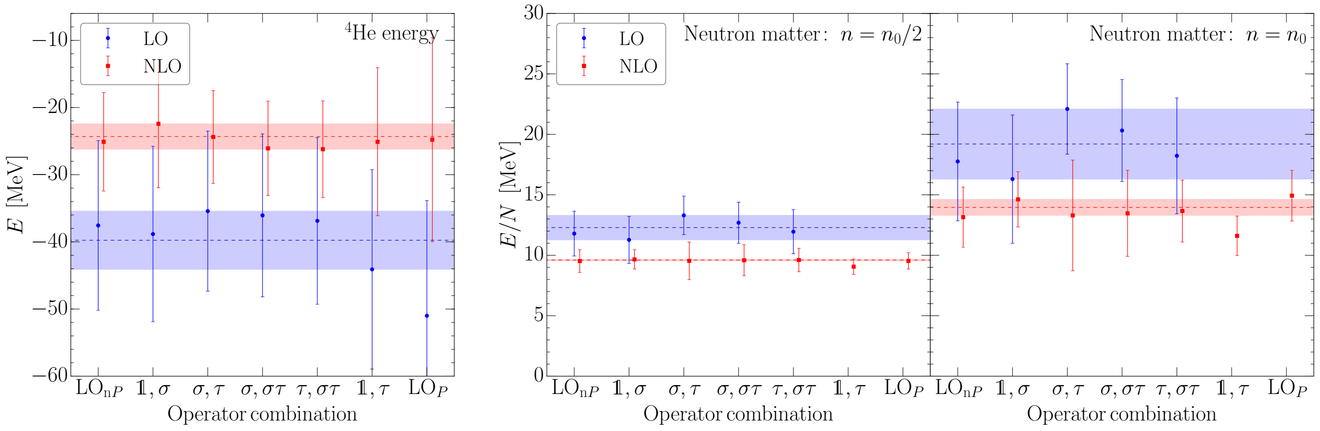

Figure 5.5.: Many-body observables at LO and NLO for different LO operator combinations taken from Ref. [111]. Here we drop the operator subscripts for legibility; i.e., $\sigma_{12} \to \sigma$, etc. The shaded regions show the spread for the various operator choices, while the dashed line denotes the centroid. When calculating the band and the centroid, we exclude the complete potentials in all cases and the $\mathbb{1}, \tau$ operator combination in the case of neutron matter. Note that for neutron matter at LO, we only show the results for five interactions, because we find bound neutron matter for the LO$_P$ and the $\mathbb{1}, \tau_{12}$ interactions. Left panel: Ground-state energy of ^{4}He. Middle panel: Neutron matter energy per particle at one half saturation density. Right panel: Neutron matter energy per particle at saturation density.

contact interactions [109]. Furthermore, it is important to note that the operator choice $\mathbb{1}, \tau_{12}$ leads to bound neutron matter for both densities. This can be easily understood from Table 5.1: the spin-isospin LEC entering the triplet P waves is of the same size as the S-wave LEC and attractive for these operators. We exclude this interaction when showing the horizontal band.

5.3 "Complete" LO potentials

As we have seen in the previous section, the choice of the LO operators clearly impacts the results for phase shifts and the energies of nuclei and neutron matter, and leads to a range of results that is not covered by typical uncertainty estimates. To correct for this regulator artifact already at LO one could also explicitly compute the correction terms and include these in the calculation. Because it is nontrivial to include nonlocal terms in QMC simulations, we will not pursue this approach here.

Instead, we follow an idea similar to the one used in Ref. [109] and construct a LO potential with a projector on $S \neq T$ partial waves. To implement this projector, we construct a complete LO potential, i.e., a potential that includes all four LO contact operators. In addition to fitting the ${}^1S_0$ and ${}^3S_1$ phase shifts (fitting C_{01} and C_{10}), we enforce that the contribution of $V_{\text{cont}}^{\text{LO}}(r, R_0)$ vanishes in the partial waves with $T = S$, i.e.,

$$
\begin{aligned}
C_{00} &= C_{\mathbb{1}} - 3C_{\sigma} - 3C_{\tau} + 9C_{\sigma\tau} = 0\,, \\
C_{11} &= C_{\mathbb{1}} + C_{\sigma} + C_{\tau} + C_{\sigma\tau} = 0\,,
\end{aligned}
\tag{5.18}
$$

where we have used Eq. (5.15). Enforcing the two conditions in Eq. (5.18) eliminates the mixing into P waves. In the following, we call this interaction LO$_{\text{n}P}$, for "no P-wave" mixing. This potential eliminates the regulator artifacts in odd-l partial waves and, hence, is closest to an LO potential that respects the Fierz-rearrangement freedom. Furthermore, it simplifies the fitting procedure for local chiral interactions at higher orders in the chiral expansion. This potential leads to a good reproduction of the P-wave phase shifts, and, for $R_0 = 1.0\,\text{fm}$, gives a ${}^4\text{He}$ ground-state energy of -37.6 MeV, and a neutron-matter energy of $11.8\ (17.8)$ MeV at $n_0/2\ (n_0)$. Results for this potential are also shown in Figs. 5.1–5.3 and 5.5.

In addition to the LO$_{\text{n}P}$ potential, we also investigated a second complete LO potential, where we fit the additional couplings to the ${}^1P_1$ and ${}^3P_2$ partial waves. We call this interaction LO$_P$. In contrast to the LO$_{\text{n}P}$ potential, the LO$_P$ potential does not eliminate any regulator artifacts at LO but instead matches them to reproduce two P-wave phase shifts. This potential, however, is too attractive in the triplet P waves, see Table 5.1, and performs worst in the ${}^3P_0$ and ${}^3P_1$ partial waves. We also investigated the alternatives of fitting this potential to the ${}^1P_1$ and one of the other ${}^3P_J$ partial waves. These lead to an excellent description of the ${}^3P_J$ wave under consideration, but an even worse reproduction of the other two triplet P waves, with, for example, $C_{11} \approx 5C_{01}$ in the fit to the ${}^1P_1$ and ${}^3P_2$ partial waves.

Due to the strong attraction in the triplet P waves, we find a large ${}^4\text{He}$ ground-state energy of ~ -51 MeV for the LO$_P$ interaction. Furthermore, this potential leads to bound neutron matter. The LO$_P$ potential, thus, performs worst in all systems that we studied. Again, results for this potential are shown in Figs. 5.1–5.3 and 5.5.

5.4 Next-to-leading order

As stated above, the violation of the Fierz-rearrangement freedom due to the local regulator will be corrected by higher-order terms. The first correction is of the order $(Q/\Lambda)^2$ and appears at NLO in chiral EFT. In the following, we investigate to what extent the subleading NLO short-range operators restore the Fierz-rearrangement freedom at LO.

At NLO, the interactions include momentum-dependent short-range contact interactions and two-pion–exchange interactions. For the contact interactions, the most general set of operators in momentum space is given by 14 different terms,

$$
\begin{aligned}
V_{\mathrm{cont}}^{(2)} =& \gamma_1 q^2 + \gamma_2 q^2 \sigma_{12} + \gamma_3 q^2 \tau_{12} + \gamma_4 q^2 \sigma_{12} \tau_{12} \\
&+ \gamma_5 k^2 + \gamma_6 k^2 \sigma_{12} + \gamma_7 k^2 \tau_{12} + \gamma_8 k^2 \sigma_{12} \tau_{12} \\
&+ \gamma_9 (\boldsymbol{\sigma}_1 + \boldsymbol{\sigma}_2) \cdot (\mathbf{q} \times \mathbf{k}) + \gamma_{10} (\boldsymbol{\sigma}_1 + \boldsymbol{\sigma}_2) \cdot (\mathbf{q} \times \mathbf{k}) \tau_{12} \\
&+ \gamma_{11} (\boldsymbol{\sigma}_1 \cdot \mathbf{q})(\boldsymbol{\sigma}_2 \cdot \mathbf{q}) + \gamma_{12} (\boldsymbol{\sigma}_1 \cdot \mathbf{q})(\boldsymbol{\sigma}_2 \cdot \mathbf{q}) \tau_{12} \\
&+ \gamma_{13} (\boldsymbol{\sigma}_1 \cdot \mathbf{k})(\boldsymbol{\sigma}_2 \cdot \mathbf{k}) + \gamma_{14} (\boldsymbol{\sigma}_1 \cdot \mathbf{k})(\boldsymbol{\sigma}_2 \cdot \mathbf{k}) \tau_{12} \, .
\end{aligned}
\tag{5.19}
$$

As before, only seven out of these 14 operators are independent for reasons of antisymmetry if no regulator is included. Just like at LO, the the Fierz-rearrangement freedom is violated at NLO in the presence of local regulators. In the following, we neglect the new regulator artifacts that originate at NLO and instead focus only on the LO regulator artifacts because they are the largest in size: The corrections to the NLO violation appear only at N^{3}LO. Furthermore, the NLO regulator artifacts in S and P waves can be partially absorbed into the LECs and the first artifacts then appear in D waves, where they are additionally suppressed by the angular momentum barrier.

In the following, we construct NLO interactions for all possible pairs of LO operators, as well as the two potentials with the complete set of LO operators (LO$_{nP}$ and LO$_P$). We fix the NLO operators to be the six local operators and the spin-orbit operator, as in Refs. [38, 39]: $\{\mathbb{1}, \sigma_{12}, \tau_{12}, \sigma_{12}\tau_{12}, (\boldsymbol{\sigma}_1 \cdot \mathbf{q})(\boldsymbol{\sigma}_2 \cdot \mathbf{q}), (\boldsymbol{\sigma}_1 \cdot \mathbf{q})(\boldsymbol{\sigma}_2 \cdot \mathbf{q})\tau_{12}\}$ and $(\boldsymbol{\sigma}_1 + \boldsymbol{\sigma}_2) \cdot (\mathbf{q} \times \mathbf{k})$. In addition to the S-wave phase shifts, we fit the LECs to the $J = 1$ mixing angle ϵ_1 and the $^1P_1$ and ^3P_J partial waves. We give the NLO LECs for all interactions in Table 5.2.

We present the NLO phase shifts in the right panels in Figs. 5.1–5.3. Regarding the S-wave phase shifts, we find a good description of the PWA results. Again, all seven interactions produce the same phase shifts. In the coupled channel, for the $J = 1$ mixing angle and the $^3D_1$ phase shift, we observe a dependence on the operator choice. The reason is that the LECs describing the NLO tensor-contact interactions are different for all operator pairs in order to reproduce the P-wave phase shifts. The different tensor interactions then lead to differences in the $^3D_1$ coupled channel, which affects the mixing angle. For the deuteron binding energy, we find an (almost) operator-independent result of $E_d = 2.113 - 2.134$ $(2.107 - 2.162)$ MeV for $R_0 = 1.0$ fm $(1.2$ fm$)$, where the range is again due to the somewhat different tensor interactions.

Turning to the P waves in Fig. 5.2, we observe two effects at NLO. First, the reproduction of the PWA phase shifts is much better for both the singlet and triplet partial waves. Second, we find that the effects of the violation of the Fierz-rearrangement freedom are considerably reduced. At LO, we found a sizable spread of the description of the P-wave phase shifts already at energies around 20 MeV. At NLO, all interactions lead to similar phase shifts up to energies of $\sim$ 100 MeV, but sizable regulator artifacts remain at higher laboratory energies. The impact of the violation of the Fierz ambiguity is worst in the $^3P_2$ wave, where the spin-orbit interaction is attractive and the tensor is weakest. Finally, for the higher-l partial waves in Fig. 5.3, we find similar results for the phase shifts as at LO: These phase shifts are already well described by the OPE interaction at LO and improvements with the chiral order are counteracted by the different tensor interactions. However, the violation of the Fierz-rearrangement freedom has only a small impact on these partial waves.

We now discuss the effects on the many-body observables. For the ^{4}He ground-state energy we find that the spread for different LO operator pairs reduces considerably: from 8.7 MeV at LO to 3.8 MeV at NLO, ranging from 22.4 MeV for the $\mathbb{1}, \sigma_{12}$ interaction to 26.2 MeV for the $\tau_{12}, \sigma_{12}\tau_{12}$ interaction. The spread is considerably smaller than the EKM uncertainties of at least 7 MeV, in contrast to the results at LO.

We show the neutron-matter energy at $n_0/2$ in the middle panel of Fig. 5.5. In contrast to the results at LO, we now find all interactions produce unbound neutron matter at roughly the same energy in the range of $9.1 - 9.7$ MeV. Thus, for neutron matter at $n_0/2$ the Fierz ambiguity is almost completely restored and the uncertainty from choosing different operator pairs is smaller than the EKM uncertainties. At higher density, n_0, the spread between different interactions remains larger at 3.0 MeV, ranging from

11.6 MeV for the $\mathbb{1}, \tau_{12}$ interaction up to 14.6 MeV for the $\mathbb{1}, \sigma_{12}$ interaction; see the right panel of Fig. 5.5. This is to be expected, as the regulator artifacts increase with momentum or density (see also Refs. [107, 170]).

Considering only the interactions that gave reasonable results already at LO, the spread reduces to 1.5 MeV and is, thus, only $1/4$ of the spread at LO (5.8 MeV) and smaller than the EKM uncertainties of ≈ 2 MeV. The ordering of the NLO results closely follows the ordering of the description of the triplet P waves, with the $\mathbb{1}, \tau_{12}$ interaction being the biggest outlier.

5.5 Summary of main results

To summarize our key findings:

- We investigated effects of the violated Fierz-rearrangement freedom that appear when using local regulators in the NN sector. In the presence of local short-range regulators, the antisymmetrization operator no longer commutes with the potential. As a consequence, the interaction depends on the choice of the operator set. We demonstrated this in two different ways, first with antisymmetrization arguments and second from the partial-wave decomposition of Gaussian regulators.

- We then constructed local chiral interactions at LO and NLO in for all possible operator pairs at LO. In addition we constructed the LO$_{\mathrm{n}P}$ and LO$_P$ interaction that considered all four LO operators. We fitted the LECs to S-wave phase shifts from the PWA from Ref. [162]. The resulting interactions were used to compare phase shifts for multiple partial waves, ^{4}He binding energy, and the neutron-matter energy at half-saturation and saturation density.

- We found a sizable violation of the Fierz-rearrangement freedom for interactions at LO. However, this violation of the Fierz ambiguity in the NN sector is considerably reduced at NLO, and always covered by the EKM uncertainties, in contrast to the results at LO. We expect the violation of the Fierz ambiguity to remain of similar size at N^{2}LO because no new two-body contact terms are introduced, but we expect that it should be almost completely removed at N^{3}LO. As a consequence of these findings, recently derived local NN potentials at N^{2}LO can be used with confidence within their uncertainties.

- Currently, we develop a code capable to do the partial-wave decomposition of local regulators automatically, so that we can perform calculations with nonlocal contact operators in momentum-space. With this we plan to investigate the violation of the Fierz ambiguity for operators at NLO in the future.

6 Cutoff dependence of local interactions

In the previous chapter we investigated the effects from the violated Fierz ambiguity by locally regularized interactions from chiral EFT. In this Chapter, we continue our research of the cutoff behavior in local interactions from chiral EFT. We investigate the behavior of local coordinate-space potentials at leading order under variation of the cutoff scale for different kinds of regulators.

Results and ideas which we present here have been reported in Ref. [113]. For completeness, we list all numerical values that we obtain in this chapter in App. E.1.

6.1 Power counting

Weinberg power counting (WPC) [23–25, 193] is based on dimensional analysis in momentum space. In the purely pionic and one-nucleon sector, due to the Goldstone-boson nature of pions, all amplitudes can be expanded in powers of the dimensionless expansion parameter Q/Λ_b, where as mentioned before, Q is a typical momentum of the system and Λ_b is the breakdown scale of the theory. In the two-nucleon sector, instead, bound states appear and the problem becomes nonperturbative. To obtain observables, WPC suggests defining the nuclear potential as the sum of all irreducible diagrams that do not contain purely nucleonic intermediate states and, thus, are not infrared enhanced. This sum is then truncated according to a power counting in Q/Λ_b. The resulting potential is iterated to all orders by solving the Lippmann-Schwinger equation (LSE) or Schroedinger equation. At the two-body level, at leading order, WPC leads to the appearance of S-wave contact interactions and the one-pion-exchange interaction, while at higher orders additional derivative contact interactions and multi-pion-exchange interactions, as well as corrections to previous topologies, have to be considered.

This approach has unsolved problems. In few- and many-body calculations, a regularization scheme has to be introduced to cut off high-momentum modes that may lead to divergences. Because the regularization scheme is arbitrary, results should be independent of this choice after the dependence of contact parameters on the regularization scale, the so-called cutoff Λ_c, is taken into account. This means that at each order there should be sufficiently many counterterms to absorb any residual cutoff dependence in the limit $\Lambda_c \to \infty$. This is problematic for singular potentials, such as OPE, which has a $1/r^3$ behavior in spin $S = 1$ channels due to the tensor force. Although the focus is to describe long-range behavior, this singular potential nevertheless generates an oscillatory wave function for $r \to 0$ that leads to the appearance of spurious bound states and cutoff-dependent results. To renormalize such a potential in a certain partial wave, i.e., to obtain cutoff-independent results for large cutoffs, a counterterm is necessary in the same partial wave [112, 194]. In WPC at LO, however, the only counterterms appear in the S waves, but not in partial waves with orbital angular momentum $l > 0$ where the singular OPE potential also contributes.

Kaplan, Savage, and Wise (KSW) [195, 196] suggested a different power counting that uses dimensional regularization (DR) with power divergence subtraction to systematically expand the nucleon-nucleon (NN) scattering amplitude in powers of Q/Λ_b instead of the potential. Within this scheme, only the LO contact interactions are treated nonperturbatively, while other contact interactions and pion exchanges are treated in finite order in perturbation theory, in order to find analytic expressions for the scattering amplitudes. Although the KSW power counting is well defined and consistent, it failed to reproduce the phase shifts from the Nijmegen PWA [162] in spin-triplet channels at N^{2}LO [197] and led to large N^{2}LO corrections. It was found that in some spin-triplet channels, the nonperturbative treatment of pion-exchange diagrams is necessary at higher momenta because the OPE tensor force is large and singular, and must be summed to all orders. This is done in WPC and reflects the fact that a correct renormalization of singular potentials is intrinsically nonperturbative [198]. A solution to this problem was suggested in Ref. [199], where the short-range part of the OPE interaction was canceled by fictitious heavy mesons.

Nogga, Timmermans, and van Kolck (NTvK) [112] studied the cutoff dependence of phase shifts at LO in WPC for nonlocal regulators and for a cutoff range of $\Lambda_c = 2-20\ \mathrm{fm}^{-1}$. They found that WPC leads to cutoff-independent results in the spin $S=0$ channels, in the ${}^3S_1$ channel, where WPC includes a counterterm, and in $S=1$ channels with repulsive tensor forces, e.g., ${}^3P_1$. However, NTvK observed strong cutoff dependences and the appearance of several spurious bound states in the other attractive tensor channels, ${}^3P_0, {}^3D_2$, and ${}^3P_2 - {}^3F_2$, where there are no counterterms present in WPC. As a solution, NTvK suggested to explicitly add counterterms to partial waves with attractive tensor interactions, i.e., ${}^3P_0$, ${}^3P_2$, and ${}^3D_2$. In higher partial waves, NTvK found that the centrifugal barrier screened the singular tensor force sufficiently so that no counterterms were necessary in the investigated cutoff range. The modification of WPC proposed by NTvK was also confirmed based on a renormalization group analysis [200].

Similar to the spirit of NTvK, in this chapter we investigate the large-cutoff behavior of local chiral interactions that were introduced in Refs. [38, 39]. In the previous chapter we showed, that local regulators induce regulator artifacts, which mix contact interactions in a certain partial wave into all higher partial waves (see also Refs. [109, 111, 170]), because the regulator does not commute with the antisymmetrizer. In this chapter, we exploit these regulator artifacts to mix LO contact interaction terms into all attractive tensor channels, to obtain cutoff-independent results for the phase shifts and deuteron ground-state energy.

6.2 Local chiral interactions at LO

As we have shown in the previous chapters, the LO potential from chiral EFT takes the form

$$V_{\mathrm{NN}}^{\mathrm{LO}}(r,R_0) = V_{\mathrm{OPE}}^{\mathrm{LO}}(r,R_0) + V_{\mathrm{cont}}^{\mathrm{LO}}(r,R_0)\,, \tag{6.1}$$

with the one-pion-exchange interaction given Eq. (4.7) and the most general set of short-range contact operators, given by

$$V_{\mathrm{cont}}^{\mathrm{LO}}(r,R_0) = (C_1 + C_\sigma\,\sigma_{12} + C_\tau\,\tau_{12} + C_{\sigma\tau}\,\sigma_{12}\,\tau_{12})\,f_{\mathrm{short}}(r,R_0)\,. \tag{6.2}$$

This general set of short-range operators describes S-wave NN scattering. In this chapter, we investigate different forms of the long- and short-range regulator. We consider the general form which we presented in Eq. (4.2) and Eq. (4.3). For convenience we repeat the expressions below:

$$\begin{aligned} f_{\mathrm{long}}(r,R_0) &= \left(1-\exp\left(-\left(\frac{r}{R_0}\right)^{n_1}\right)\right)^{n_2}\,, \\ f_{\mathrm{short}}(r,R_0) &= \frac{n}{4\pi\Gamma(3/n)R_0^3}\exp\left(-\left(\frac{r}{R_0}\right)^{n}\right)\,, \end{aligned} \tag{6.3}$$

with the coordinate-space cutoff R_0, and where n_1, n_2, and n determine the width of the regulator functions. In this work we will investigate different combinations of n_1, n_2, and n for these regulator functions, as low-energy physics should be independent of the short-range details and any regulator function should be equally valid [194].

As we showed in the previous chapter, when the regulator commutes with the antisymmetrizer, as is the case for typical nonlocal regulators, only two of the four LO operators in Eq. (6.2) are linearly independent, and one can choose any two of the four operator structures (except $\mathbb{1}, \sigma_{12}\tau_{12}$ which is linearly dependent in the two S-wave channels) for the LO potential. From the spin-isospin LECs C_{ST}, which enter partial waves with total spin S and the total isospin T, one can then determine the operator LECs

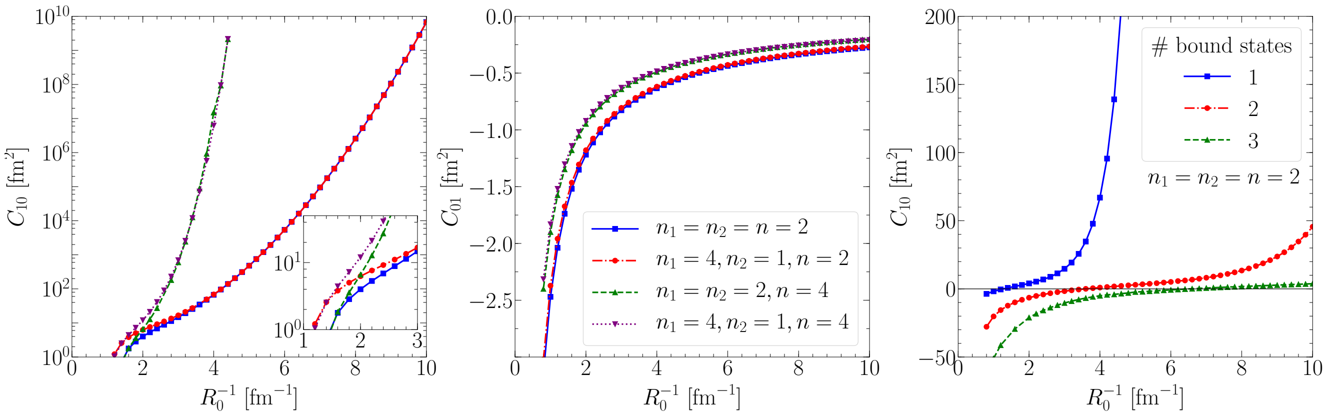

Figure 6.1.: Spin-isospin LECs C_{10} (left panel, logarithmic scale) and C_{01} (middle panel) as function of the inverse cutoff R_0^{-1} for local chiral interactions at LO with different local regulators characterized by n_1, n_2, n. Right panel: Spin-isospin LEC C_{10} as function of the inverse cutoff R_0^{-1} for local chiral interactions at LO allowing one, two, and three bound states in the coupled $^3S_1$–$^3D_1$ channel.

for different operator pairs according to Eq. (5.15). However, the Fierz ambiguity is violated when local regulators are chosen; see Ch. 5. For local regulators, the LO interaction in the S waves affects all higher partial waves. While this mixing of LO S-wave physics into higher partial waves cannot be turned off completely, one can construct interactions that vanish in the $ST = 00$ and $ST = 11$ partial waves, i.e. partial waves with odd orbital angular momentum l[1] by choosing all four operators at LO and setting $C_{00} = C_{11} = 0$. We call the latter interaction LO$_{\text{n}P}$, and it is closest to nonlocally regularized interactions.

In the following, we construct various potentials for different operator structures, different sets $\{n_1, n_2, n\}$, and different regulator values in the range $R_0^{-1} = 0.8\ \text{fm}^{-1} - 10.0\ \text{fm}^{-1}$ in steps of $0.2\ \text{fm}^{-1}$, where we use the inverse of the coordinate-space cutoff because it is connected to the momentum-space cutoff. Then, large values for R_0^{-1} imply large momentum cutoffs. For each potential, we fit the two spin-isospin LECs in the $^1S_0$ and $^3S_1$ partial waves, C_{01} and C_{10}, to the corresponding S-wave phase shifts from the Nijmegen PWA [162] up to laboratory energies of 50 MeV, as detailed in Ch. 4. When varying R_0, we renormalize the LECs $C_{ST} = C_{ST}(R_0)$ to keep the phase shifts invariant at low energies. Depending on the size and sign of the LECs, we can obtain fits with an arbitrary number of bound states. Therefore, when fitting the LECs, we additionally require that the resulting interaction allows for exactly one bound state in the deuteron channel.

We present the resulting LECs C_{10} and C_{01} as functions of the inverse cutoff R_0^{-1} in the first two panels of Fig. 6.1, respectively, for four different sets $\{n_1, n_2, n\}$ = $\{2, 2, 2\}$, $\{4, 1, 2\}$, $\{2, 2, 4\}$, and $\{4, 1, 4\}$. We find that the LEC dependence on the cutoff is regulator-dependent, see also Ref. [112], and observe a systematic behavior for the different regulator choices in both ST-channels.

We observe a strong increase of C_{10} with R_0^{-1} (in the left panel of Fig. 6.1), which is more prominent for short-range regulators with $n = 4$ (green and purple line) compared to those with $n = 2$ (blue and red line). This increase is due to the increasing attractive OPE tensor contribution in the $ST = 10$ channel when increasing R_0^{-1}. Because we only allow for one bound state in the deuteron channel, an increasing LEC is needed to balance the OPE attraction sufficiently so that no second bound state enters. We will discuss this in more detail later in this chapter. For the interactions with $n = 4$, this requires a larger LEC because the regulator is sharper. Also, for $n = 4$ we could not achieve a fit beyond $R_0^{-1} = 4.4\ \text{fm}^{-1}$, due to large numerical values and cancellations.

In the $ST = 10$ channel, at small values of R_0^{-1}, we find pairwise similar LECs for the sets $\{2, 2, 2\}$ (blue line) and $\{2, 2, 4\}$ (green line) as well as for the sets $\{4, 1, 2\}$ (red line) and $\{4, 1, 4\}$ (purple line). At large

---

(1) In two-fermion systems, the Pauli principle requires $l + S + T$ to be odd. For $S = T$ this means l has to be odd.

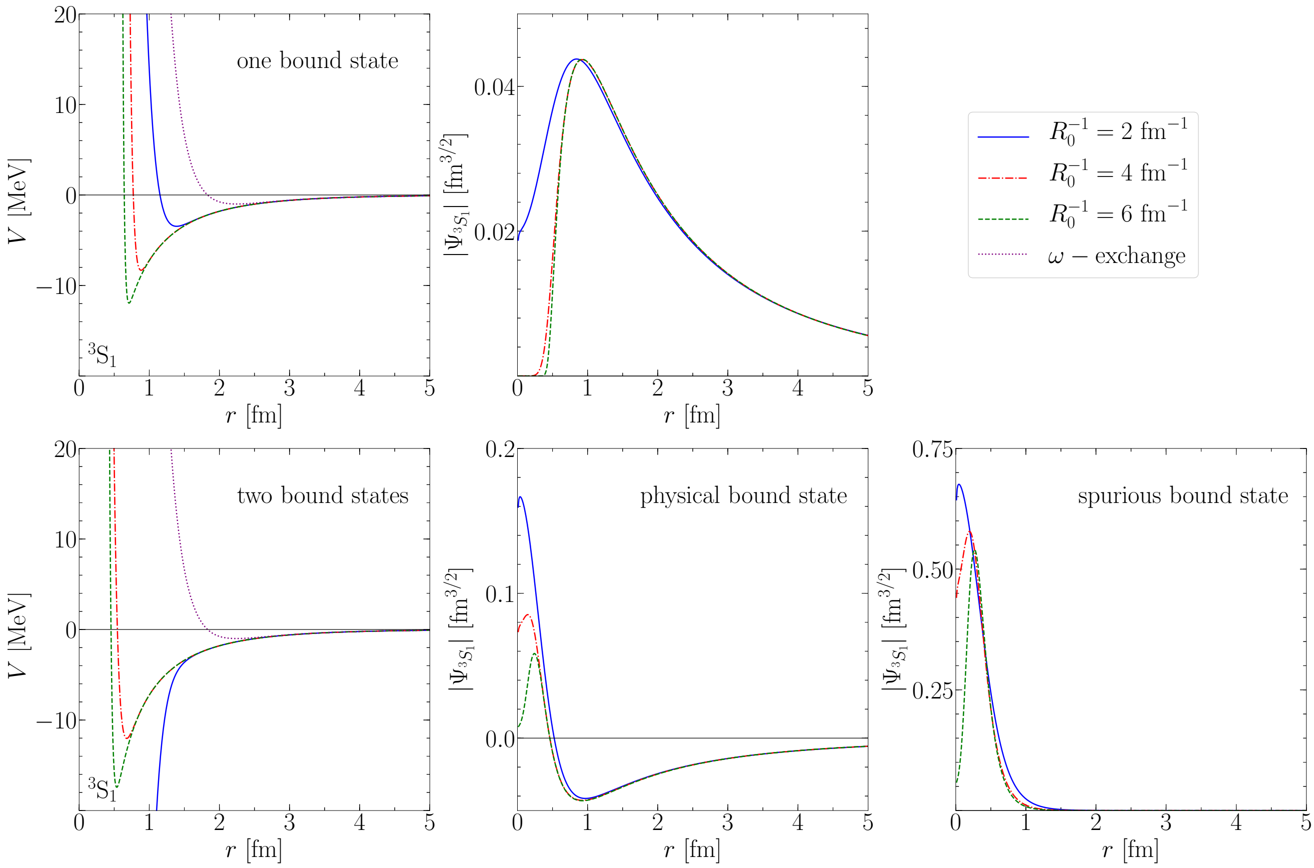

Figure 6.2.: Chiral LO potentials in the $^3S_1$ partial wave as well as the corresponding wave functions for one or two bound states for three cutoff values and $n_1 = n_2 = n = 2$. In addition, we compare the chiral LO potentials with a potential where the short-range interaction is replaced by an ω-meson-exchange potential.

values of R_0^{-1} this behavior changes, and we find pairwise similar LECs for the sets $\{2,2,2\}$ (blue line) and $\{4,1,2\}$ (red line), and for the sets $\{2,2,4\}$ (green line) and $\{4,1,4\}$ (purple line). From this we can deduce that at small R_0^{-1}, the LEC C_{10} is dominated by effects of the long-range regulator, while at large R_0^{-1}, the LEC is dominated by effects of the short-range regulator. The transition between those two regimes is found at cutoffs $R_0^{-1} \approx 2\ \text{fm}^{-1}$. This transition region is shown in the inset in the left panel of Fig. 6.1. At small R_0^{-1}, the OPE is cut off at larger distances, and the LECs are rather small, so that the relative importance of the OPE is larger and the fits are mostly sensitive to the form of the long-range regulator. This changes at large R_0^{-1}, where differences in the long-range regulator are not so important because the short-range interactions cut off the OPE at a distance scale, independent of the long-range regulator function.

In the second panel of Fig. 6.1 we show the LEC C_{01}. We again observe pairwise similar LECs for the sets $\{2,2,2\}$ (blue line) and $\{4,1,2\}$ (red line), and for the sets $\{2,2,4\}$ (green line) and $\{4,1,4\}$ (purple line), but this time we observe no crossing with R_0^{-1}. The LEC C_{01} is mostly affected by the choice of the short-range regulator because the singular tensor force does not contribute to the $^1S_0$ channel and the OPE is relatively weak. This is reflected in the LECs, which are attractive, but approach zero for increasing R_0^{-1}. The LECs can be described with high precision by a function of the form

$$C_{01}(R_0) = aR_0^b\,. \tag{6.4}$$

For the sets $\{2,2,2\}$ and $\{4,1,2\}$ with $n = 2$, we find $a = -2.47\ \text{fm}^{2+b}$ and $b = -0.98$. For the sets $\{2,2,4\}$ and $\{4,1,4\}$ with $n = 4$, we find $a = -1.83\ \text{fm}^{2+b}$ and $b = -0.96$. Thus, the LECs are proportional to R_0^{-1}.

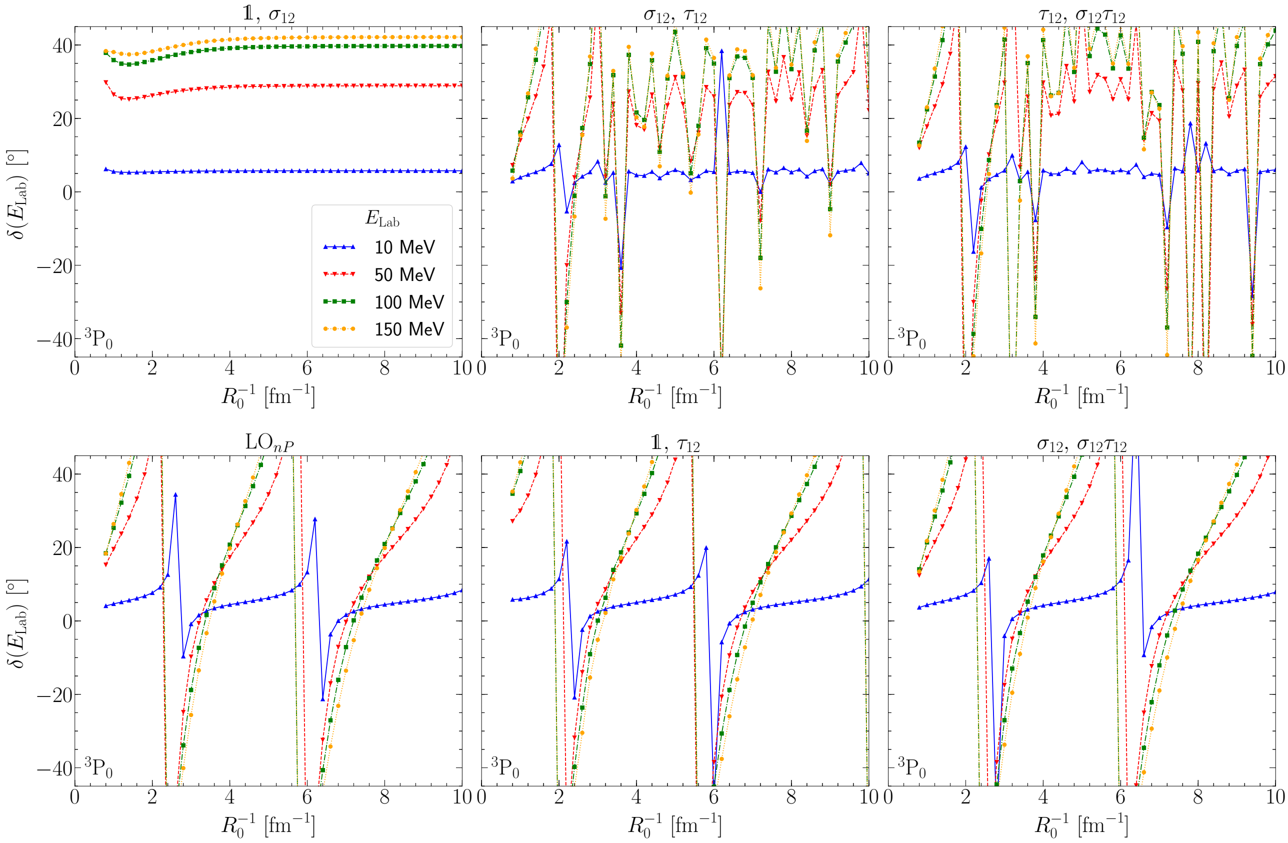

Figure 6.3.: Phase shifts in the $^3P_0$ partial wave at laboratory energy $E_{\text{lab}} = 10$, 50, 100, and 150 MeV versus the inverse cutoff R_0^{-1} for different LO operator structures and $n_1 = n_2 = n = 2$. The first panel shows the phase shifts for the operator pair $\mathbb{1}$, σ_{12}, where the spin-isospin LEC C_{11} is equal to C_{10}. The second and third panel show the operator combinations σ_{12}, τ_{12} and τ_{12}, $\sigma_{12}\tau_{12}$, where $C_{11} \sim -C_{10}$ (see Tab. 6.1). In the lower panels we show the interaction LO$_{\text{n}P}$, where $C_{11} = 0$ and which is closest to an interaction that respects Fierz rearrangement freedom, as well as the operator combinations $\mathbb{1}$, τ_{12} and σ_{12}, $\sigma_{12}\tau_{12}$, where $C_{11} \sim C_{01}$ with $C_{01} \to 0$ (see Fig. 6.1). In the lower panels we find a similar behavior as in Ref. [112].

In the third panel we show the LEC C_{10} when enforcing different numbers (one, two, or three) of bound states in the deuteron channel. As before, we observe a systematic behavior of the LECs with increasing R_0^{-1} but the LECs increase much slower for interactions with more bound states. We note that if we allow more bound states in the deuteron channel, this also leads to spurious bound states in higher partial waves with spin $S = 1$. The appearance of such spurious bound states is a signature of the fact that at short distances the description in terms of a singular NN potential is meaningless because nucleons are not relevant degrees of freedom at the corresponding distance scales.

In Fig. 6.2, we show the potentials in the $^3S_1$ partial wave, as well as the corresponding wave functions, for one allowed bound state (upper panels) and when enforcing two bound states (lower panels) for three cutoff values. In the former case, for increasing R_0^{-1}, the OPE extends to smaller distances, but is cut off at small r by the repulsive short-range contact interaction. When increasing R_0^{-1} the range of the short-range regulator function decreases as expected but this is compensated by very large LECs. This results in a hard core which does not vanish even for large values of R_0^{-1}, but cuts off the long-distance singular OPE in such a way that only one bound state can be accommodated.

Table 6.1.: Leading-order spin-isospin LECs C_{ST} in the $S=1$, $T=1$ and $S=0$, $T=0$ channels as functions of the coupling constants C_{10} and C_{01} for different operator choices. For LO$_{\mathrm{n}P}$, $C_{11}=C_{00}=0$ by definition. The second columns indicate the limit for $R_0 \to 0$.

Operators	C_{11}		C_{00}	
	exact	$R_0 \to 0$	exact	$R_0 \to 0$
$\mathbb{1}, \sigma_{12}$	C_{10}	$+\infty$	C_{01}	-0
$\mathbb{1}, \tau_{12}$	C_{01}	-0	C_{10}	$+\infty$
σ_{12}, τ_{12}	$-\frac{1}{2}(C_{10}+C_{01})$	$-\infty$	$\frac{3}{2}(C_{10}+C_{01})$	$+\infty$
$\sigma_{12}, \sigma_{12}\tau_{12}$	$-\frac{1}{3}C_{01}$	$+0$	$-3C_{10}$	$-\infty$
$\tau_{12}, \sigma_{12}\tau_{12}$	$-\frac{1}{3}C_{10}$	$-\infty$	$-3C_{01}$	$+0$

These considerations allow us to understand the large-cutoff behavior of C_{10} in Fig. 6.1. To cut off the OPE at a certain radius scale $r^{*,i}$ so that only i bound states appear, requires the short-range part of the potential at this scale to be sufficiently repulsive. For $n=2$, we have

$$V_{10}(r^{*,i}) = C_{10}\frac{1}{\pi^{\frac{3}{2}}R_0^3}\exp\left(-\left(r^{*,i}R_0^{-1}\right)^2\right) = V_0^i\,, \tag{6.5}$$

where V_{10} is the potential in the ${}^3S_1$ channel and V_0^i is the strength necessary to compensate the OPE at $r^{*,i}$. Then, it is easy to see that

$$C_{10} = V_0^i\pi^{\frac{3}{2}}R_0^3\exp\left(\left(r^{*,i}R_0^{-1}\right)^2\right)\,, \tag{6.6}$$

so C_{10} has to grow exponentially in R_0^{-2}, which is what we observe in Fig. 6.1. In fact, fitting the large-cutoff behavior for C_{10} in the case of one bound state, we find $C_{10} \sim \exp\left((r^{*,1}R_0^{-1})^b\right)$ with $b \approx 1.97$ and $r^{*,1} \approx 0.48$ fm, where the value of $r^{*,1}$ sets the scale for the crossing region in Fig. 6.1. In case of two bound states, we find $b \approx 1.97$ as before and $r^{*,2} \approx 0.20$ fm. The exponents are in very good agreement with our expectations, while $r^{*,1}$ and $r^{*,2}$ are in qualitatively good agreement with our findings in Fig. 6.2, especially considering the short-distance scale in the deuteron wave function. The resulting hard core pushes the deuteron wave function out from the center, which we see in the second panel of Fig. 6.2. When enforcing two bound states, instead, the OPE is probed also at smaller r, so that two bound states can be accommodated. In this case, $r^{*,2}$ is smaller than $r^{*,1}$, which leads to smaller values of the LECs (a smaller hard core) at a certain R_0^{-1}. Our results for large R_0^{-1} and n deuteron bound states show that there exists an effective cutoff $r^{*,n}$ in coordinate space. It would further be interesting to investigate how this behavior translates to nonlocal interactions.

We emphasize that all LECs for all numbers of bound states are fit to reproduce NN phase shifts and that this represents an ambiguity when fitting nuclear forces to the phase shifts. Because experimentally there exists only one bound state in the deuteron channel, in the following we require our interactions to be on the one-bound-state branch.

6.3 Results for phase shifts

Next, we investigate the phase-shift behavior as function of the cutoff scale. We focus on the regulator with $n_1 = n_2 = n = 2$, because this allows us to investigate the interaction also at large values for the inverse cutoff. For this set, we construct potentials for all five linearly independent operator pairs from Eq. (6.2) and the LO$_{\mathrm{n}P}$ potential. Because all interactions are fit to the two S-wave channels, we obtain

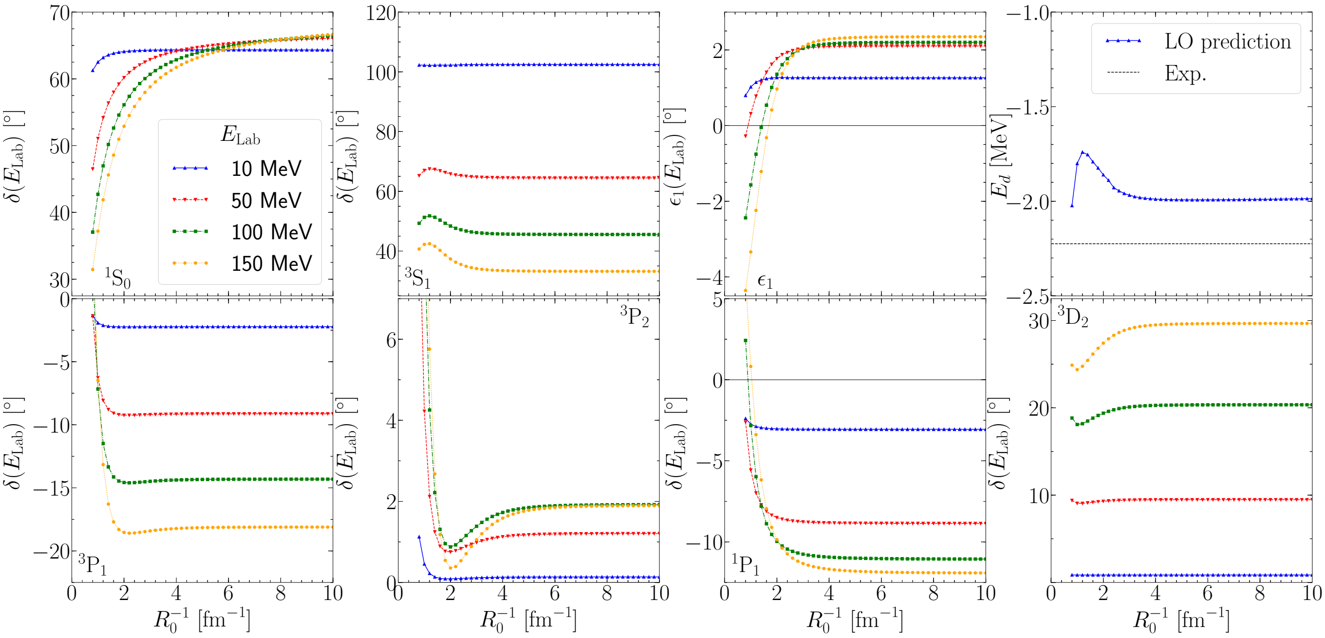

Figure 6.4.: Phase shifts in the $^1S_0$, $^3S_1$, ϵ_1, $^3D_2$, $^1P_1$, $^3P_1$, and $^3P_2$ partial waves for laboratory energies $E_{\text{lab}} = 10$, 50, 100, and 150 MeV as well as the deuteron ground-state energy E_d (upper right panel) as function of the inverse cutoff R_0^{-1} for the operators ($\mathbb{1}$, σ_{12}) and $n_1 = n_2 = n = 2$.

the same LECs C_{10} and C_{01}, but the LECs C_{00} and C_{11} depend on the operator choice, see Ch. 5 and Eq. (5.15) in particular. The values of C_{00} and C_{11} for all operator pairs are listed in Tab. 6.1, where we show both the functional dependence on C_{10} and C_{01} for each LEC, as well as the limit for $R_0 \to 0$ (see Fig. 6.1). The LECs C_{00} and C_{11} of the LO $_{\rm n}P$ interaction are exactly zero by construction.

In Fig. 6.3 we show the $^3P_0$ phase shifts at laboratory energies $E_{\text{lab}} = 10$, 50, 100, and 150 MeV as function of the inverse cutoff for each of the operator pairs and for the LO$_{{\rm n}P}$ interaction. In general, when increasing the momentum-space cutoff, i.e., taking the coordinate-space cutoff $R_0 \to 0$, the short-range regulator $f_s(r, R_0)$, becomes narrower. The long-range regulator $f_l(r, R_0)$, on the other hand, which is used in the OPE to suppress the singularity at $r = 0$ while preserving long-range physics, allows more contributions at small distances. In partial waves, where the OPE tensor part is attractive and no counterterms are present, e.g., $^3P_0$, spurious bound states appear. The signature of this effect is a limit-cycle-like behavior of the phase shift [112].

In the first row we show the operator pairs $(\mathbb{1}, \sigma_{12})$, (σ_{12}, τ_{12}), and $(\tau_{12}, \sigma_{12}\tau_{12})$, for which $C_{11} \sim C_{10}$. For the pair $(\mathbb{1}, \sigma_{12})$, the LEC is repulsive $C_{11} > 0$, and thus, acts to compensate the attractive tensor contribution from the OPE interaction. In this case, we find the results stabilize on a plateau when the cutoff is increased. This is the only operator pair for which we observe that the phase shifts become independent of R_0^{-1} for large R_0^{-1}. For the other two operator pairs the corresponding LEC is attractive, $C_{11} < 0$, which adds to OPE the attraction, and leads to the appearance of spurious bound states in the $^3P_0$ wave. This causes a highly oscillatory behavior of the phase shifts.

In the second row we show the LO$_{{\rm n}P}$, $(\mathbb{1}, \tau_{12})$, and $(\sigma_{12}, \sigma_{12}\tau_{12})$ interactions for which $C_{11} \to 0$. For the LO$_{{\rm n}P}$ interaction the P waves only receive contributions from OPE, and thus, this interaction has the closest resemblance to nonlocal chiral EFT interactions (i.e., to the case studied in Ref. [112]). The other two interactions lead to short-range contributions in the $^3P_0$ wave, but these are small, and the overall phase shifts are very similar to the LO$_{{\rm n}P}$ interaction. Phase-shift jumps in Fig. 6.3 correspond to cutoff values where new bound states enter in the $^3P_0$ wave. For the interactions in the lower panels, we find a limit-cycle-like behavior similar to the nonlocal potentials of Ref. [112] without counterterms.

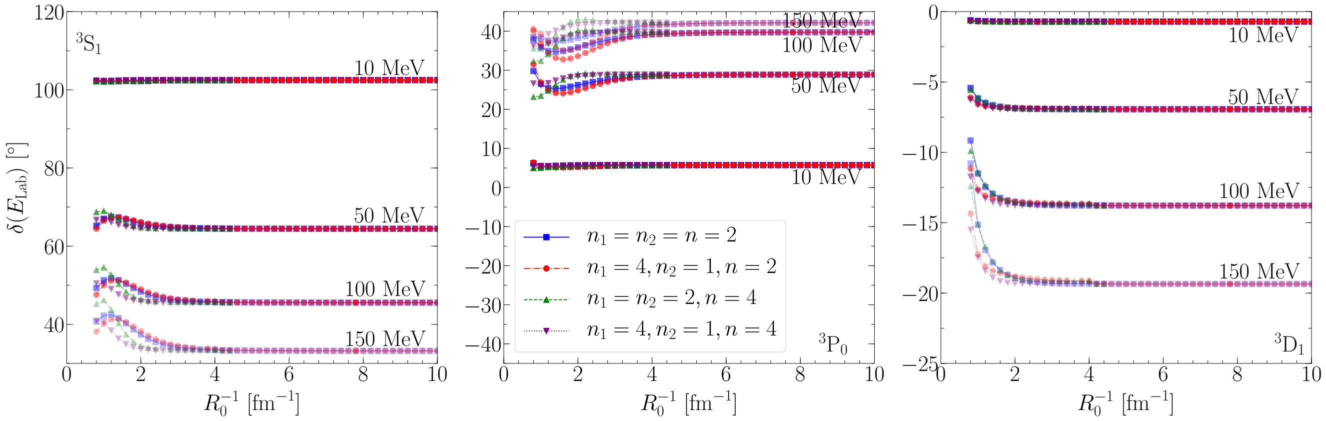

Figure 6.5.: Phase shifts in the $^3S_1$, $^3P_0$, and $^3D_1$ partial waves for different laboratory energies and for different regulator functions, as a function of the inverse cutoff R_0^{-1} for the operators $(\mathbb{1}, \sigma_{12})$.

For the interaction with operators $(\mathbb{1}, \sigma_{12})$, which leads to plateaus, we show the phase shifts in the $^1S_0$, $^3S_1$, $^3P_1$, $^3P_2$, $^1P_1$, and $^3D_2$ partial waves as well as the mixing angle ϵ_1 and the deuteron ground-state energy in Fig. 6.4, and find plateaus in all cases for $R_0^{-1} \gtrsim 4\ \mathrm{fm}^{-1}$, similar to Ref. [112] when counterterms were included there. At higher laboratory energies, the plateau is reached for higher values of R_0^{-1}. The plateau values for the phase shifts are very similar to the results found by NTvK [112], except in the attractive-tensor P and D waves, without adding any new counterterms, in contrast to NTvK. For the deuteron, we find a ground-state energy of $E_d \to -1.99$ MeV for $R_0^{-1} \to \infty$, which is close to experiment although the deuteron was not included in the fit.

In Fig. 6.5 we show the phase shifts as function of R_0^{-1} in three partial waves for different laboratory energies and different regulator choices. We find that the phase shifts converge to the same values, and that the plateaus are independent of the exponents in the regulator function. Note that for the sets $\{n_1, n_2, n\} = \{2, 2, 4\}$ and $\{4, 1, 4\}$ we do not obtain numerical results for $R_0^{-1} > 4.4\ \mathrm{fm}^{-1}$ as discussed for Fig. 6.1.

The phase shift plateaus do not necessarily have to be close to the the physical phase shift values. In Fig. 6.6 we compare the phase shifts as function of the laboratory energy in several partial waves with the PWA values for two cutoff scales ($R_0^{-1} = 1.0\ \mathrm{fm}^{-1}$ and $R_0^{-1} = 10\ \mathrm{fm}^{-1}$). The large-cutoff interaction, that lies on the phase-shift plateaus, describes the energy-dependence of the phase shifts reasonably well and in some cases much better than the result for a typical low cutoff. The only exception is the $^1S_0$ partial wave, because at LO the effective range cannot be correctly described. It is not clear if an improvement can be found at NLO due to causality bounds [201], and it will be interesting to investigate the order-by-order behavior at large R_0^{-1}.

6.4 Summary of main results

Because of the attractive singular OPE, results are very cutoff dependent in WPC without the promotion of additional counterterms. In this chapter we have explained the fact that local regulators connect the LO counterterms with all higher partial waves. For a certain class of local regulators, these regulator artifacts can compensate the attractive tensor contributions from OPE and we find cutoff-independent results. However, we state explicitly that these results do not imply that WPC is renormalizable.

Conceptually, our results are very different from the results of NTvK. While NTvK restore renormalizability of chiral interactions at LO by adding additional counterterms in channels with attractive tensor interactions and then obtain cutoff-independent results, we have seen that the regulator artifacts for

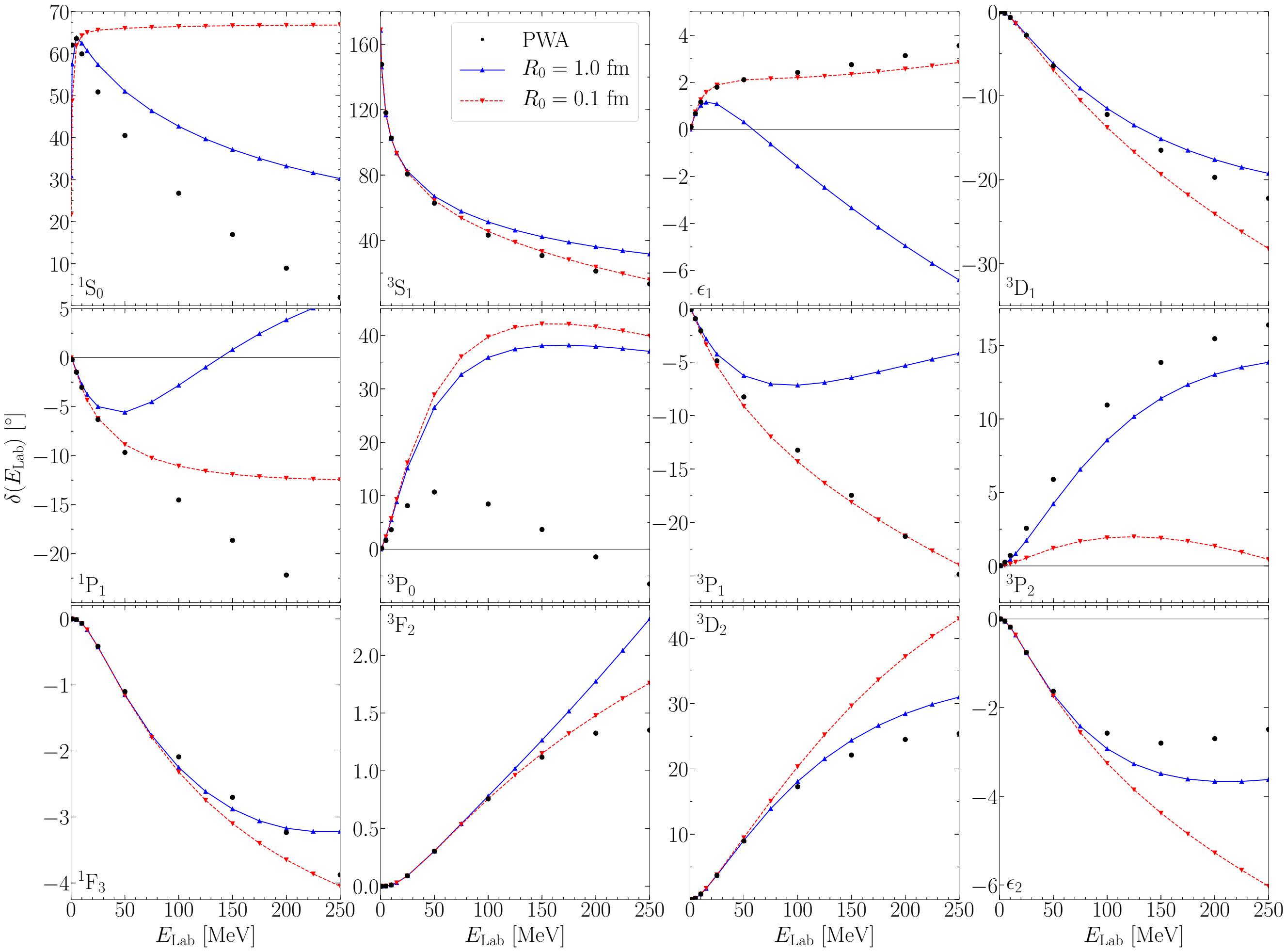

Figure 6.6.: Phase shifts in the $^1S_0$, $^3S_1$, ϵ_1, $^3D_1$, $^1P_1$, $^3P_{0,1,2}$, $^1F_3$, $^3F_2$, ϵ_2, and $^3D_2$ channels as function of the laboratory energy for the inverse cutoffs $R_0^{-1} = 1\,\mathrm{fm}^{-1}$ and $R_0^{-1} = 10\,\mathrm{fm}^{-1}$ for $n_1 = n_2 = n = 2$ in comparison to the PWA phase shifts.

local chiral interactions with the operator combination $(\mathbb{1},\ \sigma_{12})$ add additional repulsion to the same partial waves, which in turn leads to similar plateaus, see Fig. 6.3. However, the appearance of plateaus does not mean that our interactions are renormalizable.

Our findings are only possible for certain local regulators that are smooth functions. Furthermore, the appearance of plateaus is only possible because we require the interactions to remain on the branch for a single bound state. As we have explored before, in this case the width of the short-range regulator function decreases with R_0^{-1} but this is compensated by increasing values of the LECs. This results in a non-vanishing hard core which compensates the attraction from OPE in such a way that only one bound state can be accommodated.

The core is strong enough to counter the attraction in the $^3S_1 -^3 D_1$ channel (where it is strongest), and it is only natural that it is sufficiently strong to counter the attraction in higher partial waves, where we find no additional spurious bound states. This is another difference from the results of NTvK, where the introduction of additional counterterms does not eliminate the appearance of spurious bound states. If we instead allow for more bound states to appear in the $^3S_1$ channel, the values of the LECs decrease and the core is reduced in magnitude. Then, we also find a limit-cycle cutoff dependence behavior and additional counterterms need to be added in the attractive tensor channels, as NTvK found.

We remark, however, that if we would allow more bound states to enter, this would mean that the LECs $C_{ST}(R_0)$ have to jump from one bound-state branch to another bound-state branch. To our knowledge, in this case there is no clear prescription at which cutoff values these jumps have to occur, which introduces an additional ambiguity. Enforcing one bound state, on the other hand, is a reasonable and practical prescription for the construction of potentials that introduces no new ambiguity.

While the connection of the S-wave contact interactions with higher partial waves is purely a regulator artifact, such a connection can have a qualitative physical motivation. The LO counterterms in WPC absorb, among others, the effects of heavier mesons like the ρ or ω meson, which are integrated out in chiral EFT [202]. Such heavier mesons are responsible for the short-range NN repulsion and compensate the singular attraction of the OPE interaction, see also Ref. [199]. The exchange interactions for these mesons are local in the static limit and enter all partial waves, similarly to pion exchanges. Local regulators establish a similar connection of all partial waves.

For example, the central short-range repulsion in one-boson-exchange potentials originates from ω-meson exchange [5]. The exchange potential of a very heavy ω-like vector meson would be given by

$$\begin{aligned} V_\omega(m_\omega, r) \xrightarrow{m_\omega \gg m_N} \frac{e^{-M_\omega r}}{r} \Bigg\{ & \left(\mathbb{1} + \frac{1}{3}\sigma_{12} \right) \\ & - \frac{1}{6}\left(1 + \frac{3}{M_\omega r} + \frac{3}{(M_\omega r)^2} \right) S_{12}(\mathbf{r}) \Bigg\} , \end{aligned} \tag{6.7}$$

see, e.g., Eq. (F.8) in Ref. [5] with the mass of the meson m_ω and the nucleon mass m_N. In case of the local LO potential with the operator structure $(\mathbb{1}, \sigma_{12})$, we find that the operator LECs for larger cutoffs approach $C_{\mathbb{1}} = 3C_\sigma$, because $C_{01} = C_{\mathbb{1}} - 3C_\sigma \to 0$. Thus, a corresponding meson would need to have the leading operator structure $\sim \mathbb{1} + 1/3\sigma_{12}$, which is exactly the central part of an ω-like vector meson. We highlight this in the left panels of Fig. 6.2, where, in addition to the central chiral interactions, we also show the result for the ω-meson exchange. We find a behavior similar to the chiral interactions for larger cutoffs.

In conclusion we summarize our key findings below:

- We investigated the behavior of local chiral interactions in WPC when the coordinate-space cutoff is lowered. We have constructed LO interactions for cutoffs ranging from $R_0^{-1} = 0.8\ \mathrm{fm}^{-1}$ to $10.0\ \mathrm{fm}^{-1}$ for different choices of the regulator function and for different pairs of the LO operators in $\{\mathbb{1}, \sigma_{12}, \tau_{12}, \sigma_{12}\tau_{12}\}$. Our interactions were fit to reproduce the S-wave phase shifts from the Nijmegen PWA.
- We showed that for the operator combination $(\mathbb{1}, \sigma_{12})$, phase shifts in all partial waves as well as the deuteron binding energy converge to plateaus when we reduce the coordinate-space cutoff (i.e., increase the momentum-space cutoff), leading to cutoff-independent results. This is a consequence of the violated Fierz-rearrangement freedom, which we discussed in the previous chapter. For the operator choice $(\mathbb{1}, \sigma_{12})$, the LEC C_{10} in the $^3S_1$ channel is mixed into all attractive tensor channels with the same sign, providing sufficient repulsion in these channels.
- Using the artifacts of local regulators to our advantage, we constructed interactions that enable a cutoff-independent description of phase shifts. Comparing the phase-shift predictions for these hard-core interactions with phase shifts from the PWA, we found very good agreement.
- We want to stress, that these results do not imply that WPC is renormalizable. However, our findings may prove useful from a practical point of view, as they may allow to reduce regulator artifacts in many-body calculations. As described in Ref. [107], locally regularized three-nucleon forces are less repulsive those obtained with nonlocal regulators at typical cutoff scales. When lowering the $3N$ cutoff below the NN cutoff, collapses have been found in neutron matter. It will be interesting to see how the newly acquired hard NN interactions perform in those systems in the future. these issues.

7 Construction of valence-space Hamiltonians

We construct valence-space Hamiltonians for calculations in the nuclear shell model. The residual two-body interaction is based on symmetries and the low-momentum expansion from chiral effective field theory. In addition to the usual free-space contact interactions, we also include novel center-of-mass–dependent operators (introduced in Sec. 3.2). These operators arise due to the broken Galilean invariance by in-medium effects.

In this chapter, we start with the introduction of the shell-model framework. We then elaborate on the construction of valence-space Hamiltonians and explain the transformation to the harmonic-oscillator (HO) basis. After that, we introduce the data sets to which we fit the LECs and explain our fitting strategies to perform this task.

7.1 Calculations in the shell-model framework

The interacting shell model is based on the nuclear shell model by Mayer and Jensen [7–10]. It considers multi-nucleon configurations, where valence nucleons occupy several single-particle orbits and interact with each other. The first step in shell-model calculations is the selection of a model space. The model space is chosen in accordance to the nucleus/nuclei one aims to describe. A schematic drawing of the model space is shown in Fig. 7.1. The model space consists of a core (states in the blue rectangle), which is completely filled with neutrons and protons. In this case, the core is ^{16}O. In shell-model calculations, nucleons can not be excited out of the core. Above the core is the valence space (here: sd-valence space). The valence space is filled with neutrons and protons according to the nucleus at hand. A valence nucleon interacts via one-body interactions with a mean field (so-called single-particle energies), as well as with other valence-space nucleons via effective two- and many-body interactions. We consider only effective two-body interactions, as the implementation of residual three-body forces is more involved. However, in the future we aim to implement three-body forces in their normal ordered two-body approximation. Valence nucleons occupy the single-particle orbits in the valence space, but they cannot be excited out of the valence space into the external space (red rectangle) above. The external space is assumed to be unoccupied at all times. In Fig. 7.1, we depict three energy spacings. The first one, ΔE_{core} determines the single-particle energy (SPE) of the lowest single-particle orbit. The second one, ΔE_{vs}, is symbolic for the energy splitting in the valence space, and $\Delta E_{\text{ext.}}$ is the energy gap to the next major shell. For a small $\Delta E_{\text{ext.}}$, the given model space might not be sufficient for a reliable description of physical effects. For negative $\Delta E_{\text{ext.}}$, there is a shell inversion between the highest orbits of the valence space and the lowest orbits of the external space. One speaks of so-called islands of inversions [203–208], where those configurations contribute significantly.

The single-particle basis states can be generated with a one-body Hamiltonian. For that purpose, one typically uses a harmonic-oscillator (HO) potential, which is modified by an attractive spin-orbit force. The single-particle states have the following quantum numbers:

- orbital angular momentum $\mathbf{l}$,
- single-particle spin $\mathbf{s}$ (with $\langle \mathbf{s} \rangle = 1/2$ for nucleons),
- angular momentum $\mathbf{j} = \mathbf{l} + \mathbf{s}$,
- projection of $\mathbf{j}$ on the z-axis: m,
- nodal quantum number n.

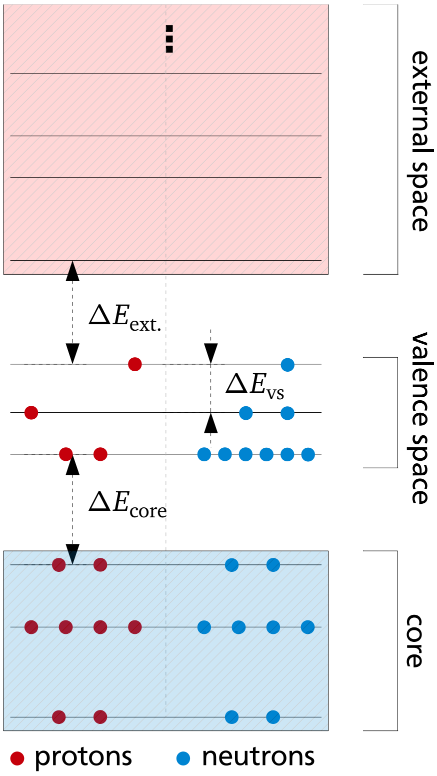

Figure 7.1.: Schematic drawing of a model space for the nuclear shell model (energies are not to scale). The figure shows the three spaces: core, valence space (vs), and external space (ext.). Protons and neutrons are depicted by red and blue circles respectively. See text for more details.

Here we denote single-particle orbits as nl_j, where we use the spectral notation from Tab. 2.5 for l. The principal quantum number N is obtained via $N = 2n + l$. All single-particle orbits with equal N have the same HO energy, which reads

$$E_{\mathrm{HO}} = \hbar\omega\left(N + \frac{3}{2}\right), \tag{7.1}$$

with the oscillator frequency $\hbar\omega$. An estimate of this frequency is given by

$$\hbar\omega \approx \left(45A^{-\frac{1}{3}} - 25A^{-\frac{2}{3}}\right)\ \mathrm{MeV}, \tag{7.2}$$

with the mass number A. In shell-model calculations, the oscillator frequency is typically adjusted to the core nucleus' radius. One usually applies a scaling factor proportional to $((A_{\mathrm{core}} + 2)/A)^{\frac{1}{3}}$ to correct this setting for matrix elements of larger nuclei. As mentioned before, single-particle orbits with the same HO energy form major shells. They are depicted in Fig. 7.2. Note that we use the nodal quantum number n to label the single-particle orbits, hence, our counting starts with $0s_{1/2}$ in the lowest s shell. Filled shells (and subshells for the $0f_{7/2}$, $0g_{9/2}$, $0h_{11/2}$ orbits and so on) lead to the nuclear magic numbers, which are denoted on the right side of the figure. The p shell is located with the two single-particle orbits $0p_{3/2}$ and $0p_{1/2}$ above the s shell. The completely filled p shell is an ^{16}O nucleus, which is the core for calculations in the sd shell on top of the p shell. The sd shell contains the $0d_{5/2}$, $1s_{1/2}$, and $0d_{3/2}$ orbits. At last we want to mention the pf shell, which contains the $0f_{7/2}$, $1p_{3/2}$, $0f_{5/2}$, and $1p_{1/2}$ subshells. As indicated in the figure, the $0f_{7/2}$ orbit is lower in energy compared to the remaining pf-shell orbits, thus, it forms the magic number 28 for a closed $0f_{7/2}$ subshell. Further shells are given in the figure.

After selecting the model space, we need to express the operators from chiral EFT in the resulting basis. The effective Hamiltonian is a sum of SPEs and two-body matrix elements (TBMEs), which describe

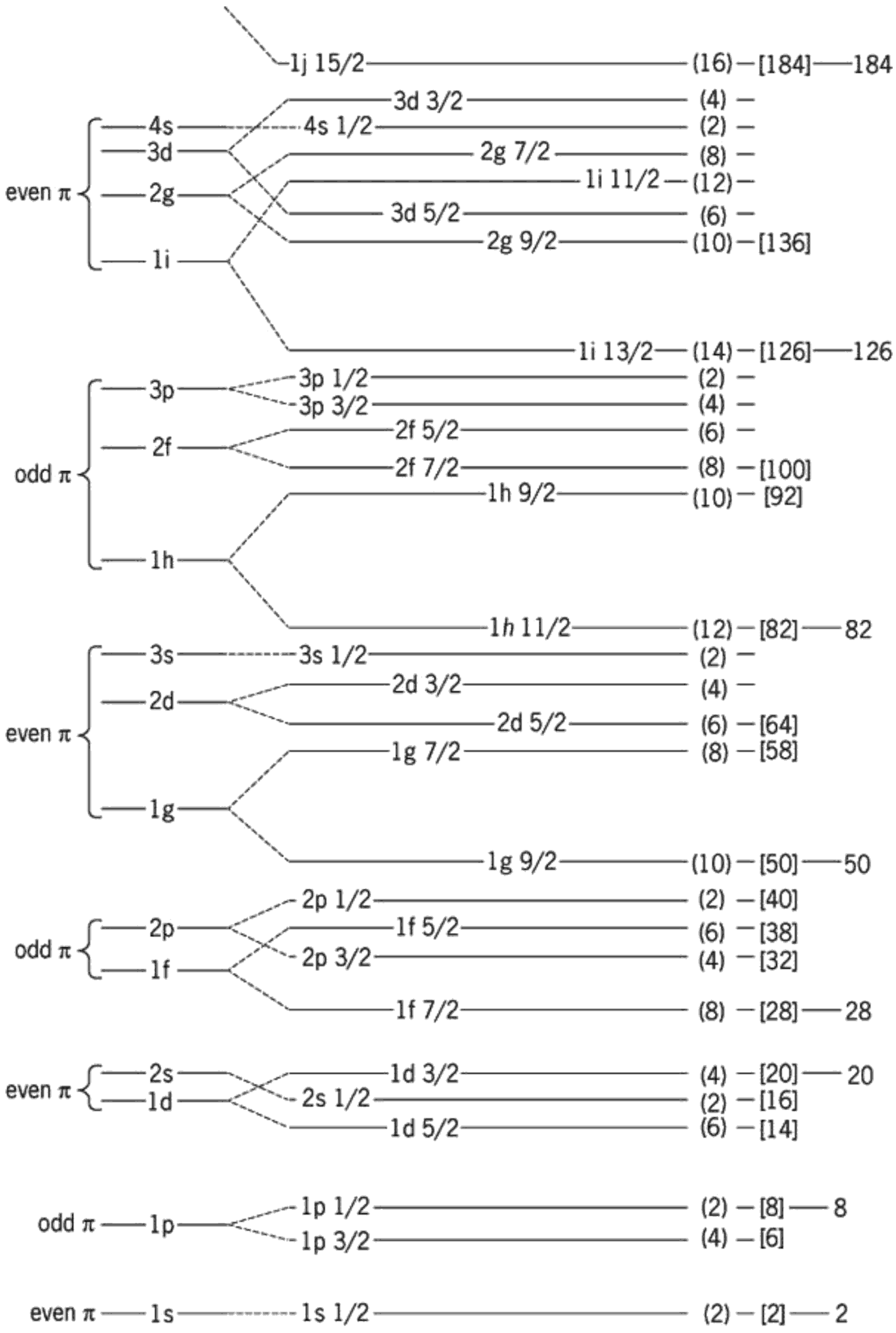

Figure 7.2.: Approximate level pattern for single-particle orbits derived from the shell model taken from Ref. [209]. The figure shows the parity π of a given orbit, the quantum numbers $(n+1)l$, with the nodal quantum number n (different from the notation nl that we use in this thesis), and the spin-orbit splitting in j. Round parenthesis (2), (4), and so on, denote the level degeneracy. Square parenthesis [2], [6], and so on, denote the total occupation number. Magic numbers at 2, 8, 20, 28, 50, and so on, are given on the right.

the residual interaction among two valence nucleons. In this work, the latter are obtained from chiral EFT. Two-body matrix elements contribute to nuclei with $A \geq 18$ ($A = 16$ core plus at least two nucleons). As mentioned above, we apply a scaling factor of $(18/A)^{1/3}$ to the TBMEs to correct the HO frequency for larger nuclei. More details about the valence-space interaction and on the transformation to the HO basis follow in the next section.

Figure 7.1 shows one possible configuration out of many that need to be considered in the construction of the effective Hamiltonian. Formally, an A-body wave function can be constructed from the single-particle wave functions $\phi_i(x_j)$ with Slater Determinants

$$\Psi(x_1, x_2, \cdots, x_A) = \frac{1}{\sqrt{A!}} \det \begin{vmatrix} \phi_1(x_1) & \phi_1(x_2) & \cdots & \phi_1(x_A) \\ \phi_2(x_1) & \phi_2(x_2) & \cdots & \phi_2(x_A) \\ \vdots & \vdots & \ddots & \vdots \\ \phi_A(x_1) & \phi_A(x_2) & \cdots & \phi_A(x_A) \end{vmatrix}, \tag{7.3}$$

where $\phi_i(x_j)$ is the single-particle orbit i, occupied by particle j.

Eigenstates and energies are obtained by diagonalizing the Hamiltonian. Even though matrix dimensions can be reduced by making use of symmetries, e.g., by using the m-scheme (see, e.g., Ref. [210]), they grow fast depending on the number of valence nucleons. Without using symmetries, the dimension is approximately given by the binomial coefficients

$$\dim(\mathrm{H}) \sim \binom{N_{\mathrm{vs}}}{n_{\mathrm{vs}}} \binom{Z_{\mathrm{vs}}}{z_{\mathrm{vs}}}, \tag{7.4}$$

with N_{vs} (Z_{vs}) possible spaces for neutrons (protons) in the valence space and n_{vs} (z_{vs}) neutrons (protons) in the valence space. Consequently, conventional solver algorithms exceed their range of applicability. Thus, one relies on efficient solving routines, which typically implement the Lanczos algorithm(1). In this work, we perform diagonalizations with the ANTOINE shell-model code from Refs. [116, 211]. The theoretical energies that we obtain from this code are used to adjust the LECs to experiment. More details follow in Sec. 7.6.

7.2 Valence-space interactions

In free space, following Weinberg's power counting [23, 24], there are two LECs at LO, seven new LECs at NLO, and 15 new LECs at N^{3}LO. The contact interactions at LO, NLO, and N^{3}LO are given in Eq. (2.59), Eq. (2.61) and Eq. (2.64) respectively.

The short-range contacts absorb all contributions that cannot be resolved in the EFT framework. They must be determined by fits to experimental data. For the chiral shell-model interactions, we fit the LECs directly to data in the valence space. In the valence space, the presence of the core breaks Galilean invariance, and therefore novel short-range operators appear that depend on the two-body center-of-mass (CM) quantum numbers, as discussed in Ch. 3 (see also Ref. [172, 173]). We call those operators valence-space operators. First contributions of the valence-space operators appear at NLO, subleading contributions enter at N^{3}LO. The operators are presented in Eq. (3.8) at NLO and in Eq. (3.14) at N^{3}LO. At NLO the valence-space LECs are labeled P_1–P_5, at N^{3}LO we label them Q_1–Q_{32}. General notes on the partial-wave decomposition of all operators are presented in App. B. The method described there uses

---

(1) The Lanczos algorithm is commonly used in the process of diagonalizing large scale Hermitian matrices. It is an iterative method to transform any Hermitian matrix into a Hermitian tri-diagonal matrix, which is then much faster to solve for eigenvalues compared to the initial matrix.

(mathematical) tensor operators as a starting point. The tensor-operator representation of all operators we consider is given in App. C.1 for operators at LO, App. C.2 for operators at NLO, and App. C.3 for operators at N^{3}LO.

Long-range contributions from the pion-exchange interactions are not renormalized in the medium. We take the long-range pion-exchange contributions directly from the free-space nuclear forces [26, 27], with the pion-nucleon LECs given in Tab. 2.4.

The resulting interaction is similar as in the chapters before, with short-range contact interactions that are adjusted to experiment and long- and intermediate-range contributions from pion physics.

7.2.1 Transformation to HO basis and regulators

In order to apply the momentum-space interactions in the valence space, we transform them to antisymmetrized, normalized two-body HO states. As detailed in App. D, this leads to two-body matrix elements (TBMEs) of the form

$$\langle (n_1 l_1 j_1)(n_2 l_2 j_2) J T | V | (n_1' l_1' j_1')(n_2' l_2' j_2') J T \rangle \,, \tag{7.5}$$

where (n_i, l_i, j_i) are the single-particle radial, orbital angular momentum, and total angular momentum quantum numbers, and J, T are the two-body total angular momentum and isospin, respectively.

The radial HO wave functions are given by

$$R_{nl}(p) = N_{nl}\,(pb)^l \exp\Big[-\frac{1}{2}(pb)^2\Big] L_n^{l+\frac{1}{2}}\Big((pb)^2\Big) \,, \tag{7.6}$$

and are plotted in Fig. 7.3 for different n, l quantum numbers relevant for sd-shell TBMEs. The oscillator length $b = \sqrt{\hbar/(m\omega)}$, with $\hbar\omega = 13.53$ MeV(2) is chosen to reproduce the radius of the ^{16}O core. For completeness, the normalization is $N_{nl} = b^{3/2}\sqrt{2n!/\Gamma(n+l+3/2)}$ and $L_n^{l+\frac{1}{2}}$ are generalized Laguerre polynomials.

Figure 7.3 shows that the radial wave functions involved in a limited valence space automatically cutoff the high-momentum parts, and therefore no additional momentum-space regulator functions are necessary. In fact, one can naively estimate the cutoff in energy due to the basis truncation by

$$\frac{\Lambda^2_{\text{naive}}}{m_N} \sim E \leqslant \varepsilon_1 + \varepsilon_2 = 2(N_{\text{valence}} + 3/2)\hbar\omega \,. \tag{7.7}$$

For the sd shell it follows that $\Lambda_{\text{naive}} \approx 300\,\text{MeV}$. A more sophisticated estimate is given in Ref. [212] leading to a cutoff estimate for the sd shell $\Lambda_{\text{HO}} \approx 375\,\text{MeV}$. In Fig. 7.3, we also compare the radial wave functions relevant for sd-shell TBMEs with commonly used regulators from chiral EFT with the two cutoff estimates described above. We observe that the radial wave functions indeed have a similar behavior in the high-momentum part as the regulator function with $\Lambda_{\text{HO}} = 375\,\text{MeV}$. Hence, there is no necessity for additional momentum-space regulator functions for the contact interactions.

7.3 Coulomb corrections

Before we regard the nuclear data set to which we fit our parameters, we need to consider Coulomb corrections as we only describe the strong interaction with our Hamiltonian. Consequently, we need to subtract the Coulomb part from experimental ground-state energies from Refs. [105, 213]. As excited states are given as a difference to the ground-state energy, the Coulomb part is (in first approximation)

---

(2) Using the estimate from Eq. (7.2) yields 13.91 MeV for ^{16}O.

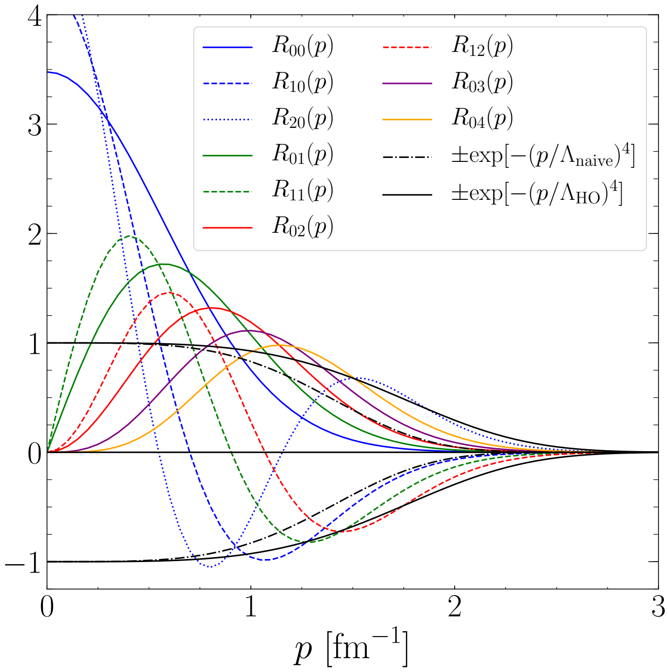

Figure 7.3.: Radial wave functions relevant for sd-shell TBMEs in comparison to typical regulators used in chiral EFT with the naive cutoff estimate $\Lambda_{\text{naive}} = 300\,\text{MeV}$ and $\Lambda_{\text{HO}} = 375\,\text{MeV}$. See text for details.

automatically subtracted there.

In order to estimate the size of the Coulomb contribution in the ground state, one typically uses a model to obtain the energy for a given nucleus. We consider two different models for Coulomb corrections. In our first approach in Ch. 8 we apply the Coulomb correction from Ref. [114] and W. Chung Ph. D. thesis, Michigan State University (not publicly available). This correction scheme depends only on the proton number Z. We refer to this correction as CH.

In Ch. 9 and Ch. 10 we take a different approach. We use the Coulomb correction from the Duflo and Zuker (DZ) mass formula [214], which is given by

$$E_C^{\text{DZ}}(N,Z) = a_C \frac{-Z(Z+1) + 0.76\,[Z(Z-1)]^{2/3}}{A^{1/3}\left[1-\left(\frac{T}{A}\right)^2\right]} \tag{7.8}$$

with the constant $a_C = 0.7043$ MeV and $T = \frac{|Z-N|}{2}$. The Coulomb correction in the shell model is obtained by taking the difference with respect to the core

$$E_C(N,Z) = E_C^{\text{DZ}}(N,Z) - E_C^{\text{DZ}}(N_{\text{core}}, Z_{\text{core}})\,, \tag{7.9}$$

with the number of core neutrons and core protons, N_{core} and Z_{core} respectively. In contrast to the CH correction, the DZ Coulomb correction depends on the proton number and the neutron number.

We list the evaluated DZ correction in the sd shell w.r.t. the ^{16}O core at $N = Z$, which we label DZ(Z) and $N = 20$, labeled as DZ(20), where the latter marks the limit in the sd shell. We compare those values to the CH Coulomb correction in Tab. 7.1. There, one can see that the DZ correction at $N = Z$ is slightly smaller than the CH correction in absolute value. In fluorine, the relative difference between the DZ and CH correction schemes is around 6% and it increases to roughly 12% up to potassium. The DZ Coulomb correction shrinks in absolute value with an increasing neutron number. The difference is more pronounced for large differences $|Z-N|$. At the neutron edge of the sd shell, i.e., $N = 20$, the relative difference in fluorine for the DZ(20) over the DZ($N = Z$) correction is larger than 50%. In potassium, the difference is only about 1%.

Table 7.1.: Coulomb corrections for sd-shell nuclei. We compare the DZ correction from Eq. (7.9) at $N = Z$ (DZ(Z)) and at $N = 20$ (DZ(20)) to the Coulomb correction from Ref. [114] (CH). The latter does not depend on the neutron number N. All Coulomb energies are given in MeV, with respect to the ^{16}O core.

Nuclei	O	F	Ne	Na	Mg	Al	Si	P	S	Cl	Ar	K
DZ(Z)	0.00	-3.27	-6.85	-10.72	-14.88	-19.31	-24.01	-28.97	-34.19	-39.65	-45.37	-51.32
DZ(20)	1.63	-1.45	-4.88	-8.65	-12.76	-17.21	-21.99	-27.09	-32.53	-38.29	-44.37	-50.78
CH	0.00	-3.48	-7.45	-11.73	-16.47	-21.48	-26.78	-32.47	-38.46	-44.74	-51.31	-58.14

7.4 Data sets

We adjust our shell-model interactions to ground-state energies from Refs. [105, 213] and excitation energies from Ref. [215] of nuclei in the valence space. It is important to exclude so-called intruder and extruder states, which are excitations from the core to the valence space or from the valence space to the external space (see Fig. 7.1)(3). In the sd shell, it is easy to detect one-body intruder states, as all states in the sd shell have positive parity. A single-particle intruder or extruder state leads to a negative parity. However, two-body intruder states do not change the parity and cannot be detected this way. Intruder states can appear, especially in states in the vicinity of the core (in terms of number of neutrons and protons). As we mentioned above, in the neutron-rich region the single-particle orbits in the external space are lowered in their energy which can even lead to shell inversions. Those regions are susceptible to extruder states. With this, we want to stress that the determination of the right data set is nontrivial, and one can not naively take all known experimental states in account.

Thankfully, B. A. Brown communicated the data set from Ref. [114] to us. Starting from this, we construct the data sets BR$_1$ and BR$_2$ in Tab. 7.2, to which we adjust our interactions in the sd shell. The original set considers 608 states in 77 nuclei in the sd shell. We do not use all states from the original data set from Ref. [114] for several reasons which we name in the following.

First, the ANTOINE shell-model code [211] shows problems when too many states are considered in a single nucleus. This manifests in low-lying artifacts in the excitation spectrum. One can see this in Fig. 7.4, where we show excitations of ^{28}Si. States that are considered in the fit are colored black, while others are colored red. The fit data set used there only considers a single $J^\pi = 2^+$ state, which is the lowest experimental state in the figure. As one can see, this state is well reproduced by the interactions in green, yellow, and blue (more details follow in the coming chapters). When we include further 2^+ states for predictions, we see that at some point a low-lying 2^+ state appears in the theoretical spectrum (annotated as "artifact" in the figure). The ANTOINE code is programmed in a way that it returns the lowest states in energy. Several identical J^π, are ordered with increasing energy. This means that if we only consider a single 2^+ state, one can be sure that this is energetically the lowest 2^+ state in the spectrum. Adding further states with this J^π should return states that increase in energy. Hence, the artifact in the spectrum is not of physical nature, but of numerical origin in the ANTOINE code. Reducing the number of states to a maximum of thirteen states per isotope (as in our data sets BR$_1$ and BR$_2$ from Tab. 7.2) reduces the risk of such spurious states greatly.

Second, we updated the experimental energies to recent data. When we first started with our shell model fits, the most recent database for experimental binding energies was the Atomic Mass Evaluation 2012 (AME12) [213]. In Chapter 8, we use the BR$_1$ data set from Tab. 7.2 with experimental ground-state energies from the AME12. The BR$_2$ data set which we use in Ch. 9 uses the more recent states from the

---

(3) Shell-model states are a superposition of several configurations. An intruder/extruder is not necessarily a purely spurious state, but it is contaminated by those excitations described here.

Table 7.2.: Datasets used to constrain the valence-space interaction. From left to right, we list the labels of the data-set, the active orbits for neutrons (n) and protons (p), the Coulomb correction model (see Tab. 7.1), the total number of the considered nuclei and the total number of the considered states. Further descriptions are given below.

Label	n orbits	p orbits	Coulomb	Nuclei	States
$\mathrm{BR}_1^{(a)}$	$0d_{5/2}$, $1s_{1/2}$, $0d_{3/2}$	$0d_{5/2}$, $1s_{1/2}$, $0d_{3/2}$	CH	77	441
$\mathrm{BR}_2^{(b)}$	$0d_{5/2}$, $1s_{1/2}$, $0d_{3/2}$	$0d_{5/2}$, $1s_{1/2}$, $0d_{3/2}$	DZ	77	451
SDF16$^{(c)}$	$(0d_{5/2})$, $1s_{1/2}$, $0d_{3/2}$, $0f_{7/2}$	$0d_{5/2}$, $1s_{1/2}$, $0d_{3/2}$	DZ	122	475

$^{(a)}$ This is the sd-shell data set from Ref. [114]. We corrected the ground-state energies according to the AME12 [213] data. The original set contains 608 states. Our set allows for a maximum of thirteen states per isotope and a maximum excitation energy of 10 MeV. In addition, we removed outdated data in accordance with the NNDC [215] database. A visualization of this data set is given in Fig. 8.1.

$^{(b)}$ Similar to $^{(a)}$ but with a maximum excitation energy of 15 MeV and ground-state energies from the AME16 [105]. We only use excited states that are in the data set from Ref. [114] and the NNDC data base simultaneously. The data set is visualized in Fig. 7.5.

$^{(c)}$ Data set for cross-shell interactions. Calculations are done on top of an ^{16}O core, but excitations out of the neutron $0d_{5/2}$ orbit are forbidden, which we indicate with the round parentheses around it $(0d_{5/2})$. The data set is visualized in Fig. 10.3.

AME16 [105]. Excited states are updated according to the NNDC database [215]. We remove some of the excited states with ambiguously defined J^π values. Third, we limit the maximum excitation energy to 10 MeV in the BR_1 set, and 15 MeV in the BR_2 set.

We use the Coulomb energy correction used in Ref. [114] (CH) for the BR_1 data set, and the Duflo-Zuker (DZ) Coulomb energy [214], given in Eq. (7.8) for the BR_2 data set.

The BR_1 set is closer related to the original data set from Ref. [114]. The BR_2 data set is still very much related to the original set, however more states have been removed so that it is in better agreement with the NNDC database. Furthermore, we show the SDF16 data set in Tab. 7.2, to which we adjust the cross-shell interactions from Ch. 10.

7.5 Uncertainty estimates

The EFT enables estimates of the theoretical uncertainty due to the truncation of the chiral expansion. We explore these uncertainties here after the chiral shell-model interactions have been fit. In future works we will explore the chiral uncertainties during the optimization. We emphasize that these theoretical uncertainties do not include the systematic uncertainties from the shell-model basis or from possible states that have a small overlap with sd-shell configurations.

For the ground-state energies, we directly apply the chiral EFT uncertainty estimate from Ref. [30]. These are obtained at LO and NLO using

$$\Delta E^{\mathrm{gs}}_{\mathrm{LO}} = |E^{\mathrm{gs}}_{\mathrm{LO}} - E^{\mathrm{gs}}_{^{16}\mathrm{O}}| Q^2 , \tag{7.10}$$

$$\Delta E^{\mathrm{gs}}_{\mathrm{NLO}} = \max\big(|E^{\mathrm{gs}}_{\mathrm{LO}} - E^{\mathrm{gs}}_{^{16}\mathrm{O}}| Q^3 , |E^{\mathrm{gs}}_{\mathrm{LO}} - E^{\mathrm{gs}}_{\mathrm{NLO}}| Q\big) , \tag{7.11}$$

and at higher orders $\nu > 2$ using

$$\Delta E^{\mathrm{gs}}_{\nu} = \max\big(\Delta E^{\mathrm{gs}}_{\nu-1}, |E^{\mathrm{gs}}_{\nu-1} - E^{\mathrm{gs}}_{\nu}|\big)\, Q , \tag{7.12}$$

where $Q = m_\pi/\Lambda_b$. For ground-state energies of medium-mass nuclei, the former is set by the pion mass m_π, and we take $\Lambda_b = \Lambda_{\mathrm{HO}} = 375$ MeV.

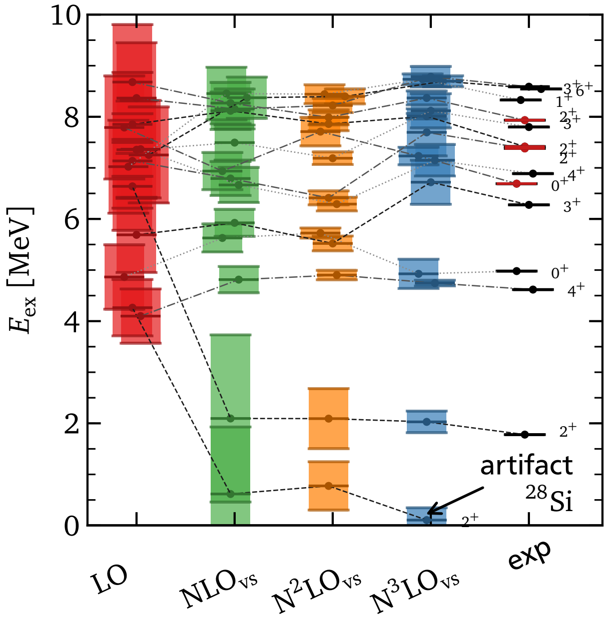

Figure 7.4.: Excitation spectrum of ^{28}Si for charge-dependent shell-model interactions fit to the BR$_2$ data set at LO, NLO$_{\mathrm{vs}}$, N^{2}LO$_{\mathrm{vs}}$, and N^{3}LO$_{\mathrm{vs}}$. The results are compared to the NNDC data base from Ref. [215]. Experimental states that are not considered in the BR$_2$ data set are colored red. The first 2^+ state is an artifact that appears in the ANTOINE code if too many states with the same J^π value are present in the data set.

For excitation energies, the uncertainty estimates are more challenging. In Ch. 8, we only fit two parameters at LO, which is not enough for a decent reproduction of the data set BR$_1$. Because the excitation energies in medium-mass nuclei are small compared to the total energy scale, and because the LO interaction performs poorly in most nuclei (as expected with only two LECs), the theoretical uncertainty would be dominated by the large difference $|E^{\mathrm{ex}}_{\mathrm{LO}} - E^{\mathrm{ex}}_{\mathrm{NLO}}|$, if we were to follow the same prescription for the excited states as for the ground-state energies above. We therefore adopt the following to estimate the uncertainties for the excitation energies

$$\Delta E^{\mathrm{ex}}_{\mathrm{LO}} = \max\big(E^{\mathrm{av}}_{sd}, |E^{\mathrm{ex}}_{\mathrm{LO}}|\big)\, Q^2\,, \tag{7.13}$$

$$\Delta E^{\mathrm{ex}}_{\mathrm{NLO}} = \max\big(E^{\mathrm{av}}_{sd}, |E^{\mathrm{ex}}_{\mathrm{NLO}}|\big)\, Q^3\,, \tag{7.14}$$

where we have introduced the scale $E^{\mathrm{av}}_{sd} = 3$ MeV, which is taken to be approximately the average of the splittings between the sd-shell orbitals. This scale sets the natural scale for excitations in the sd shell. In Ch. 9, we adjust two additional charge-dependent LECs, as well as three neutron and three proton single-particle energies already at LO. This improves the LO interaction and the description is good enough to use the following uncertainties for excitation energies

$$\Delta E^{\mathrm{ex}}_{\mathrm{LO}} = |E^{\mathrm{ex}}_{\mathrm{LO}}|\, Q^2\,, \tag{7.15}$$

$$\Delta E^{\mathrm{ex}}_{\mathrm{NLO}} = \max\big(|E^{\mathrm{ex}}_{\mathrm{LO}}| Q^3, |E^{\mathrm{ex}}_{\mathrm{LO}} - E^{\mathrm{ex}}_{\mathrm{NLO}}| Q\big)\,, \tag{7.16}$$

and at higher orders $\nu > 2$ we use

$$\Delta E^{\mathrm{ex}}_{\nu} = \max\big(\Delta E^{\mathrm{ex}}_{\nu-1}, |E^{\mathrm{ex}}_{\nu-1} - E^{\mathrm{ex}}_{\nu}|\big)\, Q\,, \tag{7.17}$$

where we do not need to introduce the scale E^{av}_{sd}.

7.6 Fitting strategies

With the operators, Coulomb corrections, the experimental data set and the shell-model code all in place, the next step is to determine the LECs. As mentioned earlier, we use the ANTOINE shell-model code from Refs. [116, 211]. For a given parameter set $\mathbf{x} = \{x_i\}$, the shell-model code returns the expectation value of the Hamiltonian. For a given state k in the data-set the expectation value reads

$$\langle \boldsymbol{H}(\mathbf{x})\rangle_k = E_k^{\mathrm{th}}(\mathbf{x}) = \sum_{i\in\mathrm{SP\ orbits}} \varepsilon_i \langle \boldsymbol{n}_i\rangle_k + \sum_{i\in\#\mathrm{LECs}} c_i \langle \boldsymbol{V}_i^{\mathrm{cont}}\rangle_k + \langle \boldsymbol{V}^{\pi}\rangle_k \,, \tag{7.18}$$

where $\langle\bullet\rangle_k$ is a short-hand notation for the expectation value with respect to the k-th state in the data set, ε_i are the single-particle (SP) energies and n_i is the number operator for the spherical orbits. Furthermore, c_i are the LECs (C_S, C_T, C_1 and so on), which accompany the contact interaction followed by all pion-exchange contributions, which we do not fit. The parameters x_i are either a SPE or a LEC.

7.6.1 χ^2-Optimization

We try to find an optimal description of the experimental data set by means of χ^2 minimization. The χ^2 value is calculated as

$$\chi^2 = \sum_{k=1}^{N} \chi_k^2(\mathbf{x}), \tag{7.19}$$

where the sum runs over all N states in the data set, and $\chi_k^2(\mathbf{x})$ is given by

$$\chi_k^2(\mathbf{x}) = \left(\frac{E_k^{\mathrm{exp}} - E_k^{\mathrm{th}}(\mathbf{x})}{\sigma_k(\mathbf{x})}\right)^2 , \tag{7.20}$$

with the experimental energy of state k, E_k^{exp}, the theoretical energy $E_k^{\mathrm{th}}(\mathbf{x})$, which we defined in Eq. (7.18), and the total uncertainty $\sigma_k(\mathbf{x})$. The uncertainty relates to the experimental and theoretical uncertainty via

$$(\sigma_k(\mathbf{x}))^2 = (\sigma_k^{\mathrm{exp}})^2 + (\sigma_k^{\mathrm{th}}(\mathbf{x}))^2 . \tag{7.21}$$

In the following, we drop the dependence on $\mathbf{x}$ for brevity. We try to find an optimal solution by setting the derivative of χ^2 with respect to the parameters to zero. For χ_k^2 we find

$$\frac{\partial \chi_k^2}{\partial x_i} = -2\frac{E_k^{\mathrm{exp}} - E_k^{\mathrm{th}}}{\sigma_k^2}\left[\frac{\partial E_k^{\mathrm{th}}}{\partial x_i} + \frac{E_k^{\mathrm{exp}} - E_k^{\mathrm{th}}}{\sigma_k}\frac{\partial \sigma_k}{\partial x_i}\right]. \tag{7.22}$$

We obtain the derivative $\frac{\partial E_k^{\mathrm{th}}}{\partial x_i}$ with the Hellmann-Feynman theorem

$$\frac{\partial E_k^{\mathrm{th}}}{\partial x_i} = \left\langle \frac{\partial \boldsymbol{H}}{\partial x_i}\right\rangle_k = \langle \boldsymbol{V}_i\rangle_k \,, \tag{7.23}$$

where $\boldsymbol{V}_i$ is either $\boldsymbol{V}_i^{\mathrm{cont}}$ or $\boldsymbol{n}_i$, depending on whether x_i is a LEC or a SPE. For the derivative of σ_k we obtain

$$\frac{\partial \sigma_k}{\partial x_i} = \frac{\sigma_k^{\mathrm{th}}}{\sigma_k}\frac{\partial \sigma_k^{\mathrm{th}}}{\partial x_i} . \tag{7.24}$$

The second derivative of χ_k^2, which we need to construct Hessian matrices, can be obtained similarly

$$\begin{aligned}\frac{\partial^2 \chi_k^2}{\partial x_i \partial x_j} = & \frac{2}{\sigma_k^4}\Bigg\{3(E_k^{\mathrm{exp}}-E_k^{\mathrm{th}})\left(\frac{\partial \sigma_k}{\partial x_i}\right)\left(\frac{\partial \sigma_k}{\partial x_j}\right)+\sigma_k^2\left[\left(\frac{\partial E_k^{\mathrm{th}}}{\partial x_i}\right)\left(\frac{\partial E_k^{\mathrm{th}}}{\partial x_j}\right)-(E_k^{\mathrm{exp}}-E_k^{\mathrm{th}})\frac{\partial^2 E_k^{\mathrm{th}}}{\partial x_i \partial x_j}\right] \\ & +(E_k^{\mathrm{exp}}-E_k^{\mathrm{th}})\sigma_k\left[2\left(\left(\frac{\partial \sigma_k}{\partial x_i}\right)\left(\frac{\partial E_k^{\mathrm{th}}}{\partial x_j}\right)+\left(\frac{\partial E_k^{\mathrm{th}}}{\partial x_i}\right)\left(\frac{\partial \sigma_k}{\partial x_j}\right)\right)-(E_k^{\mathrm{exp}}-E_k^{\mathrm{th}})\frac{\partial^2 \sigma_k}{\partial x_i \partial x_j}\right]\Bigg\} . \end{aligned} \tag{7.25}$$

For our setup the second derivative of E_k^{th} in the first line is zero. The derivative of χ^2 can be obtained by

$$\frac{\partial \chi^2}{\partial x_i} = \sum_{k=1}^{N} \frac{\partial \chi_k^2}{\partial x_i} . \tag{7.26}$$

With Eqs. (7.22 - 7.26), it is easy to construct the gradient, the Jacobian matrix, and the Hessian matrix. Below, we give the formulas for gradients, Jacobians and Hessians for a data set with N entries and p parameters.

- **Gradient**

  $$\nabla \chi^2 = \left(\frac{\partial \chi^2}{\partial x_1}, \frac{\partial \chi^2}{\partial x_2}, \cdots, \frac{\partial \chi^2}{\partial x_p}\right)^T \tag{7.27}$$

  The gradient returns a vector with length p, which points into the direction of the steepest ascent from a given point in the parameter space. The gradient is, for example, used in the BFGS algorithm [188].

- **Jacobian and Hessian matrix**
  The Jacobian matrix is obtained as

  $$\mathscr{J} = \begin{pmatrix} \frac{\partial \chi_1^2}{\partial x_1} & \frac{\partial \chi_1^2}{\partial x_2} & \cdots & \frac{\partial \chi_1^2}{\partial x_p} \\ \frac{\partial \chi_2^2}{\partial x_1} & \frac{\partial \chi_2^2}{\partial x_2} & \cdots & \frac{\partial \chi_2^2}{\partial x_p} \\ \vdots & \vdots & \ddots & \vdots \\ \frac{\partial \chi_N^2}{\partial x_1} & \frac{\partial \chi_N^2}{\partial x_2} & \cdots & \frac{\partial \chi_N^2}{\partial x_p} \end{pmatrix} , \tag{7.28}$$

  which results in a matrix with dimension $N \times p$. The Hessian matrix reads

  $$\mathscr{H} = \begin{pmatrix} \frac{\partial^2 \chi^2}{\partial x_1 \partial x_1} & \frac{\partial^2 \chi^2}{\partial x_1 \partial x_2} & \cdots & \frac{\partial^2 \chi^2}{\partial x_1 \partial x_p} \\ \frac{\partial^2 \chi^2}{\partial x_2 \partial x_1} & \frac{\partial^2 \chi^2}{\partial x_2 \partial x_2} & \cdots & \frac{\partial^2 \chi^2}{\partial x_2 \partial x_p} \\ \vdots & \vdots & \ddots & \vdots \\ \frac{\partial^2 \chi^2}{\partial x_p \partial x_1} & \frac{\partial^2 \chi^2}{\partial x_p \partial x_2} & \cdots & \frac{\partial^2 \chi^2}{\partial x_p \partial x_p} \end{pmatrix} , \tag{7.29}$$

  and is a square matrix with dimension $p \times p$. Both, the Jacobian and Hessian are used for example in the Levenberg-Marquardt algorithm see, e.g., Ref. [216].

Remarks

We found that the inclusion of the theoretical uncertainty from the EFT in the χ^2 value leads to unstable results in many cases. Calculations are more stable when we use well defined starting values. Finding those starting values becomes more difficult for a larger number of parameters. One way to do this is to take derivative-free algorithms to determine starting values like, e.g., the Nelder-Mead algorithm [217] or the POUNDerS algorithm [218, 219]. However, the convergence speed of such algorithms is reduced compared to, e.g., the Levenberg-Marquard algorithm. The applicability of those algorithms to large parameter-spaces, as we have them at N^{3}LO is however limited, as the convergence speed decreases rapidly. We want to stress the importance of fast converging algorithms for our purpose. In Fig. 7.5, we show the BR$_2$ dataset, which is representative for a shell-model fit in the sd-valence space. Each square in the figure represents an isotope in the data set and the numbers in the square show the number of considered states in each nucleus. The color coding shows the time it takes to diagonalize the corresponding Hamiltonians with the ANTOINE shell-model code (the time is given for a single-core calculation on a desktop pc). The matrix dimension of the Hamiltonian grows according to the binomial coefficient, given in Eq. (7.4). This reflects on the computational time to diagonalize the corresponding matrix, as one can see in Fig. 7.5. Besides the dimension, the number of states as well as the number of different angular momenta J^π factor into the computational time. The ANTOINE code is a single thread algorithm, which means that we can split calculations for different nuclei among several threads. Consequently, the maximum duration for a single nucleus limits the minimal duration of one iteration for the complete data set. In this example, the minimal duration for one iteration is of the order of six minutes. For calculations beyond the sd shell, this time increases rapidly. Thus, fast converging, stable methods are essential for our purposes.

A reliable method is used in Ref. [114]. The linear-combination method (LCM), which was first proposed in Ref. [220]. It converges for our applications in fewer than 50 iterations and produces stable results (i.e., fits starting from different initial values converge to the same result). However, as the name suggests, the method can only be applied if the derivative of χ^2 with respect to the parameters is linear in the parameters, rendering an uncertainty as described in Eqs. (7.15 - 7.17) unfeasible.

7.6.2 Linear-combination method

The LCM, described in Ref. [114], is a crucial component for our optimization, as it converges quickly even for a large parameter set. It searches for an optimal solution of the χ^2 value, which can formally be obtained by setting the derivative with respect to the parameters to zero:

$$\frac{\partial \chi^2}{\partial x_i} = -2 \sum_{k=1}^{N} \frac{E_k^{\text{exp}} - E_k^{\text{th}}}{\sigma_k^2} \left(\frac{\partial E_k^{\text{th}}}{\partial x_i} + \frac{E_k^{\text{exp}} - E_k^{\text{th}}}{\sigma_k} \frac{\partial \sigma_k}{\partial x_i} \right) = 0 \,, \tag{7.30}$$

where the theoretical energy can be written as follows:

$$E_k^{\text{th}} = \sum_{i=1}^{p} x_i (E_i^{\text{th}})_k \,. \tag{7.31}$$

Here, $(E_i^{\text{th}})_k$ is either the expectation value of a certain operator, given by $\langle \boldsymbol{V}_i^{\text{cont}} \rangle_k$, or the occupation number $\langle \boldsymbol{n}_i \rangle_k$ which is multiplied by SPEs (see Eq. (7.18)). The basic idea of the LCM is to decompose the original correlated parameter set into its principal components. The principal components are a subset of maximally uncorrelated parameters $\mathbf{y} = \{y_i\}$ with respect to the data set. For this, the method requires Eq. (7.30) to be linear in $\mathbf{x}$, meaning

$$\frac{\partial \sigma_k}{\partial x_i} = 0 \quad \forall i \text{ and } k \,.$$

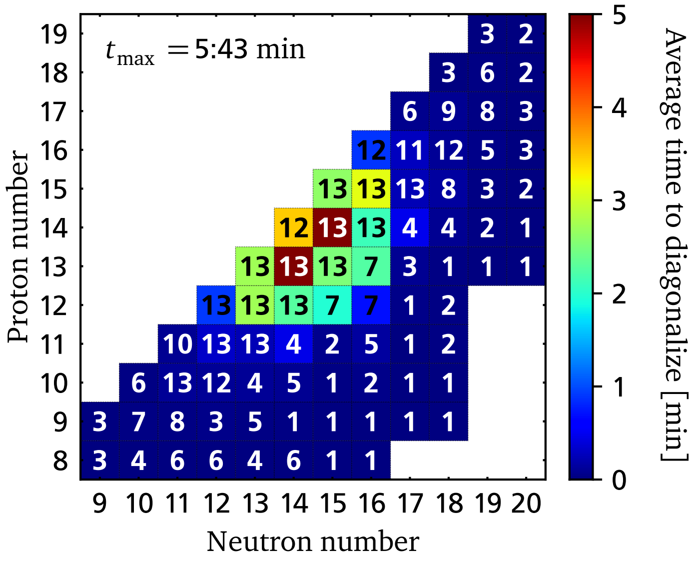

Figure 7.5.: Graphical visualization of the BR_2 data set from Tab. 7.2. Each square represents an isotope in this data set and shows the number of fitted states in the respective isotope. The color coding is according to the average time for a diagonalization with the ANTOINE code. Low computational effort is colored in blue while more involved calculations are colored red. The color coding is given on the right. The time refers to a single thread calculation on an Intel® Core™ i7-6700 CPU with 3.40 GHz. The actual time is not as relevant as the trend, for which nuclei are computationally more involved.

This is not fulfilled for uncertainties from chiral EFT as shown in this chapter. We consider a constant uncertainty σ_k from now on. With this, Eq. (7.30) can be expressed as

$$\sum_{k=1}^{N} \frac{E_k^{\mathrm{exp}} - \sum\limits_{j=1}^{p} x_j (E_j^{\mathrm{th}})_k - \langle V^{\mathrm{const}} \rangle_k}{\sigma_k^2} (E_i^{\mathrm{th}})_k \equiv e_i - G_{ij} x_j = 0\,, \tag{7.32}$$

where $\langle V^{\mathrm{const}} \rangle_k$ contains all the theoretical input that has no LEC to adjust to data. These are contributions from the pion exchange, and possibly SPEs (depending on whether one considers them as fit parameters). Furthermore, we use

$$e_i = \sum_{k=1}^{N} \frac{E_k^{\mathrm{exp}} - \langle V^{\mathrm{const}} \rangle_k}{\sigma_k^2} (E_i^{\mathrm{th}})_k \tag{7.33}$$

and

$$G_{ij} = \sum_{k=1}^{N} \frac{(E_i^{\mathrm{th}})_k (E_j^{\mathrm{th}})_k}{\sigma_k^2}\,. \tag{7.34}$$

With this, the original problem is reduced to solving a set of linear equations

$$G\mathbf{x} = \mathbf{e}\,, \tag{7.35}$$

with the $p \times p$ matrix G and the vectors of length p, $\mathbf{x}$ and $\mathbf{e}$. We perform an eigenvalue decomposition of G, which reads

$$G = A^T D A\,, \tag{7.36}$$

where the eigenvalues d_i are given in the diagonal matrix D and the eigenvectors form an orthogonal matrix A with $A^{-1} = A^T$, as G is symmetric. Rather than taking the direct solution

$$\mathbf{x} = G^{-1}\mathbf{e}\,, \tag{7.37}$$

we rewrite the equation as

$$D\mathbf{y}^{\text{in}} = A\mathbf{e}\,, \tag{7.38}$$

where $\mathbf{y}^{\text{in}} = A\mathbf{x}$. For large d_i, the corresponding y_i^{in} is well defined, as small fluctuations in $(A\mathbf{e})_i$ translate to small fluctuations in y_i^{in}. In other words, large eigenvalues d_i correspond to well determined linear combinations y_i^{in}. However, as the eigenvalues become smaller, a small fluctuation in $(A\mathbf{e})_i$ needs to be compensated by y_i. For small d_i, $y_i^{\text{out}} = (A\mathbf{e})_i/d_i$ is getting large. The idea is to adjust only the well defined values of $\mathbf{y}^{\text{in}}$. This is realized with an external "quality parameter" δ. We will take the new value $y_i^{\text{out}} = (A\mathbf{e})_i/d_i$ if $d_i \geq \delta$ and for $d_i < \delta$ we will leave $y_i^{\text{out}} = y_i^{\text{in}}$ as it is. With eigenvalues ordered decreasing in size, we get

$$\mathbf{y}^{\text{out}} = \left(\begin{array}{c} (A\mathbf{e})_1/d_1 \\ (A\mathbf{e})_2/d_2 \\ \vdots \\ (A\mathbf{e})_i/d_i \\ \hdashline y_{i+1}^{\text{in}} \\ \vdots \\ y_p^{\text{in}} \end{array}\right), \tag{7.39}$$

where d_i is the last eigenvalue that fulfills $d_i \geq \delta$. The new parameters $\mathbf{x}$ are obtained with $\mathbf{x} = A^T\mathbf{y}^{\text{out}}$.

Implementation

This method is used iteratively. We begin with a starting vector in iteration zero, $\mathbf{x}^{(0)}$, and diagonalize the resulting Hamiltonian to obtain the values $(E_i^{\text{th}})_k$. We follow all the steps from above and obtain the new starting vector for the next iteration $\mathbf{x}^{(1)}$. We diagonalize the new Hamiltonian and compare the new χ^2 value to the old one to check if the new iteration improved. If it does not, one can either change the value of δ or take different step lengths. A convergence criterion can be formulated based on the change in parameters between two subsequent iterations $||\mathbf{x}^{(i)} - \mathbf{x}^{(i-1)}||$ or based on the change in the χ^2 value. The choice $\delta = 0.01$ provides useful LECs for us that are of natural size (see Ch. 9). However it is beneficial to explore different values of δ occasionally.

The LCM described above shows a fast and stable convergence behavior. One could use the optimum from the LCM as a starting point for more refined algorithms. However, we find that the minima obtained with the LCM are rarely changed by different optimizers. In most cases, a χ^2 value close to the optimum is obtained within the first ten iterations.

We depict a general schematic process of an iterative fitting algorithm in Fig. 7.6. In the first step, starting values $\{x_i^{\text{it}=0}\}$ are used for the initial calculation. The calculation (here done with the ANTOINE shell-model code) returns the theoretical energies $\{(E_i^{\text{th}})_k\}$ as well as uncertainties. In the analysis step, we construct the χ^2 value and, depending on the optimization routine, we construct gradients, Jacobians and/or Hessians (denoted by $\nabla, \mathscr{J}$, and $\mathscr{H}$ respectively). In the optimization step we either obtain the parameters for the next iteration $\{x_i^{\text{it}+1}\}$ and the process repeats, or, given that there is no notable

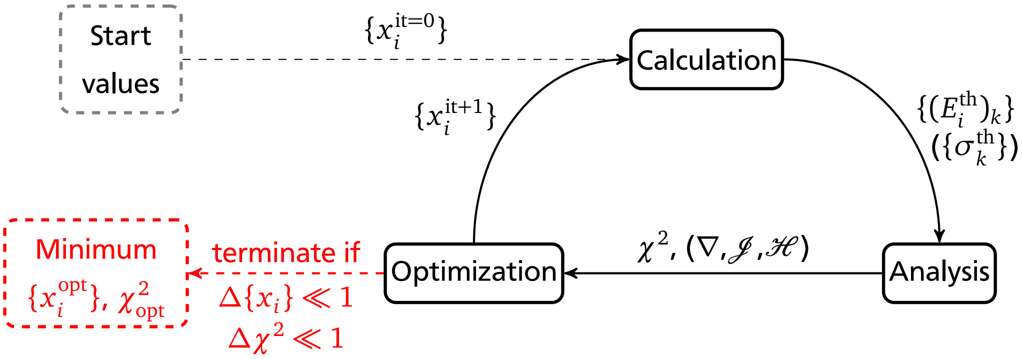

Figure 7.6.: Schematic procedure for an iterative optimization process. More information is given in the text.

change in the parameters and/or the χ^2 value, the fit terminates and we are left with the optimal result for $\{x_i^{\text{opt}}\}$ and χ^2_{opt}.

As our theoretical uncertainty has no statistical interpretation, neither does the resulting χ^2 value. Thus, we compare the root-mean-square (RMS) deviation to experiment for different interactions. The RMS deviation is given by

$$\text{RMS} = \sqrt{\frac{1}{N}\sum_{k=1}^{N}\left(E_k^{\text{exp}} - E_k^{\text{th}}\right)^2}\,. \tag{7.40}$$

This concludes the technical and theoretical background for shell-model interactions. Applications follow in the next chapters.

8 *sd*-shell fits and results at NLO

As described in the previous section, we use chiral EFT as a general operator basis at low energies and its capability to estimate theoretical uncertainties due to the EFT expansion to develop chiral shell-model interactions, where the low-energy couplings are fit directly to data in the sd shell.

In this chapter we investigate charge-independent interactions at LO, NLO, and NLO$_{\mathrm{vs}}$, where the subscript vs (valence space) denotes that this interaction includes valence-space operators. As mentioned in the previous chapter, we fit the interactions in this chapter to experimental data from the BR$_1$ data set in Tab. 7.2. This set considers 441 out of the 608 states that were used for the USDA/USDB fits [114]. The number of states we fit to is visualized in Fig. 8.1 for each isotope. As in Ref. [114], we apply a proton number dependent Coulomb correction (CH from Tab. 7.1) to the experimental ground-state energies, so that we can focus on the strong interaction part. We begin with a recap about this new operator structure. This chapter is based on our work reported in Ref. [115].

8.1 Valence-space operators at NLO

With the new CM-dependent interactions from Sec. 3.2, the full contact interaction at NLO$_{\mathrm{vs}}$ reads

$$\begin{aligned}\langle \mathbf{p},\mathbf{P}|V_{\text{cont}}^{\mathrm{NLO_{vs}}}|\mathbf{p}',\mathbf{P}\rangle =&C_S + C_T\boldsymbol{\sigma}_1\cdot\boldsymbol{\sigma}_2 + C_1\mathbf{q}^2 + C_2\mathbf{k}^2 + C_3\mathbf{q}^2\boldsymbol{\sigma}_1\cdot\boldsymbol{\sigma}_2 + C_4\mathbf{k}^2\boldsymbol{\sigma}_1\cdot\boldsymbol{\sigma}_2\\ &+\frac{i}{2}C_5\,(\boldsymbol{\sigma}_1+\boldsymbol{\sigma}_2)\cdot(\mathbf{q}\times\mathbf{k}) + C_6(\mathbf{q}\cdot\boldsymbol{\sigma}_1)(\mathbf{q}\cdot\boldsymbol{\sigma}_2) + C_7(\mathbf{k}\cdot\boldsymbol{\sigma}_1)(\mathbf{k}\cdot\boldsymbol{\sigma}_2)\\ &+P_1\mathbf{P}^2 + P_2\mathbf{P}^2\boldsymbol{\sigma}_1\cdot\boldsymbol{\sigma}_2 + P_3\,i\,(\boldsymbol{\sigma}_1-\boldsymbol{\sigma}_2)\cdot(\mathbf{q}\times\mathbf{P})\\ &+P_4\,(\boldsymbol{\sigma}_1\times\boldsymbol{\sigma}_2)\cdot(\mathbf{k}\times\mathbf{P}) + P_5\,(\boldsymbol{\sigma}_1\cdot\mathbf{P})(\boldsymbol{\sigma}_2\cdot\mathbf{P})\,. \end{aligned} \tag{8.1}$$

The CM-dependent interactions include central parts, given by the LECs P_1 and P_2, the difference- and cross-vector operators determined by P_3 and P_4, and a CM-tensor operator, given by P_5. The operators that accompany the LECs P_3–P_5 are discussed in the context of noncentral interactions in Fermi-liquid theory in Ref. [172]. From the partial-wave decomposition one can see the central and tensor parts are diagonal in two-body spin s, relative orbital angular momentum l, and total relative angular momentum j. They only contribute to the relative $^1S_0$ and $^3S_1$ waves (see general notes on the partial-wave decomposition in App. B and the tensor operator representation in App. C). Moreover, the central parts are diagonal in CM angular momentum L.

The difference- and cross-vector operators are spin-violating [172] and mix spin-singlet $^1S_0$ ($^1P_1$) with spin-triplet ^3P_j ($^3S_1$) relative partial waves. At NLO$_{\mathrm{vs}}$, they do not contribute to higher l waves. As a result of the S-P mixing and parity conservation, the spin-violating interactions also change the CM orbital angular momenta L, L' and are not necessarily diagonal in j, j'.

In order to investigate the impact of the different CM-dependent interactions, we use in the following the notation NLO$_{\mathrm{vs}_{c,v,t}}$ when only central, only vector, or only tensor operators are included, respectively.

8.2 Overview of comparison with experiment

In Fig. 8.2 we show the RMS deviation from experiment for each fitted nucleus in the sd shell for the chiral shell-model interactions at LO (left), NLO (middle), and NLO$_{\mathrm{vs}}$ (right). The RMS deviation is given by a color coding that ranges from 0 MeV (green) to 1 MeV (red). The results show a striking improvement from LO to NLO and a further improvement from NLO to NLO$_{\mathrm{vs}}$, where at NLO$_{\mathrm{vs}}$, there are only a few outliers with large RMS deviations. This demonstrates the impact of the new CM-dependent operators.

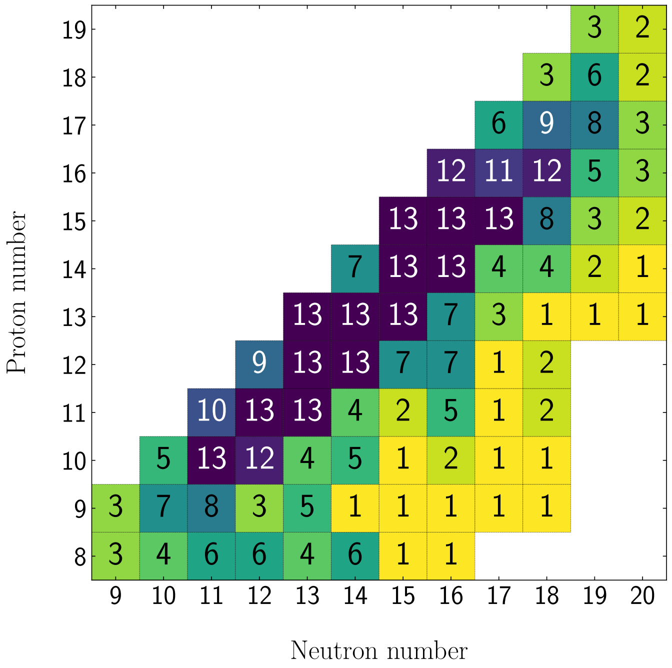

Figure 8.1.: Graphical representation of BR_1 dataset from Tab. 7.2. Each square shows the number of states fitted for a given isotope, where the color coding gets darker with increasing number of states.

We also show a quantitative overview of the comparison with experiment in Fig. 8.3. The figure is divided into two rows, where the upper row shows the difference between theoretical and experimental ground-state energies and the lower row is for the difference between theoretical and experimental excitation energies. The columns show again the results for the LO (left), NLO (middle), and $\mathrm{NLO}_{\mathrm{vs}}$ (right) shell-model interactions. The gray (orange) bands show the σ (2σ) intervals given by the RMS deviation. The order-by-order improvement from LO to NLO and from NLO to $\mathrm{NLO}_{\mathrm{vs}}$, already seen globally in Fig. 8.2, is clearly visible from the decreasing σ bands from left to right and from the systematically decreasing individual energy differences. Overall, we observe a very good reproduction of experiment at $\mathrm{NLO}_{\mathrm{vs}}$.

The results for the ground-state energies at LO in Fig. 8.3 show a systematic deviation from experiment with increasing neutron richness, especially for the oxygen to silicon isotopes, where the LO shell-model interaction leads to overbound states with respect to experiment. This trend seems to be resolved at NLO, where no clear pattern is visible. However, at $\mathrm{NLO}_{\mathrm{vs}}$, there is again a deficiency in the isospin dependence for the neon to aluminum isotopic chains. It will be interesting to see whether this will be improved at $\mathrm{N}^2\mathrm{LO}$, and whether this can be traced back to the inclusion of three-nucleon forces [221], which enter at this order.

Systematic trends of this type are not visible in the energy differences for the excited states in Fig. 8.3. Note that the number of excited states is higher for nuclei close to stability (see also Fig. 8.1), so that there are more points shown at the beginning of each element in in Fig. 8.3. However, it stands out that there is little to no improvement in the first two sodium isotopes (^{22}Na and ^{23}Na) from NLO to $\mathrm{NLO}_{\mathrm{vs}}$, which exemplary shows that additional operator structures are necessary to reach higher accuracies in the fit.

8.3 Comparison to USD-type interactions

In addition to the direct comparison with experiment, we study how the developed chiral shell-model interactions perform compared to USD-type interactions, where the TBMEs are not determined by a basis of operators but are fit overall. The RMS deviation of the USD fit is taken from Fig. 4 of Ref. [114] and is shown as solid line as a function of the number of parameters in Fig. 8.4. Note that the USD fit

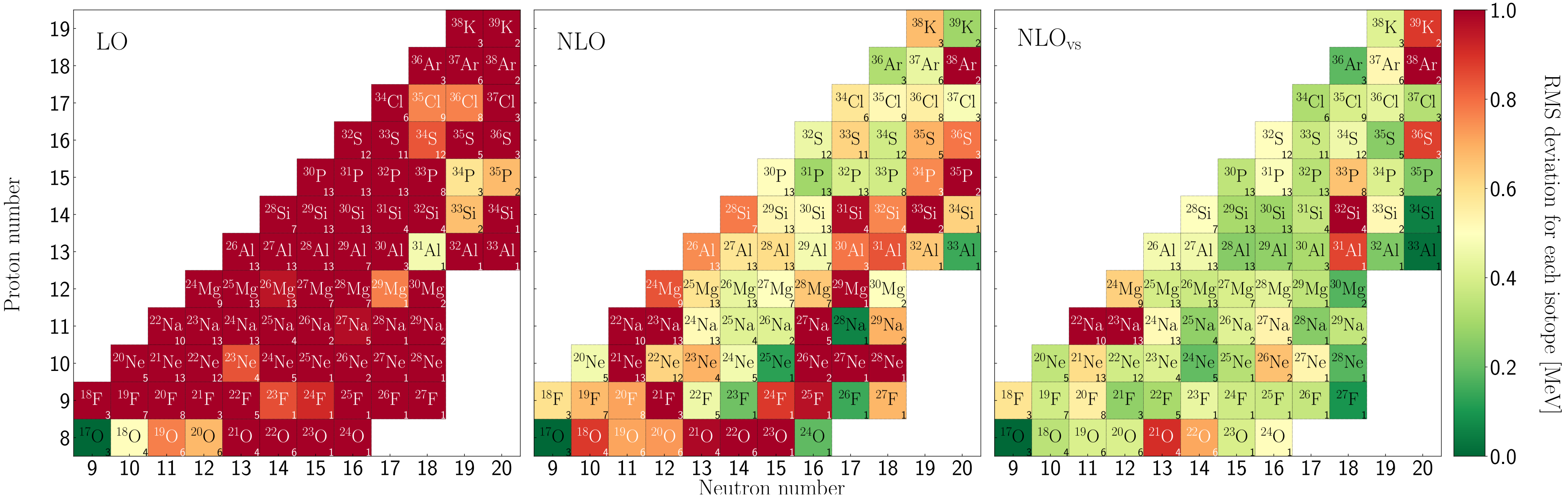

Figure 8.2.: Graphical representation of the RMS deviation from experiment for each fitted nucleus in the sd shell. The figure shows the results for the chiral shell-model interactions at LO (left), NLO (middle), and NLO_{vs}(right). The color coding of the RMS deviation is given in the bar on the right. Isotopes with a small RMS deviation are colored green, while those with a large deviation are colored red. Each square shows the isotope label and the number of fitted states in the bottom right corner. The text color changes from black to white for RMS deviations larger than 0.7 MeV.

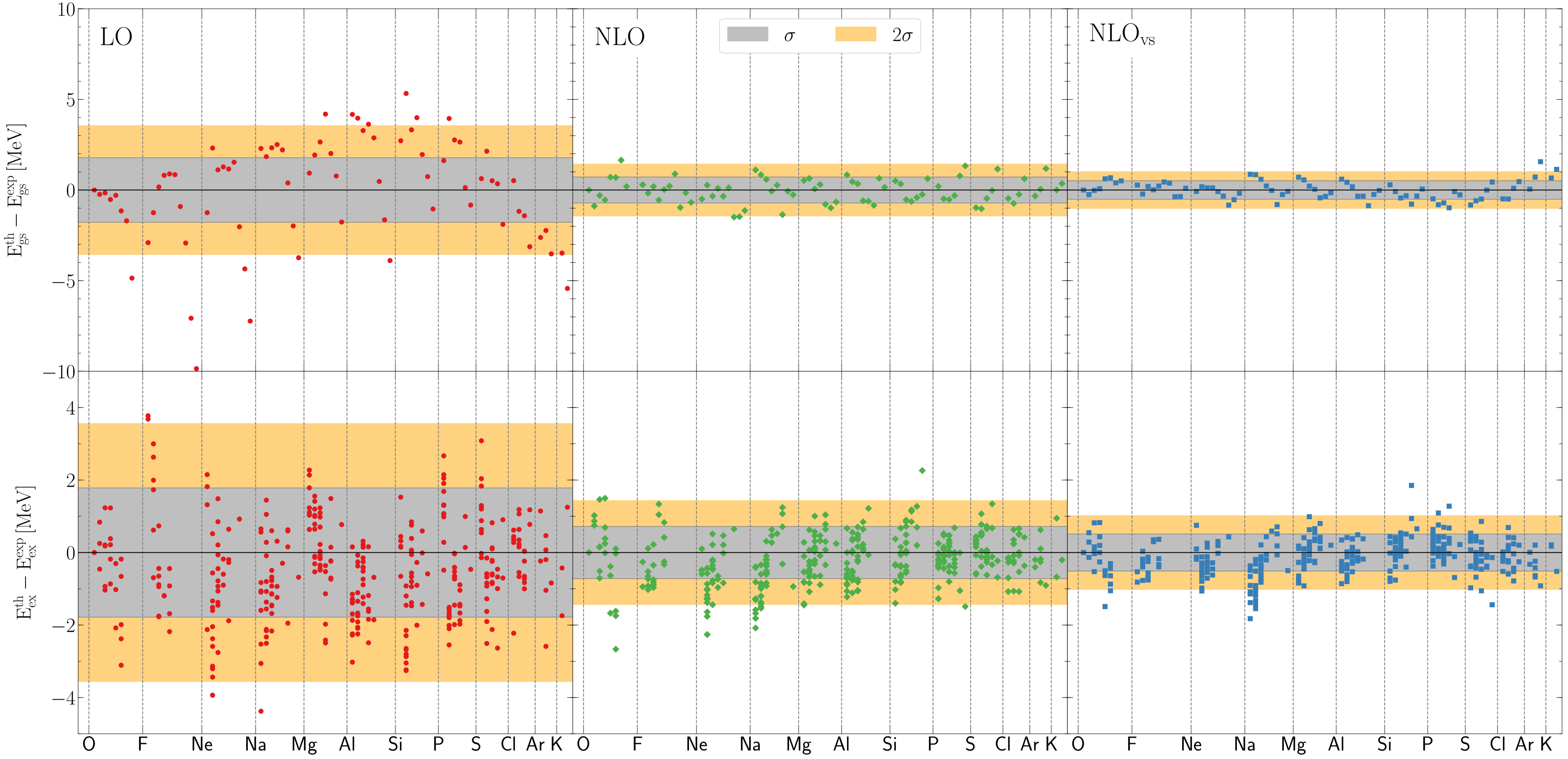

Figure 8.3.: Energy differences of the result from the chiral shell-model interactions and experiment in MeV. The upper row shows results for ground-state (gs) energies whereas the lower row is for the energies of excited (ex) states. Each dot represents a single state. The dots are ordered from oxygen to potassium, and within each bin they are ordered according to their mass number. From left to right, we show results for the LO, NLO, and NLO$_{\text{vs}}$ interaction. The gray (orange) bands show the statistical σ (2σ) spread, given by the RMS deviation.

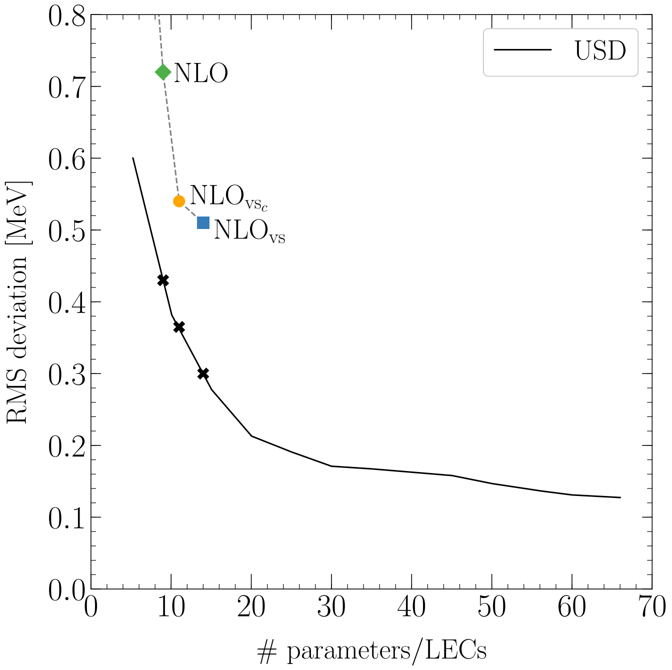

Figure 8.4.: Root-mean-square deviation of the chiral and USD-type interactions as a function of the number of parameters. The results for the USD fit are taken from Ref. [114]. The figure shows the free-space operator NLO interaction (green diamond), the $\mathrm{NLO}_{\mathrm{vs}_c}$ interaction including only the central CM-dependent operators in addition to NLO (yellow circle), and the full $\mathrm{NLO}_{\mathrm{vs}}$ shell-model interactions (blue square).

was to a data set with 608 states, while our results are for the data set of 441 states described above, so the comparison is not completely one-to-one.

In Fig. 8.4, we plot the RMS deviation as a function of the number of LECs for the different chiral shell-model interactions developed in this work. In order to assess the impact of the new CM-dependent operators, we also analyze the central (vs_c), vector (vs_v), and tensor (vs_t) contributions separately. The RMS deviations for all interactions and the number of LECs are given in Table 8.1. Note that in comparison to the RMS deviation for a given nucleus (see Fig. 8.2) or for ground and excited states separately (see Fig. 8.3) the RMS deviations discussed here are with respect to the full data set considered. As shown in Table 8.1, the RMS deviation improves from 1.8 MeV at LO to 0.7 MeV at NLO and 0.5 MeV at $\mathrm{NLO}_{\mathrm{vs}}$.

To guide the comparison with the USD-type interactions in Fig. 8.4, the latter are marked by a cross for 9, 11, and 14 parameters, which corresponds to the same number of LECs as the NLO, $\mathrm{NLO}_{\mathrm{vs}_c}$ (or $\mathrm{NLO}_{\mathrm{vs}_v}$), and $\mathrm{NLO}_{\mathrm{vs}}$ interactions, respectively (see Table 8.1). Recall that the USDA (USDB) interactions correspond to the USD fit with 30 (56) parameters [114]. We find a similar rapid decrease of the RMS deviation with increasing number of LECs, although for the same number of parameters the optimal USD fit has ~ 200 keV smaller RMS deviation. Moreover, we show in Fig. 8.4 explicitly the $\mathrm{NLO}_{\mathrm{vs}_c}$ result, because the central CM-dependent operators constitute the largest source of improvement compared to considering only free-space operators (see also Tab. 8.1).

8.3.1 Monopole matrix elements and low-energy constants

The monopole matrix elements play a special role in the shell model and for shell structure [116, 221–223]. They determine the energy gaps between the single-particle orbitals, leading to effective SPEs. Using a short-hand notation for the TBMEs, $\langle abJT|V|cdJT\rangle$, where the combined index i is short for $(n_i l_i j_i)$, the

Table 8.1.: Number of fitted LECs for the different chiral shell-model interactions considered in this work. The first two rows show the LO and NLO interactions based on free-space operators. The following rows show NLO interactions that include the CM-dependent operators from Sec. 7.2. To distinguish between central (c), vector (v), and tensor (t) contributions, we label them vs$_c$, vs$_v$, and vs$_t$, respectively. The full valence-space interaction in the last row is labeled NLO$_{\text{vs}}$. We give the RMS deviation from experiment for these fitted interactions and compare them to the RMS deviation of the USD fit from Ref. [114] for the same number of parameters. The rows are ordered with increasing number of LECs and decreasing RMS deviation.

Interaction	#LECs	RMS [keV]	USD [keV]
LO	2	1780	–
NLO	9	718	430
NLO$_{\text{vs}_t}$	10	641	380
NLO$_{\text{vs}_v}$	11	678	370
NLO$_{\text{vs}_c}$	11	538	370
NLO$_{\text{vs}}$	14	510	300

monopole matrix elements are obtained by angle averaging, i.e., by a weighted average over all possible values of the total angular momentum,

$$V_{ab}^{T} = \frac{\sum_J (2J+1)\,\langle abJT|V|abJT\rangle}{\sum_J (2J+1)}\,, \tag{8.2}$$

where in the sd shell a, b consists of the $0d_{5/2}$, $0d_{3/2}$, and $1s_{1/2}$ orbitals, which are uniquely labeled by their total angular momentum label (i.e., 5, 3, and 1).

Figure 8.5 shows the monopole matrix elements of the chiral shell-model interactions at LO, NLO, and NLO$_{\text{vs}}$ as well as those of the USDA and USDB interaction for $A = 18$ (i.e., without applying the scaling with $\hbar\omega$). In the $T = 0$ channel (left panel of Fig. 8.5), the monopole matrix elements at LO (except for 5353) deviate significantly from the other interactions, while at NLO and especially at NLO$_{\text{vs}}$ they are similar to the monopole matrix elements of USDA/USDB. In general the change from NLO to NLO$_{\text{vs}}$ is small except for the higher lying 1111 and 3333 orbitals. For the $T = 1$ channel (right panel of Fig. 8.5), the changes from LO to NLO are significantly smaller, and there are only notable deviations from USDA/USDB for the 1111 monopole matrix element. The latter was also observed in microscopic calculations of valence-space Hamiltonians [221].

The resulting LECs at different orders are shown in Fig. 8.6. To express them in natural units (see, e.g., Ref. [153]), we multiply the LO and NLO LECs by

$$C_{\text{LO}}\,[\text{nat. units}] = C_{\text{LO}} \cdot F_\pi^2\,, \tag{8.3}$$

$$C_{\text{NLO}}\,[\text{nat. units}] = C_{\text{NLO}} \cdot (F_\pi \Lambda)^2\,, \tag{8.4}$$

$$P_i\,[\text{nat. units}] = P_i \cdot (F_\pi \Lambda)^2\,, \tag{8.5}$$

with $\Lambda = \Lambda_{\text{HO}} = 375$ MeV and pion decay constant $F_\pi = 92.4$ MeV. As shown in Fig. 8.6, all fitted LECs at all orders come out to be natural, or are very small in some cases. Wigner symmetry given by $C_S \gg C_T$ is also fulfilled by our interactions. Note that neither naturalness nor Wigner symmetry was imposed as a constraint on the fit. The LECs of the new CM-dependent operators are given by P_{1-5} in Fig. 8.6. We find that all P_i are similar in magnitude. Finally, the changes from LO to NLO and NLO$_{\text{vs}}$ are also systematic for the LECs, with larger changes from NLO to NLO$_{\text{vs}}$ mainly for C_4 and C_7.

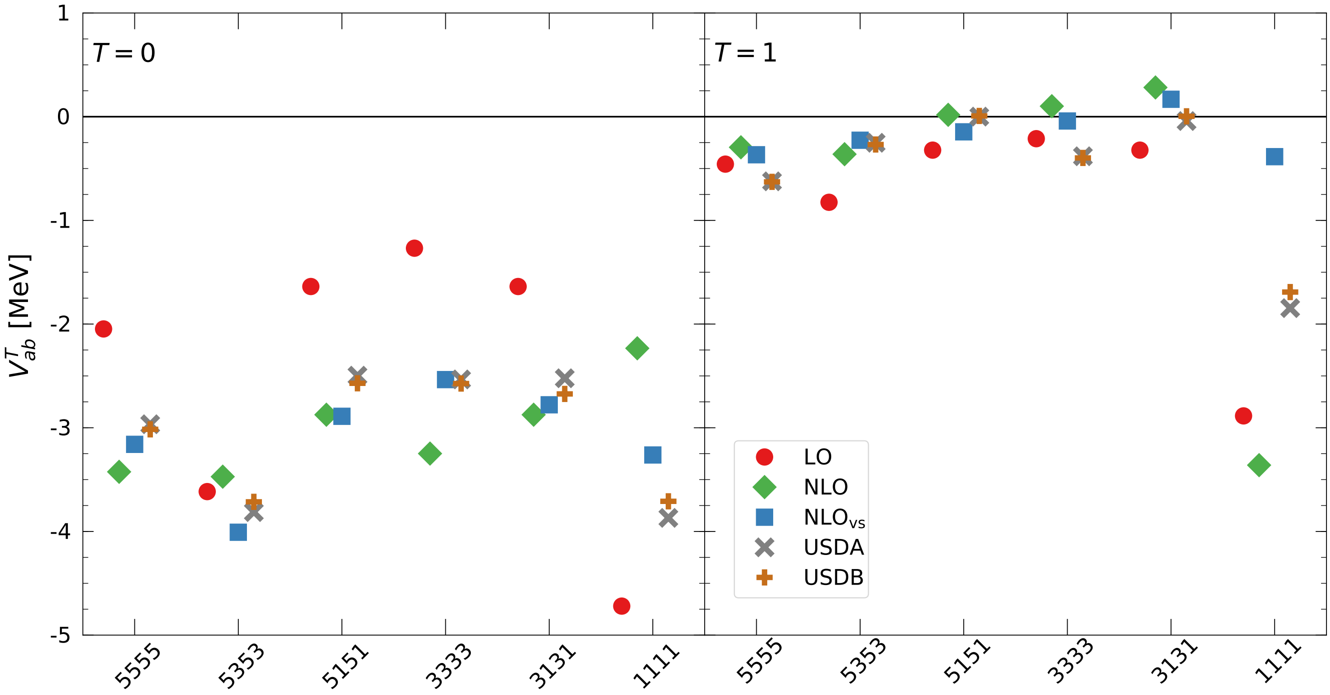

Figure 8.5.: Monopole matrix elements of the different chiral shell-model interactions for mass number $A = 18$. The left panel shows the monopole matrix elements for isospin $T = 0$ and the right panel for $T = 1$. The chiral shell-model interactions at LO, NLO, and NLO$_{\rm vs}$ are shown together with the monopole matrix elements of the USDA and USDB interactions from Ref. [114]. The matrix elements are labeled by $2j_a\,2j_b\,2j_a\,2j_b$.

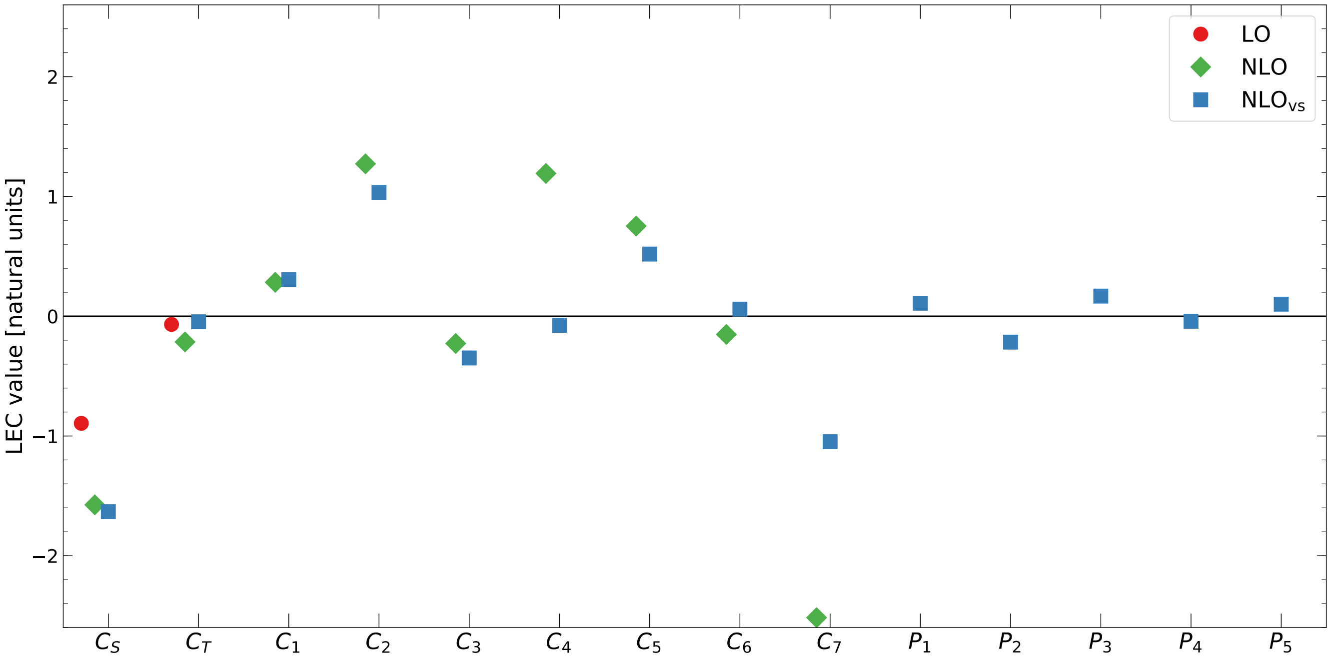

Figure 8.6.: Fitted LECs at LO, NLO, and NLO$_{\rm vs}$ in natural units, which are obtained using Eqs. (8.3)–(8.5).

8.4 Results

After a discussion of our fits and the overview of the comparison to experiment and to USD-type interactions in the previous section, we next present a more detailed picture of the quality of the chiral shell-model interactions. In most cases the experimental data shown are from the atomic mass evaluation [213] for the ground-state energies and from Ref. [215] for excitation energies. Otherwise the experimental reference is given explicitly. Moreover, experimental states included in the fit are shown in gray, and in red for predictions. We also provide the TBMEs and SPEs of the NLO$_{\mathrm{vs}}$ interaction in App. E.2.

8.4.1 Ground-state energies

In Fig. 8.7, we show the ground-state energies for the isotopic chains from oxygen to potassium based on the chiral shell-model interactions at LO, NLO, and NLO$_{\mathrm{vs}}$ including the theoretical uncertainties as discussed above. For comparison, also the USDA and USDB energies are given. We find that all states that were included in the fit are reproduced at all orders within the EFT uncertainties. However, the LO interaction predicts too much binding for the neutron-rich oxygen and fluorine isotopes that were not included in the fit. As a result, the oxygen dripline is not reproduced, being at or beyond ^{28}O at LO. Also ^{28}F and ^{29}F are overbound with respect to experiment. Remarkably, already the NLO interaction correctly reproduces the oxygen dripline as well as the two fluorine isotopes, which were not included in the fit. Moreover, the NLO and NLO$_{\mathrm{vs}}$ interactions overlap in all cases and reproduce ground-state energies equally well.

8.4.2 Spectra

In Figs. 8.8–8.10, we present our results for the spectra of excited states. These cover the sd shell for representative cases of nuclei regarding the fits. In each panel, results are given for the chiral shell-model interactions at LO, NLO, and NLO$_{\mathrm{vs}}$ including the theoretical uncertainties, in comparison to experiment and the USDA/USDB interactions. First, in Fig. 8.8, we show results for oxygen, fluorine, neon, and sodium isotopes. For the oxygen spectra (first row), the excitation energies generally change weakly from LO to NLO to NLO$_{\mathrm{vs}}$. From LO to NLO, the excitation energy usually increases, and the NLO$_{\mathrm{vs}}$ results generally lead to an improvement. In fluorine (second row), the NLO interaction already shows a clear improvement from the LO result, but overshoots the experimental value somewhat, where again then at NLO$_{\mathrm{vs}}$ the spectra are in good agreement with experiment. For the neon spectra (third row), most states show a continuous improvement from LO to NLO to NLO$_{\mathrm{vs}}$. Moreover, by including the CM-dependent operators, the correct ground state is reproduced in ^{21}Ne. For the sodium isotopes (fourth row), we show the two outliers ^{22}Na and ^{23}Na, which we already pointed to in the discussion of Fig. 8.2. In both of them we see that our interactions at NLO and NLO$_{\mathrm{vs}}$ lead to too low energies, and also that there is nearly no improvement from NLO to NLO$_{\mathrm{vs}}$. However, ^{25}Na shows again a similar behavior as the fluorine isotopes.

In Fig. 8.9, we show results for magnesium, aluminum, silicon, and phosphorus isotopes. We generally find similar order-by-order behaviors described above, with an overall improvement going to NLO$_{\mathrm{vs}}$. We note in particular the improvement for ^{26}Al, ^{31}Si, and ^{35}P, as well as the correct reproduction of the ^{32}P ground state when the CM-dependent operators are included. In Fig. 8.10, we show results for the remaining sulfur, chlorine, argon, and potassium isotopes, which exhibit similar order-by-order trends as well. Another outlier is the first excited state of ^{37}Ar, which is well reproduced by the LO and NLO interactions, but at slightly too low energy with the NLO$_{\mathrm{vs}}$ interaction. However, besides this first excited state, most of the remaining states improve with the NLO$_{\mathrm{vs}}$ interaction.

Finally, we need to comment on the theoretical uncertainties for the excited states. While the behavior of the uncertainties may not be unreasonable, the adopted prescription for the uncertainties of excitation energies is not fully satisfactory, in particular regarding the LO to NLO behavior which is not overlapping in many cases. As we show in the following chapter, the uncertainty behavior improves when one allows SPEs to vary and charge-dependent operators are present. Still, future work is needed here, with, e.g., a Bayesian analysis [35] of the order-by-order behavior of the results leading to improved estimates of the theoretical uncertainties.

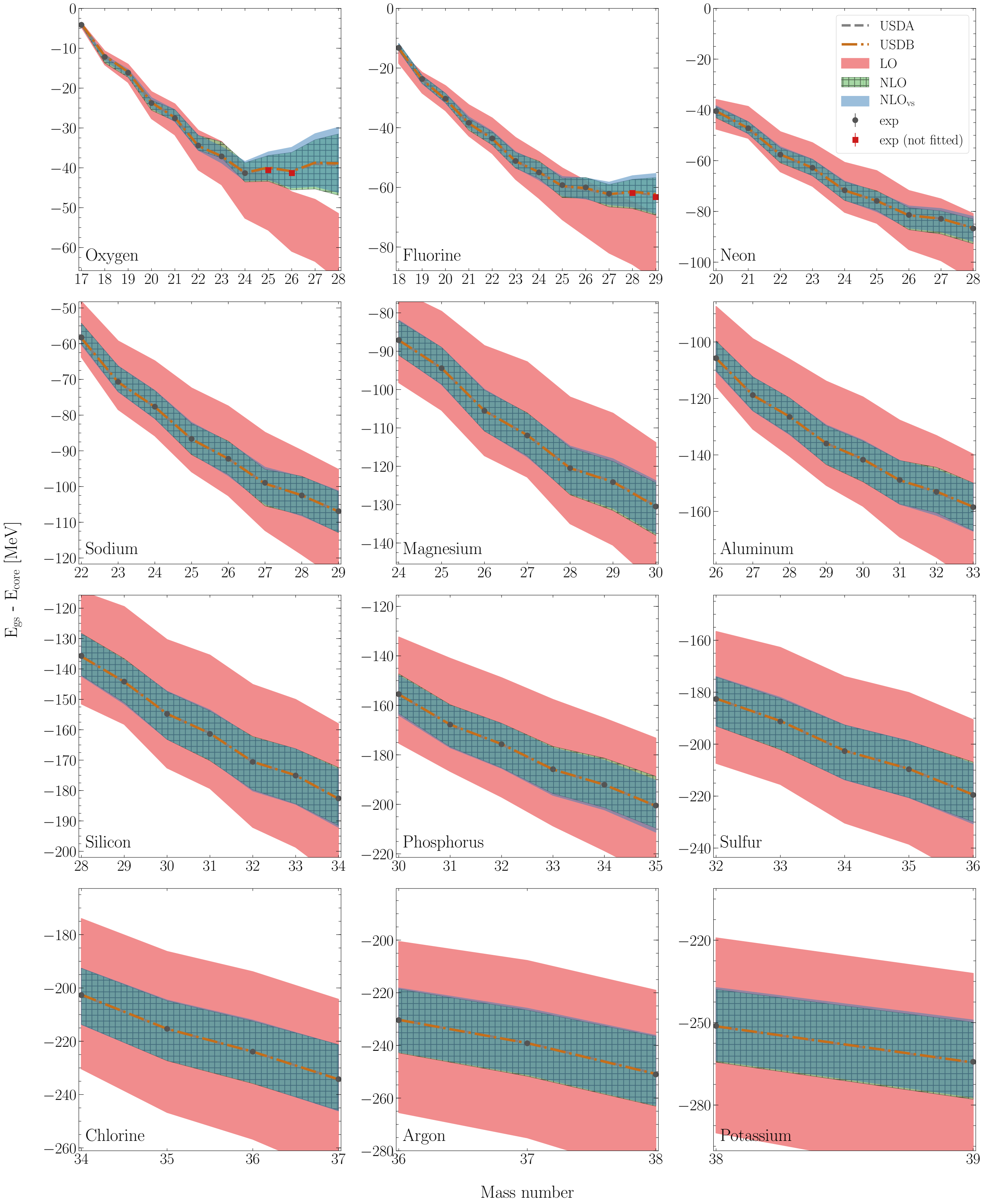

Figure 8.7.: Ground-state energies from oxygen to potassium obtained from chiral shell-model interactions at LO, NLO, and NLO$_{vs}$. The energies are given with respect to the ^{16}O core and are Coulomb corrected according to Tab. 7.1. The theoretical uncertainties are calculated with Eq. (7.10) at LO and with Eq. (7.11) at NLO. For comparison, we give the USDA and USDB results from Ref. [114]. Experimental energies that are included in the fit are given by gray circles, while states that are not included are given by red squares for ^{25,26}O and ^{28,29}F.

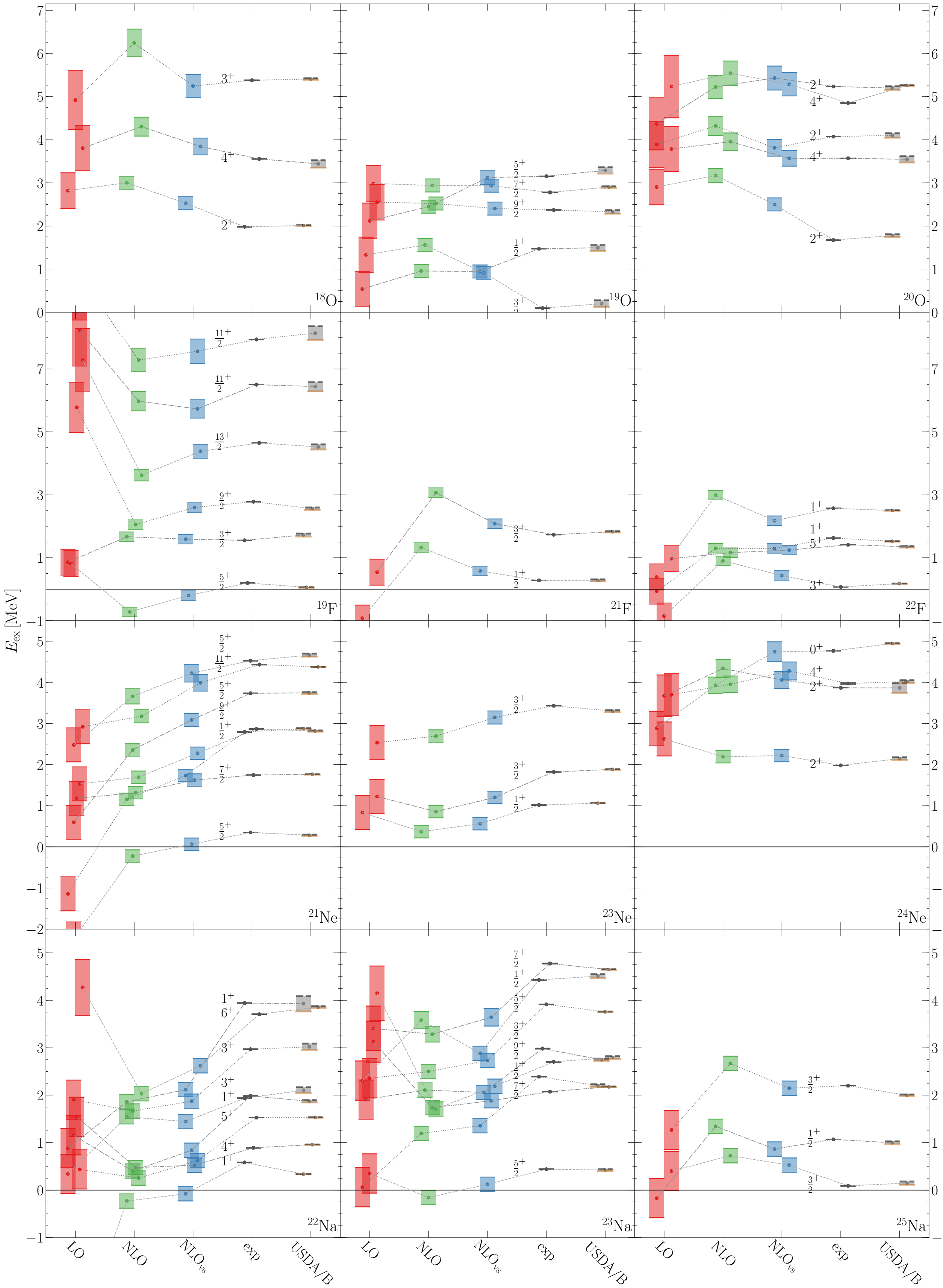

Figure 8.8.: Excitation spectra of selected isotopes from oxygen to sodium. In each panel, results are shown for the chiral shell-model interactions at LO, NLO, and NLO$_{\mathrm{vs}}$, in comparison to experiment and USDA/USDB results, where USDA (USDB) is visualized by a dashed gray (solid orange) line. The theoretical uncertainties are given by Eqs. (7.13 - 7.14) at NLO. The same states are joined by dashed lines to guide the eye. The angular momentum labels are printed next to the experimental states. Isotope labels are given in the lower right corner.

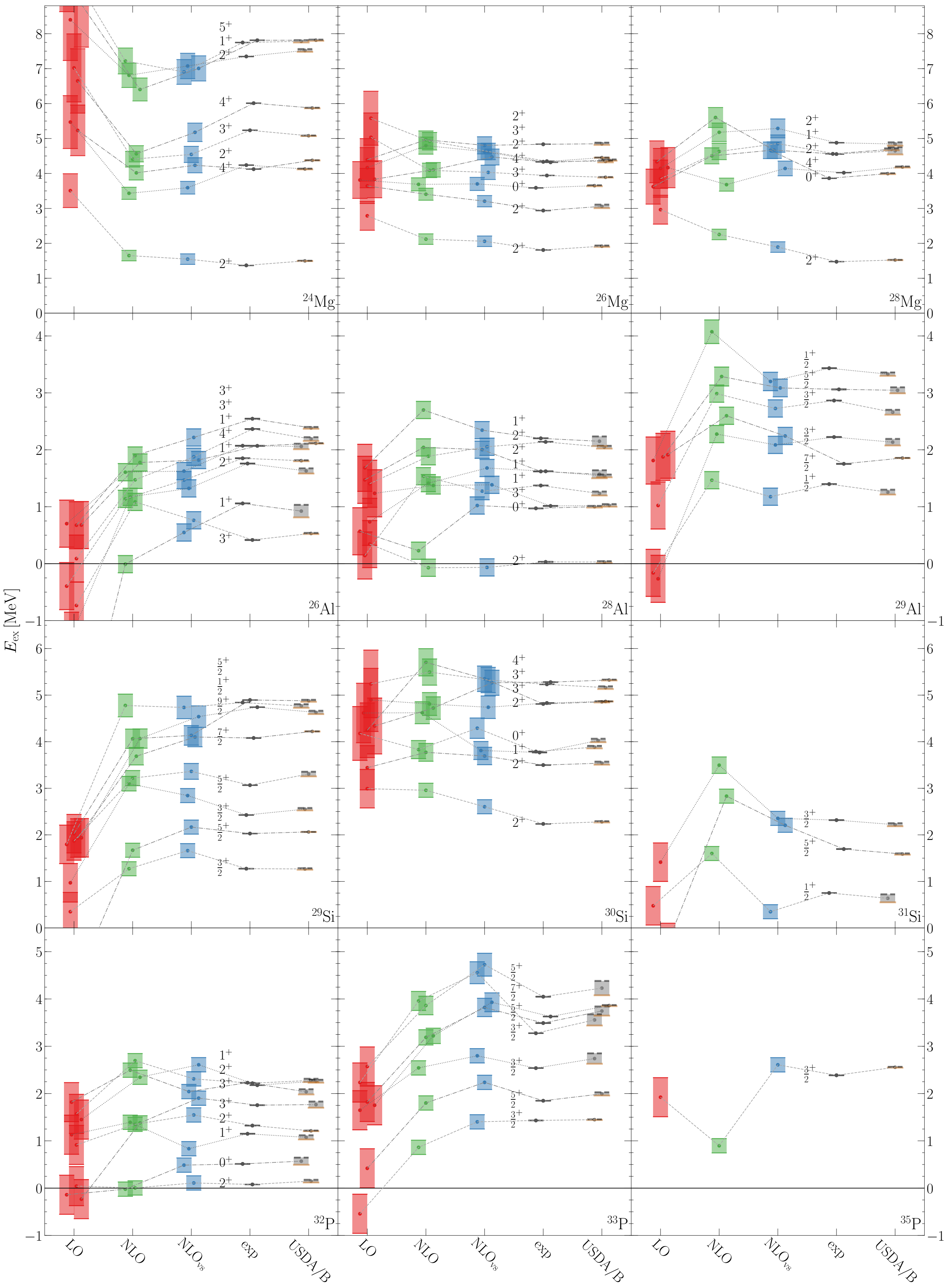

Figure 8.9.: Excitation spectra of selected isotopes from magnesium to phosphorus. For details see the caption of Fig. 8.8.

8.4.3 Predictions

After the promising prediction of the oxygen dripline at NLO and NLO$_{\mathrm{vs}}$ observed above, we also study the predictions for excited states of neutron-rich nuclei beyond the fitted data set. We focus on the spectra of neutron-rich oxygen, fluorine, and neon isotopes, which are plotted in Fig. 8.11. Only the first excited state in ^{26}Ne was included in the fit. All remaining states are predictions of the chiral shell-model interactions. Because our calculations do not include the continuum, we emphasize this by showing the neutron separation energy S_n in Fig. 8.11. For states close to or above S_n, the explicit inclusion of the continuum will lead to changes, which are often of the order of few hundred keV unless this is further resonantly enhanced.

In comparison to measured states, the chiral shell-model interactions at NLO$_{\mathrm{vs}}$ again lead to the best overall agreement, and there is generally an improvement in going from LO to NLO to NLO$_{\mathrm{vs}}$. For the oxygen isotopes this is especially visible in ^{23,24}O. Moreover, all our interactions reproduce the first 2^+ energy in ^{26}O recently measured at RIKEN [62]. This state is especially impressive, since neither the ground-state energy, nor the excitation energy was used in our dataset, and the order-by-order behavior is very stable. The agreement of our chiral shell-model interaction predictions at NLO$_{\mathrm{vs}}$ is also very good for the fluorine isotopes, especially for the low-lying states known, and for all neon isotopes shown.

8.5 Summary of main results

- We have developed chiral shell-model interactions in the sd shell, by fitting the LECs of chiral EFT operators at LO and NLO directly to 441 ground- and excited-state energies. In addition to the free-space contact interactions and pion exchanges, our interaction at NLO$_{\mathrm{vs}}$ includes novel CM-dependent operators that arise due to the breaking of Galilean invariance in the presence of the core.

- Those shell-model fits show a systematic improvement from LO to NLO and NLO$_{\mathrm{vs}}$ and result in natural LECs at all orders. The RMS derivation of the fits improves from 1.8 MeV at LO to 0.7 MeV at NLO and 0.5 MeV at NLO$_{\mathrm{vs}}$. In comparison to USD-type interactions, the RMS deviation is about 200 keV higher, but shows a similar rapid improvement with the number of LECs.

- We observed a striking improvement in the reproduction of experimental ground-state energies and excited states, when the new CM-dependent operators are included. There, the dominant contributor are the central interactions $\sim P_1$ and P_2.

- Our interactions show promising predictions for the oxygen dripline and for excited states in neutron rich oxygen and fluorine isotopes. Also, starting at NLO our interactions where able to predict the right ground-state energies for ^{28}F and ^{29}F.

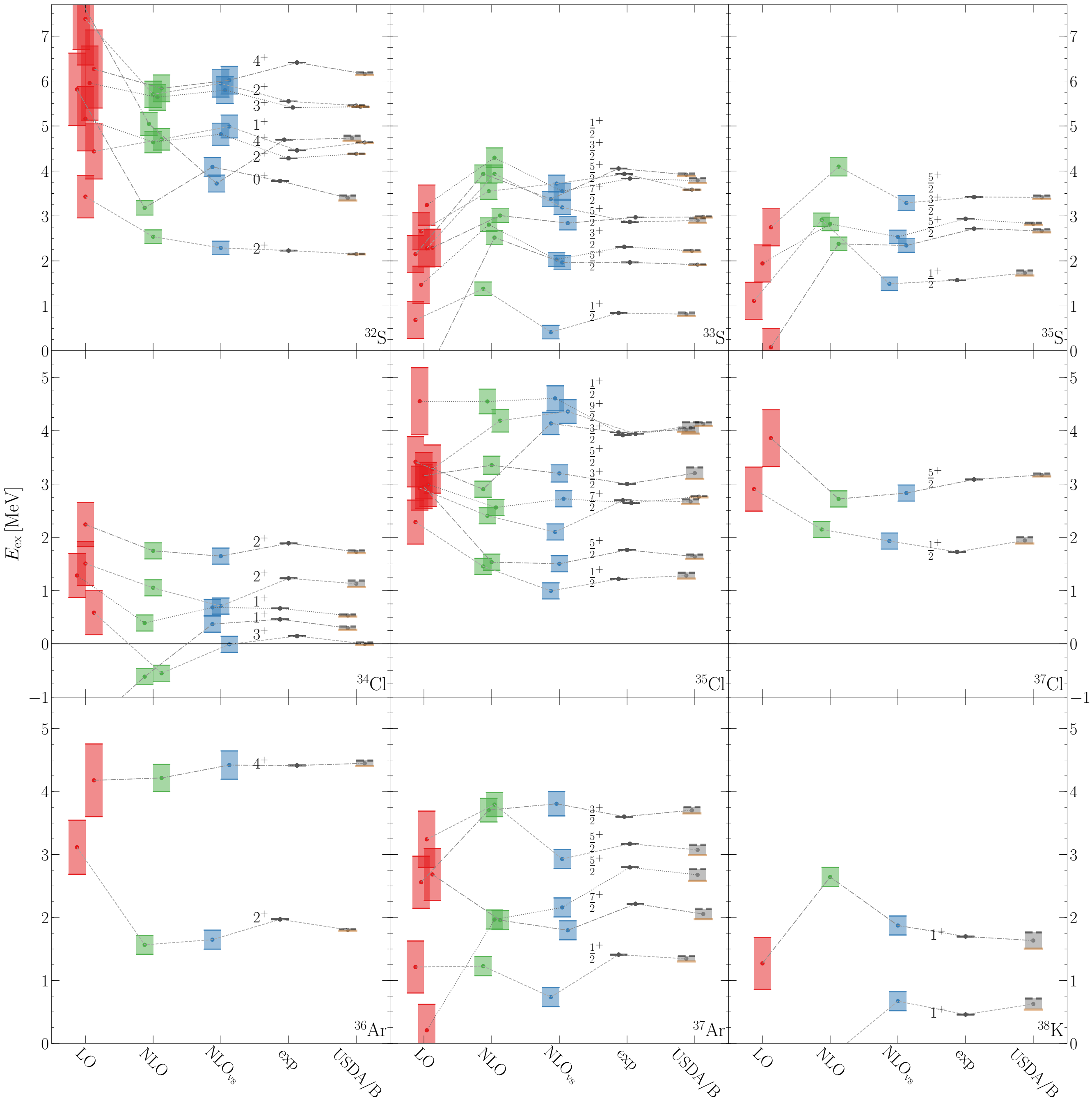

Figure 8.10.: Excitation spectra of selected isotopes from sulfur to potassium. For details see the caption of Fig. 8.8.

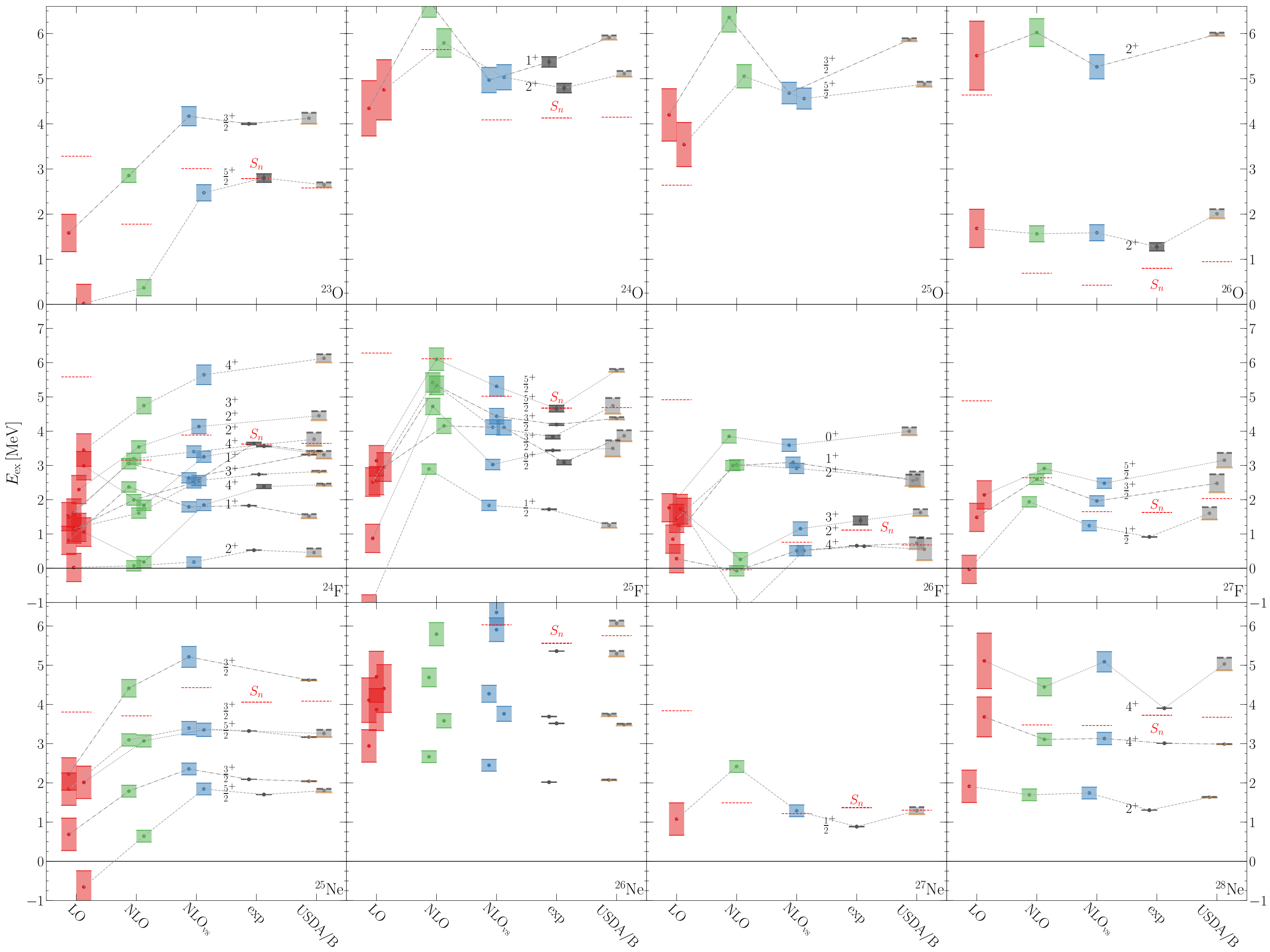

Figure 8.11.: Predictions of excited states in oxygen, fluorine, and neon isotopes. For details on the labeling see the caption of Fig. 8.8. In addition to the ENSDF [215] spectra, we compare our results to experimental data in ^{23}O [224, 225], ^{26}O [62], ^{24}F [226], and ^{25,26}F [227, 228]. Moreover, to emphasize the effects of the continuum, not included in our calculation, we give the calculated and experimental neutron separation energy S_n as horizontal dashed line (see text).

9 Shell-model interactions beyond NLO

After the great success of the shell-model interaction at NLO, we investigate subleading valence-space operators in this chapter. The next order in the chiral power counting that has new two-body contact interactions is N^{3}LO. As mentioned above, there are 15 new free-space operators and 32 new valence-space operators (see Eq. (3.14)) at this order. We fit the shell-model interactions up to N^{3}LO to the BR$_2$ data set from Tab. 7.2. A graphical representation of this data set is depicted in Fig. 7.5. Coulomb corrections are obtained with the DZ mass formula from Eq. (7.9), which differs from the Coulomb correction from the previous chapter. We use a different Coulomb correction for two reasons: First, the DZ Coulomb correction does explicitly consider the neutron number, hence, we expect it to be better suited for the neutron-rich region. Second, we aim to perform calculations outside of the sd shell later on. Starting with calcium, we have no values for the CH Coulomb correction from Ref. [114].

At N^{3}LO$_{\text{vs}}$ there are two LO LECs, seven plus five NLO LECs, 15 + 32 N^{3}LO LECs, which totals to 61 LECs. In addition to those, we include two charge-dependent LECs which enter at LO. This is one charge independence breaking operator (CIB) and one charge symmetry breaking operator (CSB), given by

$$\begin{gathered} V_{\text{CIB}}(\mathbf{p},\mathbf{p}') = C_{\text{CIB}}\frac{1+4\boldsymbol{\tau}_{1,z}\boldsymbol{\tau}_{2,z}}{2}\,, \\ \text{and} \\ V_{\text{CSB}}(\mathbf{p},\mathbf{p}') = C_{\text{CSB}}(\boldsymbol{\tau}_{1,z}+\boldsymbol{\tau}_{2,z})\,, \end{gathered} \tag{9.1}$$

with the Pauli matrices acting on the isospin of particle i, $\boldsymbol{\tau}_{i,z}$. The operators only contribute in neutron-neutron (nn) and proton-proton (pp) channels of the $^1S_0$ partial wave. Additionally we allow the SPEs to vary. In the sd channel this leads to three more parameters for neutron SPEs and proton SPEs each. We end up with 69 parameters in total, which is of the order of the parameters in the USDB (56) interaction from Ref. [114]. Those parameters are adjusted to experimental data with the LCM method (see Ch. 7).

This chapter starts with an investigation of the LECs and SPEs. After that, we compare our results to the USD-type interactions from Ref. [114]. This is followed by a general overview of the quality of the data reproduction. We then show results for ground-state energies and excitation energies. To conclude, we study some predictions in excitation spectra. Numerical values for SPEs and LECs for all interactions, as well as the TBMEs of the interaction at N^{3}LO$_{\text{vs}}$ are listed in App. E.3.

9.1 Low-energy constants

Before we compare our results to the USDA and USDB interaction from Ref. [114], we first analyze the LECs and SPEs resulting from the fit. In Fig. 9.1, we show the two LO LECs, C_S and C_T alongside the charge-dependent LECs C_{CIB} and C_{CSB} from Eq. (9.1), and the NLO LECs C_1–C_7 and P_1–P_5. At N^{3}LO, we only give the average value for the LECs D_{av} and Q_{av} to keep a structured overview. Those average LECs are plotted together with the standard deviation (thick line) and the minimum and maximum values connected by a thin line. Maxima and minima are annotated by corresponding LEC labels. All LECs are given in natural values. At LO and NLO, the natural values are obtained from Eq. (8.3) and Eq. (8.4), and at N^{3}LO we use

$$\begin{aligned} D_i\ [\text{nat. units}] &= D_i\cdot(F_\pi\Lambda^2)^2\,, \\ Q_i\ [\text{nat. units}] &= Q_i\cdot(F_\pi\Lambda^2)^2\,, \end{aligned} \tag{9.2}$$

where we take $\Lambda = \Lambda_{\text{HO}} \approx 375$ MeV. We added a yellow band to the figure, that provides a rough estimate of the region in which the LECs are considered natural. We also show an inset to enlarge the region of C_T, C_{CIB}, and C_{CSB}. The plot contains LECs of a LO, NLO$_{\mathrm{vs}}$, N^{2}LO$_{\mathrm{vs}}$, and N^{3}LO$_{\mathrm{vs}}$ interaction as well as a different result at N^{3}LO$_{\mathrm{vs}}$ with unnaturally large LECs (purple pluses). The LECs are determined with the linear-combination method from Subsec. 7.6.2. All interactions but the unnatural N^{3}LO$_{\mathrm{vs}}$ interaction are obtained with the control parameter set to $\delta = 0.01$.

One can see that all LECs aside from the D_2 and D_{14} values at N^{3}LO are located within the yellow band. However, the two outliers are located very close to this band. This is no longer the case in the unnatural N^{3}LO interaction. For those LECs we find that even the standard deviation for the D_i LECs is located outside of the region of naturalness. In addition, the minimum D_2 is roughly three times larger than the limit of the yellow band. It is worth noting that also here the D_2 (D_{14}) LEC marks the minimum (maximum) value. The Q_i values also lie further outside than we would expect for natural values. For the unnatural fit we have used a large value of the control parameter $\delta = 10$ in the LCM. From this, one sees that we are able to influence naturalness by adjusting the δ parameter in the LCM fit accordingly.

In Fig. 9.2, we depict the SPEs of the natural interactions. In the left panel, we show the LECs for neutrons and in the right panel those for protons. To have a rough estimate where the SPEs should be located at, we include the corresponding energies for ^{17}O (^{17}F) in the left (right) panel. Those energies are Coulomb corrected with Eq. (7.9) (DZ). In the left panel, the second neutron SPE is slightly off at LO compared to those at higher orders, and the third one lies far outside. The remaining orders are in good agreement. At N^{3}LO, the SPEs agree well with the first two ^{17}O energies. In the right panel, the proton SPEs are far off the ^{17}F states at LO. This might be the case because ^{17}F is not included in the BR$_2$ data set and the LO interaction has only very few parameters to adjust. As a consequence, the SPEs are forced towards different values. Again, the subleading orders agree well with each other and with the energies of ^{17}F. The order of the first two states is inverted at NLO, but they are very close to each other.

9.2 Comparison to USD-type interactions

With the new parameter set, we continue our comparison to the USD-type interactions [114] from Fig. 8.4. The complete comparison is given in Fig. 9.3. We show the RMS deviation from experiment for charge dependent interactions at LO, NLO$_{\mathrm{vs}}$, N^{2}LO$_{\mathrm{vs}}$, and N^{3}LO$_{\mathrm{vs}}$. In addition, we show results for the free-space operator interaction NLO, and the N^{3}LO$_{\mathrm{NLO,vs}}$ interaction, where the latter includes only leading valence-space operators that appear at NLO. Furthermore, we give the result for the unnatural interaction at N^{3}LO$_{\mathrm{vs}}$. The RMS deviations are plotted versus the total number of parameters, which includes LECs and SPEs. First, they are given in comparison to the results from Ref. [114] (BR). There are two major differences in this comparison. The original data set from BR includes more states than our BR$_2$ data set. This means although the RMS deviations are expected to be similar in both sets, they can not be seen as identical. The comparison is thus of a qualitative nature. Second, for the USD [114] interactions, only the number of adjusted linear combinations in the LCM method are considered as parameters. We show our results with respect to all parameters, even though the number of adjusted linear combinations is much lower.

To give an example: At N^{3}LO$_{\mathrm{vs}}$ we have 69 parameters. With δ set to 0.01, in the first step of our interaction we adjust only 49 linear combinations out of those 69 parameters. However, depending on the starting value and the progress of the fit this number changes frequently. We therefore prefer to show the total number of parameters. When we set $\delta = 10$ for the unnatural interaction, we adjust 64 of the 69 parameters in the first step.

In Fig. 9.3 we observe a very systematic decrease of the RMS deviation from order to order for our interactions. This decrease is rapid from LO to NLO and also from NLO to NLO$_{\mathrm{vs}}$. The N^{2}LO$_{\mathrm{vs}}$ interaction has the same number of LECs as the NLO$_{\mathrm{vs}}$ interaction. The difference between both orders roots in differences of the two-pion–exchange potential. In the valence space, we find that the interaction at N^{2}LO$_{\mathrm{vs}}$ performs slightly worse compared to the interaction at NLO$_{\mathrm{vs}}$. Compared to the latter two, the N^{3}LO$_{\mathrm{NLO,vs}}$ interaction has 15 new free-space operators. The RMS deviation decreases again, but not as rapidly as before. The full N^{3}LO$_{\mathrm{vs}}$ interaction has 32 new valence-space operators compared to the last

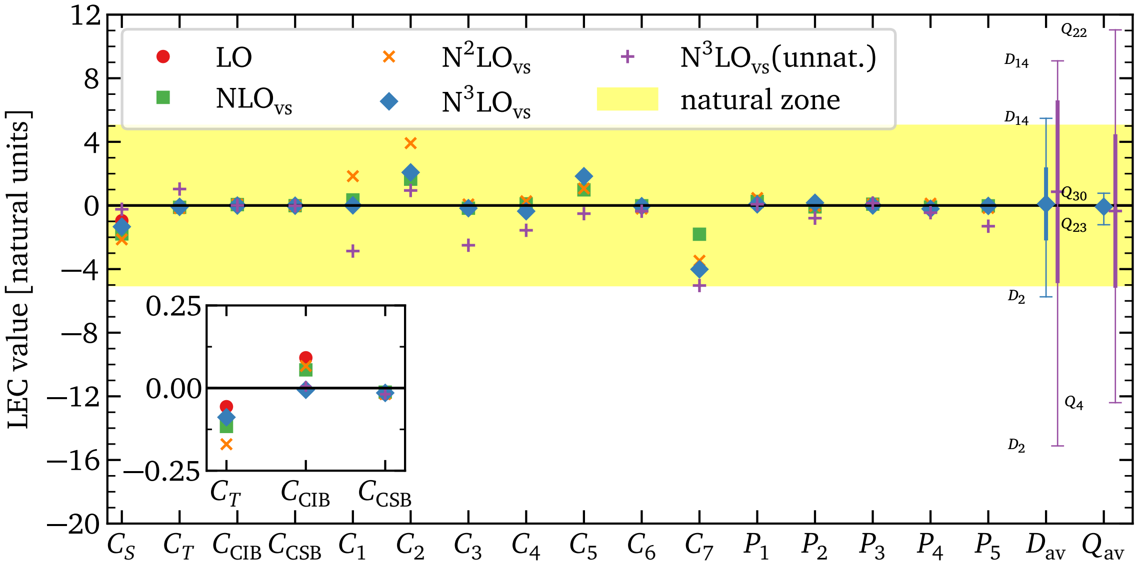

Figure 9.1.: Fitted LECs for charge-dependent shell-model interactions at LO, NLO$_{vs}$, N^{2}LO$_{vs}$, and N^{3}LO$_{vs}$ in natural units, which are obtained using Eqs. (8.3), (8.4), and (9.2). At N^{3}LO$_{vs}$, we show the average D_i and Q_i value with the standard deviation (thick line), as well as the minimum and maximum LEC connected by a thin line. The minima and maxima are labeled by the LEC that takes that value. In addition, we show an unnatural version of N^{3}LO$_{vs}$ (purple). We give a magnification for C_T, C_{CIB}, and C_{CSB} for visual purposes. The yellow band is a visual aid to determine natural parameters.

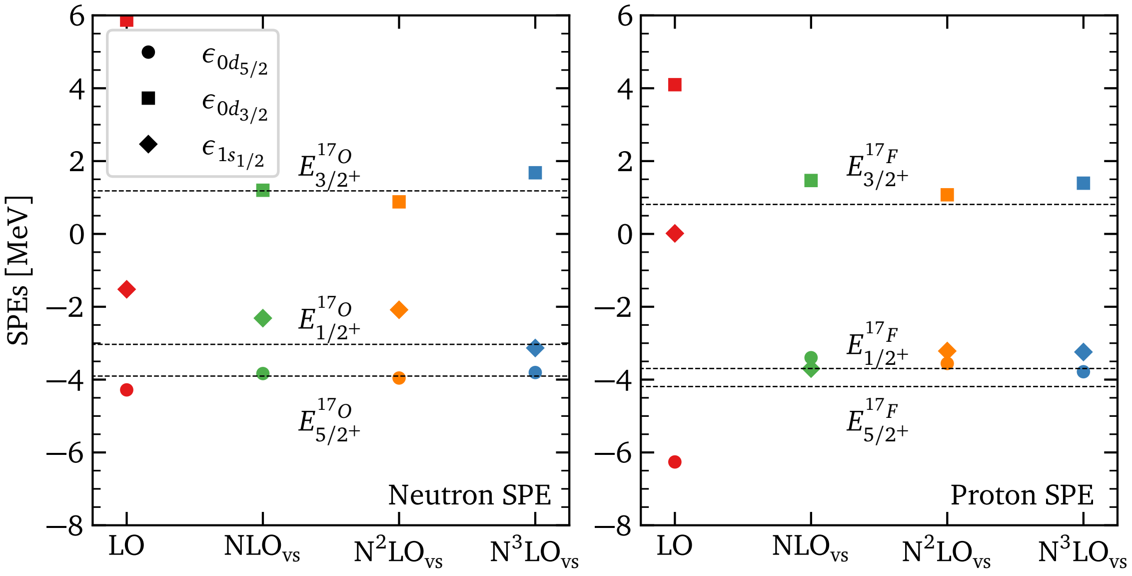

Figure 9.2.: Fitted SPEs for the charge-dependent shell-model interactions. From left to right, we show the different SPEs for the LO, NLO$_{vs}$, N^{2}LO$_{vs}$, and N^{3}LO$_{vs}$ interaction. In the left panel, we depict the neutron SPEs, in the right panel the proton SPEs. The dashed lines give the results for Coulomb corrected ^{17}O states (left panel) and Coulomb corrected ^{17}F states (right panel) (see Eq. (7.9) for the Coulomb correction).

interaction, which helps to lower the RMS deviation yet again to a level, which is comparable to that of the USDA and USDB interaction from Ref. [114]. In Tab. 9.1, we list the interaction label, the number of

Table 9.1.: We list the interaction label, number of parameters (SPEs + LECs), RMS deviation from experiment in keV for charge-dependent chiral shell-model interactions at LO, NLO, NLO_{vs}, $\text{N}^2\text{LO}_{\text{vs}}$, $\text{N}^3\text{LO}_{\text{NLO, vs}}$, and $\text{N}^3\text{LO}_{\text{vs}}$. We compare them to the RMS deviation of the USD fit from Ref. [114] for the same number of parameters (last column).

Interaction	#parameters	RMS [keV]	USD [keV]
LO	10	928	380
NLO	17	609	250
NLO_{vs}	22	437	200
$\text{N}^2\text{LO}_{\text{vs}}$	22	510	200
$\text{N}^3\text{LO}_{\text{NLO, vs}}$	37	288	170
$\text{N}^3\text{LO}_{\text{vs}}$	69	161	130
$\text{N}^3\text{LO}_{\text{vs}}$ (unnat.)	69	122	130

parameters (LECs + SPEs), the RMS deviation to experiment in keV, and the approximate RMS deviation of the BR line from Fig. 9.3 at the same number of parameters.

As one can see in Tab. 9.1, with ten parameters to adjust we obtain an RMS deviation of 928 keV at LO. The seven new free-space operators at NLO help to reduce this value to 609 keV, which is an improvement of roughly 300 keV (∼ 45 keV per new LEC). The five new valence-space operators at NLO_{vs} further reduce this value to 437 keV (∼ 30 keV per new LEC). At this order, there are 22 LECs in total, which reduce the RMS deviation by more than half compared to that at LO. As mentioned above, there is no improvement at $\text{N}^2\text{LO}_{\text{vs}}$. Comparing the $\text{N}^3\text{LO}_{\text{NLO, vs}}$ interaction with its 15 new free-space operators to NLO_{vs}, we find that the RMS value is reduced by roughly 150 keV, which is about 10 keV for each new LEC. The decreasing improvement at higher orders is exactly what we expect from chiral interactions, as the most important contributions appear at LO and the most important corrections at NLO. In the full $\text{N}^3\text{LO}_{\text{vs}}$ interaction, we achieve a RMS deviation of roughly 160 keV. This is very close to the results of the USDA (170 keV) and USDB (130 keV) interactions (see Ref. [114])⁽¹⁾. In the last row of Tab. 9.1 we show our result for the interaction that is allowed to take unnaturally large values. We obtain a RMS deviation of 122 keV, which is very close to the RMS deviation of the USDB interaction. This value marks the optimum that we can achieve with a two-body interaction for our data set. The difference to the natural version is only 36 keV.

In Fig. 9.4, we show a comparison of the TBMEs at LO, NLO_{vs}, and $\text{N}^3\text{LO}_{\text{vs}}$ to those of the USDA and USDB interactions. In the left panel, we compare TBMEs with isospin $T = 0$, in the right panel those with isospin $T = 1$ (and $m_T = 0$). Exemplary far outlying states in this figure are annotated with the single particle angular momenta and the total angular momentum denoted as $2j_a 2j_b 2j_c 2j_d(J)$. We find that all interactions have TBMEs close to the diagonal line, i.e., similar to USDA.

9.3 Overview

As in the previous chapter, we investigate the quality of our interactions by considering the RMS deviation of individual isotopes in the BR_2 data set. For each nucleus in the data set, we show a qualitative RMS deviation at LO and NLO_{vs} in Fig. 9.5, and at $\text{N}^3\text{LO}_{\text{NLO, vs}}$ and $\text{N}^3\text{LO}_{\text{vs}}$ in Fig. 9.6. The deviation is given by a color coding, where nuclei with a small RMS deviation are colored green, and those which deviate further are colored red. In both figures, we plot the proton number versus the neutron number. The states are visualized by a box which shows the isotope label. In the lower right corner of each box, we

---

(1) As mentioned above, the comparison is not exact due to slightly different data sets and Coulomb corrections.

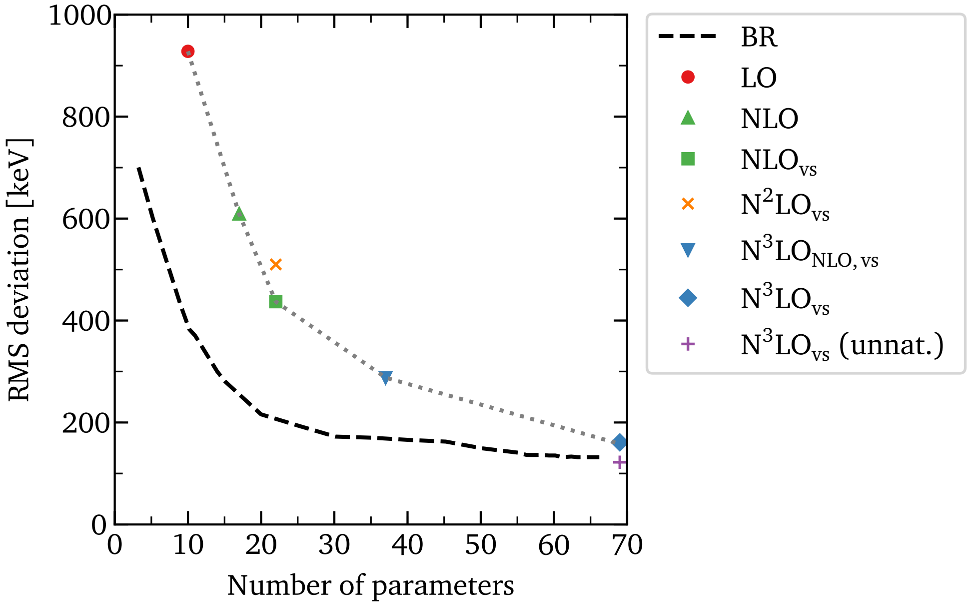

Figure 9.3.: Comparison of RMS deviation of shell-model interactions at LO, NLO, NLO$_{\mathrm{vs}}$, N^{2}LO$_{\mathrm{vs}}$, N^{3}LO$_{\mathrm{NLO,\,vs}}$, N^{3}LO$_{\mathrm{vs}}$ as well as an unnatural version (unnat.) at N^{3}LO$_{\mathrm{vs}}$ (see Fig. 9.1) fitted to the BR$_2$ data set from Tab. 7.2. For comparison, we show USD-type interactions (BR) taken from Ref. [114].

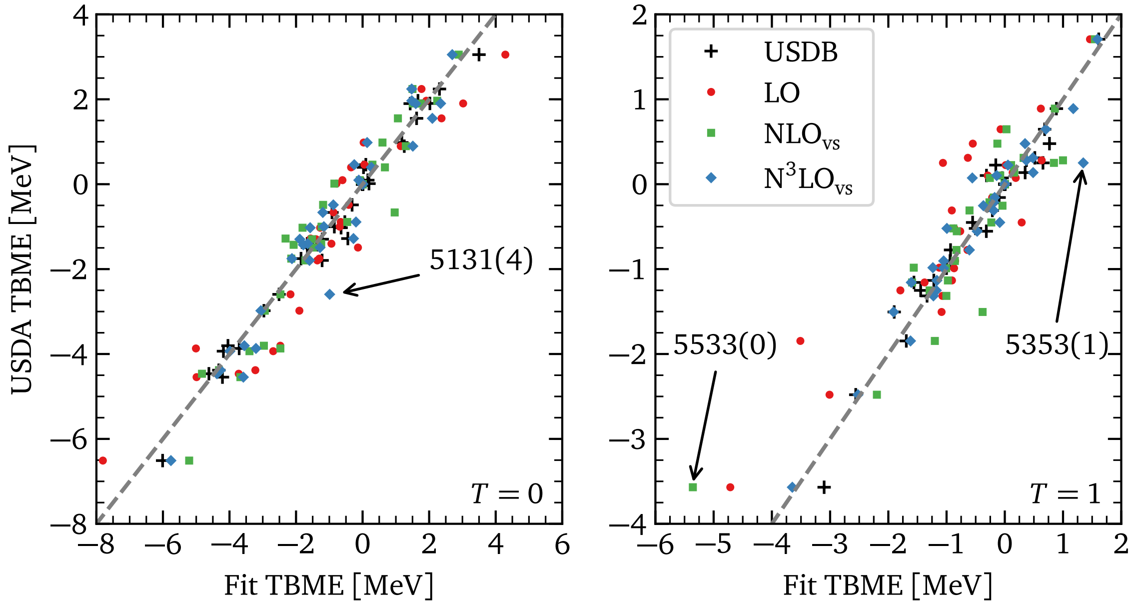

Figure 9.4.: Comparison of the TBMEs at LO, NLO$_{\mathrm{vs}}$, and N^{3}LO$_{\mathrm{vs}}$ to the USDA and USDB interactions from Ref. [114]. On the left, we display the TBMEs with isospin $T = 0$, on the right those with $T = 1$ for $m_T = 0$. Exemplary outlying states at NLO$_{\mathrm{vs}}$ and N^{3}LO$_{\mathrm{vs}}$ are annotated and labeled according to their angular momenta as $2j_a 2j_b 2j_c 2j_d(J)$.

show the total number of considered states in the isotope at hand. For the LO and NLO$_{\mathrm{vs}}$ interaction in Fig. 9.5, the color coding ranges from 0 MeV (green) to 1 MeV and above (red). For the N^{3}LO$_{\mathrm{NLO,\,vs}}$ and N^{3}LO$_{\mathrm{vs}}$ interaction in Fig. 9.6, it ranges from 0 MeV (green) to 0.5 MeV (red).

The LO interaction performs best in the neutron-rich region, compared to the rest of the data set. This is probably related to the large value of the neutron $0d_{3/2}$ SPE (see Fig. 9.2). The improvement from LO

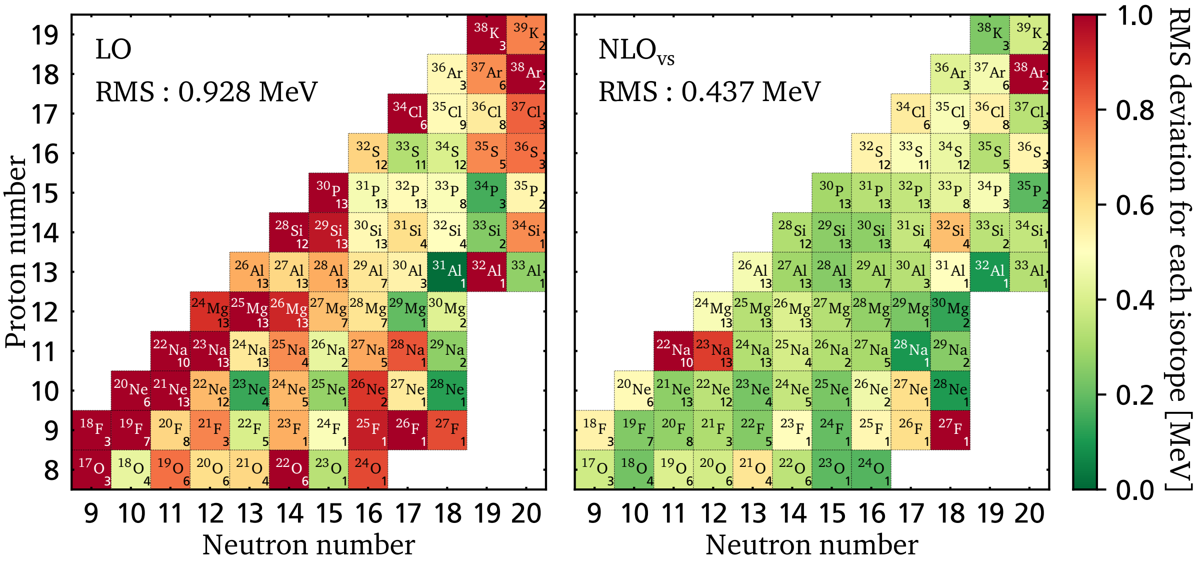

Figure 9.5.: Graphical representation of the RMS deviation from experiment for each fitted nucleus in the sd shell. The figure shows the results for the charge-dependent chiral shell-model interactions LO (left) and NLO$_{\mathrm{vs}}$ (right). The color coding of the RMS deviation is given in the bar on the right. Isotopes with a small RMS deviation are colored green, while those with a large deviation are colored red. Each square shows the isotope label and the number of fitted states in the bottom right corner. The total RMS deviation is given on the upper left side of each panel.

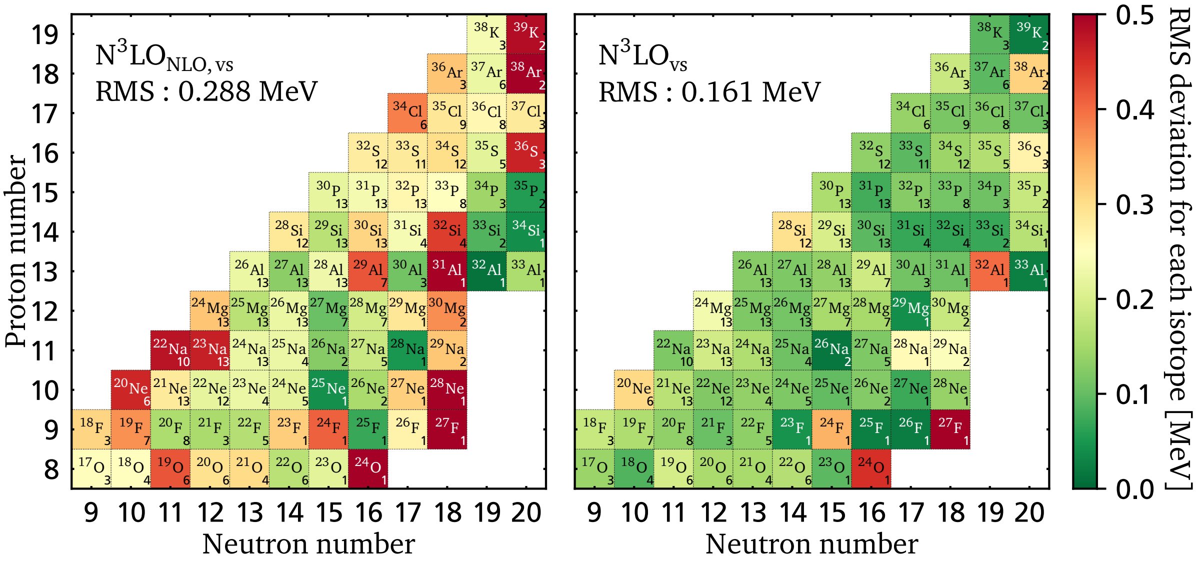

Figure 9.6.: Graphical representation of the RMS deviation from experiment for each fitted nucleus in the sd shell. The figure shows the results for the charge-dependent chiral shell-model interactions N^{3}LO$_{\mathrm{NLO,vs}}$ (left) and N^{3}LO$_{\mathrm{vs}}$ (right). The color coding of the RMS deviation is given in the bar on the right. Isotopes with a small RMS deviation are colored green, while those with a large deviation are colored red. In contrast to similar plots in this thesis, the color coding in this plot ranges only to 0.5 MeV. Each square shows the isotope label and the number of fitted states in the bottom right corner. The total RMS deviation is given on the upper left side of each panel.

to $\mathrm{NLO}_{\mathrm{vs}}$ is clearly visible. Overall, the reproduction at $\mathrm{NLO}_{\mathrm{vs}}$ looks promising, with only a few outlying states. This is similar to what we have observed for the charge-independent interaction at $\mathrm{NLO}_{\mathrm{vs}}$ in Ch. 8. The outliers are ^{22,23}Na and ^{38}Ar, which were also observed in the charge-independent interaction from Fig. 8.2. The states ^{21}O, ^{31}Al, ^{32}Si, ^{36}S, and ^{39}K, which are additional outliers of the charge-independent interaction from the previous chapter, are much better reproduced by the charge-dependent interaction. This is due to the SPEs, which are used as parameters in this interaction, as well as the charge-dependent LECs. One needs to keep in mind that the Coulomb correction schemes differ between those two interactions (see. Tab. 7.2 for BR_1 and BR_2). The largest differences between the two Coulomb corrections appear in the neutron-rich region. We discuss the outliers in ^{22}Na and ^{38}Ar explicitly in Sec. 9.5 of this chapter. One additional outlying state is ^{27}F. This one is better reproduced by the charge-independent interaction from the previous chapter. The data set only considers the ground state in this nucleus, which overestimates the binding energy by roughly 1 MeV compared to experiment. This amounts to a deviation of only 2% with respect to the ground-state energy on top of the ^{16}O core. Also, the experimental uncertainty for the ^{27}F ground-state energy is 0.39 MeV [105], which is large compared to uncertainties of other ground-state energies. This large uncertainty influences the χ^2 minimization, as it allows larger deviations of this state in the optimization compared to other states.

The improvement from $\mathrm{NLO}_{\mathrm{vs}}$ to $\mathrm{N}^3\mathrm{LO}_{\mathrm{NLO,vs}}$ is not as striking, since we change the values for the color coding from 1 MeV for the maximum deviation to 0.5 MeV in Fig. 9.6. However, the total RMS deviation given in the upper left corner of each panel decreases. Also the interaction at $\mathrm{N}^3\mathrm{LO}_{\mathrm{NLO,vs}}$, with a total RMS deviation of 288 keV performs well in the data set. There are more outliers, as the color coding is different. The outliers are very similar to those of the charge-independent interaction $\mathrm{NLO}_{\mathrm{vs}}$ from Fig. 8.2. Also here we find ^{27}F, ^{22,23}Na, and ^{38}Ar among them. The next step to the full $\mathrm{N}^3\mathrm{LO}_{\mathrm{vs}}$ interaction shows drastic improvement. Nearly all outliers at $\mathrm{N}^3\mathrm{LO}_{\mathrm{NLO,vs}}$ are sufficiently well reproduced at $\mathrm{N}^3\mathrm{LO}_{\mathrm{vs}}$ and only two of them remain. These are ^{24}O and ^{27}F. In addition, we find that ^{32}Al deteriorates a bit. For all of those states, we consider only the ground-state energy, which we discuss in detail in the following section.

In Fig. 9.7, we show a global overview of the energy difference for all states in the data set. The upper row shows results for ground-state deviations to experiment, whereas the lower row shows deviations for excitation energies. From left to right we show results for the charge-dependent LO, $\mathrm{NLO}_{\mathrm{vs}}$, $\mathrm{N}^2\mathrm{LO}_{\mathrm{vs}}$, and $\mathrm{N}^3\mathrm{LO}_{\mathrm{vs}}$ interaction. In addition, we show one- and two-σ bands that give the statistical spread. The improvement from LO to $\mathrm{NLO}_{\mathrm{vs}}$ is easily visible. At LO the statistical spread for ground states is smaller than that for excitation energies. For all higher orders, the spread for excited states is narrower than that for ground-state energies. At $\mathrm{NLO}_{\mathrm{vs}}$, the spread for excited states improves drastically compared to LO, where even the two-σ band at $\mathrm{NLO}_{\mathrm{vs}}$ is smaller than the one-σ band at LO. The spread of the ground-state energies at $\mathrm{NLO}_{\mathrm{vs}}$ is smaller compared to LO, but the reduction is not as overwhelming as for the excitation energies. At $\mathrm{NLO}_{\mathrm{vs}}$, excited states for the first sodium isotopes lie outside of the two-σ band, which coincides with the outliers from Fig. 9.5. One can see that the σ bands increase slightly from $\mathrm{NLO}_{\mathrm{vs}}$ to $\mathrm{N}^2\mathrm{LO}_{\mathrm{vs}}$. At $\mathrm{N}^3\mathrm{LO}_{\mathrm{vs}}$, the σ bands decrease drastically for ground-state and excitation energies. We annotate the ground state of ^{27}F, which is the outlying state from Fig. 9.6. One can see that this state improves at $\mathrm{N}^3\mathrm{LO}_{\mathrm{vs}}$. However, the improvement is much less than for other states. Since we were able to reproduce the ground state in Ch. 8, where a different Coulomb correction was used, this might be a signal that the DZ Coulomb correction is less favorable for neutron-rich isotopes.

9.4 Ground-state energies

In this section, we consider ground-state energies for different isotopic chains. The chains are presented in Fig. 9.8 for isotopes from oxygen to aluminum and in Fig. 9.9 for isotopes from silicon to potassium. Experimental states and uncertainties to which we fit our interaction are colored black, and experimental states that are not included in the BR_2 data set are colored red. We present our results with EFT uncer-

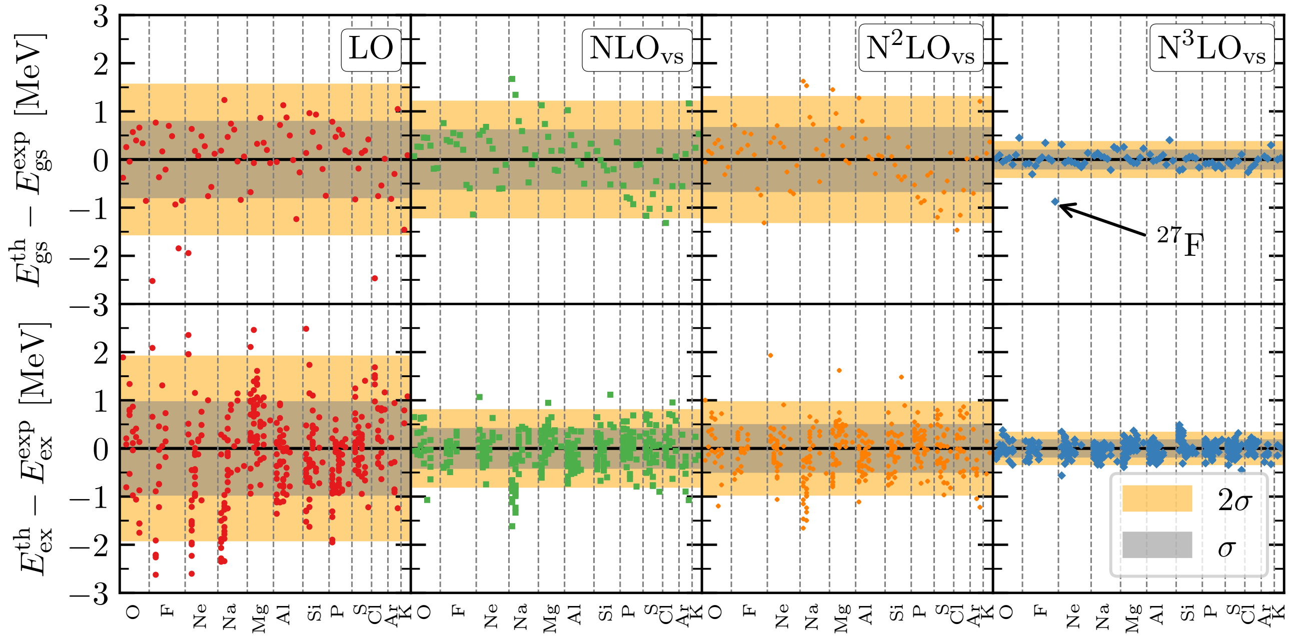

Figure 9.7.: Energy differences of the results from the chiral shell-model interactions and experiment in MeV. The upper row shows results for ground-state (gs) energies whereas the lower row is for the energies of excited (ex) states. Each dot represents a single state, and they are ordered from oxygen to potassium. Within each bin, they are ordered according to their mass number. From left to right, we present results for the charge-dependent LO, NLO$_{\mathrm{vs}}$, N^{2}LO$_{\mathrm{vs}}$, and N^{3}LO$_{\mathrm{vs}}$ interaction. The gray (orange) bands show the statistical σ (2σ) spread, given by the RMS deviation.

tainty bands at LO, NLO$_{\mathrm{vs}}$, N^{2}LO$_{\mathrm{vs}}$, and N^{3}LO$_{\mathrm{vs}}$. In the last two panels of Fig. 9.9, we show uncertainties bars rather than a band, as a band might be misleading for only a few states.

In the first panel of Fig. 9.8, we show ground-state energies for oxygen isotopes. In comparison to the oxygen isotopes from Fig. 8.7, one can immediately see that the LO interaction now reproduces the oxygen dripline correctly within uncertainties. We attribute this behavior mostly to the variation of the SPEs, and not to the new charge-dependent operators, as we find similar results for the charge-independent interactions when allowing SPEs to vary (not explicitly shown here). The experimental states are well reproduced at each order. One further sees a systematic behavior for different orders and the corresponding uncertainty bands. Within uncertainties, the dripline is predicted correctly at ^{24}O at each order, and all interactions agree with the ground-state energies of ^{25}O and ^{26}O. At N^{3}LO$_{\mathrm{vs}}$, the ^{26}O ground state is predicted to be bound as soon as Coulomb contributions are included. Without Coulomb, it is unbound under two-neutron emission. In particular, we find for the strong part of the binding energy at N^{3}LO$_{\mathrm{vs}}$

$$E_{^{24}\mathrm{O}}^{\mathrm{strong}} - E_{^{16}\mathrm{O}}^{\mathrm{strong}} = -39.61\ \mathrm{MeV}\ (-40.06\ \mathrm{MeV}), \tag{9.3}$$

$$E_{^{26}\mathrm{O}}^{\mathrm{strong}} - E_{^{16}\mathrm{O}}^{\mathrm{strong}} = -39.47\ \mathrm{MeV}\ (-39.85\ \mathrm{MeV}), \tag{9.4}$$

$$E_{^{24}\mathrm{O}}^{\mathrm{strong}} - E_{^{26}\mathrm{O}}^{\mathrm{strong}} = -0.14\ \mathrm{MeV}\ (-0.21\ \mathrm{MeV}), \tag{9.5}$$

with results from theory (experiment) in MeV. With the DZ Coulomb correction scheme, we obtain a difference of $E_{^{24}\mathrm{O}}^{\mathrm{Coul}} - E_{^{26}\mathrm{O}}^{\mathrm{Coul}} = 0.19$ MeV. Thus, the dripline at N^{3}LO$_{\mathrm{vs}}$ is predicted falsely at ^{26}O with an energy difference of 0.05 MeV compared to ^{24}O. In experiment, the energy difference between ^{24}O and ^{26}O is −0.02 MeV [62], hence, ^{26}O is unbound. However, one needs to keep in mind that the strong part of the interaction nearly reproduces the experimental energies and the energy difference is well below theoretical uncertainties. Additional investigations of the Coulomb correction in the neutron-rich region need to be considered in future work.

A similar behavior as in oxygen is visible for fluorine isotopes in the second panel. The correct trend is predicted already at LO, which was not the case for the charge-independent LO interaction. At $\mathrm{NLO_{vs}}$ and beyond, the central values of our interactions tend to slightly overestimate the binding energy in the neutron-rich region, but the shape is still well reproduced. The overestimation of the binding energies starts at ^{27}F, but this state is still correctly reproduced within uncertainties by all interactions. This also holds for the prediction of the ground-state energy of ^{28}F. The state is accurately described within uncertainties by all interactions but the central values are at higher binding energies. The predicted ground-state energy of ^{29}F is in very good agreement with the experimental result for all interactions.

The subsequent three panels show the isotopic chains of neon, sodium, and magnesium. The ground states which are included in the $\mathrm{BR_2}$ data set (black) are well reproduced by all interactions. The last two states of each of those chains are not present in the $\mathrm{BR_2}$ data set, as those states are in (or close to) the so-called island of inversion [203–206, 208]. This is a region, in which pf orbits are energetically below the $0d_{3/2}$ orbit. Thus, excitations out of the sd shell need to be considered for a correct description of the experimental data. A pure sd-shell theory is expected to underestimate the binding energy of those isotopes. This is in fact what we observe in ^{29,30}Ne, ^{30,31}Na, and ^{31,32}Mg. Our theory predicts the right trend for those states, but it underestimates the binding energy by a few MeV. This can be seen best in the $\mathrm{N^3LO_{vs}}$ interaction, where the uncertainty band is narrow.

In aluminum, all of the states we show are present in the $\mathrm{BR_2}$ data set. This is also the case for the ground states from silicon to potassium in Fig. 9.9. All of those isotopic chains are well reproduced by each of our interactions.

9.5 Excitation spectra

In this section, we show the excitation spectrum for selected isotopes in the sd shell. We compare our interactions to experimental states in the NNDC data base [215]. Experimental states that are not in the $\mathrm{BR_2}$ data set to which the interactions are fit are colored red. In each panel, we show excitations on top of the experimental ground state at LO, $\mathrm{NLO_{vs}}$, $\mathrm{N^2LO_{vs}}$, and $\mathrm{N^3LO_{vs}}$ in comparison to the experimental measurements. The states we show are positioned slightly shifted from the center position along the "x" axis, where the shifts are according to their angular momentum. Small momenta are shifted to the left, while large ones are shifted to the right. To guide the eye we connect corresponding states by a gray line. We use three different, alternating line styles for clarity. Angular momentum labels J^π are given next to the experimental states. In each of the following figures, we show excitation spectra for two different representatives of each isotope. In order to keep a clear overview, we do not necessarily show all the states that we fitted. If present in the energy spectrum, we show the neutron (two-neutron) separation energy S_n (S_{2n}) obtained with Eq. (1.2) as a red dotted (dashed) line.

In Fig. 9.10, we show spectra for ^{19,22}O, ^{19,22}F, and ^{21,26}Ne. To begin our discussion, we consider excited states in ^{19}O, ^{19}F, and ^{21}Ne and compare them to our results for the charge-independent interaction in Fig. 8.8. For the charge-independent interaction from the previous chapter, the first two excited states of ^{19}O were in the wrong order at LO and they overlapped at $\mathrm{NLO_{vs}}$. Neither of those interactions reproduced the experimental values. This issue no longer persists in the charge-dependent interaction. The correct order of those two states is already reproduced at LO, and the energy of the $1/2^+$ state is well reproduced starting with $\mathrm{NLO_{vs}}$. The energy of the first excited $3/2^+$ state is overestimated at each order. However, there is a significant improvement at $\mathrm{N^3LO_{vs}}$. The $9/2^+$ state is well described for interactions beyond LO. The $7/2^+$, $3/2^+$, and $5/2^+$ states are all overestimated at LO, $\mathrm{NLO_{vs}}$, and $\mathrm{N^2LO_{vs}}$ by roughly 1 MeV. The $7/2^+$ and $3/2^+$ agree well with experiment at $\mathrm{N^3LO_{vs}}$. The $5/2^+$ remains at the same energy as in the $\mathrm{NLO_{vs}}$ interaction.

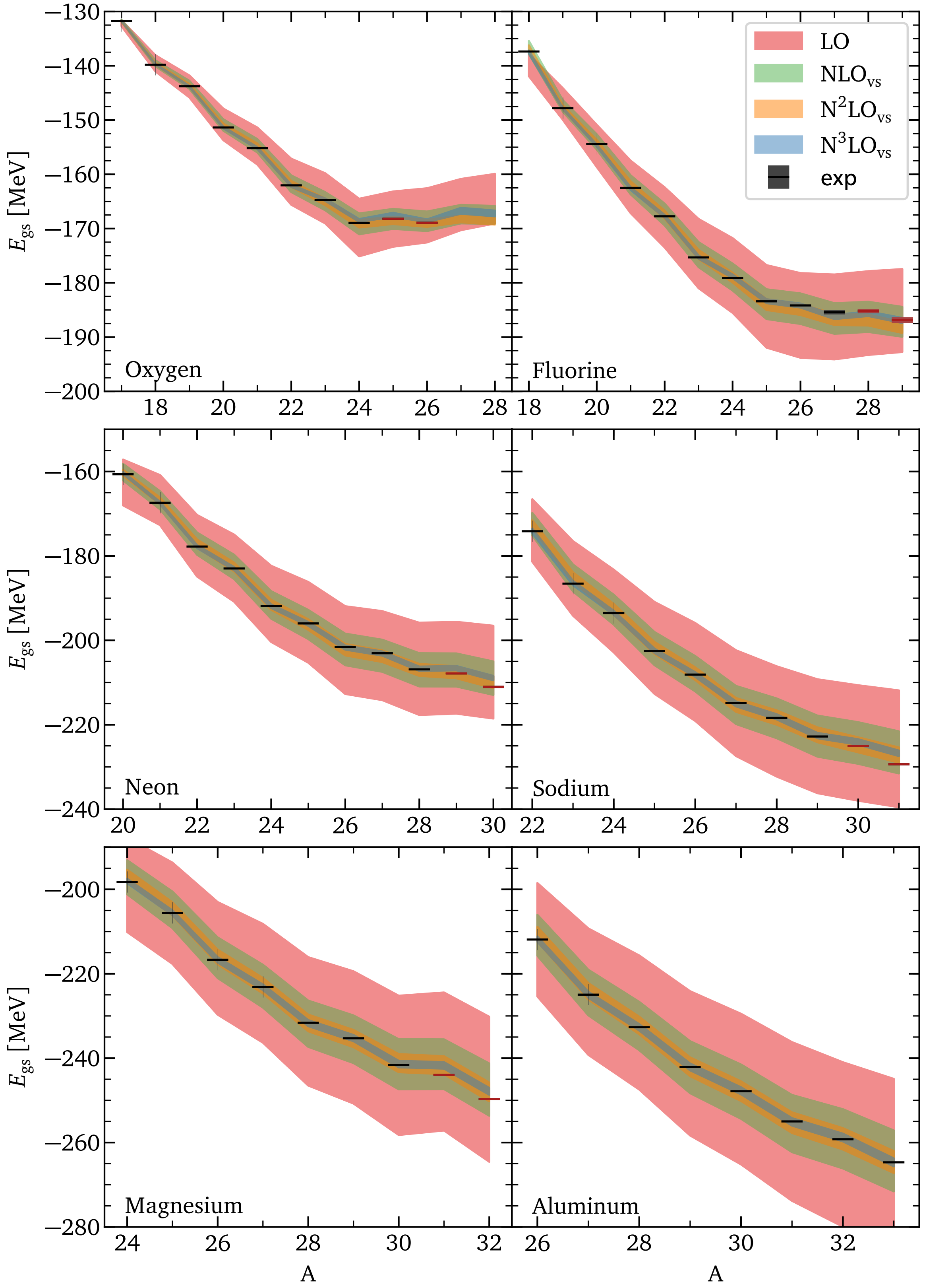

Figure 9.8.: Ground-state energies for sd-shell nuclei from oxygen to aluminum. We show results for fits to the BR$_2$ data set (see Tab. 7.2). The Coulomb energy is taken from the DZ mass formula from Eq. (7.9). We show charge-dependent interactions at LO, NLO$_{vs}$, N^{2}LO$_{vs}$, and N^{3}LO$_{vs}$ with chiral EFT uncertainties from Eqs. (7.15 - 7.17). Experimental states that are not included in the BR$_2$ data set are colored red.

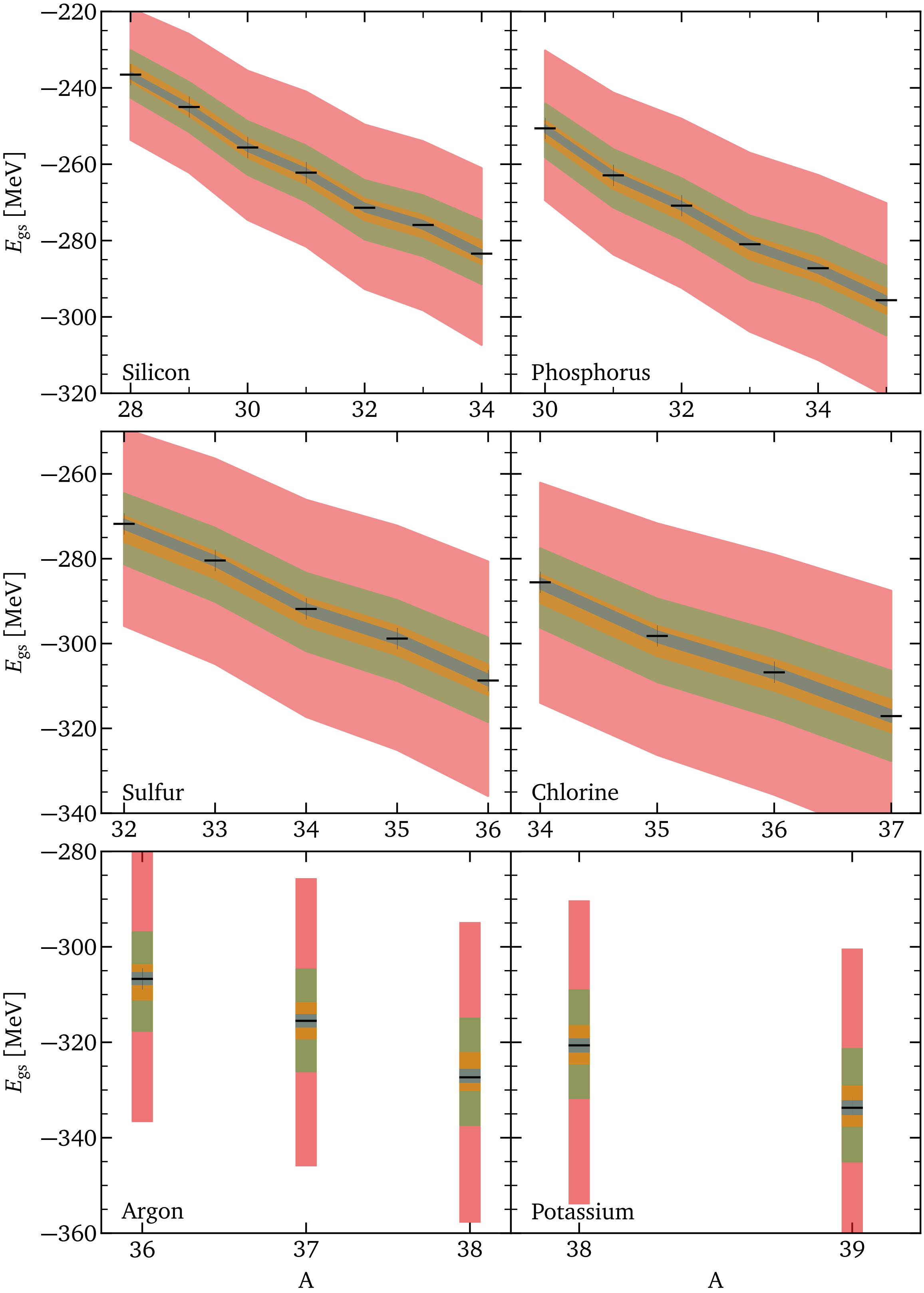

Figure 9.9.: Ground-state energies for sd-shell nuclei from silicon to potassium. For details see the legend and caption of Fig. 9.8.

For ^{19}F, our BR$_1$ and BR$_2$ data sets differ for some states. We want to compare the first excited $5/2^+$ state first. In the previous section, we were not able to reproduce the right ground state energy, as the NLO$_{\text{vs}}$ interaction returned this state at negative energies. Our charge-dependent interactions behave better. Although the NLO$_{\text{vs}}$ and N^{2}LO$_{\text{vs}}$ interaction lead to a negative $5/2^+$ excitation, the uncertainty estimates agree with the experimental state. At N^{3}LO$_{\text{vs}}$, the theory still underestimates the experimental energy, but the state is predicted at positive energies. The remaining two states in the BR$_2$ data set are well reproduced at each order. Above the $9/2^+$ state are two states, which are not in that data set. The $7/2^+$ is predicted at the right energy, the $3/2^+$ however is overestimated by more than 2 MeV. In ^{21}Ne, the LO and NLO$_{\text{vs}}$ interactions perform similar to the charge-independent version. We see that the first excited $5/2^+$ state is reproduced within uncertainties at NLO$_{\text{vs}}$. At N^{3}LO$_{\text{vs}}$, the state agrees well with the experimental result despite the narrow uncertainty. In addition, the states above are well reproduced at N^{3}LO$_{\text{vs}}$. To conclude the comparison to the charge-independent interaction, one sees that especially the reproduction of low-lying excitations improves remarkably at N^{3}LO$_{\text{vs}}$. We will focus the remaining part of the discussion mainly on the NLO$_{\text{vs}}$ and N^{3}LO$_{\text{vs}}$ interaction, as those interactions result in the best description of the experimental data.

The upper right panel depicts the spectrum of ^{22}O. The first state is well reproduced by all interactions, the 3^+ state above is underestimated at NLO$_{\text{vs}}$ by nearly 1 MeV. At N^{3}LO$_{\text{vs}}$, this state is overestimating by a few hundred keV, but it is reproduced within uncertainties. The 0^+ state is reproduced at NLO$_{\text{vs}}$ and N^{3}LO$_{\text{vs}}$. In the second panel of the right column, we depict the ^{22}F spectrum. First of all, there are many predictions provided in this spectrum. The states included in the fit are the first 3^+ and 5^+, as well as the two 1^+ states above. There is improvement in the low-lying 3^+ state as we increase the order of the power counting. At N^{3}LO$_{\text{vs}}$ the experimental state is overestimated by about 0.1 MeV. The 5^+ and 1^+ states (dashed and dash-dotted line) are underestimated at N^{3}LO$_{\text{vs}}$ by about 0.1 - 0.2 MeV each. The second 1^+ state is described well within uncertainties. Predictions at N^{3}LO$_{\text{vs}}$ for the first 2^+ and 3^+ state agree fairly well with experiment, the second 5^+ state is slightly underestimated by about 0.2 MeV. Remaining predictions, mainly for 2^+ states are not in agreement with experiment, which is evident from the steep slope of the connecting lines. Overall, the fitted states are close to the experimental states and so are predictions for the first J^π states. Further predictions for second and third J^π states predominantly disagree with experiment. In the last panel, we depict the excitation spectrum of ^{26}Ne. Both the interaction at NLO$_{\text{vs}}$ and N^{3}LO$_{\text{vs}}$ are in good agreement with the fitted 2^+ state. The interactions also agree within uncertainties with the prediction of the second 2^+ state. At N^{3}LO$_{\text{vs}}$, the interaction improves and is shifted towards the experimental energy. All interactions overestimate the 0^+ excitation, and there is only little improvement at N^{3}LO$_{\text{vs}}$. The neutron separation energy is in good agreement with the experimental value at this order.

For most of those states above, we find a good overall reproduction. This is visible by the majority of approximately horizontal connecting lines between the interaction at N^{3}LO$_{\text{vs}}$ and experiment. Only few states show larger deviations. For the rest of this section, we focus mainly on those overall observations.

In Fig. 9.11, we present excitation spectra for ^{22,24}Na, ^{25,27}Mg, and ^{29,30}Al. From the mostly horizontal connecting lines between the interaction at N^{3}LO$_{\text{vs}}$ and experiment, the good overall agreement is visible. In the first panel we show the spectrum of ^{22}Na. This is one of the outlier states at NLO$_{\text{vs}}$, which we discussed in the global observation in Sec. 9.3. There are large deviations between experiment and the interaction at NLO$_{\text{vs}}$. Starting with the first two excited states, that are at energies below 0 MeV, results from this interaction in general seam to be shifted downwards in energy by a nearly constant value compared to those at N^{3}LO$_{\text{vs}}$. At N^{3}LO$_{\text{vs}}$, the experimental values are well reproduced and the state is no longer considered an outlier. Aside from the last two predicted states in the spectrum, other predictions at N^{3}LO$_{\text{vs}}$ are in good agreement with experiment. There are some minor deviations between the N^{3}LO$_{\text{vs}}$ interaction and experiment for some states in ^{24}Na, which are of the order of 200 keV. Furthermore, predictions for the last $5/2^+$ state in ^{27}Mg and for the $9/2^+$ state in ^{29}Al differ from experiment by about 1 MeV. In the last panel in ^{30}Al, the correct ground state cannot be described at NLO$_{\text{vs}}$, as the

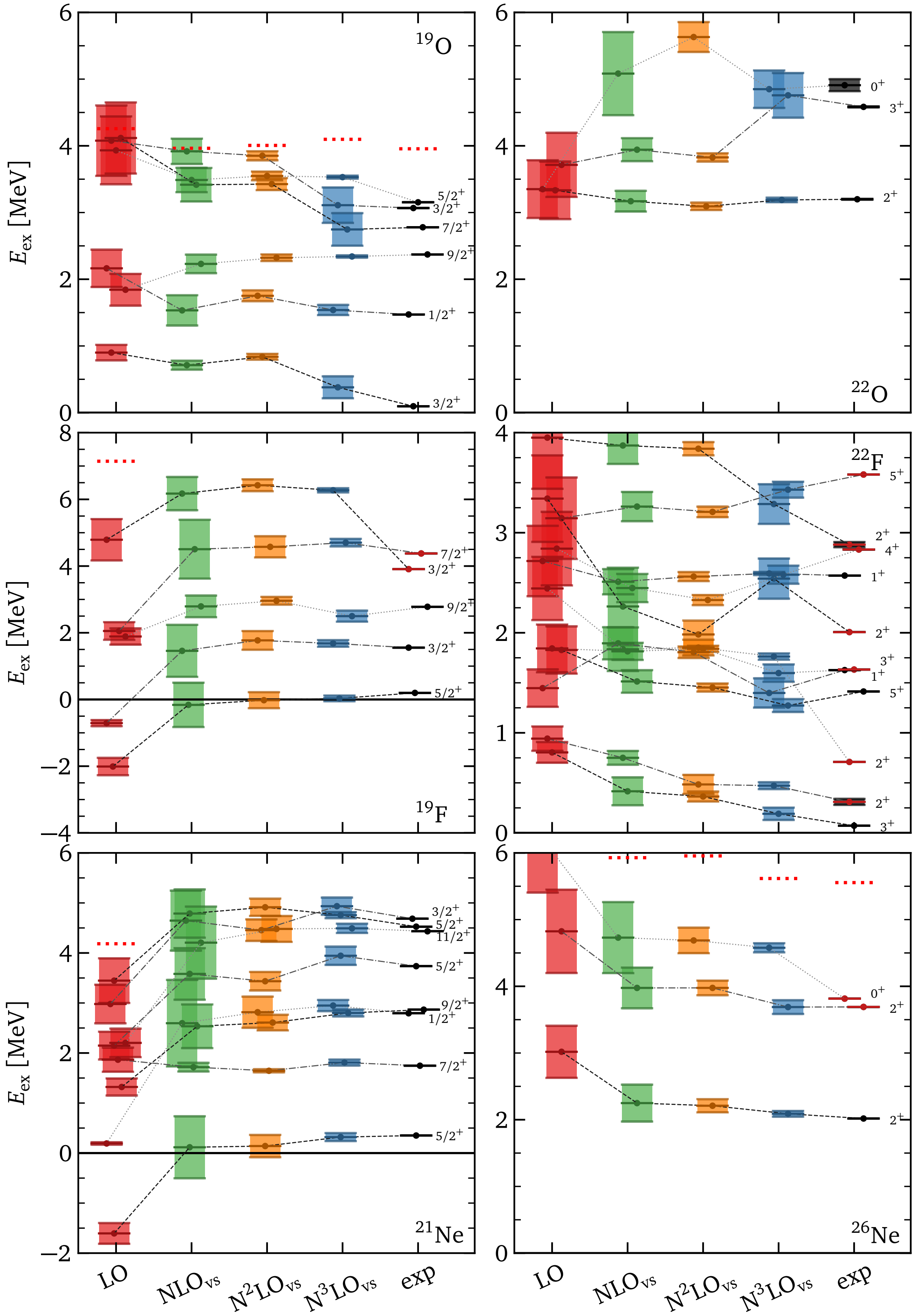

Figure 9.10.: Excitation spectra of selected isotopes from oxygen to neon. Each panel shows the chiral shell-model interactions at LO, NLO$_{\mathrm{vs}}$, N^{2}LO$_{\mathrm{vs}}$, and N^{3}LO$_{\mathrm{vs}}$ in comparison to experiment. The theoretical uncertainties are given by Eq. (2.77) at LO and by Eq. (2.78) at higher orders. The same states are joined by dashed lines to guide the eye. Angular momentum labels are given next to the experimental sates. Isotope labels are given either in the lower, or upper right corner. Experimental states in red are not included in the fit data set. We show the one (two)-neutron separation energies S_n (S_{2n}) as a dotted (dashed) red line, if they are present in the spectrum.

first excited state is at energies below 0 MeV. The second excited state reproduces experiment due to the large uncertainty. At $\mathrm{N^3LO_{vs}}$, the results are in good agreement with the experimental values.

We continue our observations for excitation spectra in silicon, phosphorus, and sulfur isotopes in Fig. 9.12. In ^{28,30}Si and ^{30}P, most states follow the trends discussed above. We find a good reproduction already at $\mathrm{NLO_{vs}}$. There are, however, some exceptions to that rule which we discuss in more detail. In ^{28}Si, the first 0^+ state is overestimated by about 0.5 MeV at $\mathrm{NLO_{vs}}$, while it is reproduced at $\mathrm{N^3LO_{vs}}$. A similar observation applies to the first 3^+ state in ^{30}Si. The prediction for the lowest lying 0^+ state in ^{30}P agrees with experiment at $\mathrm{N^3LO_{vs}}$, while lower orders predict this state as the actual ground state of the system. This is similar in ^{34}P, where the first excited state is predicted below 0 MeV at $\mathrm{NLO_{vs}}$, while the $\mathrm{N^3LO_{vs}}$ interaction reproduces the experimental state within uncertainties. In ^{33}S, the first three excited states $\mathrm{N^3LO_{vs}}$ are shifted to higher energies, towards the experimental results, in comparison to the $\mathrm{NLO_{vs}}$ interaction. All interactions agree with the $7/2^+$ result, while the second $5/2^+$ state is only reproduced at $\mathrm{N^3LO_{vs}}$. In the last panel, we show the spectrum of ^{35}S. The central value at $\mathrm{NLO_{vs}}$ underestimates the experimental state. At $\mathrm{N^3LO_{vs}}$, the result improves, but it now overestimates the energy. Both interactions reproduce the experimental result within uncertainties. The first $5/2^+$ state and $3/2^+$ state are reproduced by both interactions. For the second $5/2^+$ state the $\mathrm{NLO_{vs}}$ interaction overestimates the experimental energy. Again, at $\mathrm{N^3LO_{vs}}$ the result improves, but now it underestimates the state by about 200 keV.

In Fig. 9.13, we present spectra for the remaining sd-shell isotopes from chlorine to potassium. The overall behavior is very similar to the phenomena described above. In ^{34}Cl, the experimental states are reproduced within uncertainties already at $\mathrm{NLO_{vs}}$. There is some improvement at $\mathrm{N^3LO_{vs}}$, in particular for the first 3^+ and the first two 1^+ states. In ^{37}Cl, a good reproduction of experiment can only be achieved at $\mathrm{N^3LO_{vs}}$. In ^{37}Ar, the interaction at $\mathrm{N^3LO_{vs}}$ is shifted to higher energies towards the experimental values in comparison to the interaction at $\mathrm{NLO_{vs}}$. At $\mathrm{N^3LO_{vs}}$ all states agree with the experimental results. The largest improvement compared to $\mathrm{NLO_{vs}}$ is visible in the first $1/2^+$ (ΔE ~0.75 MeV, where ΔE is the energy shift between the $\mathrm{NLO_{vs}}$ and $\mathrm{N^3LO_{vs}}$ interaction towards the experimental value) and the first $5/2^+$ (ΔE ~0.5 MeV). Similar shifts are present in ^{38}Ar, which is among the outliers mentioned above. As one can see, the interaction improves by approximately 1 MeV when comparing the $\mathrm{NLO_{vs}}$ to the $\mathrm{N^3LO_{vs}}$ result. The second 2^+ state is predicted correctly within uncertainties, while no interaction is able to predict the 0^+ state. The left panel in the last row shows the spectrum of ^{38}K. The fit includes the first two 1^+ states, which already agree at $\mathrm{NLO_{vs}}$. The low-lying 0^+ and the 2^+ states are only predicted correctly at $\mathrm{N^3LO_{vs}}$. The 2^+ state is shifted by 1 MeV compared to the $\mathrm{NLO_{vs}}$ prediction.

As just demonstrated, the $\mathrm{N^3LO_{vs}}$ interaction shows major improvement compared to the lower orders in the chiral power counting. Only few outliers remain, like the ^{27}F and ^{24}O ground-state energy. We have seen that especially in low-lying excited states, only the $\mathrm{N^3LO_{vs}}$ interaction provides an adequate description. However, some of the experimental states cannot be described at all by our shell-model interactions. Among those states are the 2^+ states in ^{22}F, the 0^+ state in ^{26}Ne, the third $5/2^+$ state in ^{27}Mg, and the first excited 0^+ state in ^{38}Ar.

9.6 Predictions

To conclude our investigation of the charge-dependent interactions in the sd shell, we consider excited states that are not included in the $\mathrm{BR_2}$ data set and compare them to experimental values. In Fig. 9.14, we present predictions from our theory for ^{24,26}O, ^{25}F, and ^{30}Mg spectra. In ^{24}O, only the ground state is considered in the fit. As one can see by the dashed, red line, the excited states are above the one-neutron separation energy, and thus, continuum effects play a role. This typically amounts to an additional attraction of a few hundred keV, which we do not include in this step. Our interaction at $\mathrm{NLO_{vs}}$ and $\mathrm{N^3LO_{vs}}$ both predict the experimental states within uncertainties. The central values of our interactions underestimate the exact energy by a few hundred keV. Additionally, at $\mathrm{N^3LO_{vs}}$, the two excited states are clearly separated in energy, while they overlap at $\mathrm{NLO_{vs}}$. In ^{26}O, not even the ground-state energy is considered

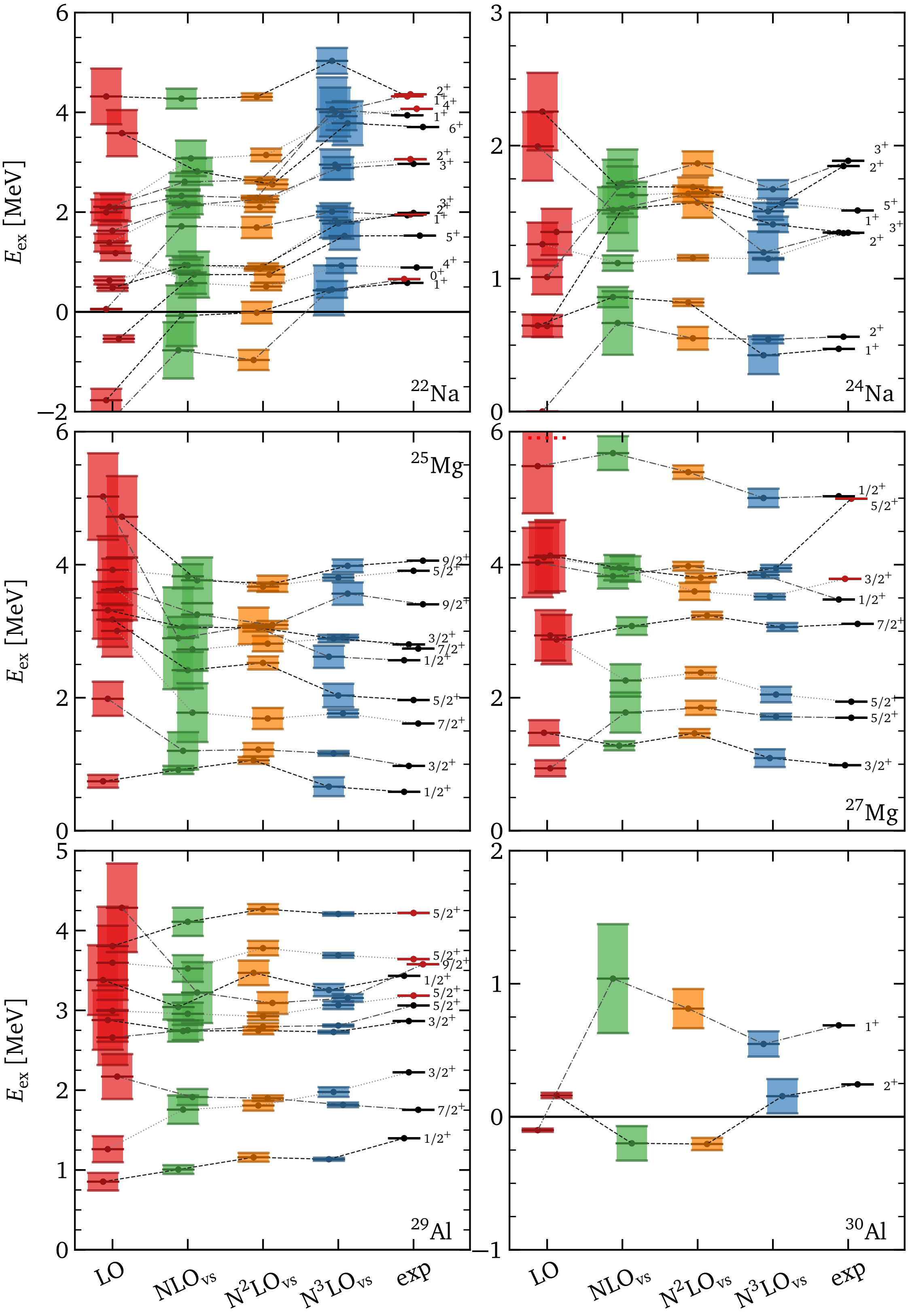

Figure 9.11.: Excitation spectra of selected isotopes from sodium to aluminum. For details see the caption of Fig. 9.10.

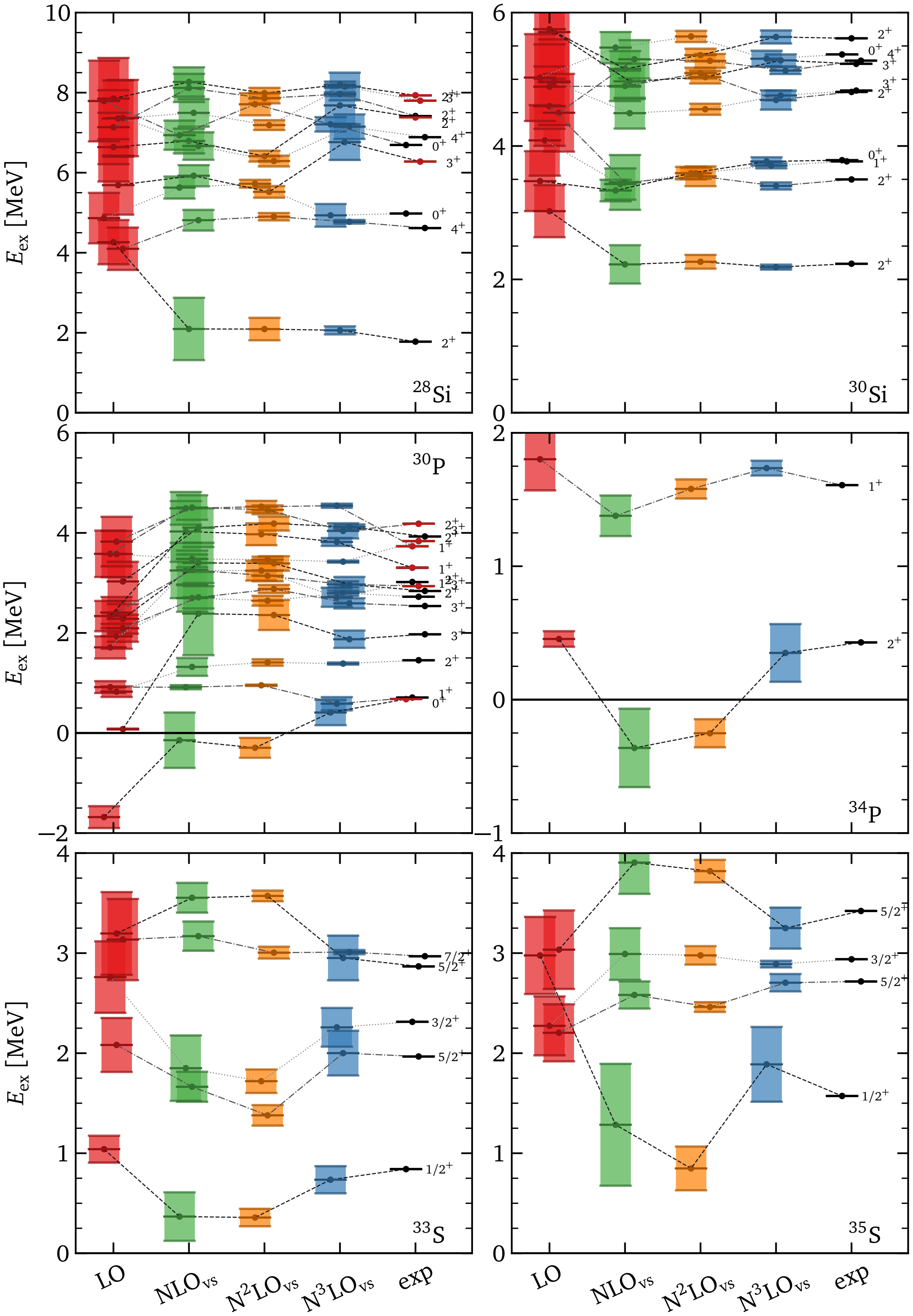

Figure 9.12.: Excitation spectra of selected isotopes from silicon to sulfur. For details see the caption of Fig. 9.10.

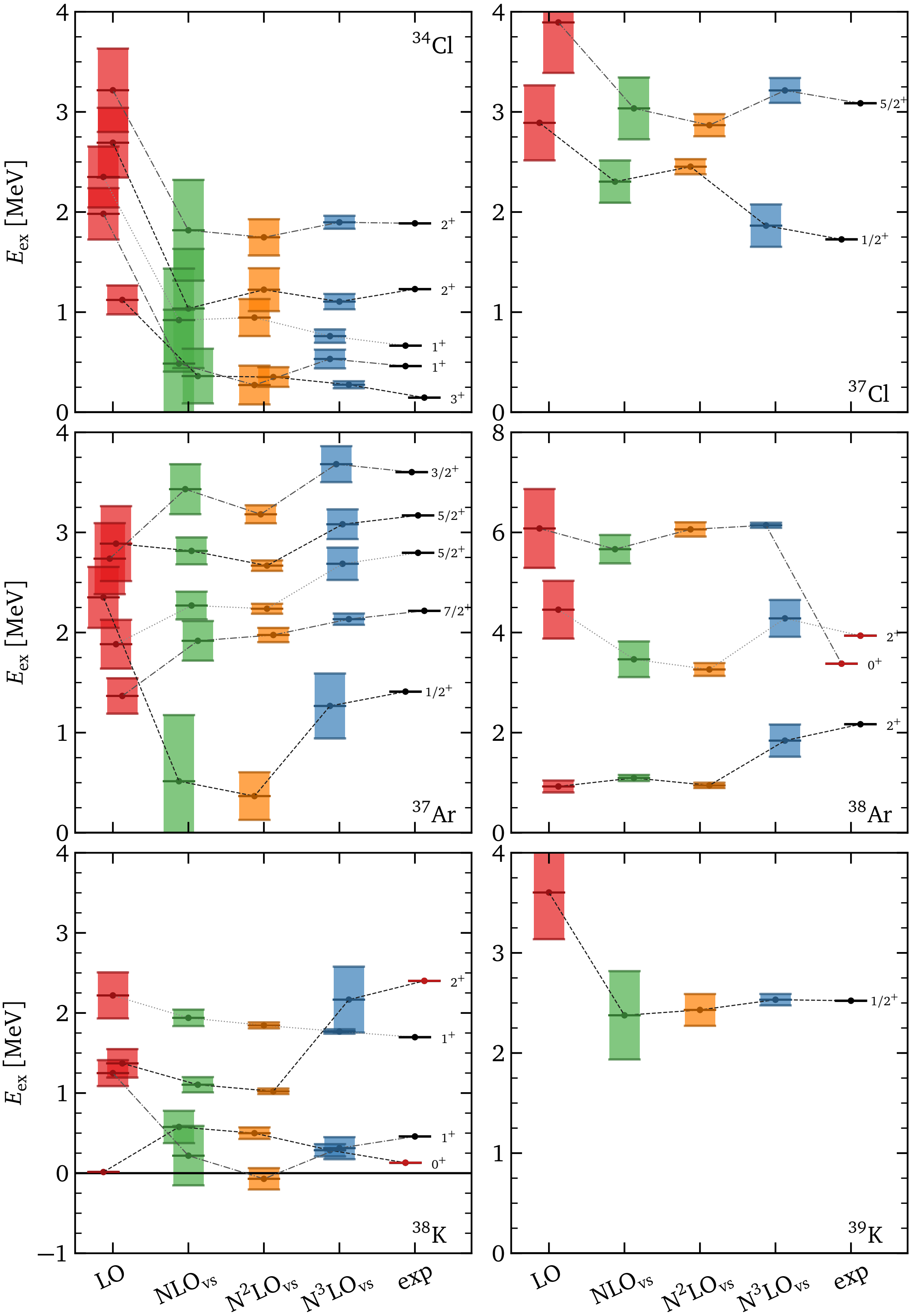

Figure 9.13.: Excitation spectra of selected isotopes from chlorine to potassium. For details see the caption of Fig. 9.10.

in the fit. As one can see in Fig. 9.8, all interactions agree with the experimental energy for the ground state within their uncertainty bands. As the state is unbound by two-neutron separation, additional continuum effects are expected. One can see the two-neutron separation energy of the $\mathrm{N^3LO_{vs}}$ interaction in the spectrum, which is due to the applied Coulomb correction scheme. For all other interactions and the experimental data, the two-neutron separation energy is below zero. We can see that the prediction at $\mathrm{NLO_{vs}}$ agrees very well with the experimental value. The $\mathrm{N^3LO_{vs}}$ interaction deteriorates in comparison, as it overestimates this state by a few hundred keV.

In the second row, we show six excited states in ^{25}F. None of those states are included in the data set to which we fit. Especially the $9/2^+$ state, as well as the first $3/2^+$ and $5/2^+$ are in good agreement with the prediction at $\mathrm{N^3LO_{vs}}$. The lowest $1/2^+$ state is predicted accurately at $\mathrm{NLO_{vs}}$, but underestimated by about 200 keV at $\mathrm{N^3LO_{vs}}$. The $7/2^+$ and second $3/2^+$ state are overestimated by roughly 250 keV at $\mathrm{N^3LO_{vs}}$. Given the fact that only the ground-state energy is part of the data set, the predictions shown here are very promising. In the next panel, we show the excitation spectrum of ^{30}Mg. One needs to be aware, that this state is in the vicinity of the island of inversion. At $\mathrm{NLO_{vs}}$ and $\mathrm{N^2LO_{vs}}$ the two 2^+ states agree well with experiment. At $\mathrm{N^3LO_{vs}}$, only the first of those two states is in agreement with experiment, the second prediction is slightly overestimated by about 150 keV compared to experiment. The 0^+ state cannot be described by our theory. This might be an extruder state, i.e., a state where two nucleons are excited out of the sd shell, which requires orbits from the pf shell for an adequate description.

Further predictions in ^{31,32}Al and ^{32,34}Si are presented in Fig. 9.15. The first panel displays the excitation spectrum of ^{31}Al. The first two energies are known from experiment (NNDC [215]), but the angular momenta are not. They are given as either $1/2^+$ or $3/2^+$. Our interactions clearly suggest that the first excited state is a $1/2^+$ state and the second excited state is a $3/2^+$ state. Above those two states, we show the energies of the second $1/2^+$ and second $3/2^+$ from our interactions. The energies at $\mathrm{N^3LO_{vs}}$ are in agreement with experimental measurements. Next to this panel, we depict the spectrum of ^{32}Al. Our predictions for this neutron-rich state do not agree with experiment. In general, we find that the closer we come towards the boundaries of the sd shell, the worse our predictions get. This is also visible in ^{34}Si in the last panel, where our interactions overestimate the experimental state by about 0.7 MeV. The third panel shows the excited states of ^{32}Si. There, the first two 2^+ states are included in the data set, results for the 0^+ and third 2^+ state are predictions. First of all, the fitted states are in good agreement with experiment. In the first 2^+ state, there is not much change between the different orders. In the second 2^+ state, the interactions improve with increasing order. The interaction at $\mathrm{N^3LO_{vs}}$ is shifted downwards in energy compared to $\mathrm{NLO_{vs}}$ and $\mathrm{N^2LO_{vs}}$, towards the experimental energy. Similar observations apply to the prediction of the third 2^+ state. The prediction of the 0^+ state does not agree with experiment at $\mathrm{NLO_{vs}}$ and $\mathrm{N^2LO_{vs}}$. However, at $\mathrm{N^3LO_{vs}}$, the energy is shifted downwards by about 1 MeV in comparison, and thus, the prediction is in good agreement with experiment.

In total, we see that many predictions of states outside of the $\mathrm{BR_2}$ data set of the $\mathrm{N^3LO_{vs}}$ interaction are very close to the experimental states. However, there are some outliers, like the 0^+ state in ^{30}Mg, and those in states close to the neutron-rich boundaries of the sd-shell as in ^{32}Al and ^{34}Si. One needs to further investigate those states, and exclude them if one comes to the conclusion that those states cannot be produced with the sd valence space.

9.7 Summary of main results

To summarize this section, we list our key findings:

- We constructed four different charge-dependent shell-model interactions at LO, $\mathrm{NLO_{vs}}$, $\mathrm{N^2LO_{vs}}$, and $\mathrm{N^3LO_{vs}}$, where we allowed the SPEs to vary. All LECs for those interactions are of natural size. The SPEs, besides at LO, agree well with the experimental energy levels of ^{17}O and ^{17}F. In addition, we found that adjusting the control parameter δ in the LCM fit influences naturalness of the LECs. We showed this by constructing an interaction with unnaturally large LECs at $\mathrm{N^3LO_{vs}}$.

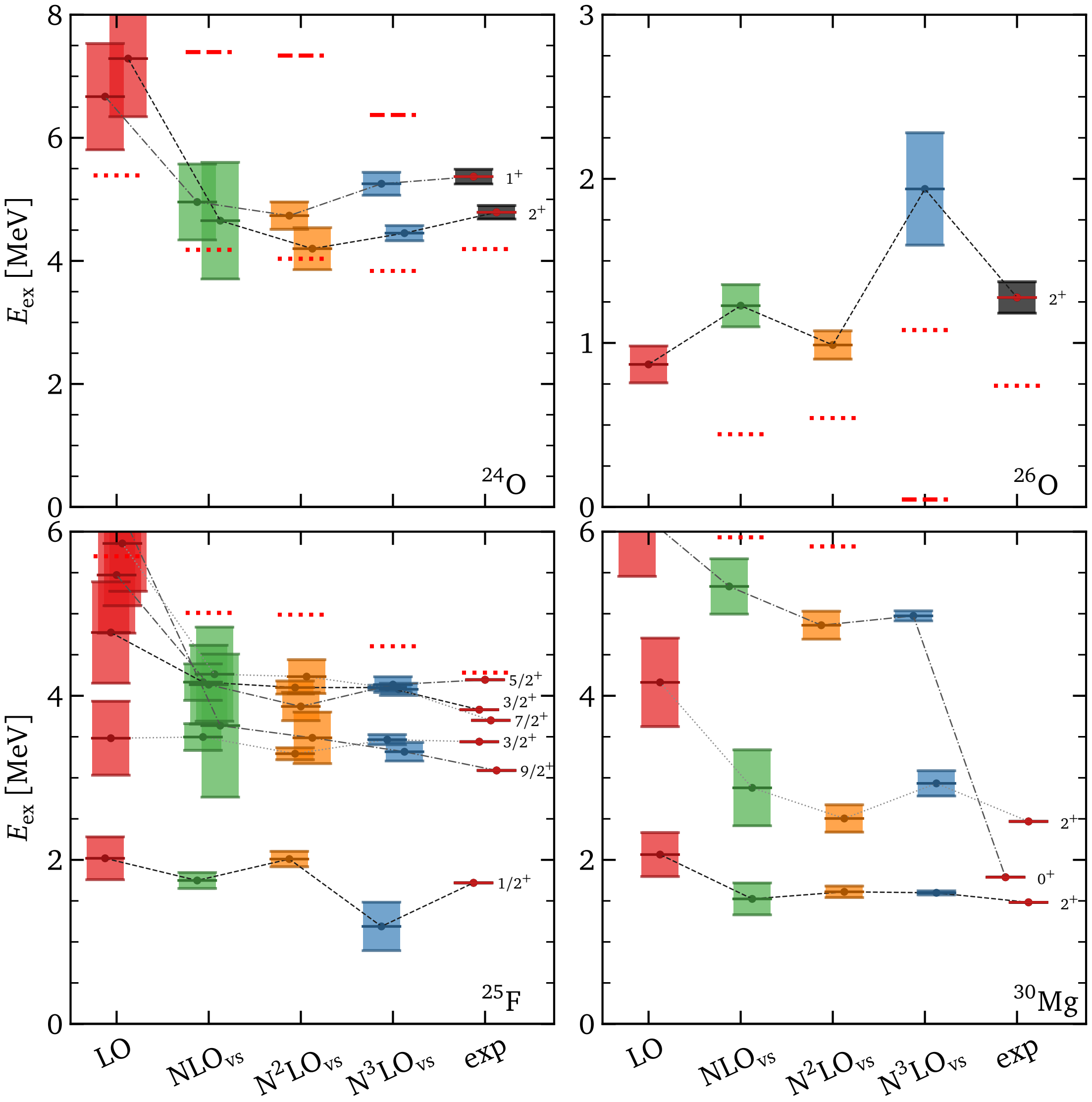

Figure 9.14.: Prediction for excitation spectra from the charge dependent LO, NLO$_{\mathrm{vs}}$, N^{2}LO$_{\mathrm{vs}}$, and N^{3}LO$_{\mathrm{vs}}$ interactions in comparison to the experimental values. The upper panels show spectra for ^{24}O and ^{26}O, the lower panels show spectra for ^{25}F and ^{30}Mg respectively. Note that the ^{26}O resonance is energetically beyond the two-neutron separation energy, and thus, unbound. None of the excitation states were included in the data set. We show the neutron separation energy S_n as a dotted red line and the two-neutron separation energy S_{2n} as a dashed red line, if they are present in the spectrum.

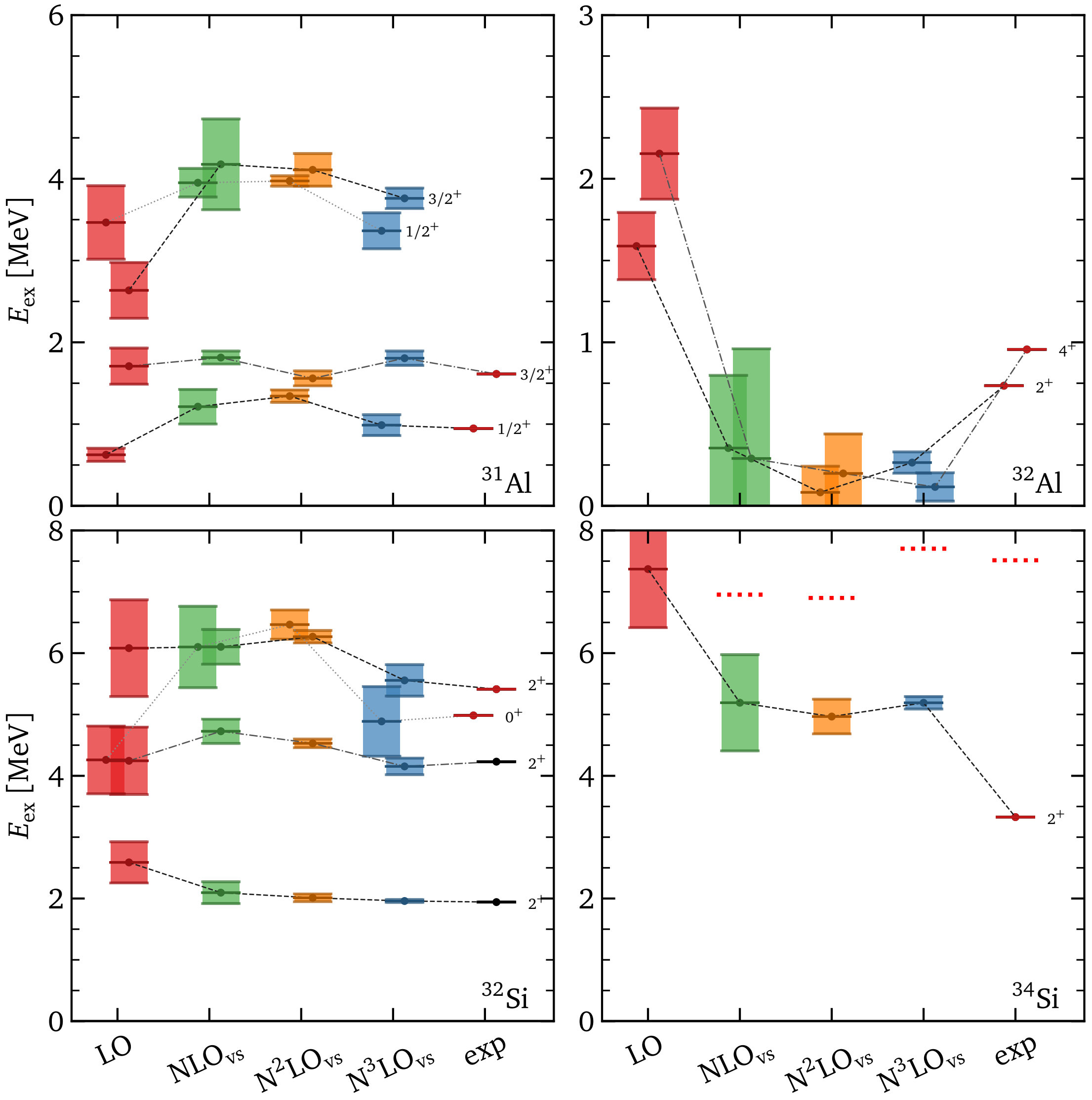

Figure 9.15.: Prediction for excitation spectra from the charge dependent LO, NLO$_{\mathrm{vs}}$, N^{2}LO$_{\mathrm{vs}}$, and N^{3}LO$_{\mathrm{vs}}$ interactions in comparison to the experimental values. The upper panels show spectra for ^{31}Al and ^{32}Al, the lower panels show spectra for ^{32}Si and ^{34}Si respectively. Only the first two 2^+ states in ^{32}Si were included in the data set. We show the neutron separation energy S_n as a dotted red line and the two-neutron separation energy S_{2n} as a dashed red line, if they are present in the spectrum.

- By using a charge-dependent interaction and allowing the SPEs to vary, we reduce the number of outlying states at NLO$_{\rm vs}$ compared to the charge-independent interaction from the previous section. However, a few of those states remain: ^{22,23}Na and ^{38}Ar and one new outlier enters in ^{27}F. The overall RMS deviation is greatly improved by the 15 new free-space LECs which are introduced at N^{3}LO$_{\rm NLO,\,vs}$. Nevertheless, those same outlying states remain. Only by including new valence-space operators at N^{3}LO$_{\rm vs}$, we are able to reproduce those states with sufficient accuracy.

- We compared our interactions to the USDA and USDB interactions from Ref. [114]. We found that all our interactions result in very similar TBME and the TBME are similar to the ones of the USDA and USDB interactions. At N^{3}LO$_{\rm vs}$, we reach an accuracy of the order of the USDA and USDB, with an RMS deviation of 161 keV.

- We investigated isotopic ground-state chains. All our interactions reproduce the ground-state energies in the data set within uncertainties. Furthermore, we investigated predictions of the $^{25-28}$O, ^{28,29}F, ^{29,30}Ne, ^{30,31}Na, and ^{31,32}Mg. Our interactions reproduce the oxygen dripline within uncertainties. However, the central value of ^{26}O is predicted to be bound at N^{3}LO$_{\rm vs}$, due to the Coulomb correction scheme we use.

- In addition, we investigated excitation spectra. As in the previous chapter, we found that many states are already in good agreement with experiment at NLO$_{\rm vs}$. Our N^{2}LO$_{\rm vs}$ interaction deteriorates compared to the one at NLO$_{\rm vs}$, but it improves largely at N^{3}LO$_{\rm vs}$. In particular, this is the only interaction which is able to obtain the right ^{19}F ground-state energy. Furthermore, our interactions show a promising predictive power for excited states.

10 First applications to cross-shell interactions

For our first application to cross-shell valence spaces, we consider the major sd shell together with the $0f_{7/2}$ neutron orbit. We fit the charge-dependent interactions, which we presented in the previous chapter at LO, $\mathrm{NLO_{vs}}$, $\mathrm{N^2LO_{vs}}$, and $\mathrm{N^3LO_{vs}}$ to the SDF16 data set from Tab. 7.2. In addition to the parameters from the last chapter, we have one more parameter, which is the SPE of the $0f_{7/2}$ neutron orbit. In total, there are 11 parameters at LO, 23 parameters at $\mathrm{NLO_{vs}}$ and $\mathrm{N^2LO_{vs}}$, and 70 parameters at $\mathrm{N^3LO_{vs}}$.

In cross-shell interactions, or more generally spoken, interactions that do not take place in a complete $N\hbar\omega$ space, results can suffer from the so-called center-of-mass problem. We give some details about the center-of-mass problem in the following section. After that, we present the LECs and an overview of the quality of the fit before we consider our predictions for ground-state energies, the neutron dripline, and show selected excitation spectra and predictions in the $sd + 0f_{7/2}$ space.

10.1 Center-of-mass problem

The center-of-mass problem refers to the spurious contamination of expectation values from many-body calculations, with A-body CM degrees of freedom [229]. It can occur whenever the many-body wave function does not factorize into CM and intrinsic coordinates

$$|\Psi\rangle \neq |\Psi_{\text{intr.}}\rangle \, |\Psi_{\text{CM}}\rangle \, , \tag{10.1}$$

i.e., when the chosen basis or model space breaks translational invariance. In a single-particle harmonic-oscillator basis, the wave function factorizes for complete $N\hbar\Omega$ spaces, as the coordinates can be transformed to Jacobi coordinates (see Ref. [230] for details). In particular, $0\hbar\Omega$ shell-model calculations as in Ch. 8 and Ch. 9 are not affected [116], as well as NCSM calculations, which are based on $N_{\text{max}}\hbar\Omega$ truncations [71, 231]. In Ref. [232], strong numerical evidence in CC calculations is presented, where it is shown that the wave function factorizes into intrinsic and CM parts for sufficiently large model spaces, even if the model space is not a complete $N\hbar\Omega$ model space. Similar observations apply to IM-SRG calculations [64].

The model space considered in this chapter allows excitations of neutrons to the $0f_{7/2}$ subshell. Exciting N neutrons to this subshell corresponds to an incomplete $N\hbar\Omega$ space. It is not yet understood, how such small, incomplete $N\hbar\Omega$ model spaces are affected by the center-of-mass problem exactly, and there is no unique prescription how to treat those spaces. One option is to shift contaminated states out of the spectrum by adding a large CM contribution to the Hamiltonian [233]

$$H_\beta = H_{\text{intr.}} + \beta H_{\text{CM}} \, , \tag{10.2}$$

with

$$H_{\text{CM}}(\omega) = \frac{1}{2mA}\mathbf{P}^2 + \frac{mA\omega^2}{2}\mathbf{R}^2 - \frac{3}{2}\hbar\omega \, , \tag{10.3}$$

where a large value for β shifts contaminated states to high energies. However, this approach is viewed controversially [234]. For instance, it does not probe the strength of the CM contamination, and consequently, even states that are barely contaminated are shifted out of the spectrum. Thus, this method does not provide a solution, but with different choices for β, it still provides a diagnostic tool to estimate the strength of the contamination [235].

In an iterative fitting routine that considers several states, the last approach is not practical, as it needs to be carried out for all nuclei with several values for β. Thus, we use the fact, that the main contribution of CM spuriousness roots in transitions of the type [116]

$$Nj \Rightarrow (N+1)j \pm 1 \, . \tag{10.4}$$

Table 10.1.: Root-mean-square deviation from experiment and number of parameters in the $sd + 0f_{7/2}$ cross-shell valence space at LO, NLO$_{\mathrm{vs}}$, N^{2}LO$_{\mathrm{vs}}$, and N^{3}LO$_{\mathrm{vs}}$. The RMS deviation is given in MeV.

Interaction	# parameters	RMS [MeV]
LO	11	2.257
NLO$_{\mathrm{vs}}$	23	0.783
N^{2}LO$_{\mathrm{vs}}$	23	1.0127
N^{3}LO$_{\mathrm{vs}}$	70	0.655

In the $sd+0f_{7/2}$ space, the dominant part is the transition $0d_{5/2} \Rightarrow 0f_{7/2}$ in neutron orbits. Consequently, we require a completely filled neutron $0d_{5/2}$ orbit and do not allow any excitations out of it. For this first approach, the main contribution of CM contamination is therefore suppressed. However, additional investigation of the center-of-mass problem is required for future works.

10.2 Low-energy constants

The LECs in natural units for cross-shell interactions at LO, NLO$_{\mathrm{vs}}$, N^{2}LO$_{\mathrm{vs}}$, and N^{3}LO$_{\mathrm{vs}}$ are presented in Fig. 10.1. We present the LECs for all operators up to those at NLO. In order to keep a structured overview, we only show the average value of the LECs D_i and Q_i at N^{3}LO. In addition to this average value, we show the standard deviation (thick line) and the maximum and minimum (thin line). The latter two are annotated by the respective LEC. Numerical values are listed in App. E.4.

It is easily visible, that all LECs are of natural size. The largest values are reached for Q_{22}, which is one of the new N^{3}LO valence-space contacts. The Q_i LECs take larger values compared to the previous chapter. At N^{2}LO$_{\mathrm{vs}}$, the C_T, C_{CIB}, C_{CSB}, C_4, and C_5 are especially pronounced compared to all other interactions.

In Fig. 10.2, we display the neutron (left) and proton (right) SPEs of the $sd + 0f_{7/2}$ interactions. The neutron spectrum contains the $0f_{7/2}$ SPE. As before, we show the lowest states of the ^{17}O and ^{17}F spectrum for comparison. This time, neither of those nuclei is in the data set. At first we focus on the neutron SPEs (left). One needs to keep in mind, that we require the $0d_{5/2}$ neutron orbit to be filled at all times, which effects the SPEs. All our interactions show the same pattern for the SPEs in comparison to the oxygen states $\varepsilon_{0d_{5/2}} < E^{^{17}O}_{5/2^+}$, $\varepsilon_{1s_{1/2}} > E^{^{17}O}_{1/2^+}$, and $\varepsilon_{0d_{3/2}} > E^{^{17}O}_{3/2^+}$. At NLO$_{\mathrm{vs}}$ and N^{3}LO$_{\mathrm{vs}}$, SPEs are close to the experimental lines. We compare the $\varepsilon_{0f_{7/2}}$ SPE to the one from the SDPF interaction from Ref. [236], which is given there at 6.22 MeV. Also here, the NLO$_{\mathrm{vs}}$ and N^{3}LO$_{\mathrm{vs}}$, interactions are close to this value. At LO and N^{2}LO$_{\mathrm{vs}}$, we find $\varepsilon_{0d_{5/2}} > \varepsilon_{0f_{7/2}}$, meaning that the ordering between those two states is not correct with respect to experimental observations. In the right figure, we show the SPEs for proton orbits. At NLO$_{\mathrm{vs}}$ and N^{3}LO$_{\mathrm{vs}}$, the SPEs are below the experimental states. At N^{3}LO$_{\mathrm{vs}}$, the energies are closest to the experimental observations and we find $\varepsilon_{0d_{5/2}} \gtrsim \varepsilon_{1s_{1/2}}$.

In essence, all interactions lead to natural LECs. We find slightly different SPEs if we compare our interactions to the experimental levels in ^{17}O and ^{17}F, but our interactions are still in the vicinity of the latter. As we effectively consider a ^{22}O core (due to the fixed neutrons in the $0d_{5/2}$ orbit), we expect SPEs to differ.

10.3 Overview

The SDF16 dataset to which we fit the cross-shell interactions to is given in Tab. 7.2. We visualize it in Fig. 10.3. As one can see in the figure, fixing the neutrons in the $0d_{5/2}$ orbit does not only help to reduce the CM problem, but also reduces the computational time. The set has more ground-states ($\#\mathrm{gs} = 122$)

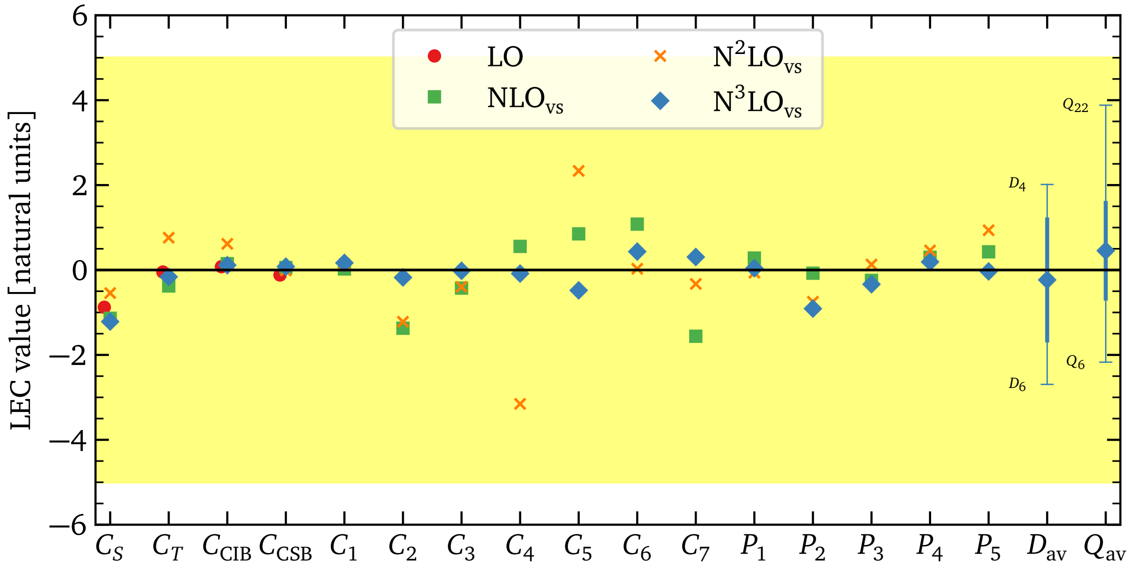

Figure 10.1.: Fitted LECs for charge-dependent interactions at LO, NLO$_{\text{vs}}$, N^{2}LO$_{\text{vs}}$, and N^{3}LO$_{\text{vs}}$ in natural units, which are obtained using Eqs. (8.3), (8.4), and (9.2). At N^{3}LO$_{\text{vs}}$, we show the average D and Q value with the standard deviation (thick) line, as well as the minimum and maximum LEC with labels, connected by a thin line. The yellow background gives an approximate region in which natural parameters should be located.

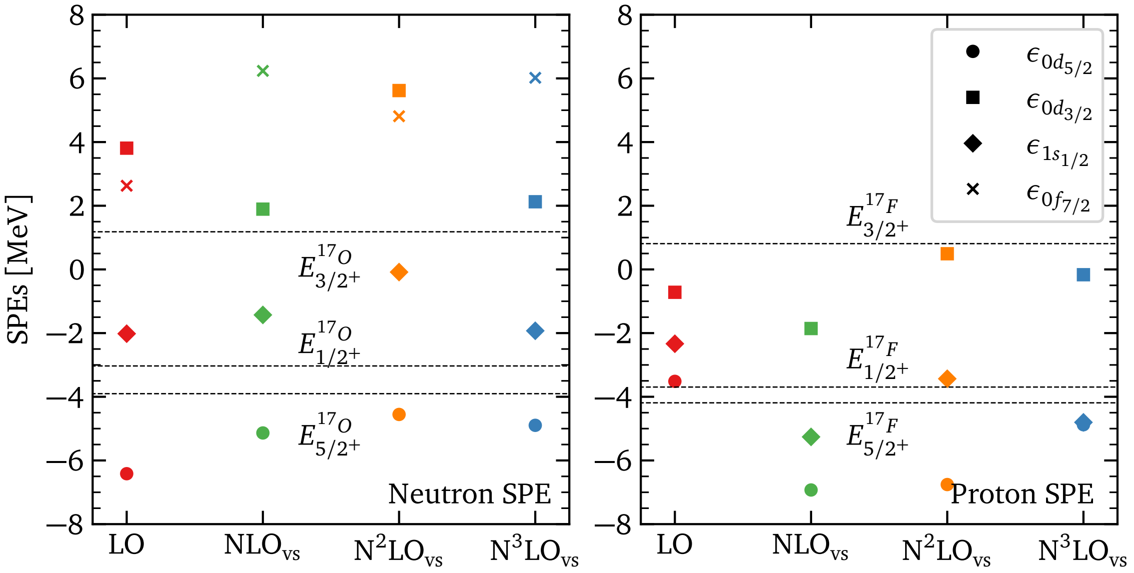

Figure 10.2.: Fitted SPEs for the charge-dependent shell-model interactions. From left to right we show the different SPEs at LO, NLO$_{\text{vs}}$, N^{2}LO$_{\text{vs}}$, and N^{3}LO$_{\text{vs}}$. In the left panel, we show the neutron SPEs, in the right panel the proton SPEs. The dashed lines give the results for Coulomb corrected ^{17}O states (left panel) and Coulomb corrected ^{17}F states (right panel).

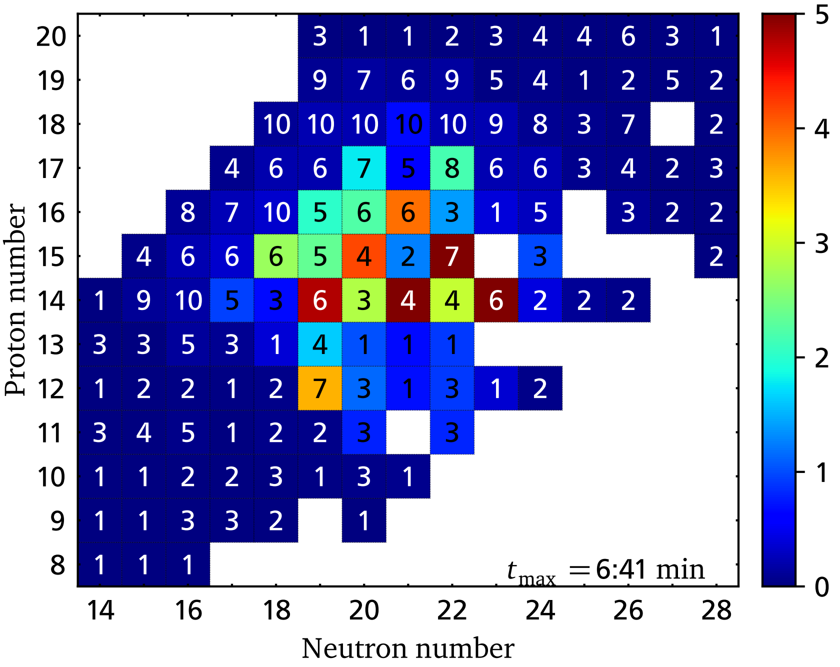

Figure 10.3.: Graphical representation of the data set and computational time for the $sd+0f_{7/2}$ cross-shell valence space. The time refers to a single thread calculation on an Intel® Core™ i7-6700 CPU with 3.40 GHz. Each square represents a nucleus in the valence space and contains the number of considered states. The color coding of the average computational time is given in the bar on the right. Isotopes with low computational costs are colored blue, while isotopes which take longer to diagonalize are colored red.

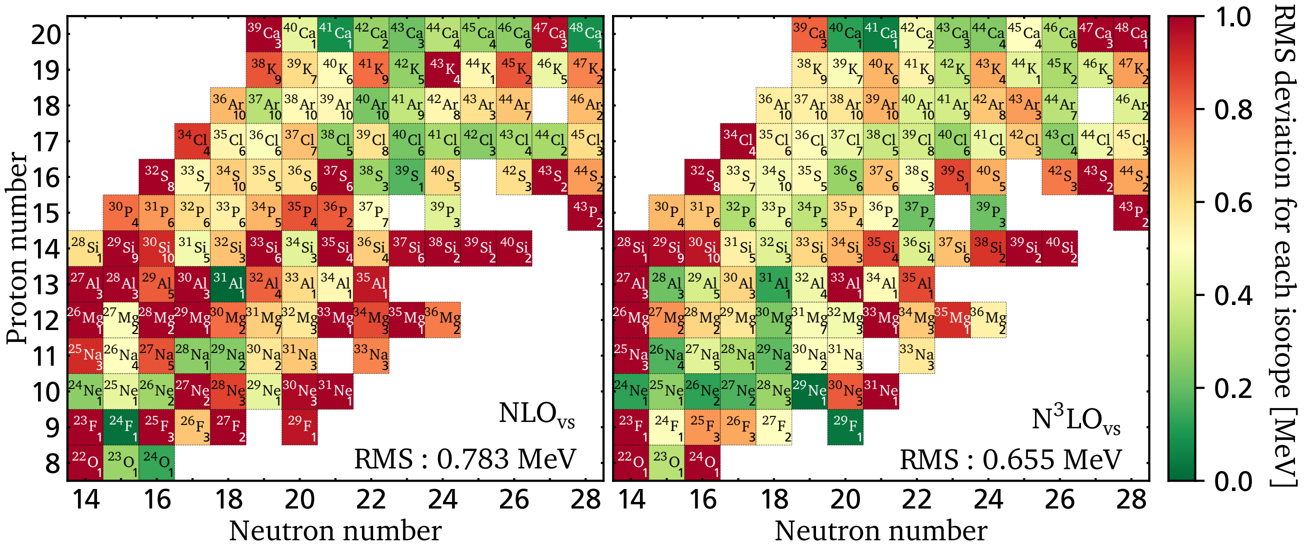

Figure 10.4.: Graphical representation of the RMS deviation from experiment for each fitted nucleus in the $sd + 0f_{7/2}$ cross-shell valence space. The figure shows the results for the charge-dependent chiral shell-model interactions $\mathrm{NLO_{vs}}$ (left) and $\mathrm{N^3LO_{vs}}$ (right). The color coding of the RMS deviation is given in the bar on the right. Isotopes with a small RMS deviation are colored green, while those with a large deviation are colored red. Each square shows the isotope label and the number of fitted states in the bottom right corner. The interaction label and the total RMS deviation is given on the lower right side of each panel.

compared to the BR_2 data set ($\#gs = 77$), but contains fewer excited states for two reasons. First, a thorough analysis of the data set is necessary to avoid intruder states in the spectrum. This is even more vital to our setup, as experimental states with configurations that have a neutron excited out of the $0d_{5/2}$ orbit cannot be reproduced in our valence space. Thus, one needs to make sure that those states are excluded from the data set. To lower the risk of having an intruder state in the set, we reduce the total number of excited states. For ground states this risk is smaller, as those configurations prefer the lowest lying orbits to be filled. Second, reducing the number of excited states also helps to reduce the risk to include states which are contaminated by spurious CM admixtures.

The average maximum computation time (w.r.t. single thread calculation on an Intel® Core™ i7-6700 CPU with 3.40 GHz) for a single nucleus in this set is about 6 - 7 minutes. Which makes this set a very good testing ground for first applications to cross-shell interactions(1).

The total RMS deviation from experiment for all interactions is listed in Tab. 10.1. From the table, one sees instantly that the interactions do not perform as well in the cross-shell valence space as they did in the sd-valence space in the previous chapter. At LO, the RMS deviation to experiment is larger than 2 MeV. This improves drastically at NLO_vs, where the RMS value drops to 783 keV. As in Ch. 9, the $\text{N}^2\text{LO}_\text{vs}$ interaction performs worse than the NLO_vs interaction. We find an $\text{N}^2\text{LO}_\text{vs}$ interaction with an RMS value larger than 1 MeV. At $\text{N}^3\text{LO}_\text{vs}$, the RMS value decreases and we end up at 655 keV. This clearly shows that the data set we consider, as well as the theoretical uncertainty estimate require further investigation. Also, one might need to consider to include more pf-shell orbits for a better description of the data set.

We present the individual RMS deviation from experiment for each isotope in the data set for our interaction at NLO_vs and $\text{N}^3\text{LO}_\text{vs}$ in Fig. 10.4. One can easily see that the interactions perform worse compared to the previous chapter. In the left panel, we depict results at NLO_vs. The interaction performs well in some oxygen, neon, and sodium isotopes as well as ^{24}F, and ^{31}Al. In addition heavier, neutron-rich nuclei in sulfur and chlorine are well reproduced, as well as some argon and calcium isotopes, and ^{42}K. The reproduction improves a lot at $\text{N}^3\text{LO}_\text{vs}$ (right). Most states are well reproduced, with outliers located mostly along the neutron-rich side and for nuclei with 14 neutrons.

10.4 Neutron dripline in $sd + 0f_{7/2}$ valence space

Even though our precision deteriorates compared to the previous chapter, we want to investigate the reproduction and predictive power of our interactions. We investigate ground-state energies for isotopes that can be described in the $sd + 0f_{7/2}$ shell. In Fig. 10.5 and Fig. 10.6, we show the central values of the ground-state energies obtained at NLO_vs, $\text{N}^2\text{LO}_\text{vs}$, and $\text{N}^3\text{LO}_\text{vs}$. For comparison, we show experimental results of the AME16 [105] (black) as well as the extrapolated values from the same reference (red). Figure 10.5 shows isotopic chains from oxygen to silicon and Fig. 10.6 shows isotopes from phosphorus to calcium. The states which were included in the dataset are shown in Fig. 10.3. To keep a clear overview, we do not show all ground states that are considered in the fit data set, as the isotopic chains would overlap in some cases. For experimental states with well defined angular momentum, we show our results corresponding to that state, for other states we show the J^π result for the NLO_vs interaction (left of the state in green) and the $\text{N}^3\text{LO}_\text{vs}$ interaction (right of the state in blue) on top of the corresponding state.

We start our discussion with Fig. 10.5. Results at $\text{N}^2\text{LO}_\text{vs}$ differ greatly from those at NLO_vs and $\text{N}^3\text{LO}_\text{vs}$ for the first three isotopic chains. The latter two reproduce the experimental dripline at ^{24}O, while $\text{N}^2\text{LO}_\text{vs}$ predicts bound nuclei for ^{26}O and ^{28}O. In general, the NLO_vs and $\text{N}^3\text{LO}_\text{vs}$ interactions follow the experimental trend, but neutron-rich aluminum and silicon isotopes are overbound compared to experiment. For the rest of this section, we focus on results from the latter two interactions.

Starting with the oxygen isotopes, the theoretical results are all close to the experimental ground-sate energies, where neutron rich isotopes beyond ^{24}O are underbound by a few MeV at NLO_vs and $\text{N}^3\text{LO}_\text{vs}$,

---

(1) For comparison, in a test run which also included the $1p_{3/2}$ shell, the average maximum is about two hours for a single nucleus in a single iteration.

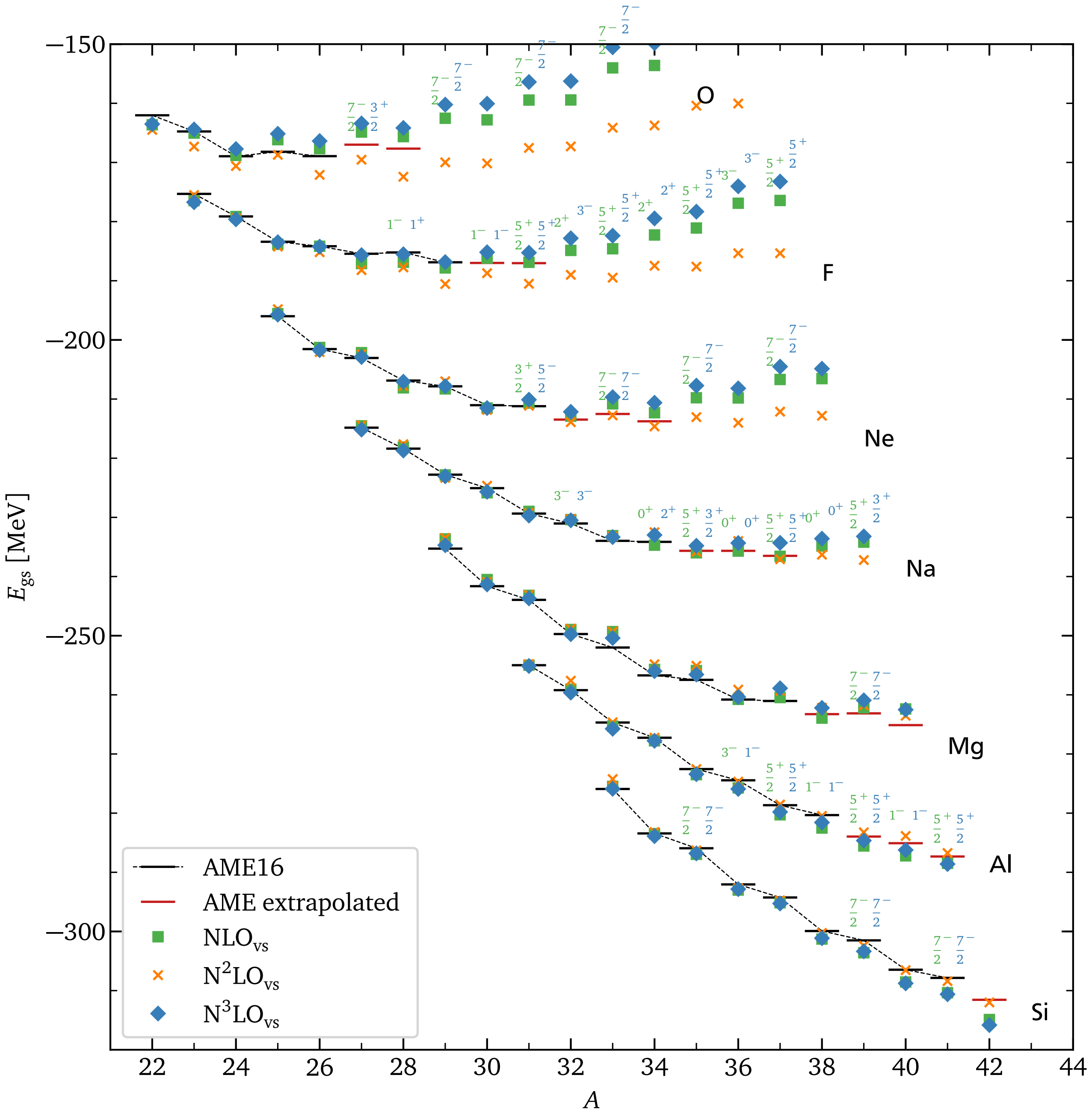

Figure 10.5.: Ground-state energies from oxygen to silicon in the $sd + 0f_{7/2}$ cross-shell valence space. We present ground-state energies from the charge-dependent interactions at NLO$_{\mathrm{vs}}$ (green), N^{2}LO$_{\mathrm{vs}}$ (orange), and N^{3}LO$_{\mathrm{vs}}$ (blue) in comparison to experimental ground-state energies from Ref. [105]. In red, we show extrapolated ground-state energies from Ref. [105]. In case of undefined angular momenta, we explicitly give the J^π predictions of the NLO$_{\mathrm{vs}}$ (green) and N^{3}LO$_{\mathrm{vs}}$ (blue) interaction above the corresponding state. At the end of each chain, we show the corresponding isotopic label. A simplified visualization that shows the neutron dripline is presented in Fig. 10.7.

while they are overbound at N^2LO_{vs}. However, the interactions reproduce the right trend up to the point where a comparison with experimental states is possible. Beyond that, the orders deviate.

A similar scenario can be seen in fluorine and neon. The energies obtained from the different interactions are close together up to ^{30}F and ^{33}Ne. Afterwards, the N^3LO_{vs} interactions predicts slightly smaller binding energies than the interaction at NLO_{vs}. For those two isotopic chains, NLO_{vs} and N^3LO_{vs} agree most of the times about the J^π value of the ground state, while in sodium they disagree in ^{34,35,39}Na. The deviation between the energies of the orders gets smaller at sodium, where it is only present in the very neutron-rich region. Also the N^2LO_{vs} results are closer to the other two interactions there. Magnesium ground-state energies agree very well with the AME16 measurements up to ^{37}Mg. Starting there, the interactions deviate, where the interaction at N^3LO_{vs} leads to smaller binding energies compared to the interaction at NLO_{vs}. At NLO_{vs}, one can clearly see that the dripline is predicted at ^{38}Mg. We will provide more details about the dripline later in our discussion about Fig. 10.7. In aluminum and silicon the two interactions lead to very similar values, but as mentioned above, they overestimate the binding energy in the neutron-rich region.

For the isotopes from phosphorus to calcium in Fig. 10.6, the general trend is very well reproduced by all interactions (including N^2LO_{vs}). In the phosphorus chain, the binding energy of the two last shown isotopes (^{42,43}P) is overestimated at NLO_{vs} and N^3LO_{vs}. For the predictions in phosphorus, NLO_{vs} and N^3LO_{vs} agree on the J^π value for all isotopes but ^{40}P. The remaining sulfur, chlorine, argon, potassium, and calcium isotopes for all interactions are in good agreement with the experimental data.

In Fig. 10.7, we present all states included in the data set together with all neutron-rich isotopes in the model space. We plot the proton number versus the neutron number. In black, we show the theoretical dripline based on the finite-range droplet macroscopic model and the folded-Yukawa single-particle microscopic model from Ref. [237], which we label MNMS95. Furthermore, we show the theoretical dripline from Skyrme-Hartree-Fock-Bogoliubov mass formulas (HFB-32) [239] as a dashed red line. We color the states which are bound (judging from the expectation value) for a given interaction as follows: If the state is bound at LO, we color the upper left corner red, if it is bound at NLO_{vs} we color the upper right corner green, if it is bound at N^2LO we color the lower left corner orange, and if it is bound at N^3LO_{vs} we color the lower right corner blue. Hence, one can easily see where each interaction predicts the neutron dripline. To determine whether an interaction predicts a bound state or not, we consider the one- and two-neutron separation energy, obtained from the central energy values of the interaction. This first consideration does not take any uncertainty into account.

All states beyond aluminum are bound at each interaction and the dripline is located outside of our valence space. We will not discuss those states any further. We start our discussion with oxygen isotopes. This is the only isotopic chain, where the dripline is known experimentally to be at ^{24}O. All interactions predict bound isotopes for $^{22-24}$O. However, only the interactions at NLO_{vs} and N^3LO_{vs} predict the correct experimental dripline at ^{24}O. At LO and N^2LO_{vs}, the dripline is predicted at ^{28}O with unbound ^{25,27}O isotopes. The latter two agree with the the HFB-32 results. In the following, we will no longer go into detail about the interaction at LO. In fluorine, the NLO_{vs}, N^2LO_{vs}, and N^3LO_{vs} interactions all predict the dripline at ^{29}F, which agrees with the HFB-32 results, however, this is not in agreement with experiment, where the dripline is known to be at or beyond ^{31}F. The ^{28}F isotope is correctly predicted to be unbound by our theory. The neon dripline is predicted at ^{32}Ne, with an unbound ^{31}Ne isotope by the NLO_{vs} and N^3LO_{vs} interaction. This is again not in agreement with experiment, where ^{31}Ne and ^{34}Ne are bound. At N^2LO_{vs} the dripline is predicted at ^{34}Ne, which agrees with both, the MNMS95 and HFB-32 results. The two interactions at NLO_{vs} and N^3LO_{vs} suggest different driplines in sodium. At NLO_{vs}, the sodium dripline is predicted at ^{37}Na, which agrees with the MNMS95 and HFB-32 results. At N^2LO_{vs}, ^{39}Na is predicted to be bound, while at N^3LO_{vs}, the dripline is predicted at ^{35}Na, with an unbound ^{34}Na. The ^{36}Na isotope is predicted to be unbound by all our interactions. The dripline in magnesium is predicted at least at ^{40}Mg by the N^2LO_{vs} and N^3LO_{vs} interactions. States beyond cannot be calculated within the considered model space. The interaction at NLO_{vs} predicts the dripline at ^{38}Mg.

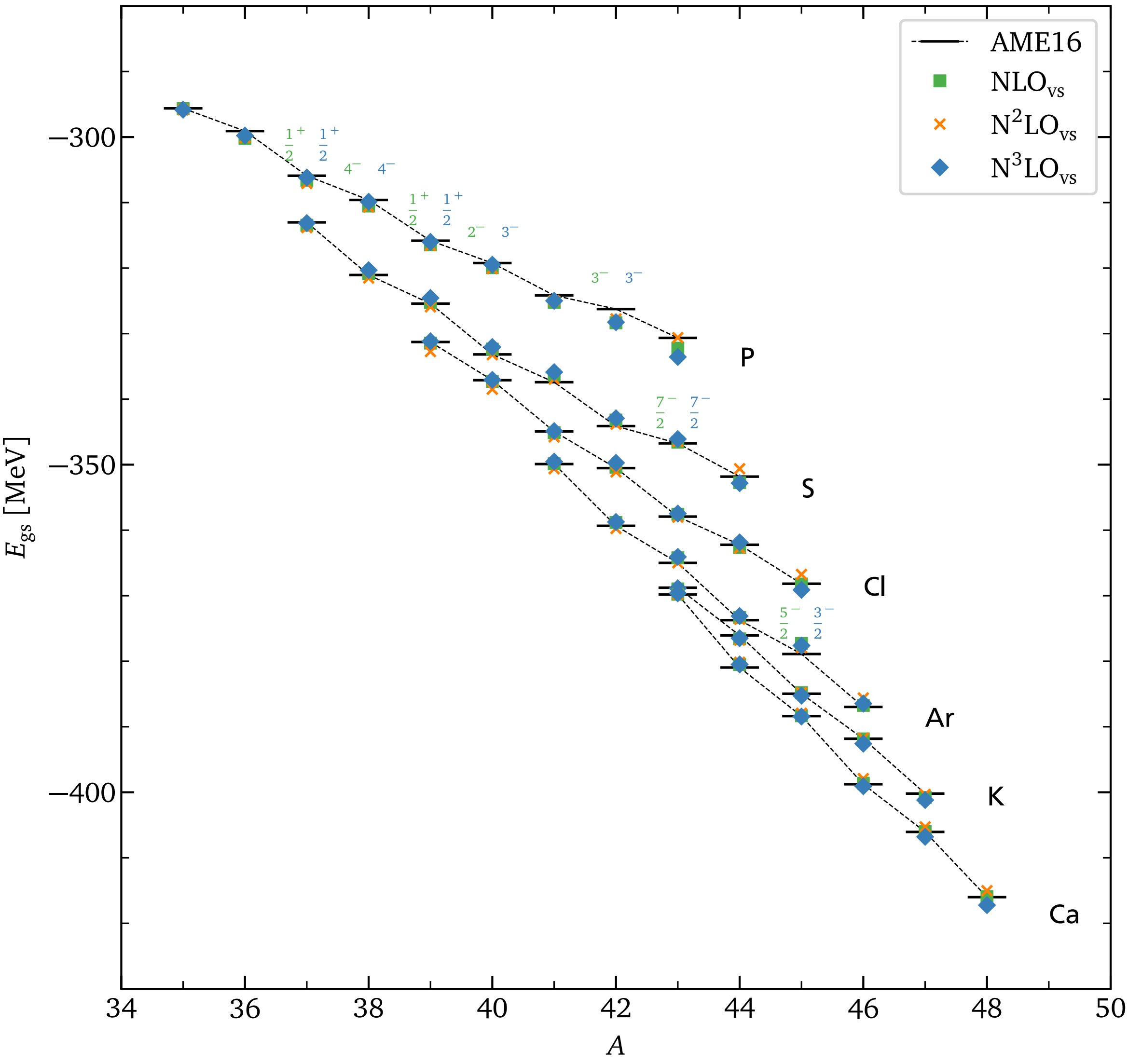

Figure 10.6.: Ground-state energies from phosphorus to calcium in the $sd + 0f_{7/2}$ cross-shell valence space. We present results for ground-states energies from the charge-dependent interactions at $\mathrm{NLO_{vs}}$ (green), $\mathrm{N^2LO_{vs}}$ (orange), and $\mathrm{N^3LO_{vs}}$ (blue) in comparison to experimental ground-state energies from Ref. [105]. In red, we show the extrapolated ground-state energies from Ref. [105]. In case of undefined angular momenta, we explicitly give the J^π predictions of the $\mathrm{NLO_{vs}}$ (green) and $\mathrm{N^3LO_{vs}}$ (blue) interaction in top of the corresponding state. At the end of each chain, we show the corresponding isotopic label.

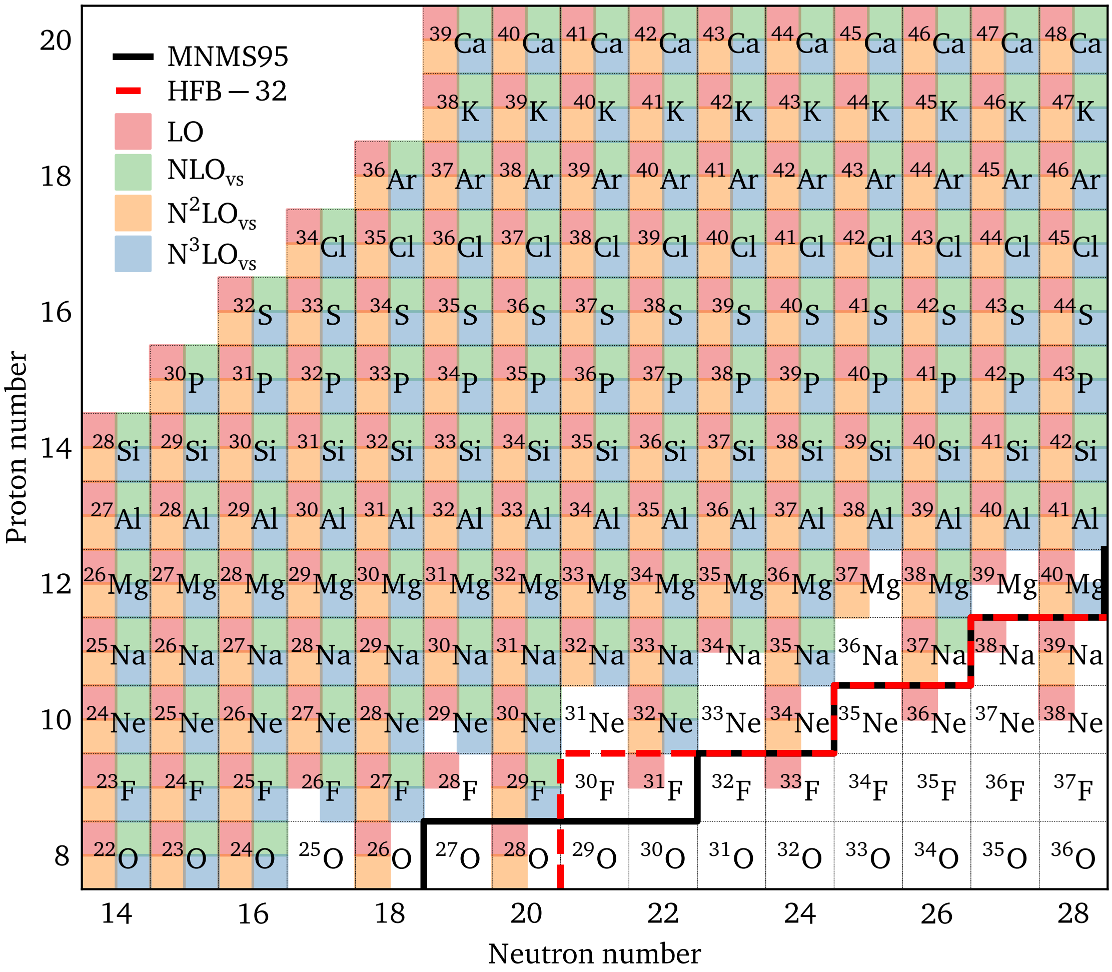

Figure 10.7.: The neutron dripline in the $sd{+}0f_{7/2}$ valence space. We show states for a given proton and neutron number and include the theoretical driplines MNMS95 from Ref. [237] (black) and Skyrme-Hartree-Fock-Bogoliubov mass formulas HFB-32 from Ref. [238] and `http://www-astro.ulb.ac.be/bruslib/nucdata/hfb32-dat` (red, dashed). For each state that is bound at a given order of our shell-model interaction, we include a colored square at a certain position in the box of this state. If the state is bound at LO, we include a red square in the upper left corner, at NLO$_{vs}$ we include a green square in the upper right corner, at N^{2}LO$_{vs}$ we include an orange square in the lower left corner, and at N^{3}LO$_{vs}$ we include a blue square in the lower right corner. All energies have been Coulomb corrected according to Eq. (7.9). Quantitative values are plotted in Fig. 10.5 and Fig. 10.6.

With this, the following conclusions apply to our research of the dripline. From Fig. 10.5, one can see that the determination of the dripline is difficult, as the ground-state energy for most isotopic chains is a flat line in the neutron-rich region. If one includes uncertainties, one needs to go to higher orders, where uncertainties are narrow, to give a definite statement. However, judging from the central values of the ground state energy, we show the dripline position of our interactions in comparison to the dripline from Refs. [237, 238]. With the focus on the NLO$_{\mathrm{vs}}$ and N^{3}LO$_{\mathrm{vs}}$, the dripline is located at ^{24}O, ^{29}F, ^{32}Ne, $^{35-37}$Na, and $^{38-\geq 40}$Mg. However, one needs to keep in mind that this is a first application to cross-shell calculation and further investigations are necessary.

10.5 Excitation spectra

Excited states from our cross-shell interaction need to be treated with caution because of possible center-of-mass contamination and our demand that the $0d_{5/2}$ neutron subshell is always filled. Nevertheless, we present spectra and predictions for selected isotopes in Fig. 10.8. We show the experimental one- (two-) neutron separation energy in each relevant panel as a dotted (dashed) red line. Excited states close to or beyond this line experience continuum effects.

In the first panel of Fig. 10.8, we show predictions for the first two excited states in ^{24}O. As one can see, the reproduction of experiment is not as good for this state, as it was in the previous chapter, which is due to the limitations forced on the neutron in the $0d_{5/2}$. In our setup, we only have two active neutrons, which is not enough to predict the experimental states. However, our interactions at NLO$_{\mathrm{vs}}$ and N^{3}LO$_{\mathrm{vs}}$ predict the ordering of the states correctly. At N^{3}LO$_{\mathrm{vs}}$, the first excited state agrees with experiment, but the second excited state overestimates the experimental value. In the second panel next to it, we show spectra in ^{27}Na. There are some minor differences between the interaction at N^{3}LO$_{\mathrm{vs}}$ and experiment. Still, the interactions improves greatly compared to NLO$_{\mathrm{vs}}$, showing the importance of the sub-leading valence-space operators. Interactions at lower orders are not capable to predict the right ground state for this nucleus.

In the second row, we show results in ^{37}P (left) and ^{46}K (right). In ^{37}P, the NLO$_{\mathrm{vs}}$ interaction already agrees with many of the excited states and we find that the interaction at N^{3}LO$_{\mathrm{vs}}$ improves further. Similar as in the sodium isotope, the spectra of ^{46}K can only be reproduced at N^{3}LO$_{\mathrm{vs}}$.

We show two more predictions in the last row. On the left, in ^{29}F, the interaction at N^{3}LO$_{\mathrm{vs}}$ overestimates the excited state, but the prediction at NLO$_{\mathrm{vs}}$ agrees with the experimental state from Ref. [240] within uncertainties. Within Ref. [240], it is suggested that this state is considered as a bound representation of the first excited 2^+ state of ^{28}O (shown on the right). Furthermore, a 2^+ excitation of ^{28}O below 3 MeV is suggested, which is consistent with our interaction at NLO$_{\mathrm{vs}}$ and N^{3}LO$_{\mathrm{vs}}$. Our interactions lead to an energy $E_{2^+} \sim 2.5$ MeV. However, as ^{28}O is unbound by two- and four-neutron emission, one needs to be aware of continuum effects.

10.6 Summary of main results

In the following, we summarize our main findings:

- We found that our valence-space interactions in the $sd + 0f_{7/2}$ space perform worse than those in the sd shell for several reasons:
  - Center-of-mass problem: Incomplete $N\hbar\omega$ spaces might be affected by spurious CM contamination. To exclude the main source of contamination, we demand the $0d_{5/2}$ neutron orbit to be filled at all times. This effects the quality as the possible configurations are limited.
  - Data set: There is fewer experimental data available for neutron-rich nuclei. Furthermore, for our first approach, we were not able to analyze the data set as thoroughly as for the sd-shell interactions. One also needs to keep in mind that due to the filled $0d_{5/2}$ neutron orbit

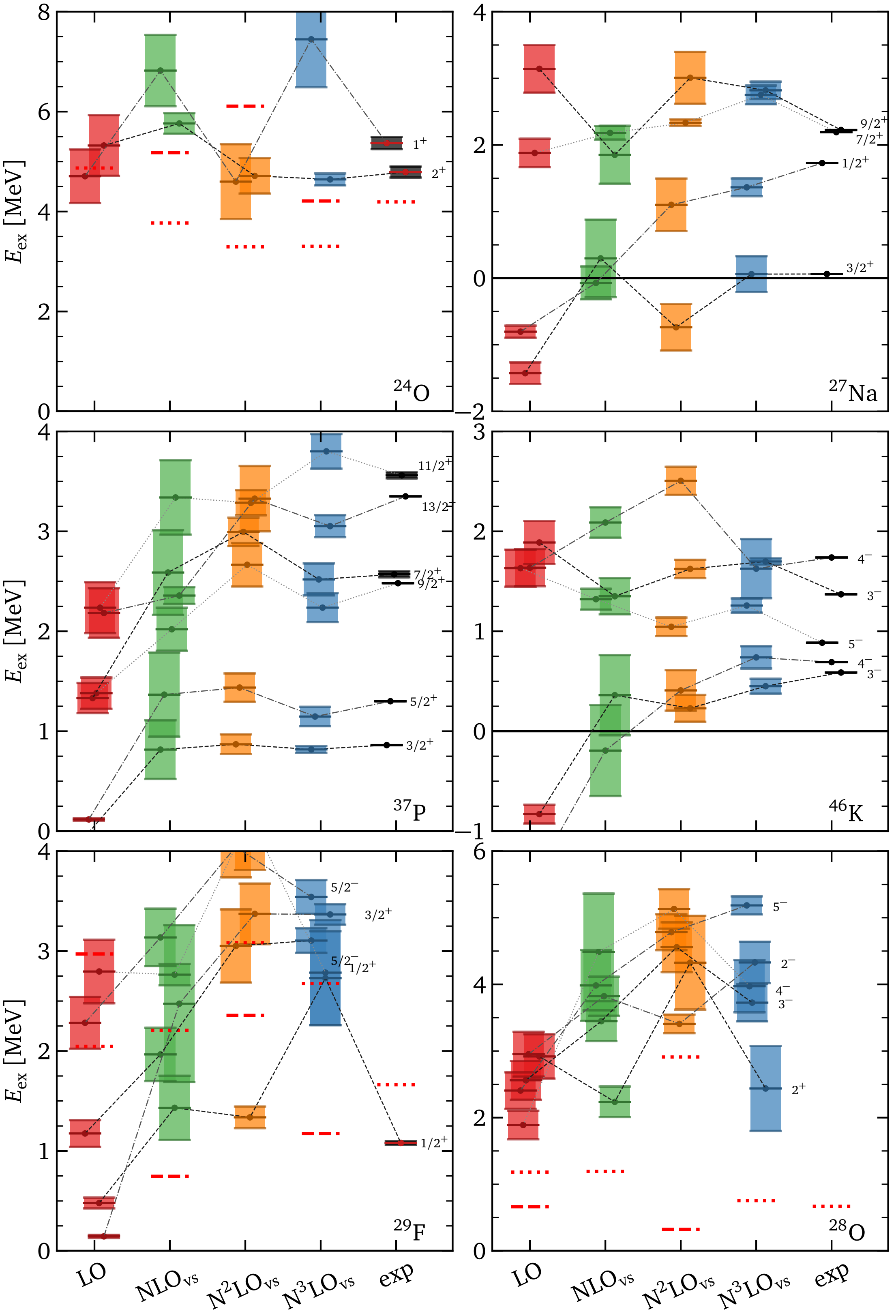

Figure 10.8.: Predictions of excited states in oxygen, fluorine, and neon isotopes. In each panel, we show results for the cross-shell interaction at LO, NLO$_{\text{vs}}$, N^{2}LO$_{\text{vs}}$, and N^{3}LO$_{\text{vs}}$ in comparison to experimental results. The same states are joined by dashed lines to guide the eye. Angular momentum labels are printed on the right. Isotope labels are given in the lower right corner. The red $1/2^+$ states in ^{29}F are taken from Ref. [240], where a 2^+ excitation is suggested below 3 MeV in ^{28}O. We show the one (two)-neutron separation energies S_n (S_{2n}) as a dotted (dashed) red line if they are present in the spectrum.

mentioned in the bullet point above, we cannot describe all states in the data set with high precision.

  - Missing three-body forces: In the future, it would be interesting to see how three-body forces factor in, as they play an important role in the neutron-rich region from *ab initio* calculations [221].

  With these drawbacks in mind, our first approach opens the door for future research of cross-shell interactions. We reach root-mean-square deviation of 655 keV at N^{3}LO$_{\rm vs}$. As in the chapter before, the interaction at N^{3}LO$_{\rm vs}$ improves compared to the one at NLO$_{\rm vs}$.The interaction at N^{2}LO$_{\rm vs}$ deteriorates compared to the one at NLO$_{\rm vs}$.

- We investigated isotopic chains to determine the dripline for neutron-rich nuclei. As the ground-state energies for neutron-rich nuclei is approximately a flat line, the determination of the dripline is complicated. We take the central energy values for our best interactions at N^{3}LO$_{\rm vs}$ and NLO$_{\rm vs}$. With this, we provide a first estimate of the neutron dripline.

- Similar complications affect the excitation spectrum. The general trend of our interactions is close to the experimental values. The precision is reduced compared to our achievements in the pure sd-shell interactions from Ch. 9. However, the N^{3}LO$_{\rm vs}$ interaction predicts the correct energy of the first excited state in ^{24}O and we give predictions for a possible excited 2^+ state in ^{28}O, which is below 3 MeV as suggested in Ref. [240].

11 Summary and outlook

To conclude this thesis we give a short summary of our findings and an outlook on future perspectives. We investigated chiral effective field theory for local two-body interactions and interactions in the nucleus, we split the summary and outlook accordingly.

11.1 Summary

In the first part of this thesis, we considered local two-body potentials from chiral EFT, where we followed closely the prescription of Ref. [39] for their construction. We fitted the LECs to phase shifts from the partial-wave analysis from Ref. [162]. Our investigations stretch over a broad cutoff range. We constructed very soft interactions with large coordinate-space cutoffs up to R_0 = 1.6 fm and investigated LO interactions at low cutoffs down to R_0 = 0.1 fm. A detailed summary follows below.

The second part focused on shell-model interactions from chiral effective field theory. Rather than adjusting LECs to few-nucleon data and subsequently transforming the resulting interactions to use them within a many-body framework, we constructed effective shell-model Hamiltonians directly by fitting the LECs to nuclear ground-state energies and excitation energies in the valence space under consideration. More details are given in the second subsection.

11.1.1 Local interactions from chiral effective field theory

In Ch. 4, we constructed new soft local interactions by lowering the momentum-space cutoff Λ (i.e., raising the coordinate-space cutoff R_0). Our interactions remain local in contrast to the conventional approach, which is to apply RG methods in order to obtain soft interactions. However, our interactions are not as soft as those obtained from RG methods. We constructed interactions for cutoffs R_0 = 1.2, 1.4 and 1.6 fm at LO, NLO and N^{2}LO. The interactions we constructed agree very well with the phase shifts from Ref. [162]. The deuteron binding energy, even though it is not explicitly included in the fit, improved from LO to N^{2}LO towards the experimental binding energy. We found that the binding energy at LO increases with increasing R_0 from 1.8 MeV for $R_0 = 1.2$ fm to 2.0 MeV for $R_0 = 1.6$ fm. At higher orders, the binding energies for different coordinate-space cutoffs are very similar. We investigated the "softness" of the different cutoffs by comparing coordinate-space and momentum-space matrix elements at N^{2}LO. In coordinate space, we saw that the S-waves interaction becomes less repulsive at zero distances as the cutoff R_0 is increased. In momentum space, off-diagonal elements are moved towards the diagonal as the cutoff increases.

We then presented first applications of our interactions, where we used them in double-folding potentials to calculate ^{16}O–^{16}O scattering cross sections. We observed an order-by-order improvement from our LO interaction up to N^{2}LO. At N^{2}LO, the cross-section results are in very good agreement to experimental measurements, especially at small scattering angles. Further results of investigations based on double-folding potentials are presented in Ref. [108].

We then investigated the violation of the Fierz-rearrangement freedom that appears when one uses local regulators. Our investigations focused on local two-nucleon interactions from chiral EFT at LO and NLO. We constructed interactions with R_0 = 1.0 and 1.2 fm at LO and NLO for all possible pairs of LO operators. We fitted the LO interaction to phase shifts in the two S-wave channels. In addition we constructed two "complete" LO interactions that feature all four operator combinations $\mathbb{1}$, $\boldsymbol{\sigma}_1 \cdot \boldsymbol{\sigma}_2$, $\boldsymbol{\tau}_1 \cdot \boldsymbol{\tau}_2$, and $(\boldsymbol{\sigma}_1 \cdot \boldsymbol{\sigma}_2)(\boldsymbol{\tau}_1 \cdot \boldsymbol{\tau}_2)$. We determined the additional two LECs for the two complete interactions as follows. For the LO$_{\mathrm{n}P}$ interaction by projecting on partial waves with $ST = 01$ and 10. In doing so, contributions from contact interactions to partial waves with odd orbital angular momenta are removed. With our different interactions, we studied phase shifts, the deuteron and ^{4}He binding energies, as well as the energy of neutron matter at different densities. As we fitted the LECs to the two $ST = 01$ and 10 channels, we found that all interactions lead to an identical phase shifts in corresponding partial waves at LO. For the $S = T$ channels, e.g., the $^1P_1$ and ^3P_J partial waves, we found instead a strong dependence on the chosen operator structure for energies of the order of 20 MeV. We also investigated the impact of different LO contact operators at NLO. We found an improved description of the phase shifts in general. The effect of the violation of the Fierz-rearrangement freedom is reduced considerably, having an effect only at energies larger than 100 MeV.

We found similar trends in our investigations of ^{4}He. The uncertainty of the ground-state energy due to the violation of the Fierz ambiguity is reduced considerably when going from LO to NLO, from 8.7 MeV to 3.8 MeV. In neutron matter, we found a sizable dependence on the chosen operator structure at LO. In particular, the LO$_{nP}$ interaction and the operator combination $\mathbb{1}, \boldsymbol{\tau}_1 \cdot \boldsymbol{\tau}_2$, lead to bound neutron matter. For the five interactions that did not show a collapse, the spread from choosing different operator pairs reduced from $2.0\,(5.8)$ MeV to $0.2\,(1.5)$ MeV when going from LO to NLO for $n = n_0/2\,(n_0)$. At NLO, this spread due to the violation of the Fierz ambiguity is much smaller than the EKM uncertainties for both densities. At saturation density, the operator dependence for the leading NN interactions was found to be smaller than that for the leading $3N$ forces at N^{2}LO, with the latter being ≈ 4 MeV for the three different operator choices in Ref. [109].

The key result of our investigation is that the violation of the Fierz ambiguity in the NN sector is sizable at LO, but restored to a large extent by including the subleading contact operators at NLO. Hence, local chiral NN interactions, can be used with confidence even though additional regulator artifacts appear. These findings have implications for $3N$ interactions. We found that the spread induced by different operator choices is sizable for the leading NN interactions. This is also the case for the leading $3N$ interactions as shown in Refs. [109, 170]. Our results demonstrate that the subleading contact interactions are necessary to reduce this spread. While in the NN sector they appear already at NLO in chiral power counting, the subleading $3N$ contact interactions only enter at N^{4}LO. The implementation of the N^{4}LO $3N$ forces is certainly challenging. Therefore, in order to reduce the violation of Fierz-rearrangement freedom in the $3N$ sector, other ideas are necessary. These include the choice of the projected V_E interaction of Ref. [109] or increasing the (momentum-space) cutoff for chiral interactions (see first developments in Ch. 6). However, we also note that we expect the EKM uncertainties to cover this effect for many (but not all) nuclear systems. In particular, for nuclear systems with densities (momenta) of the order of saturation density, we expect the EKM uncertainties to underestimate the effect coming from the violation of the Fierz ambiguity.

In Ch. 6, we further investigated the behavior of local chiral interactions at LO in WPC, when the coordinate-space cutoff is lowered. We constructed interactions for cutoffs ranging from $R_0^{-1} = 0.8\ \mathrm{fm}^{-1}$ to $10.0\ \mathrm{fm}^{-1}$ for different choices of the regulator function and different operator pairs. As before, our interactions were fit to reproduce the S-wave phase shifts. Our results show that for the operator combination $(\mathbb{1}, \sigma_{12})$, phase shifts in all partial waves as well as the deuteron ground-state energy converge on a plateau when lowering the cutoff, leading to cutoff-independent results. This can be explained by our findings from Ch. 5. Local regulators mix operator contributions into higher partial waves. It follows, that the S-wave contact interactions also contribute in P-wave and larger channels. For this particular choice of operators, the resulting C_{11} LEC is identical to the C_{10} LEC. This means that the strength needed to balance out the attractive tensor admixture in the coupled $^3S_1$-$^3D_1$ channel also enters the ^3P_J channels. Thus, using the artifacts of local regulators to our advantage allowed us to construct interactions that enable a cutoff-independent description of phase shifts and the deuteron binding energy. We found good agreement, comparing the phase-shift predictions for these hard-core interactions with the PWA phase-shift analysis. However, we explicitly state that these results do not imply a renormalizability of the WPC.

11.1.2 Shell-model interactions

We started our research on effective shell-model interactions from chiral EFT with charge-independent interactions up to NLO in the sd valence space in Ch. 8. We introduced new operators that only appear in the valence space, due to the broken Galilean invariance by the presence of a core in the shell-model framework. Those new operators depend explicitly on the two-body center-of-mass momentum. We constructed a NLO$_{\mathrm{vs}}$ interaction, consisting of the nine free-space contact operators and, in addition, of five new valence-space operators. The shell-model fits lead to a systematic improvement from LO to NLO and NLO$_{\mathrm{vs}}$ and resulted in natural LECs at all orders. The RMS derivation of the fits improved from 1.8 MeV at LO to 0.7 MeV at NLO and 0.5 MeV at NLO$_{\mathrm{vs}}$. The latter included five novel operators that depend on the two-body CM momentum, so that the total number of LECs at NLO$_{\mathrm{vs}}$ is 14. In comparison to USD-type interactions, the RMS deviation is about 200 keV higher, but shows a similar rapid improvement with the number of LECs. Moreover, the monopole matrix elements are similar to the successful USDA/USDB interactions at NLO and NLO$_{\mathrm{vs}}$. Therefore, we conclude that the chiral EFT operators efficiently capture the relevant physics at low energies.

We expanded our investigations in the sd shell by advancing in the chiral power counting up to N^{3}LO, where sub-leading valence-space operators enter. We developed the 32 new valence-space operators and constructed charge-dependent valence-space interactions at LO, NLO$_{\mathrm{vs}}$, N^{2}LO$_{\mathrm{vs}}$, and N^{3}LO$_{\mathrm{vs}}$, where we also adjusted the SPEs for protons and neutrons to the experimental data set. The RMS deviation improved at all orders, due to the additional SPE. At LO to 0.93 MeV, at NLO to 0.61 MeV, and at NLO$_{\mathrm{vs}}$ to 0.44 MeV. We found that the interaction at N^{2}LO$_{\mathrm{vs}}$ deteriorates compared to NLO$_{\mathrm{vs}}$, and results in a RMS deviation of 0.51 MeV. At N^{3}LO$_{\mathrm{vs}}$ we obtained a RMS deviation of 0.16 MeV, which reaches the quality of the USD interaction from Ref. [114]. The LECs for all of those interactions are of natural size.

The interactions show a good reproduction of experimental ground-state energies at all orders, and a striking improvement in the reproduction of excitation energies from LO to NLO$_{\mathrm{vs}}$ and from NLO$_{\mathrm{vs}}$ to N^{3}LO$_{\mathrm{vs}}$. Besides the deteriorating N^{2}LO$_{\mathrm{vs}}$ interaction, the improvement is very systematic and developed shell-model interactions show promising predictions for neutron-rich isotopes beyond the fitted data set. We showed this for the oxygen dripline, which was reproduced within uncertainties and in the excitation spectrum of neutron-rich isotopes. However, we also found that the predictive power decreased in the vicinity of the sd-shell closure, and we produced a bound ^{26}O at N^{3}LO$_{\mathrm{vs}}$ due to the Coulomb correction scheme we applied.

In order to describe very neutron-rich systems, we expanded our valence space to the $sd + 0f_{7/2}$ orbits, which also considered configurations in the neutron $0f_{7/2}$ subshell. We constructed interactions at LO, NLO$_{\mathrm{vs}}$, N^{2}LO$_{\mathrm{vs}}$, and N^{3}LO$_{\mathrm{vs}}$ and found a similar behavior for the systematic improvement as before, including the deteriorating RMS value of the N^{2}LO$_{\mathrm{vs}}$ interaction. Also here, all LECs are of natural size. Our interactions have less precision than those in the sd shell. We achieve RMS deviations of 3.29 MeV at LO, 0.88 MeV at NLO$_{\mathrm{vs}}$, 0.96 MeV at N^{2}LO$_{\mathrm{vs}}$, and 0.70 MeV at N^{3}LO$_{\mathrm{vs}}$.

We used the NLO$_{\mathrm{vs}}$ and N^{2}LO$_{\mathrm{vs}}$ interactions to predict the neutron driplines for oxygen, fluorine, neon, sodium, and magnesium. Nuclei with more protons have their dripline ouside of the $sd + 0f_{7/2}$ valence space. We found that both interaction predict the experimental oxygen dripline at ^{24}O. In total, the dripline given by the two interactions is located at ^{24}O, ^{29}F, ^{32}Ne, $^{35-37}$Na, and at, or beyond $^{38-40}$Mg.

We also investigate the excited states in the cross-shell valence space and gave a prediction for the first excited 2^+ state in ^{28}O. Our interactions at NLO$_{\mathrm{vs}}$ and N^{3}LO$_{\mathrm{vs}}$ predict this state at roughly 2.5 MeV, which is consistent with the experimental observations from Ref. [240]. However, one needs to be aware that continuum effects play an increasing role.

11.2 Outlook

11.2.1 Local interactions

Up to now, all of our local interactions have been fit to phase shifts. Phase shifts provide a convenient access point to adjust theories to, as they are given in a partial-wave decomposed representation. However, this is done by imposing a model on experimental scattering data, and hence, we referred to them as semi-empirical values. In the future, we would like to adjust our interactions directly to scattering data. This approach requires more time, which is why fits to phase shifts are sufficient for our first investigations of local interactions.

The next obvious step is to include tree-body forces that first appear at N^{2}LO and simultaneously fit two- and three-body LECs to data. One can also think about increasing the order of the interaction by taking the local operators that appear at N^{3}LO, as done in Ref. [41]. However, at N^{3}LO one cannot find a complete operator set that leaves the interaction local in the way it is possible at NLO. A perturbative treatment of non-local contributions might be feasible.

In Ch. 6, we investigated an interesting case for local interactions, that may be beneficial from a practical point of view: local interactions with larger R_0^{-1} can easily be explored with Quantum Monte Carlo methods and may allow to reduce regulator artifacts in many-body systems. In Ref. [107], it was found that lowering the $3N$ cutoff R_{3N} in pure neutron matter while keeping a constant NN cutoff R_0 leads to collapses of the many-body system. The best result was found for $R_{3N} = R_0$. If it is possible to construct chiral interactions with smaller NN cutoff and no spurious bound states, one can lower the $3N$ cutoff while at the same time avoiding such collapses. This will help to reduce $3N$ regulator artifacts, which have been found to be sizable; see Refs. [170, 241]. This, in turn, may allow to drastically reduce uncertainties in many-body calculations with local chiral interactions. For this, one would need to carry out similar investigations as in Ch. 6, but at higher orders.

11.2.2 Valence-space interactions

Our investigations of valence-space interactions open the door for very interesting follow up projects. The first steps one would need to address are the inclusion of three-body forces and possibly the exploration of consistent electroweak transition based on chiral EFT operators. Also more work needs to be invested to get a better understanding of the EFT uncertainties in the valence space. In the long run, this framework can be expanded to calculate key matrix elements, such as for neutrino-less double-beta decay.

The sd + $0f_{7/2}$ cross-shell results were a first application. Future investigations have to focus on how to handle the center-of-mass problem in a way that one can remove spurious states easily in every iteration of the fit, which would allow us to keep a more flexible model space. Furthermore, a thorough analysis of the cross-shell data set is necessary. For this, spurious excitations out of the valence space need to be singled out, as well as states in which neutrons are excited out of the $0d_{5/2}$ shell. An investigation of the sd + $0f_{7/2}$ model space, and possibly the inclusion of additional pf orbits might lead to new insights on neutron-rich regions of the nuclear chart.

The theoretical and computational framework to construct any shell-model interaction for a major shell has been laid out in this thesis. Constructing, e.g., pf-shell interactions only requires an adequate data set. Steps that need consideration are mentioned above. Expanding the model space works completely analogous to what we have discussed here. This will provide further interesting interactions in a region not yet fully accessible to *ab initio* methods. This is especially important for exotic nuclei and for heavier nuclei than in the sd shell.

A Angular momentum theory

A.1 Irreducible tensor operators

Before we go into detail, we address differences in the terminology between physical tensor operators and tensor operators in angular momentum theory, which we need to clarify. In the language of angular momentum theory, scalars are (spherical) tensor operators of rank zero, vectors are tensor operators of rank one, matrices are tensor operators of rank two and so on. Working with spherical tensor operators is often a convenient alternative, since they transform under rotation of the coordinate system, just like eigenvectors of the angular momentum operator. We can write all operators in this work as spherical tensor operators of total rank zero, which is a requirement for the operator in order to preserve the total angular momentum. For this we use expressions from Ref. [242]. The constituents may have a different rank, as long as they couple to rank zero. The most basic constituent in this work, $\mathbf{p}, \mathbf{p}', \mathbf{P}, \boldsymbol{\sigma}_i$, and $\boldsymbol{\tau}_i$, can all be expressed as spherical tensors of rank one. In particular, we can write a generic vector $\mathbf{x}$ as

$$\mathbf{x} = \sum_{\mu=-1}^{1} x_{1\mu} \mathbf{e}^{1\mu} , \tag{A.1}$$

where the basis vectors can be expressed by cartesian basis vectors:

$$\begin{aligned} \mathbf{e}^{1+1} &= -\frac{1}{\sqrt{2}}(\mathbf{e}_x - i\mathbf{e}_y) , \\ \mathbf{e}^{10} &= \mathbf{e}_z , \\ \mathbf{e}^{1-1} &= \frac{1}{\sqrt{2}}(\mathbf{e}_x + i\mathbf{e}_y) , \end{aligned} \tag{A.2}$$

and we can write $x_{1\mu}$ in terms of spherical harmonics

$$x_{1\mu} = \sqrt{\frac{4\pi}{3}} |\mathbf{x}| \mathrm{Y}_{1\mu}(\Omega_x) . \tag{A.3}$$

As a short-hand notation, we will omit the index 1 for simple vectors and only write x_μ instead of $x_{1\mu}$ for reasons of brevity. In this notation, we write scalar products and vector products as

$$\mathbf{a} \cdot \mathbf{b} = -\sqrt{3}\{a \otimes b\}_{00} \tag{A.4}$$

and

$$(\mathbf{a} \times \mathbf{b})_\mu = -i\sqrt{2}\{a \otimes b\}_{1\mu} . \tag{A.5}$$

In general, coupling two identical rank one tensors to a rank j tensor is expressed as

$$\{x \otimes x\}_{jm} = \sqrt{\frac{4\pi}{2j+1}} x^2 \, \mathrm{Y}_{jm}(\Omega_x) \, C^{j0}_{1010} , \tag{A.6}$$

while for two different arbitrary tensor operators a_{j_a} and b_{j_b}, we find:

$$\{a_{j_a} \otimes b_{j_b}\}_{jm} = \sum_{m_a, m_b} C^{jm}_{j_a m_a j_b m_b} a_{j_a m_a} b_{j_b m_b} , \tag{A.7}$$

and for the special case with $j_a = j_b = 1$ we find

$$\{a \otimes b\}_{jm} = \frac{4\pi}{3} ab \sum_{m_a, m_b = -1}^{1} C^{jm}_{1m_a 1m_b} \mathrm{Y}_{1m_a}(\Omega_a) \mathrm{Y}_{1m_b}(\Omega_b)\,, \tag{A.8}$$

where $\{a \otimes b\}_{jm}$ denotes a tensor product of two rank one tensors to a new tensor of rank j. For arbitrary commuting tensors we get

$$\{a_{j_1} \otimes b_{j_2}\}_{jm} = (-1)^{j_1 + j_2 - j} \{b_{j_2} \otimes a_{j_1}\}_{jm}\,. \tag{A.9}$$

We will drop the projection index for rank zero tensor products in the future $\{a \otimes b\}_0 \equiv \{a \otimes b\}_{00}$.

In angular momentum theory, tensor operators refer to irreducible spherical tensors of a certain rank, while in nuclear physics it refers in particular to the S_{12} operator given by

$$S_{12}(\mathbf{a}, \mathbf{b}) = \frac{1}{2}[(\boldsymbol{\sigma}_1 \cdot \mathbf{a})(\boldsymbol{\sigma}_2 \cdot \mathbf{b}) + (\boldsymbol{\sigma}_1 \cdot \mathbf{b})(\boldsymbol{\sigma}_2 \cdot \mathbf{a})] - \frac{1}{3}(\boldsymbol{\sigma}_1 \cdot \boldsymbol{\sigma}_2)(\mathbf{a} \cdot \mathbf{b})\,. \tag{A.10}$$

Following Ref. [242], we can write this operator as

$$S_{12}(\mathbf{a}, \mathbf{b}) = \sqrt{5}\{\{a \otimes b\}_2 \otimes \{\sigma_1 \otimes \sigma_2\}_2\}_0\,, \tag{A.11}$$

which is a rank two tensor in spin space. In the rest of the appendix, tensor operator in $\mathbf{q}$ or $\mathbf{k}$ refer to the physical tensor operator from Eq. (A.10). Otherwise, we refer to general tensor operators in the language of angular momentum theory.

A.2 Mathematical toolbox for angular momentum coupling

The recoupling of angular momenta of operators is often accompanied Clebsch-Gordan coefficients, spherical harmonics, and six- and nine-j-symbols. We further use the Wigner-Eckert theorem to evaluate so-called reduced matrix elements. For a comprehensive description of these topics we refer to Ref. [242]. Nevertheless, for completeness we go into detail for relevant expressions in this section.

A.2.1 Clebsch-Gordan coefficient

Clebsch-Gordan coefficients (CGs) play an important role in angular momentum coupling. The coefficient provides the amplitude for coupling two angular momenta together, e.g., the amplitude to couple angular momenta j_1 and j_2 with their projections m_1 and m_2 to the angular momentum j and projection m. We use the following notation

$$C^{jm}_{j_1 m_1 j_2 m_2} = \langle j_1 m_1, j_2 m_2 | jm \rangle = \langle jm | j_1 m_1, j_2 m_2 \rangle\,, \tag{A.12}$$

where the Clebsch-Gordan coefficient vanishes, unless the triangular inequalities

$$|j_1 - j_2| \leq j \leq j_1 + j_2\,, \tag{A.13}$$

are fulfilled and the projections add up $m = m_1 + m_2$. The six- and nine-j-symbols, which we encounter later in this chapter, can be reduced to products and sums of CGs. In the following we investigate some properties and special cases of CGs.

- **Symmetry properties**
  We can change the ordering of the angular momenta in the CG via (cf. Ref. [242] p. 245 Eqs. (10, 11))

$$\begin{aligned} C^{jm}_{j_1m_1j_2m_2} = \; & (-1)^{j_1+j_2-j}C^{jm}_{j_2m_2j_1m_1} = (-1)^{j_1-m_1}\frac{[j]}{[j_2]}C^{j_2-m_2}_{j_1m_1j-m} = (-1)^{j_1-m_1}\frac{[j]}{[j_2]}C^{j_2m_2}_{jmj_1-m_1} \\ = & (-1)^{j_1+j_2-j}C^{j-m}_{j_1-m_1j_2-m_2} = (-1)^{j_2+m_2}\frac{[j]}{[j_1]}C^{j_1-m_1}_{j-mj_2m_2} = (-1)^{j_2+m_2}\frac{[j]}{[j_1]}C^{j_1m_1}_{j_2-m_2jm}\,, \end{aligned} \tag{A.14}$$

  where we use the short-hand notation

$$[x] \equiv \sqrt{2x-1}\,. \tag{A.15}$$

- **All projections are zero**
  In the case, where all projections are zero $m_1 = m_2 = m = 0$ the CG $C^{j0}_{j_10j_20}$ vanishes unless the additional requirement:

$$j + j_1 + j_2 = \text{ even}\,, \tag{A.16}$$

  is fulfilled. Later on, we will encounter two special cases. In the first, we have $C^{j0}_{j_1010}$, which allows only $j = |j_1 \pm 1|$ and in the second case we have $C^{j0}_{j_1020}$, which only allows the configuration $j = |j_1 \pm 2|$ or $j = j_1$. This helps to reduce participating sums over j or j_1.

- **Sums that involve Clebsch-Gordon coefficients**
  A sum that involves two CGs can be reduced via

$$\sum_{m_1,m_2} C^{jm}_{j_1m_1j_2m_2}C^{j'm'}_{j_1m_1j_2m_2} = \delta_{jj'}\delta_{mm'}\,, \tag{A.17}$$

  and

$$\sum_{j,m} C^{jm}_{j_1m_1j_2m_2}C^{jm}_{j_1m_1'j_2m_2'} = \delta_{m_1m_1'}\delta_{m_2m_2'}\,. \tag{A.18}$$

  We reduce a sum that involves three CGs to

$$\sum_{m_1,m_2,m'} C^{jm}_{j_1m_1j_2m_2}C^{j''m''}_{j'm'j_2m_2}C^{j'm'}_{j_1m_1j'''m'''} = (-1)^{j+2+j+j'+j'''}[j][j']C^{j''m''}_{jmj'''m'''}\begin{Bmatrix} j_1 & j_2 & j \\ j'' & j''' & j' \end{Bmatrix}\,, \tag{A.19}$$

  where the last expression is a six-j-symbol. Together with Eq. (A.14), we can interchange the labels of Eqs. (A.17 - A.19).

- **Connection to the Wigner three-jm-symbol**
  The relation between Wigner three-jm-symbols and CGs is given by

$$\begin{pmatrix} j_1 & j_2 & j \\ m_1 & m_2 & m \end{pmatrix} = (-1)^{j+m+2j_1}\frac{1}{[j]}C^{jm}_{j_1-m_1j_2-m_2}\,, \tag{A.20}$$

  and

$$C^{jm}_{j_1m_1j_2m_2} = (-1)^{j_1-j_2+m}[j]\begin{pmatrix} j_1 & j_2 & j \\ m_1 & m_2 & -m \end{pmatrix}\,. \tag{A.21}$$

  The symmetries of the three-jm symbols are more accessible than those of the CGs, which is why they are favored for the definition of the six-j-symbols, as we will see later on.

A.2.2 Spherical harmonics

Most operators that we encounter can be expressed as spherical tensor operators, which depend on spherical harmonics

$$\mathrm{Y}_{lm}(\Omega) = \langle \Omega | lm \rangle \;, \tag{A.22}$$

$$\mathrm{Y}^*_{lm}(\Omega) = \langle lm | \Omega \rangle \;, \tag{A.23}$$

as in Eq. (A.2). In a partial-wave decomposition, there are consequently spherical harmonics from the operators under consideration as well as from the states. Consider the partial-wave decomposition of a momentum-independent trial potential $\langle \mathbf{p} | \boldsymbol{V}^{\mathrm{trial}} | \mathbf{p}' \rangle = C^{\mathrm{trial}}$ for clarification. We want to determine the following matrix element

$$\langle p''(ls)jt | \boldsymbol{V}^{\mathrm{trial}} | p'''(l's)jt \rangle = \frac{1}{(2\pi)^6} \int \mathrm{d}^3 p \int \mathrm{d}^3 p' \, \langle p''(ls)jt | \mathbf{p} \rangle \, C^{\mathrm{trial}} \, \langle \mathbf{p}' | p'''(l's)jt \rangle \;, \tag{A.24}$$

where we inserted a complete set of basis states in p and p' with $\frac{1}{(2\pi)^3} \int \mathrm{d}^3 p \, |\mathbf{p}\rangle \langle \mathbf{p}| = \mathbb{1}$. The overlap can be calculated with CGs and spherical harmonics via

$$\begin{aligned} \langle p''(ls)jt | \mathbf{p} \rangle &= \sum_{m_l, m_s} C^{j(m_l+m_s)}_{l m_l s m_s} \langle p'' l m_l | \mathbf{p} \rangle \, \langle s m_s | \\ &= (2\pi)^3 \frac{\delta(p - p'')}{p p''} \sum_{m_l, m_s} C^{j(m_l+m_s)}_{l m_l s m_s} \langle l m_l | \Omega_p \rangle \, \langle s m_s | \;, \end{aligned} \tag{A.25}$$

and similar for $\langle \mathbf{p}' | p'''(l's)jt \rangle$. Inserting this in the equation above, we find

$$\langle p''(ls)jt | \boldsymbol{V}^{\mathrm{trial}} | p'''(l's)jt \rangle = \sum_{m_l, m_{l'}} \sum_{m_s, m_{s'}} C^{j(m_l+m_s)}_{l m_l s m_s} C^{j(m_{l'}+m_{s'})}_{l' m_{l'} s m_{s'}} \int \mathrm{d}\Omega_p \int \mathrm{d}\Omega_{p'} \, \langle s | C^{\mathrm{trial}} | s \rangle \, \mathrm{Y}^*_{l m_l}\left(\Omega_p\right) \mathrm{Y}_{l' m_{l'}}\left(\Omega_{p'}\right) . \tag{A.26}$$

If the potential under consideration also contains spherical harmonics we often need to solve angular integrals over multiple spherical harmonics. We will list results for integrals over spherical harmonics in the following.

Integrals that involve spherical harmonics

Results for angular integrals, over one, two, and three spherical harmonic function(s) read

$$\int \mathrm{d}\Omega \, \mathrm{Y}^*_{lm}(\Omega) = \int \mathrm{d}\Omega \, \mathrm{Y}_{lm}(\Omega) = \sqrt{4\pi} \delta_{l0} \delta_{m0} \,. \tag{A.27}$$

$$\int \mathrm{d}\Omega \, \mathrm{Y}^*_{lm}(\Omega) \mathrm{Y}_{l'm'}(\Omega) = \int \mathrm{d}\Omega \, \langle lm | \Omega \rangle \langle \Omega | l'm' \rangle = \langle lm | l'm' \rangle = \delta_{ll'} \delta_{mm'} \,. \tag{A.28}$$

$$\int \mathrm{d}\Omega \, \mathrm{Y}^*_{lm}(\Omega) \mathrm{Y}_{l'm'}(\Omega) \mathrm{Y}_{l''m''}(\Omega) = \frac{[l'][l'']}{\sqrt{4\pi}[l]} C^{l0}_{l'0l''0} C^{lm}_{l'm'l''m''} \,, \tag{A.29}$$

where we can write a non-adjungated spherical harmonic as

$$\mathrm{Y}_{lm}(\Omega) = (-1)^m \, \mathrm{Y}^*_{l-m}(\Omega) \,. \tag{A.30}$$

In Eq. (A.27), we use the identity $\sqrt{4\pi} \, \mathrm{Y}_{00}(\Omega) = \sqrt{4\pi} \, \mathrm{Y}^*_{00}(\Omega) = 1$ and apply the normalization of the spherical harmonics from Eq. (A.28). To solve the third integral, one uses recoupling relations for two spherical harmonics

$$\mathrm{Y}_{lm}(\Omega) \mathrm{Y}_{l'm'}(\Omega) = \sum_{l''m''} \frac{[l][l']}{\sqrt{4\pi}[l'']} C^{l''0}_{l0l'0} C^{l''m''}_{lml'm'} \mathrm{Y}_{l''m''}(\Omega) \,. \tag{A.31}$$

Afterwards, the result of the integral is determined by Eq. (A.28). By applying the last step repeatedly, one can find the solution for integrals with an arbitrary given number of spherical harmonics.

Tensor products that involve spherical harmonics

In Eq. (A.2), we express tensor operators of rank one in terms of spherical harmonics. In general we are often confronted with tensor operators of rank one that are coupled together to a new tensor operator of a different rank. At first, we consider n identical operators x of rank one, that couple to a new operator or rank l_n, which read

$$\{\cdots\{\{x\otimes x\}_{l_2}\otimes x\}_{l_3}\cdots\otimes x\}_{l_n m_n}=\frac{\sqrt{4\pi}}{[l_n]}x^n\,\mathrm{Y}_{l_n m_n}(\Omega)\prod_{i=2}^{n}C^{l_i 0}_{10 l_{i-1}}\,, \tag{A.32}$$

with $l_1=1$. This results from the general recoupling scheme for two spherical harmonics with identical angles, given by

$$\{\mathrm{Y}_a(\Omega)\otimes\mathrm{Y}_b(\Omega)\}_{LM}=\frac{[a][b]}{\sqrt{4\pi}[L]}C^{L0}_{a0b0}\mathrm{Y}_{LM}(\Omega)\,. \tag{A.33}$$

For two different tensor operators of rank one, a and b, we find

$$\begin{aligned}\{a\otimes b\}_{lm}&=\frac{4\pi}{3}ab\{\mathrm{Y}_1(\Omega_a)\otimes\mathrm{Y}_1(\Omega_b)\}_{lm}\\&=\frac{4\pi}{3}ab\sum_{m_1,m_2}C^{lm}_{1m_1 1m_2}\mathrm{Y}_{1m_1}(\Omega_a)\mathrm{Y}_{1m_2}(\Omega_b)\,,\end{aligned} \tag{A.34}$$

where we use the expression,

$$\{\mathrm{Y}_{l_1}(\Omega_a)\otimes\mathrm{Y}_{l_2}(\Omega_b)\}_{lm}=\sum_{m_1,m_2}C^{lm}_{l_1m_1l_2m_2}\mathrm{Y}_{l_1m_1}(\Omega_a)\mathrm{Y}_{l_2m_2}(\Omega_b)\,. \tag{A.35}$$

With this, we can express two different tensor operators of arbitrary rank, A_{l_1} and B_{l_2}, as long as we can construct them with Eq. (A.32).

Expansion of vector products

We can also express a scalar product of two operators as a scalar product of spherical harmonics, where the latter is defined by

$$\begin{aligned}(\mathrm{Y}_l(\Omega_1)\cdot\mathrm{Y}_l(\Omega_2))&=\sum_m\mathrm{Y}^*_{lm}(\Omega_1)\mathrm{Y}_{lm}(\Omega_2)\\&=[l](-1)^l\{\mathrm{Y}_l(\Omega_1)\otimes\mathrm{Y}_l(\Omega_2)\}_{00}\,.\end{aligned} \tag{A.36}$$

For two vectors **a** and **b** this results in

$$(\mathbf{a}\cdot\mathbf{b})=\frac{4\pi}{3}ab\,(\mathrm{Y}_1(\Omega_1)\cdot\mathrm{Y}_1(\Omega_2))\,. \tag{A.37}$$

$$(\mathbf{a}\cdot\mathbf{b})^n=4\pi a^n b^n\sum_l\frac{n!}{(n-l)!!\,(n+l+1)!!}(\mathrm{Y}_l(\Omega_1)\cdot\mathrm{Y}_l(\Omega_2))\,, \tag{A.38}$$

where the sum over l takes the values 0,2,…,n for even n and 1,3,…,n for odd n.

A.2.3 Six-j-symbol

The (Wigner) six-j-symbol is used in the coupling of three angular momenta. The symbol can be expressed with sums over three-jm-symbols, which can in turn be expressed by CGs with Eq. (A.20). We will use alphabetic letters rather than indices in j_i for the definition of the six- and nine-j-symbols to keep a clear overview. Projections of those letters are denoted by the corresponding Greek letter, instead of m_i. The six-j-symbol is defined by

$$\begin{Bmatrix} a & b & c \\ d & e & f \end{Bmatrix} = \sum_{\alpha - \varphi} (-1)^{d+e+f+\delta+\varepsilon+\varphi} \begin{pmatrix} a & b & c \\ \alpha & \beta & \gamma \end{pmatrix} \begin{pmatrix} a & e & f \\ \alpha & \varepsilon & -\varphi \end{pmatrix} \begin{pmatrix} d & b & f \\ -\delta & \beta & \varphi \end{pmatrix} \begin{pmatrix} d & e & c \\ \delta & -\varepsilon & \gamma \end{pmatrix}, \tag{A.39}$$

where the sum runs over all projections from α to φ. Each triad (a, b, c), (c, d, e), (b, d, f), and (f, a, e), needs to satisfy the triangular inequations, otherwise the six-j-symbols vanishes.

Symmetries and special cases of the six-j-symbol

The six-j-symbol is invariant under the exchange of any two rows or columns, e.g.:

$$\begin{Bmatrix} a & b & c \\ d & e & f \end{Bmatrix} = \begin{Bmatrix} b & a & c \\ e & d & f \end{Bmatrix} = \begin{Bmatrix} d & e & c \\ a & b & f \end{Bmatrix}, \tag{A.40}$$

all other cases can be constructed by interchanging rows and columns with respect to this rule. We further want to investigate the special case, in which one of the elements is zero. Without loss of generality we consider $f = 0$. Different cases can be obtained by applying the symmetry rules which we mentioned earlier. The special case yields:

$$\begin{Bmatrix} a & b & c \\ d & e & 0 \end{Bmatrix} = (-1)^{a+b+c} \frac{\delta_{ae}\delta_{bd}}{[a][b]}, \tag{A.41}$$

where the triad (a, b, c) still needs to fulfill the triangular inequations.

A.2.4 Nine-j-symbol

The (Wigner) nine-j-symbol is used in the coupling of four angular momenta, which we can express in terms of six-j-symbols

$$\begin{Bmatrix} a & b & c \\ d & e & f \\ g & h & i \end{Bmatrix} = \sum_{x} (-1)^{2x} [x]^2 \begin{Bmatrix} a & b & c \\ f & i & x \end{Bmatrix} \begin{Bmatrix} d & e & f \\ b & x & h \end{Bmatrix} \begin{Bmatrix} g & h & i \\ x & a & d \end{Bmatrix}, \tag{A.42}$$

where the sum over x runs over all values that fulfill the triangular inequations of the six-j-symbols. The nine-j-symbol is defined by the following overlap

$$\begin{Bmatrix} a & b & c \\ d & e & f \\ g & h & i \end{Bmatrix} = \frac{\langle\, [(ab)c, (de)f]i \mid [(ad)g, (be)h]i \,\rangle}{[c][f][g][h]}. \tag{A.43}$$

The nine-j-symbol vanishes unless each triad (a, b, c), (d, e, f), (g, h, i), (a, d, g), (b, e, h), and (c, f, i) satisfies the triangular inequations.

Symmetries of the nine-j-symbol

The nine-j-symbol is symmetric under transposition and under cyclic permutations of rows and columns, e.g.:

$$\begin{Bmatrix} a & b & c \\ d & e & f \\ g & h & i \end{Bmatrix} = \begin{Bmatrix} a & d & g \\ b & e & h \\ c & f & i \end{Bmatrix} = \begin{Bmatrix} d & e & f \\ g & h & i \\ a & b & c \end{Bmatrix} = \begin{Bmatrix} b & c & a \\ e & f & d \\ h & i & g \end{Bmatrix}, \tag{A.44}$$

where cyclic permutation means an even number of permutations. Under odd numbers of permutations one obtains, e.g.:

$$\begin{Bmatrix} a & b & c \\ d & e & f \\ g & h & i \end{Bmatrix} = (-1)^x \begin{Bmatrix} d & e & f \\ a & b & c \\ g & h & i \end{Bmatrix} = (-1)^x \begin{Bmatrix} b & a & c \\ e & d & f \\ h & g & i \end{Bmatrix}, \tag{A.45}$$

where $x = a+b+c+d+e+f+g+h+i$ is the sum over all entries in the nine-j-symbol. Following these rules, one can construct any ordering of contributing angular momenta a – f in the nine-j-symbol.

Special cases of the nine-j-symbol

For the first special case, we consider $i = 0$ without loss of generality. Different cases can be obtained by following the symmetries of the nine-j-symbol. We get

$$\begin{Bmatrix} a & b & c \\ d & e & f \\ g & h & 0 \end{Bmatrix} = \delta_{cf}\delta_{gh} \frac{(-1)^{b+c+d+g}}{[c][g]} \begin{Bmatrix} a & b & c \\ e & d & g \end{Bmatrix}. \tag{A.46}$$

In the second case we consider $i = e = 0$, and we get

$$\begin{Bmatrix} a & b & c \\ d & 0 & f \\ g & h & 0 \end{Bmatrix} = \delta_{cd}\delta_{cf}\delta_{bg}\delta_{gh} \frac{(-1)^{a-b-c}}{[b]^2[c]^2}, \tag{A.47}$$

which can be obtained for any case by applying Eq. (A.41) to Eq. (A.46). For the case, where three arguments are zero we obtain

$$\begin{Bmatrix} a & b & c \\ d & e & f \\ 0 & 0 & 0 \end{Bmatrix} = \frac{\delta_{ad}\delta_{be}\delta_{cf}}{[a][b][c]}. \tag{A.48}$$

A.2.5 Wigner-Eckart theorem

The Wigner-Eckart theorem states, that any dependence on the orientation of an arbitrary matrix element is entirely included in a CG. We can write the matrix element of an arbitrary operator $\boldsymbol{O}_{a\alpha}$ as

$$\langle njm|\boldsymbol{O}_{a\alpha}|n'j'm'\rangle = (-1)^{2a} C^{jm}_{j'm'a\alpha} \frac{\langle nj||\boldsymbol{O}_a||n'j'\rangle}{[j]}, \tag{A.49}$$

where the factor $\langle nj||\boldsymbol{O}_a||n'j'\rangle$ is called a reduced matrix element of $\boldsymbol{O}_{a\alpha}$. Here, quantum numbers that are not relevant for the evaluation of the matrix elements are pooled in n and n'. With this, we only need to calculate the reduced matrix element of a given operator once. In order to treat different projections m and m', we only need to calculate the CG.

A.3 Tensor recoupling

In the following, we consider up to four commuting, irreducible tensor operators A, B, D, and E, where the rank is denoted by the respective lower-case letter a, b, d, and e. The tensor operators A and B and D and E can be coupled pairwise to an irreducible tensor operator of a new rank (here: c or f). We consider the general case where all participating tensor operators are coupled to an irreducible tensor operator of rank i in the end.

A.3.1 Relations for commuting irreducible tensor operators

The rearrangement of tensor products is important for us, so that we can separate tensor operators according to relative, spin, and center-of-mass contributions later on. We list the relevant contributions below:

- **Product of two tensor operators**
  Two commuting tensor operators can be rearranged via

$$\{A_a \otimes B_b\}_i = (-1)^{a+b-i}\{B_b \otimes A_a\}_i \,. \tag{A.50}$$

  This relation is used to obtain different combinations for the subsequent tensor couplings.

- **Product of three tensor operators**
  In the case of three tensor operators we find

$$\{\{A_a \otimes B_b\}_c \otimes D_d\}_i = (-1)^{b+d+i}[c]\sum_f [f]\begin{Bmatrix} a & b & c \\ i & d & f \end{Bmatrix}\{B_b \otimes \{A_a \otimes D_d\}_f\}_i \,. \tag{A.51}$$

  We can use the following commutation relation to match the actual case to the structure from the equation above:

$$\begin{aligned}\{A_a \otimes \{B_b \otimes D_d\}_f\}_i &= (-1)^{b+d-f}\{A_a \otimes \{D_d \otimes B_b\}_f\}_i = (-1)^{a+f-i}\{\{B_b \otimes D_d\}_f \otimes A_a\}_i \\ &= (-1)^{a+b+d-i}\{\{D_d \otimes B_b\}_f \otimes A_a\}_i \,, \end{aligned} \tag{A.52}$$

  which is obtained by using Eq. (A.50).

- **Product of four tensor operators**
  In this work, we use the following recoupling relations for tensor products with four operators

$$\{\{A_a \otimes B_b\}_c \otimes \{D_d \otimes E_e\}_f\}_i = \sum_{g,h}[c][f][g][h]\begin{Bmatrix} a & b & c \\ d & e & f \\ g & h & i \end{Bmatrix}\{\{A_a \otimes D_d\}_g \otimes \{B_b \otimes E_e\}_h\}_i \,, \tag{A.53}$$

  and

$$\begin{aligned}\{\{A_a \otimes B_b\}_c \otimes \{D_d \otimes E_e\}_f\}_i = \sum_{g,h}(-1)^{h+b-i-e}[c]^2[f]^2[g]^2[h]^2 \begin{Bmatrix} a & b & c \\ g & d & h \end{Bmatrix}\begin{Bmatrix} d & e & f \\ i & c & g \end{Bmatrix} \\ \times \{\{\{A_a \otimes D_d\}_h \otimes B_b\}_g \otimes E_e\}_i \,. \end{aligned} \tag{A.54}$$

A.3.2 Decoupling of two subsystems

In view of partial-wave decompositions, we often encounter operators, that are coupled together with spin operators. We want the expectation value in a system, where the spin s and orbital angular momentum l are coupled together to the angular momentum j. In general, we can apply the following equation to decouple such systems which are decomposed out of the subsystems A and B, where the tensor operator of rank a, A_a acts on the subsystem A and the tensor operator of rank b, B_b acts on the subsystem B

$$\langle n_A n_B (j_A j_B) jm | \{A_a \otimes B_b\}_{c\gamma} | n'_A n'_B (j'_A j'_B) j'm' \rangle = (-1)^{2c} [c][j'] C^{jm}_{j'm'c\gamma} \begin{Bmatrix} a & b & c \\ j_A & j_B & j \\ j'_A & j'_B & j' \end{Bmatrix} \times \langle n_A j_A || A_a || n'_A j'_A \rangle \, \langle n_B j_B || B_b || n'_B j'_B \rangle \,, \tag{A.55}$$

where n_A (n_B) and n'_A (n'_B) pool all remaining variables on which the subsystem A (B) depends.

B Partial-wave decomposition

Symmetries of the Hamiltonian allow us to work in a partial-wave decomposed basis, defined by angular-momentum and spin quantum numbers. In a partial-wave basis, we couple radial and spin contributions. It is often more convenient to work with this basis, compared to a basis which is spanned by regular vectors in p- or r-space. Depending on the order in the chiral power counting, and especially in our case where we have an explicit operator dependence on the CM momentum, the task of performing a partial-wave decomposition can be very involved and is susceptible to mistakes, if performed by hand.

For this reason, we developed a computer program that is capable of decoupling any legal combination of relative ($\sim \mathbf{q}$ or $\mathbf{k}$), spin ($\sim \boldsymbol{\sigma}_1$ and $\boldsymbol{\sigma}_2$), and center-of-mass ($\sim \mathbf{P}$) two-nucleon contact operators into the respective partial waves. The program does not perform any numerical integration but relies on recoupling relations of tensor products from Ref [242]. The code takes a momentum-space vector representation of the desired operator as an input and returns all non-vanishing partial-wave expressions which will only depend on absolute values of the momenta p, p', and P.

This chapter starts with the general evaluation process that we need to undergo for our partial-wave decomposition (PWD). Afterwards, we will elaborate how to evaluate these expressions in the spin, relative, and the CM system respectively, in a way that one can easily implement it as computer code. All this is explained for unregulated interactions in momentum space. Nonlocal regulators typically depend on the absolute values of the momenta $\mathbf{p}$ and $\mathbf{p}'$ and not the angle between them. Thus, they do not interfere with the PWD, and can be added afterwards. The most commonly used nonlocal regulators [30, 34, 153, 159] take the form:

$$f^{\text{nonlocal}}_{\Lambda,n}(p,p') = \exp\left[-\frac{p^{2n}+p'^{2n}}{\Lambda^{2n}}\right], \tag{B.1}$$

with the momentum-space cutoff Λ. Local regulators that depend on the relative distance $\mathbf{r} = \mathbf{r}_1 - \mathbf{r}_2$, and can be written as [39] (see also Ref. [192] for local regulators in momentum space):

$$f^{\text{local}}_{R_0,n}(r) = \mathcal{N} \exp\left[-\left(\frac{\mathbf{r}}{R_0}\right)^{2n}\right], \tag{B.2}$$

where R_0 is the coordinate space cutoff and $\mathcal{N}$ a normalization factor. In the case of local Gaussian regulators ($n = 1$), the regulator transforms to momentum space exactly as

$$f^{\text{local}}_{R_0,1}(r) \longrightarrow \tilde{f}^{\text{local}}_{\Lambda,1}(q) = \exp\left[-\left(\frac{\mathbf{q}}{\Lambda}\right)^{2}\right], \tag{B.3}$$

where $\Lambda = \frac{2}{R_0}$ in this case. As one can see, the regulator depends on $\mathbf{q}^2 = p^2 + p'^2 - 2\mathbf{p}\cdot\mathbf{p}'$, which contains the angle between $\mathbf{p}$ and $\mathbf{p}'$. For a PWD of local operators, we need to take the regulator into consideration right from the beginning. In this appendix, we focus on nonlocal regulators. Following these guidelines one can develop a generalized transformation scheme that is also able to transform local operators. In the last part of this appendix, we show how our method can be applied to decompose the one-pion exchange that enters at LO.

B.1 General evaluation process

We start from a certain (contact) operator from chiral EFT in a momentum-space representation and want to obtain the PWD of this operator. The most general operator $\boldsymbol{O}$ that we encounter in this work may depend on the momentum transfer $\mathbf{q}$ and/or $\mathbf{k}$, spin operators $\boldsymbol{\sigma}_i$ that act on particle i (analogous for the isospin operators $\boldsymbol{\tau}_i$(1)), and the CM-momentum operator $\mathbf{P}$. In order to fulfill the commutation relation

$$[H, \mathbf{J}] = 0 ,$$

which is equivalent to rotational invariance of the Hamiltonian, all contributing operators need to be couplet such that O is a scalar. This means, we can write our operator as a (mathematical) tensor operator of rank zero, denoted by $\mathbf{O}_0$(2). We list the tensor-operator representation of all tensor operators up to N^{3}LO in App. C. In the following, we will denote tensor operators in the relative, spin and CM system by

$$\mathbf{R}_{a\alpha}, \ \Sigma_{b\beta}, \text{ and } \mathbf{P}_{c\gamma}$$

respectively, where Latin letters denote the rank of the tensor and Greek letters the projection. Each vector operator (i.e., $\mathbf{q}$, $\mathbf{k}$, $\mathbf{P}$, and $\boldsymbol{\sigma}_i$) can be written as an irreducible tensor operator of rank one. In the process, we pick up certain factors that depend on the kind of coupling (i.e., scalar, vector, or tensor) in O, as detailed in App. A.1. In the first step, we rewrite our momentum-space vector representation of O in terms of irreducible tensor operators. In the general case, we will not end up with separated contributions, such as $\mathbf{R}_{a\alpha}$, $\Sigma_{b\beta}$, and $\mathbf{P}_{c\gamma}$, but we will find mixed contributions where for example, spins might still be coupled with relative or CM operators. This means our next step is to apply tensor recoupling relations to clearly separate all operators according to the system they act in. The recoupling relations can be found in Ref. [242], but we listed all necessary relations for our purposes in App. A.3. We aim to obtain a tensor operator of the form

$$\begin{aligned} \mathbf{O}_0 &= \sum_{a,b,c} c_{abc} \{\{\mathbf{R}_a \otimes \Sigma_b\}_c \otimes \mathbf{P}_c\}_0 \ ^{(3)} \\ &\equiv \sum_{a,b,c} c_{abc} \mathbf{O}_0^{abc} , \end{aligned} \tag{B.4}$$

where c_{abc} contains all factors that appear during the recoupling of the tensor operators. For this work, we decided to couple the relative motion to the spin motion and the resulting angular momentum j to the CM motion. First of all, this means that the rank of the CM operator c must be equal to the rank to which we couple the relative operator with the spin operator. Otherwise we could not couple all operators to a total rank of zero. Second, the basis in which our partial-wave matrix elements are given takes the form $|pP[(ls)jL]Jt\rangle$. Furthermore, as one can see in the equation above, a single momentum-space operator might translate to several tensor operators, which we denote by a sum over the operator ranks a, b, and c. To give an example, the operator $(\mathbf{q}\cdot\boldsymbol{\sigma}_1)(\mathbf{q}\cdot\boldsymbol{\sigma}_2)$ can be expressed as

$$\begin{aligned} (\mathbf{q}\cdot\boldsymbol{\sigma}_1)(\mathbf{q}\cdot\boldsymbol{\sigma}_2) &= \{\{\mathbf{q}_1 \otimes \mathbf{q}_1\}_0 \otimes \{(\boldsymbol{\sigma}_1)_1 \otimes (\boldsymbol{\sigma}_2)_1\}_0\}_0 + \sqrt{5}\{\{\mathbf{q}_1 \otimes \mathbf{q}_1\}_2 \otimes \{(\boldsymbol{\sigma}_1)_1 \otimes (\boldsymbol{\sigma}_2)_1\}_2\}_0 \\ &\propto \{\mathbf{R}_0 \otimes \Sigma_0\}_0 + \sqrt{5}\{\mathbf{R}_2 \otimes \Sigma_2\}_0 . \end{aligned} \tag{B.5}$$

Here we find two different ranks for the tensor operators (zero and two), and since we do not have a CM operator ($c = 0$) we need to couple the relative and spin part to zero in both cases.

We can now express the partial-wave matrix elements of our momentum-space operator O in terms of the tensor operator $\mathbf{O}_0$ via

$$\langle pP[(ls)jL]JM|\mathbf{O}|p'P'[(l's')j'L']J'M'\rangle = \eta \sum_{a,b,c} c_{abc} \langle pP[(ls)jL]JM|\mathbf{O}_0^{abc}|p'P'[(l's')j'L']J'M'\rangle , \tag{B.6}$$

---

(1) Here we omit the isospin dependence as its inclusion is trivial and can be treated separately.

(2) A simplistic introduction to angular momentum theory with tensor operators and notes about the tensor-operator notation is provided in App. A.

(3) As mentioned above, the application of these relations is susceptible for mistakes if one performs them by hand, as they contain sums over six-j and nine-j-symbols and one can quickly loose track of indices and ranks.

where η contains all factors that appear in the process of writing the momentum-space operators as coupled tensor operators. With further relations from Ref. [242], the matrix elements of $\mathbf{O}_0^{abc}$ read

$$\begin{aligned}
&\langle pP[(ls)jL]JM|\mathbf{O}_0^{abc}|p'P'[(l's')j'L']J'M'\rangle \\
&\quad= \delta_{JJ'}\delta_{MM'}\frac{(-1)^{L+J+j'+c}}{[c]}\begin{Bmatrix} j & L & J \\ L' & j' & c \end{Bmatrix} \langle p(ls)j||\{\mathbf{R}_a \otimes \Sigma_b\}_c||p'(l's')j'\rangle \, \langle PL||\mathbf{P}_c||P'L'\rangle \\
&\quad= \delta_{JJ'}\delta_{MM'}[j][j'](-1)^{L+J+j'+c}\begin{Bmatrix} a & b & c \\ l & s & j \\ l' & s' & j' \end{Bmatrix}\begin{Bmatrix} j & L & J \\ L' & j' & c \end{Bmatrix} \langle pl||\mathbf{R}_a||p'l'\rangle \, \langle s||\Sigma_b||s'\rangle \, \langle PL||\mathbf{P}_c||P'L'\rangle \; .
\end{aligned} \tag{B.7}$$

The final expression depends on reduced matrix elements, denoted as $\langle \cdot||\mathbf{O}||\cdot\rangle$. They are evaluated with the Wigner-Eckart theorem (WET) [243, 244] (for more details see App. A.2.5). The brackets with six and nine elements are the six-j and nine-j-symbols which are detailed in App. A.2.3 and App. A.2.4, respectively. We use the shorthand notation $[x] \equiv \sqrt{2x+1}$ as those expressions appear frequently in tensor operator evaluations.

In the case where we have no CM operators ($\mathbf{P}_c = \mathbb{1}$), the expression from above simplifies to

$$\begin{aligned}
&\langle pP[(ls)jL]JM|\mathbf{O}_0^{abc}|p'P'[(l's')j'L']J'M'\rangle = \\
&\delta_{JJ'}\delta_{MM'}\delta_{LL'}(2\pi)^3\delta(\mathbf{P}-\mathbf{P}')\underbrace{\frac{(-1)^{j+s+l'+a}}{[a]}\delta_{jj'}\delta_{ab}\begin{Bmatrix} l & s & j \\ s' & l' & a \end{Bmatrix}\langle pl||\mathbf{R}_a||p'l'\rangle \, \langle s||\Sigma_a||s'\rangle \; .}_{=\langle p(ls)jm|\{\mathbf{R}_a \otimes \Sigma_b\}_0|p'(l's')j'm'\rangle}
\end{aligned} \tag{B.8}$$

This reduces the initial problem of finding the PWD of a momentum-space vector-like operator to a much simpler task, where we just have to evaluate the reduced matrix elements of $\mathbf{R}_{a\alpha}$, $\Sigma_{b\beta}$, and $\mathbf{P}_{c\gamma}$ separately.

B.2 Reduced matrix elements

As mentioned above, we evaluate the reduced matrix elements with the WET given in Eq. (A.49) and Refs. [242, 245]. With the WET, we decompose a matrix element into a reduced matrix element and a CG (CGs are given in App. A.2.1). The CG carries all the geometric information about the system and the reduced matrix element is a mere proportionality factor. The advantage of this approach is, that the reduced matrix elements need to be evaluated only once and can be applied to arbitrary quantum numbers l, l', s, s', L, and L', as they appear in Eq. (B.7). In the following subsections, we will provide all reduced matrix elements which we encounter in spin space, the relative system, and the CM system respectively.

B.2.1 Spin operators

In our case, the spin operator Σ_b consists of the Pauli tensor-operators of rank one $(\boldsymbol{\sigma}_1)_1$ and $(\boldsymbol{\sigma}_2)_1$ for particle one and two respectively. Due to the particle-exchange symmetry requirement, the two operators have to appear pairwise. We will encounter the following combinations in this work

$$\Sigma_b^{\otimes} \equiv \{(\boldsymbol{\sigma}_1)_1 \otimes (\boldsymbol{\sigma}_2)_1\}_b \, , \tag{B.9}$$

$$\Sigma_{b=1}^{\pm} \equiv (\boldsymbol{\sigma}_1)_1 \pm (\boldsymbol{\sigma}_2)_1 = \{(\boldsymbol{\sigma})_1 \otimes \mathbb{1}\}_1 \pm \{\mathbb{1} \otimes (\boldsymbol{\sigma})_1\}_1 \, . \tag{B.10}$$

The Pauli operators relate to the single-particle spin operator as $(\boldsymbol{\sigma}_i)_1 = 2(\mathbf{s}_i)_1$. We evaluate the reduced matrix elements $\langle s||\Sigma_b||s'\rangle$ in a coupled basis, which reads $|s\rangle = |(\frac{1}{2}\frac{1}{2})s\rangle$. The following relations hold in the single-particle basis and in the coupled basis (see Ref. [242]):

$$\langle\lambda||\mathbb{1}||\lambda'\rangle = \delta_{\lambda\lambda'}[\lambda], \tag{B.11}$$

$$\langle\lambda||\Lambda_1||\lambda'\rangle = \delta_{\lambda\lambda'}[\lambda]\sqrt{\lambda(\lambda+1)}, \tag{B.12}$$

where $|\lambda\rangle$ and Λ_1 are either both a coupled basis $|s\rangle$ and a coupled tensor operator $\mathbf{S}_1 = (\mathbf{s}_1)_1 + (\mathbf{s}_2)_1$, or a single-particle basis $|\frac{1}{2}\rangle$ and a one-body tensor operator $(\mathbf{s}_i)_1$, where i can be particle one or two. For the Pauli matrices we find in the single-particle and coupled basis

$$\langle\frac{1}{2}||(\boldsymbol{\sigma}_i)_1||\frac{1}{2}\rangle = \sqrt{6}, \tag{B.13}$$

$$\langle(\frac{1}{2}\frac{1}{2})s||(\boldsymbol{\sigma}_1)_1||(\frac{1}{2}\frac{1}{2})s'\rangle = (-1)^{s'}\sqrt{6}[s][s']\begin{Bmatrix} s & 1/2 & 1/2 \\ 1/2 & s' & 1 \end{Bmatrix}, \tag{B.14}$$

$$\langle(\frac{1}{2}\frac{1}{2})s||(\boldsymbol{\sigma}_2)_1||(\frac{1}{2}\frac{1}{2})s'\rangle = (-1)^{s}\sqrt{6}[s][s']\begin{Bmatrix} s & 1/2 & 1/2 \\ 1/2 & s' & 1 \end{Bmatrix}. \tag{B.15}$$

For the reduced matrix elements of the operators from Eqs. (B.9) and (B.10) we get

$$\langle s||\Sigma_b^{\otimes}||s'\rangle = 6[b][s][s']\begin{Bmatrix} 1 & 1 & b \\ 1/2 & 1/2 & s \\ 1/2 & 1/2 & s' \end{Bmatrix}, \tag{B.16}$$

$$\langle s||\Sigma_1^{\pm}||s'\rangle = \sqrt{6}[s][s']\Big((-1)^{s'} \pm (-1)^{s}\Big)\begin{Bmatrix} s & 1/2 & 1/2 \\ 1/2 & s' & 1 \end{Bmatrix}. \tag{B.17}$$

The operators $\Sigma_0^{\otimes}$, $\Sigma_2^{\otimes}$, and Σ_1^{+} are all diagonal in spin space, while $\Sigma_1^{\otimes}$ and Σ_1^{-} are purely off diagonal. The latter two only appear together with CM operators. The equations (B.11, B.16, B.17) cover every reduced matrix element in spin space that we encounter in this work.

B.2.2 Relative operators

The relative operators, which depend on $\mathbf{q}_1$ and $\mathbf{k}_1$ (and thus on the relative momentum operators $\mathbf{p}_1$ and $\mathbf{p}'_1$), do not follow the usual decomposition rules as in Eqs. (B.11,B.12). For clarification, we start this subsection with some general remarks on relative momentum-space operators from chiral EFT before we give the expressions for the reduced matrix elements $\langle pl||\mathbf{R}_a||p'l'\rangle$.

General remarks

Consider the momentum-space representation of the LO contact interaction from chiral EFT given by

$$\langle\mathbf{p}|V^{\text{LO}}_{\text{cont.}}|\mathbf{p}'\rangle = C_S + \boldsymbol{\sigma}_1\cdot\boldsymbol{\sigma}_2 C_T\,. \tag{B.18}$$

From this, it is clear that we do not have a simple identity operator in momentum-space, because an identity operator would yield $\langle\mathbf{p}|\mathbb{1}|\mathbf{p}'\rangle = (2\pi)^3\delta^{(3)}(\mathbf{p}-\mathbf{p}')$. Given Eq. (B.18), the operator must have the form

$$O^{\text{LO}}_{\text{cont.}} = \int\frac{\mathrm{d}^3p''}{(2\pi)^3}\int\frac{\mathrm{d}^3p'''}{(2\pi)^3}\,|\mathbf{p}''\rangle\langle\mathbf{p}'''|\,, \tag{B.19}$$

in order to fulfill

$$\langle \mathbf{p}|\boldsymbol{O}^{\mathrm{LO}}_{\mathrm{cont.}}|\mathbf{p}'\rangle = \int \frac{\mathrm{d}^3p''}{(2\pi)^3} \int \frac{\mathrm{d}^3p'''}{(2\pi)^3} \langle \mathbf{p}|\mathbf{p}''\rangle \langle \mathbf{p}'''|\mathbf{p}'\rangle = 1\,. \tag{B.20}$$

Analogous, at higher orders the structure of, e.g., the $\mathbf{q}^2$ operator at NLO takes the form

$$\boldsymbol{O}^{\mathrm{NLO}}_{q^2} = \int \frac{\mathrm{d}^3p''}{(2\pi)^3} \int \frac{\mathrm{d}^3p'''}{(2\pi)^3} |\mathbf{p}''\rangle (\mathbf{p}''-\mathbf{p}''')^2 \langle \mathbf{p}'''|\,, \tag{B.21}$$

so that

$$\langle \mathbf{p}|\boldsymbol{O}^{\mathrm{NLO}}_{q^2}|\mathbf{p}'\rangle = (\mathbf{p}-\mathbf{p}')^2 = \mathbf{q}^2\,, \tag{B.22}$$

is fulfilled. The same idea can be applied to any other operator at a given order. This means that the operator structure evaluated in momentum space is actually more complicated if we look at the unevolved operator.

We are interested in the reduced matrix element $\langle pl||\mathbf{R}_a||p'l'\rangle$, which can be obtained from the matrix element $\langle plm_l|\mathbf{R}_{a\alpha}|p'l'm_l'\rangle$ with the WET. For the overlap between the partial wave basis and the momentum-space basis we get

$$\langle plm_l|\mathbf{p}''\rangle = (2\pi)^3 \frac{\delta(p-p'')}{pp''} \langle lm_l|\Omega_{p''}\rangle\,, \tag{B.23}$$

$$\langle \mathbf{p}''|p'l'm_l'\rangle = (2\pi)^3 \frac{\delta(p'-p''')}{p'p'''} \langle \Omega_{p'''}|l'm_l'\rangle\,, \tag{B.24}$$

with the spherical harmonics $\langle lm_l|\Omega_p\rangle = \mathrm{Y}^*_{lm_l}\left(\Omega_p\right)$ and $\langle \Omega_{p'}|l'm_l'\rangle = \mathrm{Y}_{l'm_l'}\left(\Omega_{p'}\right)$ (see App. A.2.2 for more details on spherical harmonics). Our matrix elements read

$$\langle plm_l|\mathbf{R}_{a\alpha}|p'l'm_l'\rangle = \int \mathrm{d}\Omega_p \int \mathrm{d}\Omega_{p'}\, \langle lm_l|\Omega_p\rangle \langle \mathbf{p}|\mathbf{R}_{a\alpha}|\mathbf{p}'\rangle \langle \Omega_{p'}|l'm_l'\rangle\,, \tag{B.25}$$

which allows us to insert a momentum-space tensor-operator representation for $\mathbf{R}_{a\alpha}$. We can rewrite all operators $\mathbf{q}_1$ and $\mathbf{k}_1$ in terms of the relative momentum operators $\mathbf{p}_1$ and $\mathbf{p}_1'$ according to

$$\mathbf{q}_1 = \quad \mathbf{p}_1 - \mathbf{p}_1' \quad = \frac{\sqrt{4\pi}}{\sqrt{3}} \left(p\mathrm{Y}_1\left(\Omega_p\right) - p'\mathrm{Y}_1\left(\Omega_{p'}\right)\right)\,, \tag{B.26}$$

$$\mathbf{k}_1 = \frac{1}{2}(\mathbf{p}_1 + \mathbf{p}_1') = \frac{\sqrt{4\pi}}{2\sqrt{3}} \left(p\mathrm{Y}_1\left(\Omega_p\right) + p'\mathrm{Y}_1\left(\Omega_{p'}\right)\right)\,. \tag{B.27}$$

We work with so-called bipolar harmonics, here denoted as $\mathscr{Y}^{l_1l_2}_{LM}$. Bipolar harmonics are two spherical harmonics with angular momenta l_1 and l_2 with different angles, which are coupled to a tensor operator of rank L and projection M, written as

$$\mathscr{Y}^{l_1l_2}_{LM} \equiv \{\mathrm{Y}_{l_1}\left(\Omega_p\right) \otimes \mathrm{Y}_{l_2}\left(\Omega_{p'}\right)\}_{LM}\,. \tag{B.28}$$

Using the identity $1 = \sqrt{4\pi}\,\mathrm{Y}_{00}\left(\Omega_x\right)$ we can rewrite the two operators from above as

$$\mathbf{q}_1 = \frac{4\pi}{\sqrt{3}} \left(p\{\mathrm{Y}_1\left(\Omega_p\right) \otimes \mathrm{Y}_0\left(\Omega_{p'}\right)\}_1 - p'\{\mathrm{Y}_0\left(\Omega_p\right) \otimes \mathrm{Y}_1\left(\Omega_{p'}\right)\}_1\right) = \frac{4\pi}{\sqrt{3}} \left(p\mathscr{Y}^{10}_1 - p'\mathscr{Y}^{01}_1\right)\,, \tag{B.29}$$

$$\mathbf{k}_1 = \frac{2\pi}{\sqrt{3}} \left(p\{\mathrm{Y}_1\left(\Omega_p\right) \otimes \mathrm{Y}_0\left(\Omega_{p'}\right)\}_1 + p'\{\mathrm{Y}_0\left(\Omega_p\right) \otimes \mathrm{Y}_1\left(\Omega_{p'}\right)\}_1\right) = \frac{2\pi}{\sqrt{3}} \left(p\mathscr{Y}^{10}_1 + p'\mathscr{Y}^{01}_1\right)\,. \tag{B.30}$$

In the absence of a momentum operator, we can write $1 = 4\pi\{\mathrm{Y}_0\left(\Omega_p\right) \otimes \mathrm{Y}_0\left(\Omega_{p'}\right)\}_0 = 4\pi\mathscr{Y}^{00}_{0}$. This notation is very powerful, since we are able to apply coupling relations for the bipolar harmonics (more details in App. A.2.2). Two different operators of this form couple via

$$\{\mathscr{Y}^{bc}_{a} \otimes \mathscr{Y}^{ef}_{d}\}_{gm} = \frac{[a-f]}{4\pi} \sum_{hi} \begin{Bmatrix} a & b & c \\ d & e & f \\ g & h & i \end{Bmatrix} C^{h0}_{b0e0} C^{i0}_{c0f0} \mathscr{Y}^{hi}_{gm} , \tag{B.31}$$

with the shorthand notation $[a-f] \equiv [a][b][c][d][e][f]$. Hence we can construct a sum of resulting bipolar spherical harmonics, accompanied by absolute values of p and p' to a certain power for any given combination of operators $\mathbf{q}_1$ and $\mathbf{k}_1$. A CG of the form C^{c0}_{a0b0} only contributes if $a+b+c$ is an even number and if the triangular inequations are satisfied, which can be used to reduce the summations in the equation above.

Reduced matrix elements of $\mathbf{R}_a$

In the previous subsection, we learned that we can write any operator $\mathbf{R}_a$ as a sum of the form

$$\langle \mathbf{p}|\mathbf{R}_{a\alpha}|\mathbf{p}'\rangle = \sum_{l_1,l_2,n,m} c_{l_1l_2mna}\, p^n p'^m\, \mathscr{Y}^{l_1l_2}_{a\alpha} . \tag{B.32}$$

We need to keep track of occurring powers of p and p' and the different bipolar spherical harmonics as well as their factors (absorbed in $c_{l_1l_2mna}$), which we obtain with the coupling relation from Eq. (B.31). With that, Eq. (B.25) reduces to

$$\langle plm_l|\mathbf{R}_{a\alpha}|p'l'm_l'\rangle = \sum_{l_1,l_2,n,m} c_{l_1l_2mna}\;\, p^n p'^m \int \mathrm{d}\Omega_p \int \mathrm{d}\Omega_{p'}\, \langle lm_l|\Omega_p\rangle\, \mathscr{Y}^{l_1l_2}_{a\alpha}\, \langle \Omega_{p'}|l'm_l'\rangle . \tag{B.33}$$

With relations from the spherical harmonics section (App. A.2.2), we can rewrite the bipolar harmonics as

$$\begin{aligned} \mathscr{Y}^{l_1l_2}_{a\alpha} &= \sum_{m_1,m_2} (-1)^{m_2} C^{a\alpha}_{l_1m_1l_2m_2} \mathrm{Y}_{l_1m_1}\left(\Omega_p\right) \mathrm{Y}^*_{l_2-m_2}\left(\Omega_{p'}\right) \\ &= \sum_{m_1,m_2} (-1)^{m_2} C^{a\alpha}_{l_1m_1l_2m_2} \langle \Omega_p|l_1m_1\rangle \langle l_2-m_2|\Omega_{p'}\rangle . \end{aligned} \tag{B.34}$$

This can be used to solve the integrals in Eq. (B.33) as follows:

$$\begin{aligned} &\int \mathrm{d}\Omega_p \int \mathrm{d}\Omega_{p'}\, \langle lm_l|\Omega_p\rangle\, \mathscr{Y}^{l_1l_2}_{a\alpha}\, \langle \Omega_{p'}|l'm_{l'}\rangle \\ &\qquad = \sum_{m_1,m_2} (-1)^{m_2} C^{a\alpha}_{l_1m_1l_2m_2} \int \mathrm{d}\Omega_p \int \mathrm{d}\Omega_{p'}\, \langle lm_l|\Omega_p\rangle \langle \Omega_p|l_1m_1\rangle \langle l_2-m_2|\Omega_{p'}\rangle \langle \Omega_{p'}|l'm_{l'}\rangle \\ &\qquad = (-1)^{m_{l'}} C^{a\alpha}_{lm_ll'-m_{l'}} \delta_{ll_1} \delta_{l'l_2} . \end{aligned} \tag{B.35}$$

As a last step, we rearrange the angular momenta in the CG according to Eq. (A.14), so that we obtain

$$\langle lm_l|\mathscr{Y}^{l_1l_2}_{a\alpha}|l'm_{l'}\rangle = C^{lm_l}_{l'm_{l'}a\alpha} \frac{(-1)^{l'-2a}[a]\delta_{ll_1}\delta_{l'l_2}}{[l]} , \tag{B.36}$$

which matches exactly the definition of the WET. One can read off the reduced matrix element directly

$$\langle l||\mathscr{Y}_a^{l_1 l_2}||l'\rangle = (-1)^{l'-2a}[a]\delta_{ll_1}\delta_{l'l_2}\,. \tag{B.37}$$

We can now express the reduced matrix elements of $\mathbf{R}_a$ through

$$\langle l||\mathbf{R}_a||l'\rangle = (-1)^{l'-2a}[a]\sum_{n,m} c_{ll'mna}\,p^n p'^m\,. \tag{B.38}$$

In summary, we need to retrace all factors due to coupling the tensor operators $\mathbf{q}_1$ and $\mathbf{k}_1$ and the factors from the coupling of two bipolar harmonics in $c_{ll'mna}$. Further, we need to keep track of the powers of p and p'. All this is done in the computer algorithm, which allows us to evaluate arbitrary relative operators at any given order.

B.2.3 Center-of-mass operators

The CM-momentum operators obey the usual decomposition as in the case of the spin operators. We find

$$\langle \mathbf{P}|\mathbb{1}|\mathbf{P}'\rangle = (2\pi)^3\delta^{(3)}(\mathbf{P}-\mathbf{P}')\,, \tag{B.39}$$

and can determine the reduced matrix elements of the identity and of an arbitrary spherical harmonic function as

$$\langle L||\mathbb{1}||L'\rangle = [L]\delta_{LL'}\,, \tag{B.40}$$

$$\langle L||\mathrm{Y}_c(\Omega_P)||L'\rangle = \frac{[c][L']}{\sqrt{4\pi}}C^{L0}_{L'0c0}\,. \tag{B.41}$$

This facilitates the evaluation of the reduced matrix elements dramatically. We can use the expression

$$\begin{aligned}\mathbf{P}^{n,\{l_i\}}_{c\gamma} &\equiv \{\cdots\{\{P_1\otimes P_1\}_{l_2}\otimes P_1\}_{l_3}\cdots\otimes P_1\}_{c\gamma}\\ &= \frac{\sqrt{4\pi}}{[c]}P^n\mathrm{Y}_{c\gamma}(\Omega_P)\prod_{i=2}^{n}C^{l_i0}_{10l_{i-1}0}\,,\end{aligned} \tag{B.42}$$

with $l_1 = 1$ and $l_n = c$. We define the operator $\mathbf{P}^{n,\{l_i\}}_{c\gamma}$ in a way that the subscript $c\gamma$ denotes the rank of the tensor operator, the superscript n denotes the multiplicity of single tensor operators P_1, and the set $\{l_i\}$ keeps track over intermediate tensor couplings. Another possibility is to write the tensor operator as

$$\mathbf{P}_1 = \frac{\sqrt{4\pi}}{\sqrt{3}}P\mathrm{Y}_1(\Omega_P)\,, \tag{B.43}$$

and use coupling relations of the spherical harmonics. For the first approach, we determine the reduced matrix elements via

$$\langle PL||\mathbf{P}^{n,\{l_i\}}_{c\gamma}||P'L'\rangle = (2\pi)^3\frac{\delta(P-P')}{PP'}[L']C^{L0}_{L'0c0}P^n\prod_{i=2}^{n}C^{l_i0}_{10l_{i-1}0}\,. \tag{B.44}$$

This means that as soon as we know the set $\{l_i\}$, the evaluation of the reduced matrix element is trivial. For the second approach, we need to store factors due to the coupling of spherical harmonics and powers of momenta. The reduced matrix elements are given by Eq. (B.41). The latter method is better suited for the implementation in our computer code.

B.3 Partial-wave decomposition of the one-pion–exchange potential

Typically, a PWD of pion-exchange interactions is done using numerical integrals over Legendre polynomials as in Refs. [246, 247]. Here, we present a different approach that relies on the truncation of a sum. For the PWD of the leading-order OPE, we start with the momentum-space representation, given by

$$\langle \mathbf{p}|V_{\mathrm{LO}}^{\mathrm{OPE}}|\mathbf{p}'\rangle = -\left(\frac{g_A}{2F_\pi}\right)^2 \boldsymbol{\tau}_1\cdot\boldsymbol{\tau}_2 \frac{(\boldsymbol{\sigma}_1\cdot\mathbf{q})(\boldsymbol{\sigma}_2\cdot\mathbf{q})}{\mathbf{q}^2+m_\pi^2}\,, \tag{B.45}$$

with the pion decay constant F_π, the axial coupling constant g_A ,and the pion mass m_π. The isospin dependence can be solved trivially with $\langle t|\boldsymbol{\tau}_1\cdot\boldsymbol{\tau}_2|t\rangle = 2t(t+1)-3$, thus, we will pool it together with the constant in the beginning in a factor c_t, which reads:

$$c_t \equiv -\left(\frac{g_A}{2F_\pi}\right)^2 (2t(t+1)-3)\,.$$

We can now focus on the fraction, in which the numerator has the same form as the tensor operator in $\mathbf{q}$ at NLO, which we already decomposed in our example in Eq. (B.5). The difference here is that we also have a momentum dependence in the denominator, which cannot be treated perturbatively in $\mathbf{q}$. As demonstrated earlier, we can rewrite the OPE in terms of spherical tensor operators, leading to

$$\begin{aligned}\langle \mathbf{p}|V_{\mathrm{LO}}^{\mathrm{OPE}}|\mathbf{p}'\rangle &= c_t \sum_{a=0,2}[a]\{(\mathbf{q}^2+m_\pi^2)^{-1}\{q\otimes q\}_a\otimes\{\sigma_1\otimes\sigma_2\}_a\}_0\,,\\ &\equiv c_t\sum_{a=0,2}[a]\{\mathbf{R}_a\otimes\boldsymbol{\Sigma}_a^{\otimes}\}_0\,.\end{aligned} \tag{B.46}$$

In the following, we will omit the sum to focus on the tensor operator $\{\mathbf{R}_a\otimes\boldsymbol{\Sigma}_a^{\otimes}\}_0$. Since the OPE does not depend on CM quantum numbers, we perform the decomposition only in relative and spin space, as demonstrated in Eq. (B.8). We consider the basis states $|p(ls)jt\rangle$ which leads to the decomposition

$$\langle p(ls)jt|\{\mathbf{R}_a\otimes\boldsymbol{\Sigma}_a^{\otimes}\}_0|p'(l's)jt\rangle = \frac{(-1)^{s+l'+j+a}}{[a]}\begin{Bmatrix} l & s & j\\ s & l' & a\end{Bmatrix}\langle pl||\mathbf{R}_a||p'l'\rangle\,\langle s||\boldsymbol{\Sigma}_a^{\otimes}||s\rangle\,. \tag{B.47}$$

The reduced matrix element of the spin operator is given in Eq. (B.16). This leaves us with the evaluation of the reduced matrix elements of the relative operator. However, we cannot rewrite the denominator as a power series in $\mathbf{q}$ since it is not small compared to the pion mass m_π. Rather than expanding the denominator in $\mathbf{q}$, we write it as

$$\mathbf{R}_a = \frac{\{\mathbf{q}_1\otimes\mathbf{q}_1\}_a}{p^2+p'^2-2\mathbf{p}\cdot\mathbf{p}'+m_\pi^2}\,. \tag{B.48}$$

Rearranging the denominator leads to

$$\frac{1}{p^2+p'^2-2\mathbf{p}\cdot\mathbf{p}'+m_\pi^2} = \left(\frac{1}{p^2+p'^2+m_\pi^2}\right)\left(\frac{1}{1-\frac{2\mathbf{p}\cdot\mathbf{p}'}{p^2+p'^2+m_\pi^2}}\right)\,. \tag{B.49}$$

For all $\mathbf{p}$ and $\mathbf{p}'$ the condition $p^2+p'^2 \geq 2|\mathbf{p}\cdot\mathbf{p}'|$ is satisfied. Together with the pion mass, we find

$$\left|\frac{2\mathbf{p}\cdot\mathbf{p}'}{p^2+p'^2+m_\pi^2}\right| < 1\,.$$

Ultimately, we use a geometric series to express the second fraction in Eq. (B.49) as

$$\frac{1}{1-\frac{2\mathbf{p}\cdot\mathbf{p}'}{p^2+p'^2+m_\pi^2}} = \sum_{n=0}^{\infty}\left(\frac{-8\pi pp'}{p^2+p'^2+m_\pi^2}\right)^n (\mathscr{Y}_0^{11})^n\,, \tag{B.50}$$

where we define $(\mathscr{Y}_0^{11})^2 = \{\mathscr{Y}_0^{11}\otimes\mathscr{Y}_0^{11}\}_0$. We use Eq. (B.31) to couple the different contributions of the bipolar harmonics. Since this series converges, we can truncate the sum at a certain N. Herewith, we shift the angular dependence from the denominator to the numerator, where we already know the reduced matrix elements from the sections above. In total, we find for the reduced matrix element

$$\langle pl||\mathbf{R}_a||p'l'\rangle = \frac{1}{p^2+p'^2+m_\pi^2}\sum_{n=0}^{\infty}\left(\frac{-8\pi pp'}{p^2+p'^2+m_\pi^2}\right)^n \{\{\mathbf{q}_1\otimes\mathbf{q}_1\}_a\otimes(\mathscr{Y}_0^{11})^n\}_a\,. \tag{B.51}$$

We find that S-wave matrix elements of the potential do not change noticeably, comparing truncation at $N=10$ and $N=100$ for momenta up to 5 fm^{-1}.

The fast convergence allows us to decompose the leading-order OPE without the need to introduce integrals over the angle in $\mathbf{p}\cdot\mathbf{p}'$. However, the decomposition is not straight forward as in previous subsections of this chapter, as one cannot simply construct a power series in $\mathbf{q}$. The expansion of the two-pion exchange (TPE) at NLO contains two nested sums. The outer runs over a part similar to the denominator of the OPE to the power of n, where n runs up to infinity. This multiplication is computationally expensive, even for small n. In theory, this approach would be applicable for two- and multi-pion exchanges, but it is not feasible from a numerical point of view (yet). This is why we obtain partial-wave matrix elements of pion exchanges beyond LO with the well known helicity approach from Ref. [246]. Our matrix elements for the leading-order OPE coincide with those obtained by the helicity method.

C Tensor-operator representation

In App. B we demonstrate a generalized PWD of contact operators from chiral EFT. The PWD relies on a tensor-operator representation. Since the operators are usually given in a vector representation, we show how to translate them to a tensor representation in the following subsections. We start with operators at LO and show all two-body operators up to N^{3}LO, including the novel center-of-mass (CM) momentum operators.

C.1 Operators at LO

The LO ($\nu = 0$) contact operators from Eq. (2.59) take the following form as mathematical tensor operators

$$\mathbb{1} = 4\pi \mathscr{Y}_0^{00} \,, \tag{C.1}$$

$$\boldsymbol{\sigma}_1 \cdot \boldsymbol{\sigma}_2 = -4\pi\sqrt{3}\,\{\mathscr{Y}_0^{00} \otimes \boldsymbol{\Sigma}_0^{\otimes}\}_0 \,, \tag{C.2}$$

where the symbol for bipolar harmonics $\mathscr{Y}_L^{ll'}$ and the spin operator $\boldsymbol{\Sigma}_0^{\times}$ are detailed in App. B.

C.2 Operators at NLO

At NLO ($\nu = 2$), there are seven new momentum-dependent operators in the free-space interaction and five new valence-space (vs) operators, with explicit CM-momentum dependence. The free-space potential reads

$$\begin{aligned} V_{\text{cont}}^{(2)}(\mathbf{p},\mathbf{p}') =& C_1\mathbf{q}^2 + C_2\mathbf{k}^2 + \left(C_3\mathbf{q}^2 + C_4\mathbf{k}^2\right)\boldsymbol{\sigma}_1\cdot\boldsymbol{\sigma}_2 + C_5\frac{i}{2}(\mathbf{q}\times\mathbf{k})\cdot(\boldsymbol{\sigma}_1+\boldsymbol{\sigma}_2) \\ &+ C_6(\mathbf{q}\cdot\boldsymbol{\sigma}_1)(\mathbf{q}\cdot\boldsymbol{\sigma}_2) + C_7(\mathbf{k}\cdot\boldsymbol{\sigma}_1)(\mathbf{k}\cdot\boldsymbol{\sigma}_2)\,, \end{aligned} \tag{C.3}$$

and the valence-space potential is given by

$$\begin{aligned} V_{\text{cont,vs}}^{(2)}(\mathbf{p},\mathbf{p}',\mathbf{P}) =& (P_1 + P_2(\boldsymbol{\sigma}_1\cdot\boldsymbol{\sigma}_2))\mathbf{P}^2 + P_3 i\,(\mathbf{q}\times\mathbf{P})\cdot(\boldsymbol{\sigma}_1-\boldsymbol{\sigma}_2) + P_4\,(\mathbf{k}\times\mathbf{P})\cdot(\boldsymbol{\sigma}_1\times\boldsymbol{\sigma}_2) \\ &+ P_5(\mathbf{P}\cdot\boldsymbol{\sigma}_1)(\mathbf{P}\cdot\boldsymbol{\sigma}_2)\,. \end{aligned} \tag{C.4}$$

Transforming the free-space operators leads to

$$\mathbf{q}^2 = -\sqrt{3}\{\mathbf{q}_1 \otimes \mathbf{q}_1\}_0 \,, \tag{C.5}$$

$$\mathbf{k}^2 = -\sqrt{3}\{\mathbf{k}_1 \otimes \mathbf{k}_1\}_0 \,, \tag{C.6}$$

$$\mathbf{q}^2(\boldsymbol{\sigma}_1\cdot\boldsymbol{\sigma}_2) = 3\{\{\mathbf{q}_1 \otimes \mathbf{q}_1\}_0 \otimes \boldsymbol{\Sigma}_0^{\otimes}\}_0 \,, \tag{C.7}$$

$$\mathbf{k}^2(\boldsymbol{\sigma}_1\cdot\boldsymbol{\sigma}_2) = 3\{\{\mathbf{k}_1 \otimes \mathbf{k}_1\}_0 \otimes \boldsymbol{\Sigma}_0^{\otimes}\}_0 \,, \tag{C.8}$$

$$\frac{i}{2}(\mathbf{q}\times\mathbf{k})\cdot(\boldsymbol{\sigma}_1+\boldsymbol{\sigma}_2) = -\sqrt{\frac{3}{2}}\{\{\mathbf{q}_1 \otimes \mathbf{k}_1\}_1 \otimes \boldsymbol{\Sigma}_1^{+}\}_0 \,, \tag{C.9}$$

$$(\mathbf{q}\cdot\boldsymbol{\sigma}_1)(\mathbf{q}\cdot\boldsymbol{\sigma}_2) = \{\{\mathbf{q}_1 \otimes \mathbf{q}_1\}_0 \otimes \boldsymbol{\Sigma}_0^{\otimes}\}_0 + \sqrt{5}\{\{\mathbf{q}_1 \otimes \mathbf{q}_1\}_2 \otimes \boldsymbol{\Sigma}_2^{\otimes}\}_0 \,, \tag{C.10}$$

$$(\mathbf{k}\cdot\boldsymbol{\sigma}_1)(\mathbf{k}\cdot\boldsymbol{\sigma}_2) = \{\{\mathbf{k}_1 \otimes \mathbf{k}_1\}_0 \otimes \boldsymbol{\Sigma}_0^{\otimes}\}_0 + \sqrt{5}\{\{\mathbf{k}_1 \otimes \mathbf{k}_1\}_2 \otimes \boldsymbol{\Sigma}_2^{\otimes}\}_0 \,, \tag{C.11}$$

while the valence-space operators read

$$\mathbf{P}^2 = -\sqrt{3}\{\mathbf{P}_1 \otimes \mathbf{P}_1\}_0\,, \tag{C.12}$$

$$\mathbf{P}^2(\boldsymbol{\sigma}_1 \cdot \boldsymbol{\sigma}_2) = 3\{\{\mathbf{P}_1 \otimes \mathbf{P}_1\}_0 \otimes \Sigma_0^{\otimes}\}_0\,, \tag{C.13}$$

$$i\,(\mathbf{q} \times \mathbf{P}) \cdot (\boldsymbol{\sigma}_1 - \boldsymbol{\sigma}_2) = \sqrt{6}\{\{\mathbf{q}_1 \otimes \Sigma_1^{-}\}_1 \otimes \mathbf{P}_1\}_0\,, \tag{C.14}$$

$$(\mathbf{k} \times \mathbf{P}) \cdot (\boldsymbol{\sigma}_1 \times \boldsymbol{\sigma}_2) = -\sqrt{12}\{\{\mathbf{k}_1 \otimes \Sigma_1^{\otimes}\}_1 \otimes \mathbf{P}_1\}_0\,, \tag{C.15}$$

$$(\mathbf{P} \cdot \boldsymbol{\sigma}_1)(\mathbf{P} \cdot \boldsymbol{\sigma}_2) = \{\Sigma_0^{\otimes} \otimes \{\mathbf{P}_1 \otimes \mathbf{P}_1\}_0\}_0 + \sqrt{5}\{\Sigma_2^{\otimes} \otimes \{\mathbf{P}_1 \otimes \mathbf{P}_1\}_2\}_0\,. \tag{C.16}$$

We write the tensor products in q and k in terms of p and p' in order to express it in terms of bipolar harmonics as

$$\begin{aligned}\{\mathbf{q}_1 \otimes \mathbf{q}_1\}_a &= \{\mathbf{p}_1 \otimes \mathbf{p}_1\}_a + \{\mathbf{p}'_1 \otimes \mathbf{p}'_1\}_a - (1 + (-1)^a)\{\mathbf{p}_1 \otimes \mathbf{p}'_1\}_a \\ &= 4\pi \left[\frac{1}{[a]} C^{a0}_{1010} \left(p^2 \mathscr{Y}^{a0}_a + p'^2 \mathscr{Y}^{0a}_a \right) - \frac{1 + (-1)^a}{3} p p' \mathscr{Y}^{11}_a \right],\end{aligned} \tag{C.17}$$

and similar for the other contributions.

C.3 Operators at N^{3}LO

There are no new two-body contact interactions at N^{2}LO ($\nu = 3$) neither in the free-space, nor in the valence-space sector. At N^{3}LO ($\nu = 4$), 15 new free-space operators and 32 new valence-space operators appear. The free-space contact interaction is given in Eq. (2.64) and their transformation to tensor operators yields

$$\mathbf{q}^4 = 3\{\{\mathbf{q}_1 \otimes \mathbf{q}_1\}_0 \otimes \{\mathbf{q}_1 \otimes \mathbf{q}_1\}_0\}_0\,, \tag{C.18}$$

$$\mathbf{k}^4 = 3\{\{\mathbf{k}_1 \otimes \mathbf{k}_1\}_0 \otimes \{\mathbf{k}_1 \otimes \mathbf{k}_1\}_0\}_0\,, \tag{C.19}$$

$$\mathbf{q}^2\mathbf{k}^2 = 3\{\{\mathbf{q}_1 \otimes \mathbf{q}_1\}_0 \otimes \{\mathbf{k}_1 \otimes \mathbf{k}_1\}_0\}_0\,, \tag{C.20}$$

$$(\mathbf{q} \times \mathbf{k})^2 = 2\sqrt{3}\{\{\mathbf{q}_1 \otimes \mathbf{k}_1\}_1 \otimes \{\mathbf{q}_1 \otimes \mathbf{k}_1\}_1\}_0\,, \tag{C.21}$$

$$\mathbf{q}^4(\boldsymbol{\sigma}_1 \cdot \boldsymbol{\sigma}_2) = -3\sqrt{3}\{\{\{\mathbf{q}_1 \otimes \mathbf{q}_1\}_0 \otimes \{\mathbf{q}_1 \otimes \mathbf{q}_1\}_0\}_0 \otimes \Sigma_0^{\otimes}\}_0\,, \tag{C.22}$$

$$\mathbf{k}^4(\boldsymbol{\sigma}_1 \cdot \boldsymbol{\sigma}_2) = -3\sqrt{3}\{\{\{\mathbf{k}_1 \otimes \mathbf{k}_1\}_0 \otimes \{\mathbf{k}_1 \otimes \mathbf{k}_1\}_0\}_0 \otimes \Sigma_0^{\otimes}\}_0\,, \tag{C.23}$$

$$\mathbf{q}^2\mathbf{k}^2(\boldsymbol{\sigma}_1 \cdot \boldsymbol{\sigma}_2) = -3\sqrt{3}\{\{\{\mathbf{q}_1 \otimes \mathbf{q}_1\}_0 \otimes \{\mathbf{k}_1 \otimes \mathbf{k}_1\}_0\}_0 \otimes \Sigma_0^{\otimes}\}_0\,, \tag{C.24}$$

$$(\mathbf{q} \times \mathbf{k})^2(\boldsymbol{\sigma}_1 \cdot \boldsymbol{\sigma}_2) = -6\{\{\{\mathbf{q}_1 \otimes \mathbf{k}_1\}_1 \otimes \{\mathbf{q}_1 \otimes \mathbf{k}_1\}_1\}_0 \otimes \Sigma_0^{\otimes}\}_0\,, \tag{C.25}$$

$$\frac{i}{2}(\boldsymbol{\sigma}_1 + \boldsymbol{\sigma}_2) \cdot (\mathbf{q} \times \mathbf{k})\mathbf{q}^2 = -\frac{3}{\sqrt{2}}\{\{\{\mathbf{q}_1 \otimes \mathbf{k}_1\}_1 \otimes \{\mathbf{q}_1 \otimes \mathbf{q}_1\}_0\}_1 \otimes \Sigma_1^{+}\}_0\,, \tag{C.26}$$

$$\frac{i}{2}(\boldsymbol{\sigma}_1 + \boldsymbol{\sigma}_2) \cdot (\mathbf{q} \times \mathbf{k})\mathbf{k}^2 = -\frac{3}{\sqrt{2}}\{\{\{\mathbf{q}_1 \otimes \mathbf{k}_1\}_1 \otimes \{\mathbf{k}_1 \otimes \mathbf{k}_1\}_0\}_1 \otimes \Sigma_1^{+}\}_0\,, \tag{C.27}$$

$$\begin{aligned}\mathbf{q}^2(\mathbf{q} \cdot \boldsymbol{\sigma}_1)(\mathbf{q} \cdot \boldsymbol{\sigma}_2) = &-\sqrt{3}\{\{\{\mathbf{q}_1 \otimes \mathbf{q}_1\}_0 \otimes \{\mathbf{q}_1 \otimes \mathbf{q}_1\}_0\}_0 \otimes \Sigma_0^{\otimes}\}_0 \\ &-\sqrt{15}\{\{\{\mathbf{q}_1 \otimes \mathbf{q}_1\}_2 \otimes \{\mathbf{q}_1 \otimes \mathbf{q}_1\}_0\}_0 \otimes \Sigma_2^{\otimes}\}_0\,,\end{aligned} \tag{C.28}$$

$$\begin{aligned}\mathbf{k}^2(\mathbf{q} \cdot \boldsymbol{\sigma}_1)(\mathbf{q} \cdot \boldsymbol{\sigma}_2) = &-\sqrt{3}\{\{\{\mathbf{q}_1 \otimes \mathbf{q}_1\}_0 \otimes \{\mathbf{k}_1 \otimes \mathbf{k}_1\}_0\}_0 \otimes \Sigma_0^{\otimes}\}_0 \\ &-\sqrt{15}\{\{\{\mathbf{q}_1 \otimes \mathbf{q}_1\}_2 \otimes \{\mathbf{k}_1 \otimes \mathbf{k}_1\}_0\}_0 \otimes \Sigma_2^{\otimes}\}_0\,,\end{aligned} \tag{C.29}$$

$$\begin{aligned}\mathbf{q}^2(\mathbf{k} \cdot \boldsymbol{\sigma}_1)(\mathbf{k} \cdot \boldsymbol{\sigma}_2) = &-\sqrt{3}\{\{\{\mathbf{k}_1 \otimes \mathbf{k}_1\}_0 \otimes \{\mathbf{q}_1 \otimes \mathbf{q}_1\}_0\}_0 \otimes \Sigma_0^{\otimes}\}_0 \\ &-\sqrt{15}\{\{\{\mathbf{k}_1 \otimes \mathbf{k}_1\}_2 \otimes \{\mathbf{q}_1 \otimes \mathbf{q}_1\}_0\}_0 \otimes \Sigma_2^{\otimes}\}_0\,,\end{aligned} \tag{C.30}$$

$$\mathbf{k}^2(\mathbf{k} \cdot \boldsymbol{\sigma}_1)(\mathbf{k} \cdot \boldsymbol{\sigma}_2) = -\sqrt{3}\{\{\{\mathbf{k}_1 \otimes \mathbf{k}_1\}_0 \otimes \{\mathbf{k}_1 \otimes \mathbf{k}_1\}_0\}_0 \otimes \Sigma_0^{\otimes}\}_0$$

$$
\begin{aligned}
&-\sqrt{15}\{\{\{\mathbf{k}_1\otimes\mathbf{k}_1\}_2\otimes\{\mathbf{k}_1\otimes\mathbf{k}_1\}_0\}_0\otimes\Sigma_2^{\otimes}\}_0\,,
\end{aligned}
\tag{C.31}
$$

$$
\begin{aligned}
((\mathbf{q}\times\mathbf{k})\cdot\boldsymbol{\sigma}_1)((\mathbf{q}\times\mathbf{k})\cdot\boldsymbol{\sigma}_2) = &-2\{\{\{\mathbf{q}_1\otimes\mathbf{k}_1\}_1\otimes\{\mathbf{q}_1\otimes\mathbf{k}_1\}_1\}_0\otimes\Sigma_0^{\otimes}\}_0\\
&-2\sqrt{5}\{\{\{\mathbf{q}_1\otimes\mathbf{k}_1\}_1\otimes\{\mathbf{q}_1\otimes\mathbf{k}_1\}_1\}_2\otimes\Sigma_2^{\otimes}\}_0\,.
\end{aligned}
\tag{C.32}
$$

The valence-space contact potential at N^{3}LO is given in Eq. (3.14). The relation to the mathematical tensor operators, starting with the central operators, reads

$$\mathbf{q}^2\mathbf{P}^2 = 3\{\{\mathbf{q}_1\otimes\mathbf{q}_1\}_0\otimes\{\mathbf{P}_1\otimes\mathbf{P}_1\}_0\}_0\,, \tag{C.33}$$

$$(\mathbf{q}\times\mathbf{P})^2 = 2\{\{\mathbf{q}_1\otimes\mathbf{q}_1\}_0\otimes\{\mathbf{P}_1\otimes\mathbf{P}_1\}_0\}_0-\sqrt{5}\{\{\mathbf{q}_1\otimes\mathbf{q}_1\}_2\otimes\{\mathbf{P}_1\otimes\mathbf{P}_1\}_2\}_0\,, \tag{C.34}$$

$$\mathbf{k}^2\mathbf{P}^2 = 3\{\{\mathbf{k}_1\otimes\mathbf{k}_1\}_0\otimes\{\mathbf{P}_1\otimes\mathbf{P}_1\}_0\}_0\,, \tag{C.35}$$

$$(\mathbf{k}\times\mathbf{P})^2 = 2\{\{\mathbf{k}_1\otimes\mathbf{k}_1\}_0\otimes\{\mathbf{P}_1\otimes\mathbf{P}_1\}_0\}_0-\sqrt{5}\{\{\mathbf{k}_1\otimes\mathbf{k}_1\}_2\otimes\{\mathbf{P}_1\otimes\mathbf{P}_1\}_2\}_0\,, \tag{C.36}$$

$$\mathbf{P}^4 = 3\{\{\mathbf{P}_1\otimes\mathbf{P}_1\}_0\otimes\{\mathbf{P}_1\otimes\mathbf{P}_1\}_0\}_0\,, \tag{C.37}$$

$$\mathbf{q}^2\mathbf{P}^2(\boldsymbol{\sigma}_1\cdot\boldsymbol{\sigma}_2) = -3\sqrt{3}\{\{\{\mathbf{q}_1\otimes\mathbf{q}_1\}_0\otimes\Sigma_0^{\otimes}\}_0\otimes\{\mathbf{P}_1\otimes\mathbf{P}_1\}_0\}_0\,, \tag{C.38}$$

$$
\begin{aligned}
(\mathbf{q}\times\mathbf{P})^2(\boldsymbol{\sigma}_1\cdot\boldsymbol{\sigma}_2) = &-2\sqrt{3}\{\{\{\mathbf{q}_1\otimes\mathbf{q}_1\}_0\otimes\Sigma_0^{\otimes}\}_0\otimes\{\mathbf{P}_1\otimes\mathbf{P}_1\}_0\}_0\\
&+\sqrt{15}\{\{\{\mathbf{q}_1\otimes\mathbf{q}_1\}_2\otimes\Sigma_0^{\otimes}\}_2\otimes\{\mathbf{P}_1\otimes\mathbf{P}_1\}_2\}_0\,,
\end{aligned}
\tag{C.39}
$$

$$\mathbf{k}^2\mathbf{P}^2(\boldsymbol{\sigma}_1\cdot\boldsymbol{\sigma}_2) = -3\sqrt{3}\{\{\{\mathbf{k}_1\otimes\mathbf{k}_1\}_0\otimes\Sigma_0^{\otimes}\}_0\otimes\{\mathbf{P}_1\otimes\mathbf{P}_1\}_0\}_0\,, \tag{C.40}$$

$$
\begin{aligned}
(\mathbf{k}\times\mathbf{P})^2(\boldsymbol{\sigma}_1\cdot\boldsymbol{\sigma}_2) = &-2\sqrt{3}\{\{\{\mathbf{k}_1\otimes\mathbf{k}_1\}_0\otimes\Sigma_0^{\otimes}\}_0\otimes\{\mathbf{P}_1\otimes\mathbf{P}_1\}_0\}_0\\
&+\sqrt{15}\{\{\{\mathbf{k}_1\otimes\mathbf{k}_1\}_2\otimes\Sigma_0^{\otimes}\}_2\otimes\{\mathbf{P}_1\otimes\mathbf{P}_1\}_2\}_0\,,
\end{aligned}
\tag{C.41}
$$

$$\mathbf{P}^4 = -3\sqrt{3}\{\Sigma_0^{\otimes}\otimes\{\{\mathbf{P}_1\otimes\mathbf{P}_1\}_0\otimes\{\mathbf{P}_1\otimes\mathbf{P}_1\}_0\}_0\}_0\,. \tag{C.42}$$

The vector operators are rewritten as

$$i(\boldsymbol{\sigma}_1-\boldsymbol{\sigma}_2)\cdot(\mathbf{q}\times\mathbf{P})\mathbf{q}^2 = 3\sqrt{2}\{\{\{\mathbf{q}_1\otimes\{\mathbf{q}_1\otimes\mathbf{q}_1\}_0\}_1\otimes\Sigma_1^{-}\}_1\otimes\mathbf{P}_1\}_0\,, \tag{C.43}$$

$$i(\boldsymbol{\sigma}_1-\boldsymbol{\sigma}_2)\cdot(\mathbf{q}\times\mathbf{P})\mathbf{k}^2 = 3\sqrt{2}\{\{\{\mathbf{q}_1\otimes\{\mathbf{k}_1\otimes\mathbf{k}_1\}_0\}_1\otimes\Sigma_1^{-}\}_1\otimes\mathbf{P}_1\}_0\,, \tag{C.44}$$

$$i(\boldsymbol{\sigma}_1-\boldsymbol{\sigma}_2)\cdot(\mathbf{q}\times\mathbf{P})\mathbf{P}^2 = 3\sqrt{2}\{\{\mathbf{q}_1\otimes\Sigma_1^{-}\}_1\otimes\{\mathbf{P}_1\otimes\{\mathbf{P}_1\otimes\mathbf{P}_1\}_0\}_1\}_0\,, \tag{C.45}$$

$$i(\boldsymbol{\sigma}_1-\boldsymbol{\sigma}_2)\cdot(\mathbf{k}\times\mathbf{P})(\mathbf{q}\cdot\mathbf{k}) = 3\sqrt{2}\{\{\{\mathbf{k}_1\otimes\{\mathbf{q}_1\otimes\mathbf{k}_1\}_0\}_1\otimes\Sigma_1^{-}\}_1\otimes\mathbf{P}_1\}_0\,, \tag{C.46}$$

$$
\begin{aligned}
i(\boldsymbol{\sigma}_1-\boldsymbol{\sigma}_2)\cdot(\mathbf{q}\times\mathbf{k})(\mathbf{k}\cdot\mathbf{P}) = &-\sqrt{2}\{\{\{\{\mathbf{q}_1\otimes\mathbf{k}_1\}_1\otimes\mathbf{k}_1\}_0\otimes\Sigma_1^{-}\}_1\otimes\mathbf{P}_1\}_0\\
&-\sqrt{5}\{\{\{\{\mathbf{q}_1\otimes\mathbf{k}_1\}_1\otimes\mathbf{k}_1\}_1\otimes\Sigma_1^{-}\}_1\otimes\mathbf{P}_1\}_0\\
&-\sqrt{10}\{\{\{\{\mathbf{q}_1\otimes\mathbf{k}_1\}_2\otimes\mathbf{k}_1\}_1\otimes\Sigma_1^{-}\}_1\otimes\mathbf{P}_1\}_0\,,
\end{aligned}
\tag{C.47}
$$

$$
\begin{aligned}
i(\boldsymbol{\sigma}_1-\boldsymbol{\sigma}_2)\cdot((\mathbf{q}\times\mathbf{k})\times(\mathbf{q}\times\mathbf{P})) = &-2\sqrt{2}\{\{\{\mathbf{q}_1\otimes\{\mathbf{q}_1\otimes\mathbf{k}_1\}_1\}_0\otimes\Sigma_1^{-}\}_1\otimes\mathbf{P}_1\}_0\\
&+\sqrt{6}\{\{\{\mathbf{q}_1\otimes\{\mathbf{q}_1\otimes\mathbf{k}_1\}_1\}_1\otimes\Sigma_1^{-}\}_1\otimes\mathbf{P}_1\}_0\\
&+\sqrt{10}\{\{\{\mathbf{q}_1\otimes\{\mathbf{q}_1\otimes\mathbf{k}_1\}_2\}_1\otimes\Sigma_1^{-}\}_1\otimes\mathbf{P}_1\}_0\,,
\end{aligned}
\tag{C.48}
$$

$$(\boldsymbol{\sigma}_1\times\boldsymbol{\sigma}_2)\cdot(\mathbf{k}\times\mathbf{P})\mathbf{q}^2 = -6\{\{\{\mathbf{k}_1\otimes\{\mathbf{q}_1\otimes\mathbf{q}_1\}_0\}_1\otimes\Sigma_1^{\otimes}\}_1\otimes\mathbf{P}_1\}_0\,, \tag{C.49}$$

$$(\boldsymbol{\sigma}_1\times\boldsymbol{\sigma}_2)\cdot(\mathbf{k}\times\mathbf{P})\mathbf{k}^2 = -6\{\{\{\mathbf{k}_1\otimes\{\mathbf{k}_1\otimes\mathbf{k}_1\}_0\}_1\otimes\Sigma_1^{\otimes}\}_1\otimes\mathbf{P}_1\}_0\,, \tag{C.50}$$

$$(\boldsymbol{\sigma}_1\times\boldsymbol{\sigma}_2)\cdot(\mathbf{k}\times\mathbf{P})\mathbf{P}^2 = -6\{\{\mathbf{k}_1\otimes\Sigma_1^{\otimes}\}_1\otimes\{\mathbf{P}_1\otimes\{\mathbf{P}_1\otimes\mathbf{P}_1\}_0\}_1\}_0\,, \tag{C.51}$$

$$(\boldsymbol{\sigma}_1\times\boldsymbol{\sigma}_2)\cdot(\mathbf{q}\times\mathbf{P})(\mathbf{q}\cdot\mathbf{k}) = -6\{\{\{\mathbf{q}_1\otimes\{\mathbf{q}_1\otimes\mathbf{k}_1\}_0\}_1\otimes\Sigma_1^{\otimes}\}_1\otimes\mathbf{P}_1\}_0\,, \tag{C.52}$$

$$
\begin{aligned}
(\boldsymbol{\sigma}_1\times\boldsymbol{\sigma}_2)\cdot(\mathbf{q}\times\mathbf{k})(\mathbf{q}\cdot\mathbf{P}) = &\,2\{\{\{\{\mathbf{q}_1\otimes\mathbf{k}_1\}_1\otimes\mathbf{q}_1\}_0\otimes\Sigma_1^{\otimes}\}_1\otimes\mathbf{P}_1\}_0\\
&+2\sqrt{3}\{\{\{\{\mathbf{q}_1\otimes\mathbf{k}_1\}_1\otimes\mathbf{q}_1\}_1\otimes\Sigma_1^{\otimes}\}_1\otimes\mathbf{P}_1\}_0\\
&+2\sqrt{5}\{\{\{\{\mathbf{q}_1\otimes\mathbf{k}_1\}_1\otimes\mathbf{q}_1\}_2\otimes\Sigma_1^{\otimes}\}_1\otimes\mathbf{P}_1\}_0\,,
\end{aligned}
\tag{C.53}
$$

$$\frac{i}{2}(\boldsymbol{\sigma}_1+\boldsymbol{\sigma}_2)\cdot(\mathbf{q}\times\mathbf{k})\mathbf{P}^2 = \frac{3}{\sqrt{2}}\{\{\{\mathbf{q}_1\otimes\mathbf{k}_1\}_1\otimes\Sigma_1^{+}\}_0\otimes\{\mathbf{P}_1\otimes\mathbf{P}_1\}_0\}_0\,, \tag{C.54}$$

$$\begin{aligned}
\frac{i}{2}(\boldsymbol{\sigma}_1+\boldsymbol{\sigma}_2)\cdot(\mathbf{k}\times\mathbf{P})(\mathbf{q}\cdot\mathbf{P}) =& \frac{1}{\sqrt{2}}\{\{\{\mathbf{k}_1\otimes\mathbf{q}_1\}_1\otimes\boldsymbol{\Sigma}_1^{+}\}_0\otimes\{\mathbf{P}_1\otimes\mathbf{P}_1\}_0\}_0 \\
&- \frac{\sqrt{5}}{2\sqrt{2}}\{\{\{\mathbf{k}_1\otimes\mathbf{q}_1\}_1\otimes\boldsymbol{\Sigma}_1^{+}\}_2\otimes\{\mathbf{P}_1\otimes\mathbf{P}_1\}_2\}_0 \\
&- \frac{\sqrt{15}}{2\sqrt{2}}\{\{\{\mathbf{k}_1\otimes\mathbf{q}_1\}_2\otimes\boldsymbol{\Sigma}_1^{+}\}_2\otimes\{\mathbf{P}_1\otimes\mathbf{P}_1\}_2\}_0\,, \qquad \text{(C.55)}
\end{aligned}$$

$$\begin{aligned}
\frac{i}{2}(\boldsymbol{\sigma}_1+\boldsymbol{\sigma}_2)\cdot(\mathbf{q}\times\mathbf{P})(\mathbf{k}\cdot\mathbf{P}) =& \frac{1}{\sqrt{2}}\{\{\{\mathbf{q}_1\otimes\mathbf{k}_1\}_1\otimes\boldsymbol{\Sigma}_1^{+}\}_0\otimes\{\mathbf{P}_1\otimes\mathbf{P}_1\}_0\}_0 \\
&- \frac{\sqrt{5}}{2\sqrt{2}}\{\{\{\mathbf{q}_1\otimes\mathbf{k}_1\}_1\otimes\boldsymbol{\Sigma}_1^{+}\}_2\otimes\{\mathbf{P}_1\otimes\mathbf{P}_1\}_2\}_0 \\
&- \frac{\sqrt{15}}{2\sqrt{2}}\{\{\{\mathbf{q}_1\otimes\mathbf{k}_1\}_2\otimes\boldsymbol{\Sigma}_1^{+}\}_2\otimes\{\mathbf{P}_1\otimes\mathbf{P}_1\}_2\}_0\,, \qquad \text{(C.56)}
\end{aligned}$$

$$\begin{aligned}
\frac{i}{2}(\boldsymbol{\sigma}_1+\boldsymbol{\sigma}_2)\cdot((\mathbf{q}\times\mathbf{P})\times(\mathbf{k}\times\mathbf{P})) =& \frac{1}{\sqrt{2}}\{\{\{\mathbf{q}_1\otimes\mathbf{k}_1\}_1\otimes\boldsymbol{\Sigma}_1^{+}\}_0\otimes\{\mathbf{P}_1\otimes\mathbf{P}_1\}_0\}_0 \\
&+ \frac{\sqrt{5}}{2\sqrt{2}}\{\{\{\mathbf{q}_1\otimes\mathbf{k}_1\}_1\otimes\boldsymbol{\Sigma}_1^{+}\}_2\otimes\{\mathbf{P}_1\otimes\mathbf{P}_1\}_2\}_0\,. \qquad \text{(C.57)}
\end{aligned}$$

Finally, the tensor operators are expressed as

$$\begin{aligned}
\mathbf{q}^2(\mathbf{P}\cdot\boldsymbol{\sigma}_1)(\mathbf{P}\cdot\boldsymbol{\sigma}_2) =& -\sqrt{3}\{\{\{\mathbf{q}_1\otimes\mathbf{q}_1\}_0\otimes\boldsymbol{\Sigma}_0^{\otimes}\}_0\otimes\{\mathbf{P}_1\otimes\mathbf{P}_1\}_0\}_0 \\
&- \sqrt{15}\{\{\{\mathbf{q}_1\otimes\mathbf{q}_1\}_0\otimes\boldsymbol{\Sigma}_2^{\otimes}\}_2\otimes\{\mathbf{P}_1\otimes\mathbf{P}_1\}_2\}_0\,, \qquad \text{(C.58)}
\end{aligned}$$

$$\begin{aligned}
\mathbf{k}^2(\mathbf{P}\cdot\boldsymbol{\sigma}_1)(\mathbf{P}\cdot\boldsymbol{\sigma}_2) =& -\sqrt{3}\{\{\{\mathbf{k}_1\otimes\mathbf{k}_1\}_0\otimes\boldsymbol{\Sigma}_0^{\otimes}\}_0\otimes\{\mathbf{P}_1\otimes\mathbf{P}_1\}_0\}_0 \\
&- \sqrt{15}\{\{\{\mathbf{k}_1\otimes\mathbf{k}_1\}_0\otimes\boldsymbol{\Sigma}_2^{\otimes}\}_2\otimes\{\mathbf{P}_1\otimes\mathbf{P}_1\}_2\}_0\,, \qquad \text{(C.59)}
\end{aligned}$$

$$\begin{aligned}
\mathbf{P}^2(\mathbf{P}\cdot\boldsymbol{\sigma}_1)(\mathbf{P}\cdot\boldsymbol{\sigma}_2) =& -\sqrt{3}\{\boldsymbol{\Sigma}_0^{\otimes}\otimes\{\{\mathbf{P}_1\otimes\mathbf{P}_1\}_0\otimes\{\mathbf{P}_1\otimes\mathbf{P}_1\}_0\}_0\}_0 \\
&- \sqrt{15}\{\boldsymbol{\Sigma}_2^{\otimes}\otimes\{\{\mathbf{P}_1\otimes\mathbf{P}_1\}_2\otimes\{\mathbf{P}_1\otimes\mathbf{P}_1\}_0\}_2\}_0\,, \qquad \text{(C.60)}
\end{aligned}$$

$$\begin{aligned}
(\mathbf{q}\cdot\boldsymbol{\sigma}_1)(\mathbf{q}\cdot\boldsymbol{\sigma}_2)\mathbf{P}^2 =& -\sqrt{3}\{\{\{\mathbf{q}_1\otimes\mathbf{q}_1\}_0\otimes\boldsymbol{\Sigma}_0^{\otimes}\}_0\otimes\{\mathbf{P}_1\otimes\mathbf{P}_1\}_0\}_0 \\
&- \sqrt{15}\{\{\{\mathbf{q}_1\otimes\mathbf{q}_1\}_2\otimes\boldsymbol{\Sigma}_2^{\otimes}\}_2\otimes\{\mathbf{P}_1\otimes\mathbf{P}_1\}_0\}_0\,, \qquad \text{(C.61)}
\end{aligned}$$

$$\begin{aligned}
(\mathbf{k}\cdot\boldsymbol{\sigma}_1)(\mathbf{k}\cdot\boldsymbol{\sigma}_2)\mathbf{P}^2 =& -\sqrt{3}\{\{\{\mathbf{k}_1\otimes\mathbf{k}_1\}_0\otimes\boldsymbol{\Sigma}_0^{\otimes}\}_0\otimes\{\mathbf{P}_1\otimes\mathbf{P}_1\}_0\}_0 \\
&- \sqrt{15}\{\{\{\mathbf{k}_1\otimes\mathbf{k}_1\}_2\otimes\boldsymbol{\Sigma}_2^{\otimes}\}_2\otimes\{\mathbf{P}_1\otimes\mathbf{P}_1\}_0\}_0\,, \qquad \text{(C.62)}
\end{aligned}$$

$$\begin{aligned}
((\mathbf{q}\times\mathbf{P})\cdot\boldsymbol{\sigma}_1)((\mathbf{q}\times\mathbf{P})\cdot\boldsymbol{\sigma}_2) =& -\frac{2}{\sqrt{3}}\{\{\{\mathbf{q}_1\otimes\mathbf{q}_1\}_0\otimes\boldsymbol{\Sigma}_0^{\otimes}\}_0\otimes\{\mathbf{P}_1\otimes\mathbf{P}_1\}_0\}_0 \\
&+ \frac{\sqrt{5}}{\sqrt{3}}\{\{\{\mathbf{q}_1\otimes\mathbf{q}_1\}_2\otimes\boldsymbol{\Sigma}_2^{\otimes}\}_0\otimes\{\mathbf{P}_1\otimes\mathbf{P}_1\}_0\}_0 \\
&+ \frac{\sqrt{5}}{\sqrt{3}}\{\{\{\mathbf{q}_1\otimes\mathbf{q}_1\}_0\otimes\boldsymbol{\Sigma}_2^{\otimes}\}_2\otimes\{\mathbf{P}_1\otimes\mathbf{P}_1\}_2\}_0 \\
&+ \frac{\sqrt{5}}{\sqrt{3}}\{\{\{\mathbf{q}_1\otimes\mathbf{q}_1\}_2\otimes\boldsymbol{\Sigma}_2^{\otimes}\}_0\otimes\{\mathbf{P}_1\otimes\mathbf{P}_1\}_0\}_0 \\
&- \frac{\sqrt{35}}{\sqrt{3}}\{\{\{\mathbf{q}_1\otimes\mathbf{q}_1\}_2\otimes\boldsymbol{\Sigma}_2^{\otimes}\}_2\otimes\{\mathbf{P}_1\otimes\mathbf{P}_1\}_2\}_0\,, \qquad \text{(C.63)}
\end{aligned}$$

$$\begin{aligned}
((\mathbf{k}\times\mathbf{P})\cdot\boldsymbol{\sigma}_1)((\mathbf{k}\times\mathbf{P})\cdot\boldsymbol{\sigma}_2) =& -\frac{2}{\sqrt{3}}\{\{\{\mathbf{k}_1\otimes\mathbf{k}_1\}_0\otimes\boldsymbol{\Sigma}_0^{\otimes}\}_0\otimes\{\mathbf{P}_1\otimes\mathbf{P}_1\}_0\}_0 \\
&+ \frac{\sqrt{5}}{\sqrt{3}}\{\{\{\mathbf{k}_1\otimes\mathbf{k}_1\}_2\otimes\boldsymbol{\Sigma}_2^{\otimes}\}_0\otimes\{\mathbf{P}_1\otimes\mathbf{P}_1\}_0\}_0
\end{aligned}$$

$$
\begin{aligned}
&+\frac{\sqrt{5}}{\sqrt{3}}\{\{\{\mathbf{k}_1\otimes\mathbf{k}_1\}_0\otimes\Sigma_2^{\otimes}\}_2\otimes\{\mathbf{P}_1\otimes\mathbf{P}_1\}_2\}_0\\
&+\frac{\sqrt{5}}{\sqrt{3}}\{\{\{\mathbf{k}_1\otimes\mathbf{k}_1\}_2\otimes\Sigma_2^{\otimes}\}_0\otimes\{\mathbf{P}_1\otimes\mathbf{P}_1\}_0\}_0\\
&-\frac{\sqrt{35}}{\sqrt{3}}\{\{\{\mathbf{k}_1\otimes\mathbf{k}_1\}_2\otimes\Sigma_2^{\otimes}\}_2\otimes\{\mathbf{P}_1\otimes\mathbf{P}_1\}_2\}_0\,. \qquad \text{(C.64)}
\end{aligned}
$$

D Transformation to HO basis

To calculate the TBMEs, we transform the partial-wave momentum-space matrix elements to the relative-CM HO basis

$$\begin{aligned}&\langle nN[(ls)jL]J|V|n'N'[(l's')j'L']J\rangle\\&=\int dp p^2 R_{nl}(p)\int dp' p'^2 R_{n'l'}(p')\\&\times\int dP P^2 R_{NL}(P) R_{N'L'}(P)\,\langle \text{rel,CM}|V^J|\text{rel}',\text{CM}'\rangle\;.\end{aligned}\tag{D.1}$$

The relative-CM HO matrix elements are then transformed to the TBMEs using the Talmi-Moshinsky transformation. Including also the isospin part, this leads to

$$\begin{aligned}&\langle nN[(ls)jL]JT|V|n'N'[(l's')j'L']JT\rangle \to\\&\langle (n_1 l_1 j_1)(n_2 l_2 j_2)JT|V|(n_1' l_1' j_1')(n_2' l_2' j_2')JT\rangle =\\&\left\langle n_1 n_2\Big[(l_1\frac{1}{2})j_1(l_2\frac{1}{2})j_2\Big]JT\,\middle|\,V\,\middle|\,n_1' n_2'\Big[(l_1'\frac{1}{2})j_1'(l_2'\frac{1}{2})j_2'\Big]JT\right\rangle .\end{aligned}\tag{D.2}$$

To this end, we first recouple the two-body states to $|n_1 n_2[(l_1 l_2)\Lambda(\frac{1}{2}\frac{1}{2})s]J\rangle$, with total orbital angular momentum $\mathbf{\Lambda}=\mathbf{l}_1+\mathbf{l}_2$ or in terms of relative and CM angular momenta $\mathbf{\Lambda}=\mathbf{L}+\mathbf{l}$, and then to two-body states $|Nn[(Ll)\Lambda s]J\rangle$, which can be recoupled to the desired relative-CM states $|nN[(ls)jL]J\rangle$. Combining this, we have for antisymmetrized, normalized two-body states

$$\begin{aligned}&\left|n_1 n_2\Big[(l_1\frac{1}{2})j_1(l_2\frac{1}{2})j_2\Big]JT\right\rangle=\sum_{\Lambda s}[\Lambda][s][j_1][j_2]\begin{Bmatrix} l_1 & l_2 & \Lambda\\ 1/2 & 1/2 & s\\ j_1 & j_2 & J\end{Bmatrix}\\&\times\sum_{nlNL}\langle Nn(Ll)\Lambda|n_1 n_2(l_1 l_2)\Lambda\rangle_{d=1}\\&\times\sum_j(-1)^{l+s+j}[\Lambda][j]\begin{Bmatrix} L & l & \Lambda\\ s & J & j\end{Bmatrix}\mathscr{F}\,|nN[(ls)jL]JT\rangle\;,\end{aligned}\tag{D.3}$$

where $\mathscr{F}=(1-(-1)^{l+s+T})/\sqrt{2(1+\delta_{n_1 n_2}\delta_{l_1 l_2}\delta_{j_1 j_2})}$ takes into account the normalization and antisymmetrization of the two-body states, and $\langle Nn(Ll)\Lambda|n_1 n_2(l_1 l_2)\Lambda\rangle_{d=1}$ is the Talmi-Moshinsky bracket in the conventions of Ref. [248]. Note that for calculating the TMBEs the sum is over all s,s', j,j', N,N', and L,L', contrary to the case for free-space interactions when these are diagonal.

E Two-body matrix elements and low-energy constants

Throughout this thesis, we regularly fit LECs to data. In some cases, we present the values already in the corresponding chapter. In other cases the values are presented in figures rather than tables to keep a structured overview. We list all the data that was not presented directly in the thesis in this part of the appendix.

E.1 Low-energy constants of LO interactions from chapter 6

In Ch. 6, we investigated different regulator functions for a wide range of coordinate space cutoffs. We list our results for the LO LECs C_{01} and C_{10}.

Table E.1.: Low-energy constant C_{01} and C_{10} in fm^2 for a given value of the inverse coordinate-space cutoff R_0^{-1} in fm^{-1}. We show LECs from $R_0^{-1} = 0.8$ – 4.4 fm^{-1} for short- and long-range regulator functions from Eq. (4.3) and Eq. (4.2) with $n = 4$ and $n_1 = n_2 = 2$. The operator LECs can be obtained with Eq. (5.15). We cannot find further numerical values beyond $R_0^{-1} = 4.4$ fm^{-1} with only one bound state in the deuteron for this setup.

R_0^{-1}	C_{01}	C_{10}
0.8	-0.31343	-2.58679
1.0	-0.30429	-1.34482
1.2	-0.29566	-0.34292
1.4	-0.28749	0.64849
1.6	-0.27974	1.83894
1.8	-0.27239	3.57236
2.0	-0.26541	6.60138
2.2	-0.25877	$1.27849 \cdot 10^{1}$
2.4	-0.25243	$2.71750 \cdot 10^{1}$
2.8	-0.24637	$1.81446 \cdot 10^{2}$
3.0	-0.24056	$5.99447 \cdot 10^{2}$
3.2	-0.23499	$2.42644 \cdot 10^{3}$
3.4	-0.22963	$1.25736 \cdot 10^{4}$
3.6	-0.22449	$8.88628 \cdot 10^{4}$
3.8	-0.21956	$9.23646 \cdot 10^{5}$
4.0	-0.21485	$1.51067 \cdot 10^{7}$
4.0	-0.21035	$1.51067 \cdot 10^{7}$
4.2	-0.20607	$9.28102 \cdot 10^{7}$
4.4	-0.20199	$2.12351 \cdot 10^{9}$

Table E.2.: Low-energy constants C_{01} and C_{10} in fm^2 for a given value of the inverse coordinate-space cutoff R_0^{-1} in fm^{-1}. We show the value of C_{10} for one, two and three bound states in the deuteron channel ($\#E_D$). The C_{01} value is independent of the number of bound states. The table is divided into two sections, which we separate by two vertical lines: on the left, we show LECs from R_0^{-1} = 0.8 – 5.4 fm^{-1}, on the right those for R_0^{-1} = 5.6 – 10 fm^{-1}. All LECs correspond to the short- and long-range regulator functions from Eq. (4.3) and Eq. (4.2) with $n = n_1 = n_2 = 2$. The operator LECs can be obtained with Eq. (5.15).

R_0^{-1}	C_{01}	C_{10}			R_0^{-1}	C_{01}	C_{10}		
		$\#E_D = 1$	$\#E_D = 2$	$\#E_D = 3$			$\#E_D = 1$	$\#E_D = 2$	$\#E_D = 3$
0.8	-3.145	-3.670	-27.804		5.6	-0.465	$1.943 \cdot 10^3$	4.178	-1.385
1.0	-2.470	-1.786	-20.220	-50.981	5.8	-0.451	$3.213 \cdot 10^3$	4.629	-1.053
1.2	-2.038	-0.423	-15.552	-41.330	6.0	-0.437	$5.408 \cdot 10^3$	5.108	-0.743
1.4	-1.739	0.718	-12.311		6.2	-0.424	$9.264 \cdot 10^3$	5.729	-0.445
1.6	-1.519	1.779	-9.895	-29.423	6.4	-0.412	$1.615 \cdot 10^4$	6.175	-0.163
1.8	-1.351	2.850	-8.005	-21.062	6.6	-0.401	$2.865 \cdot 10^4$	6.779	0.104
2.0	-1.218	4.003	-6.476	-18.240	6.8	-0.390	$5.170 \cdot 10^4$	7.446	0.361
2.2	-1.111	5.317	-5.206	-15.821	7.0	-0.380	$9.494 \cdot 10^4$	8.178	0.608
2.4	-1.022	6.881	-4.131	-13.737	7.2	-0.370	$1.774 \cdot 10^5$	9.004	0.848
2.6	-0.947	8.843	-3.206	-11.930	7.4	-0.361	$3.371 \cdot 10^5$	9.921	1.080
2.8	-0.883	$1.137 \cdot 10^1$	-2.401	-10.357	7.6	-0.352	$6.518 \cdot 10^5$	10.957	1.303
3.0	-0.827	$1.474 \cdot 10^1$	-1.692	-8.986	7.8	-0.344	$1.282 \cdot 10^6$	12.141	1.523
3.2	-0.779	$1.932 \cdot 10^1$	-1.061	-7.792	8.0	-0.336	$2.565 \cdot 10^6$	13.467	1.740
3.4	-0.736	$2.569 \cdot 10^1$	-0.493	-6.754	8.2	-0.328	$5.219 \cdot 10^6$	14.982	1.947
3.6	-0.698	$3.474 \cdot 10^1$	0.025	-5.851	8.4	-0.321	$1.080 \cdot 10^7$	16.736	2.158
3.8	-0.664	$4.779 \cdot 10^1$	0.504	-5.064	8.6	-0.314	$2.274 \cdot 10^7$	18.744	2.358
4.0	-0.633	$6.696 \cdot 10^1$	0.952	-4.373	8.8	-0.308	$4.872 \cdot 10^7$	21.061	2.559
4.2	-0.606	$9.559 \cdot 10^1$	1.379	-4.373	9.0	-0.302	$1.061 \cdot 10^8$	23.745	2.761
4.4	-0.580	$1.390 \cdot 10^2$	1.790	-4.054	9.2	-0.296	$2.351 \cdot 10^8$	26.860	2.964
4.6	-0.557	$2.061 \cdot 10^2$	2.192	-3.497	9.4	-0.290	$5.299 \cdot 10^8$	30.484	3.168
4.8	-0.536	$3.112 \cdot 10^2$	2.590	-2.994	9.6	-0.284	$1.215 \cdot 10^9$	34.735	3.370
5.0	-0.516	$4.786 \cdot 10^2$	2.990	-2.287	9.8	-0.279	$2.832 \cdot 10^9$	39.727	3.570
5.2	-0.498	$7.498 \cdot 10^2$	3.396	-2.123	10.	-0.274	$6.717 \cdot 10^9$	45.578	3.771
5.4	-0.481	$1.196 \cdot 10^3$	3.751	-1.742					

Table E.3.: Low-energy constants C_{01} and C_{10} in fm^2 for a given value of the inverse coordinate-space cutoff R_0^{-1} in fm^{-1}. The table is divided into two sections, which we separate by two vertical lines: on the left, we show LECs from $R_0^{-1} = 0.8$ – 5.4 fm^{-1}, on the right those for $R_0^{-1} = 5.6$ – 10 fm^{-1}. All LECs correspond to the long-range regulator function from Eq. (4.2) with n_1=4 and $n_2 = 1$. On the left of each section, we show LECs for the short-range regulator function from Eq. (4.3) with $n = 4$ and on the right of each section those for $n = 2$. The operator LECs can be obtained with Eq. (5.15). For the C_{10} LECs with $n = 4$, we cannot find numerical values with only one bound state in the deuteron beyond $R_0^{-1} = 4.4$ fm^{-1}. The values for C_{10} we show after this point are for two bound states in the deuteron.

R_0^{-1}	$n = 4$		$n = 2$		R_0^{-1}	$n = 4$		$n = 2$	
	C_{01}	C_{10}	C_{01}	C_{10}		C_{01}	C_{10}	C_{01}	C_{10}
0.8	-2.315	-1.868	-3.023	-2.596	5.6	-0.356	$1.512 \cdot 10^1$	-0.471	$1.943 \cdot 10^3$
1.0	-1.831	-0.318	-2.372	-0.407	5.8	-0.344	$2.003 \cdot 10^1$	-0.456	$3.213 \cdot 10^3$
1.2	-1.519	1.053	-1.959	1.214	6.0	-0.334	$2.707 \cdot 10^1$	-0.441	$5.408 \cdot 10^3$
1.4	-1.302	2.532	-1.673	2.574	6.2	-0.324	$3.739 \cdot 10^1$	-0.428	$9.264 \cdot 10^3$
1.6	-1.142	4.426	-1.465	3.813	6.4	-0.315	$5.286 \cdot 10^1$	-0.415	$1.615 \cdot 10^4$
1.8	-1.019	7.246	-1.465	3.813	6.6	-0.306	$7.703 \cdot 10^1$	-0.403	$2.865 \cdot 10^4$
2.0	-0.921	$1.204 \cdot 10^1$	-1.305	5.019	6.8	-0.298	$1.156 \cdot 10^2$	-0.392	$5.170 \cdot 10^4$
2.2	-0.841	$2.124 \cdot 10^1$	-1.179	6.263	7.0	-0.290	$1.790 \cdot 10^2$	-0.381	$9.494 \cdot 10^4$
2.4	-0.775	$4.115 \cdot 10^1$	-1.077	7.620	7.2	-0.282	$2.865 \cdot 10^2$	-0.371	$1.774 \cdot 10^5$
2.6	-0.719	$9.020 \cdot 10^1$	-0.992	9.185	7.4	-0.275	$4.753 \cdot 10^2$	-0.362	$3.371 \cdot 10^5$
2.8	-0.670	$2.297 \cdot 10^2$	-0.920	$1.109 \cdot 10^1$	7.6	-0.269	$8.185 \cdot 10^2$	-0.353	$6.517 \cdot 10^5$
3.0	-0.629	$6.966 \cdot 10^2$	-0.859	$1.351 \cdot 10^1$	7.8	-0.262	$1.466 \cdot 10^3$	-0.336	$1.282 \cdot 10^6$
3.2	-0.594	$2.581 \cdot 10^3$	-0.806	$1.673 \cdot 10^1$	8.0	-0.256	$2.734 \cdot 10^3$	-0.328	$2.564 \cdot 10^6$
3.4	-0.562	$1.199 \cdot 10^4$	-0.760	$2.116 \cdot 10^1$	8.2	-0.250	$5.326 \cdot 10^3$	-0.320	$5.219 \cdot 10^6$
3.6	-0.533	$7.177 \cdot 10^4$	-0.718	$2.739 \cdot 10^1$	8.4	-0.245	$1.085 \cdot 10^4$	-0.313	$1.080 \cdot 10^7$
3.8	-0.507	$5.701 \cdot 10^5$	-0.682	$4.938 \cdot 10^1$	8.6	-0.240	$2.317 \cdot 10^4$	-0.306	$2.274 \cdot 10^7$
4.0	-0.484	$6.203 \cdot 10^6$	-0.649	$6.869 \cdot 10^1$	8.8	-0.235	$5.198 \cdot 10^4$	-0.300	$4.871 \cdot 10^7$
4.2	-0.463	$9.566 \cdot 10^7$	-0.619	$9.651 \cdot 10^1$	9.0	-0.230	$1.228 \cdot 10^5$	-0.293	$1.061 \cdot 10^8$
4.4	-0.443	$2.168 \cdot 10^9$	-0.592	$1.398 \cdot 10^2$	9.2	-0.225	$3.062 \cdot 10^5$	-0.287	$2.351 \cdot 10^8$
4.6	-0.426	4.646	-0.568	$2.068 \cdot 10^2$	9.4	-0.221	$8.084 \cdot 10^5$	-0.282	$5.299 \cdot 10^8$
4.8	-0.410	5.705	-0.545	$3.118 \cdot 10^2$	9.6	-0.216	$2.267 \cdot 10^6$	-0.276	$1.215 \cdot 10^9$
5.0	-0.394	7.277	-0.525	$4.792 \cdot 10^2$	9.8	-0.212	$6.775 \cdot 10^6$	-0.271	$2.832 \cdot 10^9$
5.2	-0.381	9.069	-0.505	$7.503 \cdot 10^2$	10.	-0.208	$2.166 \cdot 10^7$	-0.265	$6.716 \cdot 10^9$
5.4	-0.368	$1.160 \cdot 10^1$	-0.488	$1.197 \cdot 10^3$					

E.2 Two-body matrix elements from chapter 8

For completeness, we list the TBMEs of the charge-independent NLO$_{\mathrm{vs}}$ interaction from Ch. 8 in Table E.4. The corresponding SPEs are $\varepsilon_{0d_{5/2}} = -4.14308\,\mathrm{MeV}$, $\varepsilon_{1s_{1/2}} = -3.27235\,\mathrm{MeV}$, and $\varepsilon_{0d_{3/2}} = 0.94172\,\mathrm{MeV}$, taken from the spectrum of ^{17}O.

Table E.4.: Two-body matrix elements for the charge-independent NLO$_{\mathrm{vs}}$ interaction for a given isospin T and total angular momentum J. The single-particle orbits are labeled by $2j_a\,2j_b\,2j_c\,2j_d$.

orbitals	T	$J=0$	$J=1$	$J=2$	$J=3$	$J=4$	$J=5$
5555	0	–	−2.962356	–	−1.348477	–	−4.366727
	1	−1.561786	–	−0.591304	–	−0.109698	–
5553	0	–	2.203146	–	1.185351	–	–
	1	–	–	−0.782881	–	−0.958506	–
5551	0	–	–	–	−1.671394	–	–
	1	–	–	−0.744657	–	–	–
5533	0	–	0.893444	–	0.528466	–	–
	1	−5.086935	–	−1.053896	–	–	–
5531	0	–	0.568667	–	–	–	–
	1	–	–	0.908236	–	–	–
5511	0	–	−0.106744	–	–	–	–
	1	−1.483464	–	–	–	–	–
5353	0	–	−5.783199	−4.103275	−2.055604	−4.881107	–
	1	–	0.302405	0.624787	−0.239897	−0.866801	–
5351	0	–	–	−1.513283	1.363597	–	–
	1	–	–	−0.029187	0.039135	–	–
5333	0	–	−1.067963	–	1.696282	–	–
	1	–	–	−0.728416	–	–	–
5331	0	–	1.558985	−2.312917	–	–	–
	1	–	0.083957	0.922578	–	–	–
5311	0	–	1.400007	–	–	–	–
	1	–	–	–	–	–	–
5151	0	–	–	−1.943009	−3.565486	–	–
	1	–	–	−0.654884	0.217367	–	–
5133	0	–	–	–	0.001177	–	–
	1	–	–	−0.684786	–	–	–
5131	0	–	–	−1.984955	–	–	–
	1	–	–	1.534945	–	–	–
3333	0	–	−1.635266	–	−2.921386	–	–
	1	−0.014457	–	−0.046811	–	–	–
3331	0	–	−0.996922	–	–	–	–
	1	–	–	0.179512	–	–	–
3311	0	–	−0.309804	–	–	–	–
	1	−1.585586	–	–	–	–	–
3131	0	–	−3.190265	−2.531388	–	–	–
	1	–	0.054273	0.236452	–	–	–
3111	0	–	0.139808	–	–	–	–
	1	–	–	–	–	–	–
1111	0	–	−3.262572	–	–	–	–
	1	−0.385534	–	–	–	–	–

E.3 Single-particle energies, low-energy constants, and TBMEs from chapter 9

The tables below show the SPEs and LECs for the fits of the charge-dependent interactions at LO, NLO, NLO$_{\mathrm{vs}}$, N^{2}LO$_{\mathrm{vs}}$, N^{3}LO$_{\mathrm{NLO,\,vs}}$, and N^{3}LO$_{\mathrm{vs}}$ to the BR$_2$ data set from Tab. 7.2. We show values for the SPEs in Tab. E.5. The LECs C_S, C_T, C_{CIB}, and C_{CSB} are presented in Tab. E.6, C_1–C_7, P_1–P_5, D_1–D_{15}, and Q_1–Q_{32} are presented in Tab. E.7, Tab. E.8, Tab. E.9, and Tab. E.10 respectively. Furthermore, we present the TBMEs of the N^{3}LO$_{\mathrm{vs}}$ interactions in Tab. E.11.

Table E.5.: Single-particle energies for neutrons and protons of the shell-model interactions at LO, NLO, NLO$_{\mathrm{vs}}$, N^{2}LO$_{\mathrm{vs}}$, N^{3}LO$_{\mathrm{NLO,\,vs}}$, and N^{3}LO$_{\mathrm{vs}}$. The SPEs are given in MeV.

	neutrons			protons		
	$\varepsilon_{0d_{5/2}}$	$\varepsilon_{0d_{3/2}}$	$\varepsilon_{1s_{1/2}}$	$\varepsilon_{0d_{5/2}}$	$\varepsilon_{0d_{3/2}}$	$\varepsilon_{1s_{1/2}}$
LO	−4.28227	5.87080	−1.52043	−6.26124	4.09793	0.01450
NLO	−4.06791	1.47058	−1.95435	−3.20546	2.46191	−1.98297
NLO$_{\mathrm{vs}}$	−3.83422	1.19913	−2.31276	−3.39805	1.46680	−3.69862
N^{2}LO$_{\mathrm{vs}}$	−3.87882	0.98755	−3.11351	−3.55700	1.07437	−3.21568
N^{3}LO$_{\mathrm{NLO,\,vs}}$	−3.84567	1.53128	−2.65322	−3.66970	1.42351	−3.19351
N^{3}LO$_{\mathrm{vs}}$	−3.80551	1.67939	−3.13205	−3.68955	1.26087	−3.15938

Table E.6.: Low-energy constants C_S, C_T, C_{CIB}, and C_{CSB} at LO, NLO, NLO$_{\mathrm{vs}}$, N^{2}LO$_{\mathrm{vs}}$, N^{3}LO$_{\mathrm{NLO,\,vs}}$, and N^{3}LO$_{\mathrm{vs}}$. The LECs are given in fm^2.

	C_S	C_T	C_{CIB}	C_{CSB}
LO	−4.37421	−0.25651	0.41826	−0.07982
NLO	−7.05913	−0.62968	0.38121	−0.08463
NLO$_{\mathrm{vs}}$	−8.16229	−0.52944	0.25095	−0.05624
N^{2}LO$_{\mathrm{vs}}$	−9.73741	−0.77484	0.30442	−0.08387
N^{3}LO$_{\mathrm{NLO,\,vs}}$	−6.74060	0.52606	0.04102	−0.09085
N^{3}LO$_{\mathrm{vs}}$	−6.13037	−0.35837	0.07129	−0.08806

Table E.7.: Low-energy constants C_1–C_7 at NLO, NLO$_{\mathrm{vs}}$, N^{2}LO$_{\mathrm{vs}}$, N^{3}LO$_{\mathrm{NLO,\,vs}}$, and N^{3}LO$_{\mathrm{vs}}$. The LECs are given in fm^4.

	C_1	C_2	C_3	C_4	C_5	C_6	C_7
NLO	0.295 32	1.545 57	−0.228 01	1.058 57	1.489 67	−0.384 01	−2.400 01
NLO$_{\mathrm{vs}}$	0.442 60	2.086 83	−0.217 37	0.126 58	1.238 68	−0.022 72	−2.283 92
N^{2}LO$_{\mathrm{vs}}$	2.325 18	4.948 48	0.088 57	0.337 41	1.347 42	−0.256 21	−4.389 28
N^{3}LO$_{\mathrm{NLO,\,vs}}$	0.095 20	2.899 64	−0.815 30	−0.685 32	2.555 62	0.106 14	−5.166 18
N^{3}LO$_{\mathrm{vs}}$	0.003 43	2.640 34	−0.217 51	−0.380 23	2.506 15	−0.020 87	−5.077 49

Table E.8.: Low-energy constants P_1 – P_5 at NLO$_{\mathrm{vs}}$, N^{2}LO$_{\mathrm{vs}}$, N^{3}LO$_{\mathrm{NLO,\,vs}}$, and N^{3}LO$_{\mathrm{vs}}$. The LECs are given in fm^4.

	P_1	P_2	P_3	P_4	P_5
NLO$_{\mathrm{vs}}$	0.322 19	−0.111 48	0.104 78	−0.124 73	−0.028 47
N^{2}LO$_{\mathrm{vs}}$	0.594 35	−0.046 99	0.112 76	0.150 62	−0.203 22
N^{3}LO$_{\mathrm{NLO,\,vs}}$	0.191 62	−0.283 74	0.026 80	−0.344 99	0.358 76
N^{3}LO$_{\mathrm{vs}}$	−0.015 38	0.176 47	−0.034 99	−0.359 85	−0.162 35

Table E.9.: Low-energy constants D_1 – D_{15} at N^{3}LO$_{\mathrm{NLO,\,vs}}$ and N^{3}LO$_{\mathrm{vs}}$. The LECs are given in fm^6.

LEC	N^{3}LO$_{\mathrm{NLO,\,vs}}$	N^{3}LO$_{\mathrm{vs}}$	LEC	N^{3}LO$_{\mathrm{NLO,\,vs}}$	N^{3}LO$_{\mathrm{vs}}$
D_1	−0.08049	−0.15370	D_9	−0.64603	−0.53973
D_2	−1.64781	−1.88648	D_{10}	−0.30665	0.16518
D_3	0.19550	0.51884	D_{11}	0.03333	0.09187
D_4	0.53070	0.68873	D_{12}	−0.28109	−0.17577
D_5	0.04022	−0.03106	D_{13}	−0.03219	−0.31227
D_6	−0.28951	−0.25158	D_{14}	2.00608	1.88017
D_7	0.76516	0.57180	D_{15}	0.24025	0.34159
D_8	−0.24233	−0.25412			

Table E.10.: Low-energy constants Q_1 – Q_{32} at N^{3}LO$_{\mathrm{vs}}$. The LECs are given in fm^6.

LEC	N^{3}LO$_{\mathrm{vs}}$	LEC	N^{3}LO$_{\mathrm{vs}}$	LEC	N^{3}LO$_{\mathrm{vs}}$
Q_1	0.12437	Q_{12}	−0.12711	Q_{23}	−0.31909
Q_2	0.09414	Q_{13}	−0.02599	Q_{24}	0.01747
Q_3	−0.01669	Q_{14}	0.05755	Q_{25}	−0.27701
Q_4	−0.05505	Q_{15}	0.23004	Q_{26}	−0.09506
Q_5	0.00417	Q_{16}	−0.38569	Q_{27}	0.14704
Q_6	−0.08624	Q_{17}	0.09955	Q_{28}	0.07728
Q_7	0.05914	Q_{18}	−0.14604	Q_{29}	−0.05205
Q_8	0.02153	Q_{19}	0.01828	Q_{30}	0.33057
Q_9	−0.02714	Q_{20}	0.12059	Q_{31}	−0.02148
Q_{10}	−0.05991	Q_{21}	−0.25483	Q_{32}	0.09966
Q_{11}	−0.02892	Q_{22}	−0.17051		

Table E.11.: Two-body matrix elements for the charge-dependent N^{3}LO$_{\mathrm{vs}}$ interaction for a given isospin T, the projection M_T, and total angular momentum J. The single-particle orbits are labeled by $2j_a\,2j_b\,2j_c\,2j_d$. Note that this table is split across two pages.

orbitals	T	M_T	$J=0$	$J=1$	$J=2$	$J=3$	$J=4$	$J=5$
5555	0	0	–	−1.780385	–	−1.651817	–	−4.272049
	1	−1	−2.128806	–	−0.967983	–	−0.148893	–
	1	0	−2.521073	–	−1.051820	–	−0.189171	–
	1	1	−2.459370	–	−1.044265	–	−0.179330	–
5553	0	0	–	2.694774	–	1.475638	–	–
	1	−1	–	–	−0.134659	–	−1.154982	–
	1	0	–	–	−0.192606	–	−1.225702	–
	1	1	–	–	−0.176827	–	−1.217222	–
5551	0	0	–	–	–	−1.596613	–	–
	1	−1	–	–	−0.541676	–	–	–
	1	0	–	–	−0.607944	–	–	–
	1	1	–	–	−0.593127	–	–	–
5533	0	0	–	1.477929	–	0.136866	–	–
	1	−1	−3.382920	–	−1.102373	–	–	–
	1	0	−3.648889	–	−1.166246	–	–	–
	1	1	−3.648473	–	−1.160202	–	–	–
5531	0	0	–	0.264504	–	–	–	–
	1	−1	–	–	1.129751	–	–	–
	1	0	–	–	1.176060	–	–	–
	1	1	–	–	1.174750	–	–	–
5511	0	0	–	−0.199191	–	–	–	–
	1	−1	−1.479864	–	–	–	–	–
	1	0	−1.606182	–	–	–	–	–
	1	1	−1.592410	–	–	–	–	–
5353	0	0	–	−5.760414	−3.583405	−1.887294	−4.374703	–
	1	−1	–	1.306485	0.103403	0.328652	−1.031634	–
	1	0	–	1.347632	0.054461	0.347815	−1.176220	–
	1	1	–	1.305148	0.065790	0.329033	−1.151884	–
5351	0	0	–	–	−1.575739	1.510226	–	–
	1	−1	–	–	−0.090604	−0.074248	–	–
	1	0	–	–	−0.139912	−0.086880	–	–
	1	1	–	–	−0.126364	−0.073673	–	–
5333	0	0	–	−0.003950	–	1.597656	–	–
	1	−1	–	–	−0.956288	–	–	–
	1	0	–	–	−0.994336	–	–	–
	1	1	–	–	−0.998115	–	–	–
5331	0	0	–	2.096630	−0.274160	–	–	–
	1	−1	–	−0.562151	0.339817	–	–	–
	1	0	–	−0.558065	0.367726	–	–	–
	1	1	–	−0.563287	0.368732	–	–	–
5311	0	0	–	2.345593	–	–	–	–
	1	−1	–	–	–	–	–	–
	1	0	–	–	–	–	–	–
	1	1	–	–	–	–	–	–

orbitals	T	M_T	$J=0$	$J=1$	$J=2$	$J=3$	$J=4$	$J=5$
5151	0	0	–	–	−0.879172	−3.987293	–	–
	1	−1	–	–	−0.948167	0.693076	–	–
	1	0	–	–	−1.050021	0.704170	–	–
	1	1	–	–	−1.025612	0.694403	–	–
5133	0	0	–	–	–	−0.249895	–	–
	1	−1	–	–	−0.438989	–	–	–
	1	0	–	–	−0.474418	–	–	–
	1	1	–	–	−0.477862	–	–	–
5131	0	0	–	–	−0.989772	–	–	–
	1	−1	–	–	1.528501	–	–	–
	1	0	–	–	1.591462	–	–	–
	1	1	–	–	1.592318	–	–	–
3333	0	0	–	−1.279541	–	−3.056723	–	–
	1	−1	−1.625660	–	−0.118538	–	–	–
	1	0	−1.909317	–	−0.174522	–	–	–
	1	1	−1.847731	–	−0.161456	–	–	–
3331	0	0	–	−1.163958	–	–	–	–
	1	−1	–	–	0.433338	–	–	–
	1	0	–	–	0.486504	–	–	–
	1	1	–	–	0.466612	–	–	–
3311	0	0	–	−0.113704	–	–	–	–
	1	−1	−1.132659	–	–	–	–	–
	1	0	−1.235059	–	–	–	–	–
	1	1	−1.223088	–	–	–	–	–
3131	0	0	–	−3.553688	−2.123289	–	–	–
	1	−1	–	0.453259	−0.291107	–	–	–
	1	0	–	0.482808	−0.367284	–	–	–
	1	1	–	0.452019	−0.342555	–	–	–
3111	0	0	–	−1.195110	–	–	–	–
	1	−1	–	–	–	–	–	–
	1	0	–	–	–	–	–	–
	1	1	–	–	–	–	–	–
1111	0	0	–	−3.204846	–	–	–	–
	1	−1	−1.323746	–	–	–	–	–
	1	0	−1.619102	–	–	–	–	–
	1	1	−1.591631	–	–	–	–	–

E.4 Single-particle energies and low-energy constants from chapter 10

The tables below show the SPEs and LECs for the fits of the charge-dependent interactions at LO, NLO$_{\mathrm{vs}}$, N^{2}LO$_{\mathrm{vs}}$, and N^{3}LO$_{\mathrm{vs}}$ to the SDF16 data set from Tab. 7.2. We show values for the SPEs in Tab. E.12. The LECs C_S, C_T, C_{CIB}, and C_{CSB} are presented in Tab. E.13, C_1–C_7 and P_1–P_5 are presented in Tab. E.14 and Tab. E.15 respectively, and D_1–D_{15} and Q_1–Q_{32} are presented in Tab. E.16 and ab. E.17 respectively.

Table E.12.: Single-particle energies for neutrons and protons of the shell-model interactions at LO, NLO$_{\text{vs}}$, N^{2}LO$_{\text{vs}}$, and N^{3}LO$_{\text{vs}}$. The SPEs are given in MeV.

	neutrons				protons		
	$\varepsilon_{0d_{5/2}}$	$\varepsilon_{0d_{3/2}}$	$\varepsilon_{1s_{1/2}}$	$\varepsilon_{0f_{7/2}}$	$\varepsilon_{0d_{5/2}}$	$\varepsilon_{0d_{3/2}}$	$\varepsilon_{1s_{1/2}}$
LO	$-6.416\,14$	$3.808\,63$	$-2.018\,43$	$2.628\,06$	$-3.515\,39$	$-0.718\,12$	$-2.334\,53$
NLO$_{\text{vs}}$	$-5.136\,55$	$1.893\,37$	$-1.429\,12$	$6.236\,10$	$-6.927\,62$	$-1.856\,14$	$-5.259\,99$
N^{2}LO$_{\text{vs}}$	$-4.555\,19$	$5.617\,99$	$-0.083\,73$	$4.811\,03$	$-6.756\,76$	$0.492\,29$	$-3.433\,87$
N^{3}LO$_{\text{vs}}$	$-4.896\,82$	$2.125\,22$	$-1.927\,67$	$6.018\,57$	$-4.877\,87$	$-0.166\,73$	$-4.803\,21$

Table E.13.: Low-energy constants C_S, C_T, C_{CIB}, and C_{CSB} at LO, NLO, NLO$_{\text{vs}}$, N^{2}LO$_{\text{vs}}$, N^{3}LO$_{\text{NLO, vs}}$, and N^{3}LO$_{\text{vs}}$. The LECs are given in fm^2.

	C_S	C_T	C_{CIB}	C_{CSB}
LO	$-4.003\,14$	$-0.216\,88$	$0.354\,66$	$-0.537\,51$
NLO$_{\text{vs}}$	$-5.188\,35$	$-1.718\,26$	$0.679\,03$	$0.262\,49$
N^{2}LO$_{\text{vs}}$	$-2.477\,85$	$3.468\,55$	$2.811\,23$	$-0.053\,03$
N^{3}LO$_{\text{vs}}$	$-5.542\,99$	$-0.735\,84$	$0.518\,55$	$0.359\,16$

Table E.14.: Low-energy constants C_1–C_7 at NLO$_{\text{vs}}$, N^{2}LO$_{\text{vs}}$, and N^{3}LO$_{\text{vs}}$. The LECs are given in fm^4.

	C_1	C_2	C_3	C_4	C_5	C_6	C_7
NLO$_{\text{vs}}$	$0.031\,08$	$-1.732\,71$	$-0.538\,10$	$0.701\,83$	$1.075\,84$	$1.365\,38$	$-1.970\,53$
N^{2}LO$_{\text{vs}}$	$0.180\,33$	$-1.540\,42$	$-0.501\,71$	$-3.982\,45$	$2.948\,28$	$0.036\,87$	$-0.414\,41$
N^{3}LO$_{\text{vs}}$	$0.211\,60$	$-0.221\,64$	$-0.023\,75$	$-0.106\,34$	$-0.605\,79$	$0.547\,55$	$0.386\,67$

Table E.15.: Low-energy constants P_1 – P_5 at NLO$_{\text{vs}}$, N^{2}LO$_{\text{vs}}$, and N^{3}LO$_{\text{vs}}$. The LECs are given in fm^4.

	P_1	P_2	P_3	P_4	P_5
NLO$_{\text{vs}}$	$0.355\,47$	$-0.095\,24$	$-0.309\,13$	$0.378\,78$	$0.540\,90$
N^{2}LO$_{\text{vs}}$	$-0.080\,51$	$-0.945\,56$	$0.163\,64$	$0.582\,87$	$1.182\,56$
N^{3}LO$_{\text{vs}}$	$0.052\,69$	$-1.148\,40$	$-0.424\,26$	$0.241\,26$	$-0.042\,00$

Table E.16.: Low-energy constants D_1 – D_{15} at N^{3}LO$_{\mathrm{vs}}$. The LECs are given in fm^6.

LEC	N^{3}LO$_{\mathrm{vs}}$	LEC	N^{3}LO$_{\mathrm{vs}}$
D_1	−0.170 60	D_9	−0.826 81
D_2	−0.709 96	D_{10}	−0.100 55
D_3	0.663 08	D_{11}	0.090 45
D_4	0.704 49	D_{12}	−0.772 67
D_5	−0.049 54	D_{13}	0.163 25
D_6	−0.942 29	D_{14}	0.228 78
D_7	−0.041 92	D_{15}	0.579 55
D_8	−0.040 17		

Table E.17.: Low-energy constants Q_1 – Q_{32} at N^{3}LO$_{\mathrm{vs}}$. The LECs are given in fm^6.

LEC	N^{3}LO$_{\mathrm{vs}}$	LEC	N^{3}LO$_{\mathrm{vs}}$	LEC	N^{3}LO$_{\mathrm{vs}}$
Q_1	−0.082 09	Q_{12}	−0.090 43	Q_{23}	−0.074 59
Q_2	0.152 57	Q_{13}	−0.172 11	Q_{24}	−0.327 47
Q_3	0.098 24	Q_{14}	0.269 48	Q_{25}	0.386 60
Q_4	−0.148 54	Q_{15}	−0.316 32	Q_{26}	0.270 94
Q_5	−0.022 05	Q_{16}	0.403 72	Q_{27}	0.670 52
Q_6	−0.758 97	Q_{17}	0.302 71	Q_{28}	−0.308 74
Q_7	0.459 87	Q_{18}	0.342 77	Q_{29}	0.730 44
Q_8	0.630 40	Q_{19}	−0.436 33	Q_{30}	0.379 43
Q_9	−0.115 13	Q_{20}	0.722 67	Q_{31}	0.042 51
Q_{10}	0.239 45	Q_{21}	0.174 98	Q_{32}	0.384 00
Q_{11}	−0.078 62	Q_{22}	1.357 77		

Bibliography

[1] E. Rutherford, Phil. Mag. Ser. 6 **21**, 669 (1911).

[2] J. Chadwick, Nature **129**, 312 (1932).

[3] H. Yukawa, Proc. Phys. Math. Soc. Jap. **17**, 48 (1935), [Prog. Theor. Phys. Suppl. 1,1(1935)].

[4] M. Lacombe, B. Loiseau, J. M. Richard, R. V. Mau, J. Côté, P. Pirès, and R. de Tourreil, Phys. Rev. C **21**, 861 (1980).

[5] R. Machleidt, K. Holinde, and C. Elster, Physics Reports **149**, 1 (1987).

[6] R. Machleidt, Phys. Rev. C **63**, 024001 (2001).

[7] M. G. Mayer, Phys. Rev. **74**, 235 (1948).

[8] M. G. Mayer, Phys. Rev. **75**, 1969 (1949).

[9] O. Haxel, J. H. D. Jensen, and H. E. Suess, Phys. Rev. **75**, 1766 (1949).

[10] M. Mayer and J. Jensen, *Elementary Theory of Nuclear Shell Structure*, Structure of matter series (John Wiley & Sons, 1955).

[11] M. Gell-Mann, Phys. Lett. **8**, 214 (1964).

[12] G. Zweig, Devel. in the Quark Theory of Hadrons, Volume 1. Edited by D. Lichtenberg and S. Rosen. pp. 22-101 , 22 (1964).

[13] E. D. Bloom, D. H. Coward, H. DeStaebler, J. Drees, G. Miller, L. W. Mo, R. E. Taylor, M. Breidenbach, J. I. Friedman, G. C. Hartmann, and H. W. Kendall, Phys. Rev. Lett. **23**, 930 (1969).

[14] M. Breidenbach, J. I. Friedman, H. W. Kendall, E. D. Bloom, D. H. Coward, H. DeStaebler, J. Drees, L. W. Mo, and R. E. Taylor, Phys. Rev. Lett. **23**, 935 (1969).

[15] S. L. Adler, Remarks on the history of quantum chromodynamics, arXiv:hep-ph/0412297 .

[16] H. Leutwyler, Mod. Phys. Lett. **A29**, 1430023 (2014).

[17] R. Machleidt, in *Proceedings, International Conference on Nuclear Theory in the Supercomputing Era (NTSE-2013): Ames, Iowa, USA, May 13-17, 2013* (2013) p. 336, arXiv:1308.0103 .

[18] R. B. Wiringa, V. G. J. Stoks, and R. Schiavilla, Phys. Rev. C **51**, 38 (1995).

[19] S. C. Pieper, V. R. Pandharipande, R. B. Wiringa, and J. Carlson, Phys. Rev. C **64**, 014001 (2001).

[20] J. Carlson, Phys. Rev. C **36**, 2026 (1987).

[21] S. C. Pieper and R. B. Wiringa, Ann. Rev. Nucl. Part. Sci. **51**, 53 (2001).

[22] S. C. Pieper, R. B. Wiringa, and J. Carlson, Phys. Rev. C **70**, 054325 (2004).

[23] S. Weinberg, Phys. Lett. B **251**, 288 (1990).

[24] S. Weinberg, Nucl. Phys. B **363**, 3 (1991).

[25] S. Weinberg, Phys. Lett. B **295**, 114 (1992).

[26] E. Epelbaum, H.-W. Hammer, and U.-G. Meißner, Rev. Mod. Phys. **81**, 1773 (2009).

[27] R. Machleidt and D. R. Entem, Phys. Rep. **503**, 1 (2011).

[28] H.-W. Hammer, A. Nogga, and A. Schwenk, Rev. Mod. Phys. **85**, 197 (2013).

[29] S. Bacca and S. Pastore, J. Phys. G: Nucl. Part. Phys. **41**, 123002 (2014).

[30] E. Epelbaum, H. Krebs, and U.-G. Meißner, Eur. Phys. J. A **51**, 53 (2015).

[31] E. Epelbaum, H. Krebs, and U.-G. Meißner, Phys. Rev. Lett. **115**, 122301 (2015).

[32] A. Ekström, G. R. Jansen, K. A. Wendt, G. Hagen, T. Papenbrock, B. D. Carlsson, C. Forssén, M. Hjorth-Jensen, P. Navrátil, and W. Nazarewicz, Phys. Rev. C **91**, 051301(R) (2015).

[33] B. D. Carlsson, A. Ekström, C. Forssén, D. F. Strömberg, G. R. Jansen, O. Lilja, M. Lindby, B. A. Mattsson, and K. A. Wendt, Phys. Rev. X **6**, 011019 (2016).

[34] D. R. Entem, R. Machleidt, and Y. Nosyk, Phys. Rev. C **96**, 024004 (2017).

[35] R. J. Furnstahl, N. Klco, D. R. Phillips, and S. Wesolowski, Phys. Rev. C **92**, 024005 (2015).

[36] R. J. Furnstahl, D. R. Phillips, and S. Wesolowski, J. Phys. G **42**, 034028 (2015).

[37] M. R. Schindler and D. R. Phillips, Ann. Phys. **324**, 682 (2009), [Erratum: Ann. Phys. **324**, 2051 (2009)].

[38] A. Gezerlis, I. Tews, E. Epelbaum, S. Gandolfi, K. Hebeler, A. Nogga, and A. Schwenk, Phys. Rev. Lett. **111**, 032501 (2013).

[39] A. Gezerlis, I. Tews, E. Epelbaum, M. Freunek, S. Gandolfi, K. Hebeler, A. Nogga, and A. Schwenk, Phys. Rev. C **90**, 054323 (2014).

[40] I. Tews, *Quantum Monte Carlo calculations with chiral effective field theory interactions*, Ph.D. thesis, Technische Universiät Darmstadt (2015).

[41] M. Piarulli, L. Girlanda, R. Schiavilla, R. Navarro Pérez, J. E. Amaro, *et al.*, Phys. Rev. C **91**, 024003 (2015).

[42] M. Piarulli, L. Girlanda, R. Schiavilla, A. Kievsky, A. Lovato, L. E. Marcucci, S. C. Pieper, M. Viviani, and R. B. Wiringa, Phys. Rev. C **94**, 054007 (2016).

[43] K. Hebeler and A. Schwenk, Phys. Rev. C **82**, 014314 (2010).

[44] K. Hebeler, S. K. Bogner, R. J. Furnstahl, A. Nogga, and A. Schwenk, Phys. Rev. C **83**, 031301(R) (2011).

[45] K. Hebeler and R. J. Furnstahl, Phys. Rev. C **87**, 031302 (2013).

[46] K. Hebeler, J. M. Lattimer, C. J. Pethick, and A. Schwenk, Astrophys. J. **773**, 11 (2013).

[47] I. Tews, T. Krüger, K. Hebeler, and A. Schwenk, Phys. Rev. Lett. **110**, 032504 (2013).

[48] G. Baardsen, A. Ekström, G. Hagen, and M. Hjorth-Jensen, Phys. Rev. C **88**, 054312 (2013).

[49] A. Carbone, A. Polls, and A. Rios, Phys. Rev. C **88**, 044302 (2013).

[50] S. Gandolfi, A. Lovato, J. Carlson, and K. E. Schmidt, Phys. Rev. C **90**, 061306 (2014).

[51] N. Kaiser, Phys. Rev. C **91**, 065201 (2015).

[52] C. Wellenhofer, J. W. Holt, and N. Kaiser, Phys. Rev. C **92**, 015801 (2015).

[53] C. Drischler, K. Hebeler, and A. Schwenk, Phys. Rev. C **93**, 054314 (2016).

[54] J. M. Lattimer and M. Prakash, Science **304**, 536 (2004).

[55] M. Arnould, S. Goriely, and K. Takahashi, Phys. Rep. **450**, 97 (2007).

[56] M. Busso, R. Gallino, and G. J. Wasserburg, Ann. Rev. Astron. Astrophys. **37**, 239 (1999).

[57] M. Arnould and S. Goriely, Phys. Rep. **384**, 1 (2003).

[58] M. Langevin, E. Quiniou, M. Bernas, J. Galin, J. Jacmart, F. Naulin, F. Pougheon, R. Anne, C. Détraz, D. Guerreau, *et al.*, Phys. Lett. B **150**, 71 (1985).

[59] D. Guillemaud-Mueller, J. C. Jacmart, E. Kashy, A. Latimier, A. C. Mueller, F. Pougheon, A. Richard, Y. E. Penionzhkevich, A. G. Artuhk, A. V. Belozyorov, *et al.*, Phys. Rev. C **41**, 937 (1990).

[60] O. Tarasov, R. Allatt, J. Angélique, R. Anne, C. Borcea, Z. Dlouhy, C. Donzaud, S. Grévy, D. Guillemaud-Mueller, M. Lewitowicz, *et al.*, Phys. Lett. B **409**, 64 (1997).

[61] C. Caesar, J. Simonis, T. Adachi, Y. Aksyutina, J. Alcantara, S. Altstadt, H. Alvarez-Pol, N. Ashwood, T. Aumann, V. Avdeichikov, *et al.* (R3B collaboration), Phys. Rev. C **88**, 034313 (2013).

[62] Y. Kondo, T. Nakamura, R. Tanaka, R. Minakata, S. Ogoshi, N. A. Orr, N. L. Achouri, T. Aumann, H. Baba, F. Delaunay, *et al.*, Phys. Rev. Lett. **116**, 102503 (2016).

[63] T. Aumann and H. Simon, Nucl. Phys. News **24**, 5 (2014).

[64] H. Hergert, S. K. Bogner, T. D. Morris, A. Schwenk, and K. Tsukiyama, Phys. Rept. **621**, 165 (2016).

[65] J. Carlson, S. Gandolfi, F. Pederiva, S. C. Pieper, R. Schiavilla, K. E. Schmidt, and R. B. Wiringa, Rev. Mod. Phys. **87**, 1067 (2015).

[66] J. E. Lynn, I. Tews, J. Carlson, S. Gandolfi, A. Gezerlis, K. E. Schmidt, and A. Schwenk, Phys. Rev. C **96**, 054007 (2017).

[67] D. Lonardoni, S. Gandolfi, J. E. Lynn, C. Petrie, J. Carlson, K. E. Schmidt, and A. Schwenk, Phys. Rev. C **97**, 044318 (2018).

[68] D. Lonardoni, J. Carlson, S. Gandolfi, J. E. Lynn, K. E. Schmidt, A. Schwenk, and X. B. Wang, Phys. Rev. Lett. **120**, 122502 (2018).

[69] D. Lonardoni, A. Lovato, S. C. Pieper, and R. B. Wiringa, Phys. Rev. C **96**, 024326 (2017).

[70] P. Navrátil and W. E. Ormand, Phys. Rev. C **68**, 034305 (2003).

[71] P. Navrátil, S. Quaglioni, I. Stetcu, and B. R. Barrett, J. Phys. G **36**, 083101 (2009).

[72] R. Roth, S. Binder, K. Vobig, A. Calci, J. Langhammer, and P. Navrátil, Phys. Rev. Lett. **109**, 052501 (2012).

[73] B. R. Barrett, P. Navrátil, and J. P. Vary, Prog. Part. Nucl. Phys. **69**, 131 (2013).

[74] E. Dikmen, A. F. Lisetski, B. R. Barrett, P. Maris, A. M. Shirokov, and J. P. Vary, Phys. Rev. C **91**, 064301 (2015).

[75] K. Kowalski, D. J. Dean, M. Hjorth-Jensen, T. Papenbrock, and P. Piecuch, Phys. Rev. Lett. **92**, 132501 (2004).

[76] A. Signoracci, T. Duguet, G. Hagen, and G. Jansen, Phys. Rev. C **91**, 064320 (2015).

[77] G. Hagen, T. Papenbrock, A. Ekström, K. Wendt, G. Baardsen, S. Gandolfi, M. Hjorth-Jensen, and C. J. Horowitz, Phys. Rev. C **89**, 014319 (2014).

[78] G. Hagen, T. Papenbrock, M. Hjorth-Jensen, and D. J. Dean, Rep. Prog. Phys. **77**, 096302 (2014).

[79] G. R. Jansen, J. Engel, G. Hagen, P. Navrátil, and A. Signoracci, Phys. Rev. Lett. **113**, 142502 (2014).

[80] G. R. Jansen, A. Signoracci, G. Hagen, and P. Navrátil, Phys. Rev. C **94**, 011301(R) (2016).

[81] K. Tsukiyama, S. K. Bogner, and A. Schwenk, Phys. Rev. C **85**, 061304(R) (2012).

[82] S. K. Bogner, H. Hergert, J. D. Holt, A. Schwenk, S. Binder, A. Calci, J. Langhammer, and R. Roth, Phys. Rev. Lett. **113**, 142501 (2014).

[83] S. R. Stroberg, A. Calci, H. Hergert, J. D. Holt, S. K. Bogner, R. Roth, and A. Schwenk, Phys. Rev. Lett. **118**, 032502 (2017).

[84] K. Tsukiyama, S. K. Bogner, and A. Schwenk, Phys. Rev. Lett. **106**, 222502 (2011).

[85] H. Hergert, S. K. Bogner, S. Binder, A. Calci, J. Langhammer, R. Roth, and A. Schwenk, Phys. Rev. C **87**, 034307 (2013).

[86] N. M. Parzuchowski, T. D. Morris, and S. K. Bogner, Phys. Rev. C **95**, 044304 (2017).

[87] J. Simonis, S. R. Stroberg, K. Hebeler, J. D. Holt, and A. Schwenk, Phys. Rev. C **96**, 014303 (2017).

[88] V. Somà, T. Duguet, and C. Barbieri, Phys. Rev. C **84**, 064317 (2011).

[89] V. Somà, C. Barbieri, and T. Duguet, Phys. Rev. C **87**, 011303 (2013).

[90] V. Somà, A. Cipollone, C. Barbieri, P. Navrátil, and T. Duguet, Phys. Rev. C **89**, 061301(R) (2014).

[91] J. Goldstone, Proceedings of the Royal Society of London A: Mathematical, Physical and Engineering Sciences **239**, 267 (1957).

[92] B. R. Barrett and M. W. Kirson, Nucl. Phys. A **148**, 145 (1970).

[93] J. D. Holt, J. Menéndez, J. Simonis, and A. Schwenk, Phys. Rev. C **90**, 024312 (2014).

[94] L. Coraggio, A. Covello, A. Gargano, N. Itaco, and T. T. S. Kuo, Prog. Part. Nucl. Phys. **62**, 135 (2009).

[95] M. Hjorth-Jensen, T. T. S. Kuo, and E. Osnes, Phys. Rep. **261**, 125 (1995).

[96] J. Simonis, K. Hebeler, J. D. Holt, J. Menéndez, and A. Schwenk, Phys. Rev. C **93**, 011302(R) (2016).

[97] N. Tsunoda, T. Otsuka, N. Shimizu, M. Hjorth-Jensen, K. Takayanagi, and T. Suzuki, Phys. Rev. C **95**, 021304 (2017).

[98] W. Nazarewicz, J. Phys. G **43**, 044002 (2016).

[99] J. Erler, N. Birge, M. Kortelainen, W. Nazarewicz, E. Olsen, A. M. Perhac, and M. Stoitsov, Nature **486**, 509 (2012).

[100] P. Hohenberg and W. Kohn, Phys. Rev. **136**, B864 (1964).

[101] J. Dobaczewski, J. Phys. Conf. Ser. **312**, 092002 (2011).

[102] S. Goriely, M. Samyn, J. M. Pearson, and M. Onsi, Nucl. Phys. A **750**, 425 (2005).

[103] S. Goriely, N. Chamel, and J. M. Pearson, Phys. Rev. C **82**, 035804 (2010).

[104] S. Goriely, N. Chamel, and J. M. Pearson, Phys. Rev. C **88**, 024308 (2013).

[105] W. Huang, G. Audi, M. Wang, F. Kondev, S. Naimi, and X. Xu, Chin. Phys. C **41**, 030002 (2017).

[106] E. Gebrerufael, K. Vobig, H. Hergert, and R. Roth, Phys. Rev. Lett. **118**, 152503 (2017).

[107] I. Tews, S. Gandolfi, A. Gezerlis, and A. Schwenk, Phys. Rev. C **93**, 024305 (2016).

[108] V. Durant, P. Capel, L. Huth, A. Balantekin, and A. Schwenk, Phy. Lett. B **782**, 668 (2018).

[109] J. E. Lynn, I. Tews, J. Carlson, S. Gandolfi, A. Gezerlis, K. E. Schmidt, and A. Schwenk, Phys. Rev. Lett. **116**, 062501 (2016).

[110] A. Lovato, O. Benhar, S. Fantoni, and K. E. Schmidt, Phys. Rev. C **85**, 024003 (2012).

[111] L. Huth, I. Tews, J. E. Lynn, and A. Schwenk, Phys. Rev. C **96**, 054003 (2017).

[112] A. Nogga, R. G. E. Timmermans, and U. van Kolck, Phys. Rev. C **72**, 054006 (2005).

[113] I. Tews, L. Huth, and A. Schwenk, (2018), arXiv:1806.00233 .

[114] B. A. Brown and W. A. Richter, Phys. Rev. C **74**, 034315 (2006).

[115] L. Huth, V. Durant, J. Simonis, and A. Schwenk, arXiv:1804.04990 .

[116] E. Caurier, G. Martinez-Pinedo, F. Nowacki, A. Poves, and A. P. Zuker, Rev. Mod. Phys. **77**, 427 (2005).

[117] F. Wilczek, Annu. Rev. Nucl. Part. Sci. **32**, 177 (1982).

[118] G. Prosperi, M. Raciti, and C. Simolo, Prog. Part. Nucl. Phys. **58**, 387 (2007).

[119] A. Deur, S. J. Brodsky, and G. F. de Téramond, Prog. Part. Nucl. Phys. **90**, 1 (2016).

[120] S. R. Beane, W. Detmold, K. Orginos, and M. J. Savage, Prog. Part. Nucl. Phys. **66**, 1 (2011).

[121] S. R. Beane, P. F. Bedaque, K. Orginos, and M. J. Savage, Phys. Rev. Lett. **97**, 012001 (2006).

[122] R. A. Briceño, Z. Davoudi, and T. C. Luu, J. Phys. G **42**, 023101 (2015).

[123] S. R. Beane, E. Chang, S. Cohen, W. Detmold, H. W. Lin, K. Orginos, A. Parreño, M. J. Savage, and B. C. Tiburzi (NPLQCD Collaboration), Phys. Rev. Lett. **113**, 252001 (2014).

[124] K. Orginos, A. Parreño, M. J. Savage, S. R. Beane, E. Chang, and W. Detmold (NPLQCD Collaboration), Phys. Rev. D **92**, 114512 (2015).

[125] F. Winter, W. Detmold, A. S. Gambhir, K. Orginos, M. J. Savage, P. E. Shanahan, and M. L. Wagman (NPLQCD Collaboration), Phys. Rev. D **96**, 094512 (2017).

[126] W. Detmold, K. Orginos, A. Parreño, M. J. Savage, B. C. Tiburzi, S. R. Beane, and E. Chang (NPLQCD Collaboration), Phys. Rev. Lett. **116**, 112301 (2016).

[127] S. Dürr, Z. Fodor, J. Frison, C. Hoelbling, R. Hoffmann, S. D. Katz, S. Krieg, T. Kurth, L. Lellouch, T. Lippert, K. K. Szabo, and G. Vulvert, Science **322**, 1224 (2008).

[128] C. Patrignani *et al.* (Particle Data Group), Chin. Phys. C **40**, 100001 (2016).

[129] H. D. Politzer, Phys. Rev. Lett. **30**, 1346 (1973).

[130] K. G. Wilson, Phys. Rev. D **10**, 2445 (1974).

[131] R. Aaij, B. Adeva, M. Adinolfi, Z. Ajaltouni, S. Akar, J. Albrecht, F. Alessio, M. Alexander, S. Ali, G. Alkhazov, *et al.* (LHCb Collaboration), Phys. Rev. Lett. **118**, 022003 (2017).

[132] R. Aaij, B. Adeva, M. Adinolfi, A. Affolder, Z. Ajaltouni, S. Akar, J. Albrecht, F. Alessio, M. Alexander, S. Ali, *et al.* (LHCb Collaboration), Phys. Rev. Lett. **115**, 072001 (2015).

[133] H. Fritzsch, M. Gell-Mann, and H. Leutwyler, Phys. Lett. B **47**, 365 (1973).

[134] A. J. MacFarlane, A. Sudbery, and P. H. Weisz, *Communications in Mathematical Physics*, (1969).

[135] J. Goldstone, A. Salam, and S. Weinberg, Phys. Rev. **127**, 965 (1962).

[136] C. Dominguez, Nucl. Phys. B - Proc. Suppl. **207-208**, 281 (2010), proceedings of the QCD 10: 15th High-Energy Physics International Conference on Quantum Chromodynamics.

[137] N. Kaiser, Phys. Rev. C **62**, 024001 (2000).

[138] N. Kaiser, Phys. Rev. C **63**, 044010 (2001).

[139] A. Ekström, G. Hagen, T. D. Morris, T. Papenbrock, and P. D. Schwartz, Phys. Rev. C **97**, 024332 (2018).

[140] H. Krebs, A. Gasparyan, and E. Epelbaum, Phys. Rev. C **85**, 054006 (2012).

[141] E. Epelbaum, H. Krebs, and U.-G. Meißner, Nucl. Phys. A **806**, 65 (2008).

[142] H. Krebs, E. Epelbaum, and U.-G. Meißner, Eur. Phys. J. A **32**, 127 (2007).

[143] V. R. Pandharipande, D. R. Phillips, and U. v. Kolck, Phys. Rev. C **71**, 064002 (2005).

[144] H. Krebs, A. M. Gasparyan, and E. Epelbaum, arXiv:1803.09613 .

[145] E. Epelbaum, Prog. Part. Nucl. Phys. **57**, 654 (2006).

[146] E. Epelbaum, arXiv:1001.3229 .

[147] D. R. Entem, N. Kaiser, R. Machleidt, and Y. Nosyk, Phys. Rev. C **92**, 064001 (2015).

[148] U. van Kolck, Phys. Rev. C **49**, 2932 (1994).

[149] N. Kalantar-Nayestanaki, E. Epelbaum, J. G. Messchendorp, and A. Nogga, Reports on Progress in Physics **75**, 016301 (2012).

[150] K. Hebeler, J. D. Holt, J. Menéndez, and A. Schwenk, Ann. Rev. Nucl. Part. Sci. **65**, 457 (2015).

[151] J. Liu, M. P. Mendenhall, A. T. Holley, H. O. Back, T. J. Bowles, L. J. Broussard, R. Carr, S. Clayton, S. Currie, B. W. Filippone, *et al.* (UCNA Collaboration), Phys. Rev. Lett. **105**, 181803 (2010).

[152] R. Machleidt and F. Sammarruca, Physica Scripta **91**, 083007 (2016).

[153] E. Epelbaum, W. Glöckle, and U.-G. Meißner, Nucl. Phys. A **747**, 362 (2005).

[154] N. Kaiser, R. Brockmann, and W. Weise, Nucl. Phys. A **625**, 758 (1997).

[155] E. Epelbaum, W. Glöckle, and U.-G. Meißner, Eur. Phys. J. A **19**, 401 (2004).

[156] R. A. Arndt, W. J. Briscoe, I. I. Strakovsky, and R. L. Workman, Phys. Rev. C **74**, 045205 (2006).

[157] M. C. M. Rentmeester, R. G. E. Timmermans, and J. J. de Swart, Phys. Rev. C **67**, 044001 (2003).

[158] M. C. M. Rentmeester, R. G. E. Timmermans, J. L. Friar, and J. J. de Swart, Phys. Rev. Lett. **82**, 4992 (1999).

[159] D. R. Entem and R. Machleidt, Phys. Rev. C **68**, 041001(R) (2003).

[160] N. Fettes, U.-G. Meißner, and S. Steininger, Nucl. Phys. A **640**, 199 (1998).

[161] N. Kaiser, Phys. Rev. C **64**, 057001 (2001).

[162] V. G. J. Stoks, R. A. M. Klomp, M. C. M. Rentmeester, and J. J. de Swart, Phys. Rev. C **48**, 792 (1993), Nijmegen NN online program, http://nn-online.org/.

[163] B. A. Lippmann and J. Schwinger, Phys. Rev. **79**, 469 (1950).

[164] B. D. Carlsson, Phys. Rev. C **95**, 034002 (2017).

[165] M. Piarulli, A. Baroni, L. Girlanda, A. Kievsky, A. Lovato, E. Lusk, L. E. Marcucci, S. C. Pieper, R. Schiavilla, M. Viviani, and R. B. Wiringa, Phys. Rev. Lett. **120**, 052503 (2018).

[166] J. E. Lynn, J. Carlson, E. Epelbaum, S. Gandolfi, A. Gezerlis, and A. Schwenk, Phys. Rev. Lett. **113**, 192501 (2014).

[167] P. Klos, J. E. Lynn, I. Tews, S. Gandolfi, A. Gezerlis, H. W. Hammer, M. Hoferichter, and A. Schwenk, Phys. Rev. C **94**, 054005 (2016).

[168] J.-W. Chen, W. Detmold, J. E. Lynn, and A. Schwenk, Phys. Rev. Lett. **119**, 262502 (2017).

[169] S. Gandolfi, H.-W. Hammer, P. Klos, J. E. Lynn, and A. Schwenk, Phys. Rev. Lett. **118**, 232501 (2017).

[170] A. Dyhdalo, R. J. Furnstahl, K. Hebeler, and I. Tews, Phys. Rev. C **94**, 034001 (2016).

[171] E. Epelbaum, A. Nogga, W. Glöckle, H. Kamada, U.-G. Meißner, and H. Witała, Phys. Rev. C **66**, 064001 (2002).

[172] A. Schwenk and B. Friman, Phys. Rev. Lett. **92**, 082501 (2004).

[173] M. Conze, H. Feldmeier, and P. Manakos, Phys. Lett. B **43**, 101 (1973).

[174] S. K. Bogner, T. T. S. Kuo, and A. Schwenk, Phys. Rep. **386**, 1 (2003).

[175] S. K. Bogner, R. J. Furnstahl, and A. Schwenk, Prog. Part. Nucl. Phys. **65**, 94 (2010).

[176] S. D. Glazek and K. G. Wilson, Phys. Rev. D **48**, 5863 (1993).

[177] S. D. Glazek and K. G. Wilson, Phys. Rev. D **49**, 4214 (1994).

[178] F. Wegner, Ann. Phys. **506**, 77 (1994).

[179] S. K. Bogner, R. J. Furnstahl, and R. J. Perry, Phys. Rev. C **75**, 061001(R) (2007).

[180] R. Roth, S. Reinhardt, and H. Hergert, Phys. Rev. C **77**, 064003 (2008).

[181] R. Roth, J. Langhammer, A. Calci, S. Binder, and P. Navrátil, Phys. Rev. Lett. **107**, 072501 (2011).

[182] R. J. Furnstahl, Nucl. Phys. Proc. Suppl. **228**, 139 (2012).

[183] R. J. Furnstahl and K. Hebeler, Rep. Prog. Phys. **76**, 126301 (2013).

[184] S. Binder, J. Langhammer, A. Calci, and R. Roth, Phys. Lett. B **736**, 119 (2014).

[185] R. Roth, A. Calci, J. Langhammer, and S. Binder, Phys. Rev. C **90**, 024325 (2014).

[186] H. Feldmeier, T. Neff, R. Roth, and J. Schnack, Nucl. Phys. A **632**, 61 (1998).

[187] A. D. Lee, "A Python package for first- and second-order automatic differentation," `http://pythonhosted.org/ad/`.

[188] J. Nocedal and S. J. Wright, *Numerical Optimization*, 2nd ed. (Springer, New York, 2006) p. 136.

[189] S. Aoki, Eur. Phys. J. A **49**, 81 (2013).

[190] P. Capel, V. Durant, L. Huth, H.-W. Hammer, D. R. Phillips, and A. Schwenk, J. Phys. Conf. Ser. **1023**, 012010 (2018).

[191] H. G. Bohlen, E. Stiliaris, B. Gebauer, W. von Oertzen, M. Wilpert, T. Wilpert, A. Ostrowski, D. T. Khoa, A. S. Demyanova, and A. A. Ogloblin, Z. Phys. A **346**, 189 (1993).

[192] P. Navrátil, Few-Body Syst. **41**, 117 (2007).

[193] S. Weinberg, Physica A **96**, 327 (1979).

[194] S. R. Beane, P. F. Bedaque, L. Childress, A. Kryjevski, J. McGuire, and U. van Kolck, Phys. Rev. A **64**, 042103 (2001).

[195] D. B. Kaplan, M. J. Savage, and M. B. Wise, Nucl. Phys. B **534**, 329 (1998).

[196] D. B. Kaplan, M. J. Savage, and M. B. Wise, Phys. Lett. B **424**, 390 (1998).

[197] S. Fleming, T. Mehen, and I. W. Stewart, Nucl. Phys. A **677**, 313 (2000).

[198] S. Beane, P. Bedaque, M. Savage, and U. van Kolck, Nucl. Phys. A **700**, 377 (2002).

[199] S. R. Beane, D. B. Kaplan, and A. Vuorinen, Phys. Rev. C **80**, 011001 (2009).

[200] M. C. Birse, Phys. Rev. C **74**, 014003 (2006).

[201] D. R. Phillips and T. D. Cohen, Phys. Lett. B **390**, 7 (1997).

[202] E. Epelbaum, U.-G. Meißner, W. Glöckle, and C. Elster, Phys. Rev. C **65**, 044001 (2002).

[203] M. Seidlitz, P. Reiter, R. Altenkirch, B. Bastin, C. Bauer, A. Blazhev, N. Bree, B. Bruyneel, P. A. Butler, J. Cederkäll, *et al.*, Phys. Rev. C **89**, 024309 (2014).

[204] V. Tripathi, S. L. Tabor, P. F. Mantica, C. R. Hoffman, M. Wiedeking, A. D. Davies, S. N. Liddick, W. F. Mueller, T. Otsuka, A. Stolz, *et al.*, Phys. Rev. Lett. **94**, 162501 (2005).

[205] V. Tripathi, S. L. Tabor, P. F. Mantica, Y. Utsuno, P. Bender, J. Cook, C. R. Hoffman, S. Lee, T. Otsuka, J. Pereira, *et al.*, Phys. Rev. C **76**, 021301 (2007).

[206] P. Doornenbal, H. Scheit, N. Kobayashi, N. Aoi, S. Takeuchi, K. Li, E. Takeshita, Y. Togano, H. Wang, S. Deguchi, *et al.*, Phys. Rev. C **81**, 041305 (2010).

[207] S. M. Lenzi, F. Nowacki, A. Poves, and K. Sieja, Phys. Rev. C **82**, 054301 (2010).

[208] G. Wilson, W. Catford, N. Orr, C. Diget, A. Matta, G. Hackman, S. Williams, I. Celik, N. Achouri, H. A. Falou, *et al.*, Phys. Lett. B **759**, 417 (2016).

[209] M. Arienzo, Atoms **1**, 2 (2013).

[210] A. de SHALIT and I. TALMI, eds., *Nuclear Shell Theory*, Pure and Applied Physics, Vol. 14 (Elsevier, 1963) pp. 245 – 260.

[211] E. Caurier and F. Nowacki, Acta Phys. Polon. B **30**, 705 (1999).

[212] S. König, S. K. Bogner, R. J. Furnstahl, S. N. More, and T. Papenbrock, Phys. Rev. C **90**, 064007 (2014).

[213] M. Wang, G. Audi, A. H. Wapstra, F. G. Kondev, M. MacCormick, X. Xu, and B. Pfeiffer, Chin. Phys. C **36**, 1603 (2012).

[214] J. Duflo and A. Zuker, Phys. Rev. C **52**, R23 (1995).

[215] http://www.nndc.bnl.gov/ensdf/, .

[216] P. E. Gill and W. Murray, SIAM Journal on Numerical Analysis **15**, 977 (1978).

[217] J. A. Nelder and R. Mead, The Computer Journal **7**, 308 (1965).

[218] S. M. Wild, J. Sarich, and N. Schunck, J. Phys. G **42**, 034031 (2015).

[219] T. Munson, J. Sarich, S. M. Wild, S. Benson, and J. Curfman McInne, Technical Memorandum ANL/MCS-TM-322, Argonne National Laboratory, Argonne, Illinois (2012), see http://www.mcs.anl.gov/tao.

[220] A. Arima, S. Cohen, R. Lawson, and M. MacFarlane, Nucl. Phys. A **108**, 94 (1968).

[221] T. Otsuka, T. Suzuki, J. D. Holt, A. Schwenk, and Y. Akaishi, Phys. Rev. Lett. **105**, 032501 (2010).

[222] T. Otsuka, T. Suzuki, M. Honma, Y. Utsuno, N. Tsunoda, K. Tsukiyama, and M. Hjorth-Jensen, Phys. Rev. Lett. **104**, 012501 (2010).

[223] J. D. Holt, T. Otsuka, A. Schwenk, and T. Suzuki, J. Phys. G **39**, 085111 (2012).

[224] Z. Elekes, Z. Dombrádi, N. Aoi, S. Bishop, Z. Fülöp, J. Gibelin, T. Gomi, Y. Hashimoto, N. Imai, N. Iwasa, *et al.*, Phys. Rev. Lett. **98**, 102502 (2007).

[225] A. Schiller, N. Frank, T. Baumann, D. Bazin, B. A. Brown, J. Brown, P. A. DeYoung, J. E. Finck, A. Gade, J. Hinnefeld, *et al.*, Phys. Rev. Lett. **99**, 112501 (2007).

[226] L. Cáceres, A. Lepailleur, O. Sorlin, M. Stanoiu, D. Sohler, Z. Dombrádi, S. K. Bogner, B. A. Brown, H. Hergert, J. D. Holt, *et al.*, Phys. Rev. C **92**, 014327 (2015).

[227] Z. Vajta, M. Stanoiu, D. Sohler, G. R. Jansen, F. Azaiez, Z. Dombrádi, O. Sorlin, B. A. Brown, M. Belleguic, C. Borcea, *et al.*, Phys. Rev. C **89**, 054323 (2014).

[228] M. Vandebrouck, A. Lepailleur, O. Sorlin, T. Aumann, C. Caesar, M. Holl, V. Panin, F. Wamers, S. R. Stroberg, J. D. Holt, *et al.* (R3B collaboration), Phys. Rev. C **96**, 054305 (2017).

[229] J. P. Elliott and T. H. R. Skyrme, Proceedings of the Royal Society of London A: Mathematical, Physical and Engineering Sciences **232**, 561 (1955).

[230] H. A. Bethe and M. E. Rose, Phys. Rev. **51**, 283 (1937).

[231] P. Navrátil, G. P. Kamuntavičius, and B. R. Barrett, Phys. Rev. C **61**, 044001 (2000).

[232] G. Hagen, T. Papenbrock, and D. J. Dean, Phys. Rev. Lett. **103**, 062503 (2009).

[233] D. Gloeckner and R. Lawson, Phys. Lett. B **53**, 313 (1974).

[234] R. R. Whitehead, A. Watt, B. J. Cole, and I. Morrison, Adv. Nucl. Phys. **9**, 123 (1977).

[235] R. Roth, J. R. Gour, and P. Piecuch, Phys. Lett. B **679**, 334 (2009).

[236] F. Nowacki and A. Poves, Phys. Rev. C **79**, 014310 (2009).

[237] P. Moller, J. Nix, W. Myers, and W. Swiatecki, Atomic Data and Nuclear Data Tables **59**, 185 (1995).

[238] S. Goriely, N. Chamel, and J. M. Pearson, Phys. Rev. C **93**, 034337 (2016).

[239] S. Goriely, N. Chamel, and J. M. Pearson, J. Phys. Conf. Ser. **665**, 012038 (2016).

[240] P. Doornenbal, H. Scheit, S. Takeuchi, Y. Utsuno, N. Aoi, K. Li, M. Matsushita, D. Steppenbeck, H. Wang, H. Baba, E. Ideguchi, *et al.*, Phys. Rev. C **95**, 041301 (2017).

[241] I. Tews, J. Carlson, S. Gandolfi, and S. Reddy, Astrophys. J. **860**, 149 (2018).

[242] D. A. Varshalovich, A. N. Moskalev, and V. K. Khersonskii, *Quantum Theory Of Angular Momentum* (World Scientific, Singapore, 1988).

[243] E. P. Wigner, Zeitschrift für Physik **43**, 624 (1927).

[244] C. Eckart, Rev. Mod. Phys. **2**, 305 (1930).

[245] J. J. Sakurai and J. Napolitano, *Modern Quantum Mechanics, Second Edition* (Pearson Education Inc., San Fransico, 2011).

[246] K. Erkelenz, R. Alzetta, and K. Holinde, Nucl. Phys. A **176**, 413 (1971).

[247] J. Golak, D. Rozpędzik, R. Skibiński, K. Topolnicki, H. Witała, W. Glöckle, A. Nogga, E. Epelbaum, H. Kamada, C. Elster, and I. Fachruddin, Eur. Phys. J. A **43**, 241 (2010).

[248] G. P. Kamuntavičius, R. K. Kalinauskas, B. R. Barrett, S. Mickevičius, and D. Germanas, Nucl. Phys. A **695**, 191 (2001).

Acknowledgments

I want to express my gratitude towards Prof. Achim Schwenk for providing me with the great opportunity, freedom, and council to follow my scientific interests. I also want to thank him for the many opportunities to present my research, like the TRIUMF summer institute, the collaboration with Dr. Ingo Tews in Seattle, and the ISNET-5 conference in York, to name a few.

I want to thank Prof. Jens Braun for taking the time to be the second reviewer of this thesis.

Special thanks goes to Sabrina Schäfer, Dr. Ingo Tews, Prof. Achim Schwenk, Dr. Richard Trippel, Victoria Durant, and Dr. Toño Coello for proof reading my thesis.

Furthermore, I want to thank my close collaborators Dr. Ingo Tews, Victoria Durant, Dr. Joel E. Lynn, Prof. Achim Schwenk, Apl.Prof. Pierre Capel, and Dr. Johannes Simonis. In addition I want to thank Prof. G. F. Bertsch and Prof. H. Feldmeier for usefull discussions, Prof. B. A. Brown for communicating to us the USDA/B experimental data set, and Institute for Nuclear Theory in Seattle for its hospitality.

As life consists of much more than just work, I must express my sincere thanks to my friends and colleagues in the theory building and especially the members of the STRONGINT group: Toño, Victoria, Svenja, Kai, Jan, Philipp, Sebastian, Joel, Rodric, Sabrina, Marc, Achim, Corbinian, and Lars, as well as the former members I had the pleasure of meeting: Alexander, Pierre, Arianna, Christian, Martin, Thomas, Johannes, Ingo, Sulamith, and Kyle. Thank you guys for the amazing years. I also feel the strong urge to thank Richard for teaching me the importance of always locking my screen and for fighting the giants with me. Also I want to thank Roland and Stefan for their advice on countless questions considering the formalities of the doctoral defense.

Here is to my friends at home, which I will list in alphabetical order of their pet name to avoid having fewer after this sentence: Thank you AK, Chrissimaus, Flo, Hannes, Ilka, Johnny, Kai, Lari, Lea, Lina, Martin, Menne, Michael, Niko, Ritschi, Tobi, and Tui. You, ..., you all know way too much!

A large portion of my thanks goes to my family. Thank you Mum and Dad for your constant unconditional support over all the years, this would have clearly not been possible without the love and encouragement from your side. I want to further thank my aunt Ulrike and grandma Rosa for taking such good care of me and my brother when you were needed.
Thank you Sabrina, thank you for your support and love. I cannot even begin to fathom how lucky I am that our paths have crossed.

Kudos to the unsung heroes, open source and free-ware developers all around the globe, especially to the architects of Python and Python's numpy, scipy, ad, and matplotlib modules, as well as the whole community behind it. Please keep on making modern science possible. I also want to thank the developers of the ANTOINE shell-model code for making it available publicly.

This work was supported by the ERC Grant No. 307986 STRONGINT and the German Research Foundation Contract No. SFB 1245.

So long, and thanks for all the fish.

Curriculum Vitae

Frank **Lukas** Huth

Date of birth: 01.08.1988
Place of birth: Friedberg (Hessen), Germany

2015 – 2018	Doctoral studies in physics Technische Universität Darmstadt, Darmstadt, Germany Advisor: Prof. Ph.D. A. Schwenk
2012 – 2014	Master studies in physics Technische Universität Darmstadt, Darmstadt, Germany Gesellschaft für Schwerionenforschung (GSI), Darmstadt-Wixhausen, Germany Advisor: Prof. Dr. H. Feldmeier Thesis: "Fitting a non-local realistic interaction for low-momentum Hilbert spaces" Masters degree, 26.11.2014
2009 – 2012	Bachelor studies in physics Technische Universität Darmstadt, Darmstadt, Germany Advisor: Prof. Dr. R. Roth Thesis: "Streuphasenerhaltung in der Similarity Renormalization Group" Bachelors degree, 20.09.2012
1999 – 2008	Higher education entrance qualification Friedrich-Dessauer-Gymnasium, Aschaffenburg, Germany Abitur, 27.06.2008

Erklärung zur Dissertation

Hiermit versichere ich, die vorliegende Dissertation ohne Hilfe Dritter nur mit den angegebenen Quellen und Hilfsmitteln angefertigt zu haben. Alle Stellen, die aus Quellen entnommen wurden, sind als solche kenntlich gemacht. Diese Arbeit hat in gleicher oder ähnlicher Form noch keiner Prüfungsbehörde vorgelegen.

Darmstadt, den 25.06.2018

(Frank Lukas Huth)